



HAL
open science

Investigation of highly flexible, deployable structures : review, modelling, control, experiments and application

Noémi Friedman

► **To cite this version:**

Noémi Friedman. Investigation of highly flexible, deployable structures : review, modelling, control, experiments and application. Other. École normale supérieure de Cachan - ENS Cachan; Budapesti műszaki és gazdaságtudományi egyetem (Budapest), 2011. English. NNT : 2011DENS0060 . tel-00675481

HAL Id: tel-00675481

<https://theses.hal.science/tel-00675481>

Submitted on 1 Mar 2012

HAL is a multi-disciplinary open access archive for the deposit and dissemination of scientific research documents, whether they are published or not. The documents may come from teaching and research institutions in France or abroad, or from public or private research centers.

L'archive ouverte pluridisciplinaire **HAL**, est destinée au dépôt et à la diffusion de documents scientifiques de niveau recherche, publiés ou non, émanant des établissements d'enseignement et de recherche français ou étrangers, des laboratoires publics ou privés.

Ecole Doctorale Sciences Pratiques

61, avenue du Président Wilson
94235 CACHAN CEDEX - FRANCE
+33 1 47 40 75 77 - www.edsp.ens-cachan.fr

Mots clefs : structures déployables, structures transformables, antiprismatic

Dans cette thèse, nous nous intéressons d'abord à de possibilités d'application des structures déployables en architecture et dans l'industrie de construction. Le thème principale de la recherche a été l'étude des structures subissant de grandes déformations et en passant par état d'instabilité au cours d'un programme de chargement. Le but était la description générale du comportement mécanique d'un système modèle d'une structure antiprismatique, auto-déployable proposée par Hegedus. La plus grande importance a été mis sur exploitation du comportement de la structure au cours de son emballage, de qui a été examiné en considérant différentes possibilités de contrôle de procédure. En utilisant des simulations numériques, dont les résultats ont été vérifiés par les approches analytiques, on a clarifié le comportement mécanique du système anti prismatique, et on a donné des formules simple permettant d'évaluer de principaux paramètres géométriques et mécaniques pour faciliter le pré-dimensionnement de la structure. L'importance de l'influence de l'intensité et de la fréquence du déplacement relatif interne généré brusquement au cours d'emballage a été également étudiée. Dans le cadre de la thèse on a analysé également les caractéristiques mécaniques d'une système différent de la structure d'origine. Pour les deux différent systèmes structuraux on a préparé des modèles physiques expérimentaux, dont les résultat ont conduit aux nouveaux types des structures, lesquelles sont les structures spatiales pliables à plat. On a proposé alors quelques idées et schémas pour la possibilité d'application architecturale de systèmes treillis antiprismatiques.

Keywords: deployable structures, transformable structures, antiprismatic, yoshimura pattern

In this thesis, an extensive review on different transformable systems used in architecture and civil engineering is given. After the review, structures undergoing large displacements and instability phenomenon were highlighted. The main goal of the dissertation was to investigate the general behavior of a specific, immature self-deploying system, the antiprismatic structure proposed by Hegedus. The emphasis was mainly taken to the analysis of the packing behavior. First, a simplified planar model was identified sharing similar, highly nonlinear packing behavior. For both the 2D and the 3D structures numerical simulation of the packing was performed with different type of controls and the results were confirmed by analytical investigations. The research clarifies the mechanical behavior of the chosen system, provides tools to simulate the packing of the structure, options for control, and gives very simple approximations for main mechanical characteristics of the antiprismatic system in order to facilitate preliminary design and verification of the numerical results. The significance of snap-back behavior, occurring at the force-displacement diagram during packing was analyzed. Within the framework of the thesis a novel type of system, slightly deviating from the original one was also investigated. For the specific systems, small physical models were built and presented in this work, which led to the proposal of a novel type of expandable tube. An attempt was given to provide ideas for application of antiprismatic structures by combining the investigated system and different learnt existing systems from the architectural review.

FRIEDMAN Noémi - Investigation of highly flexible, deployable structures

ENSC - N° ordre

THESE DE DOCTORAT DE L'ECOLE NORMALE SUPERIEURE DE CACHAN

Présentée par Civilité FRIEDMAN Noémi

pour obtenir le grade de

**DOCTEUR DE L'ECOLE NORMALE SUPERIEURE DE
CACHAN**

Domaine : Génie Civil

**Titre de la thèse : Investigation of highly flexible, deployable
structures: review, modeling, control, experiments and application**



Thèse présentée et soutenue à Cachan le 09/12/2011 devant le jury composé de :

M. Jean-Marc ROELANDT	Professeur	Présidente
Mme Anikó CSÉBFALVI	Professuer	Rapporteuse
M. Luc DAVENNE	MDC, HDC	Rapporteur
M Antal LOVAS	Professeur	Examineur
M. Adnan IBRAHIMBEGOVIC	Professuer	Directeur de thèse
M. György FARKAS	Professuer	Co-directeur de thèse

Nom du Laboratoire LMT
ENS CACHAN/CNRS/UMR

61, avenue du Président Wilson, 94235 CACHAN CEDEX (France)

ENSC.....

**A thesis presented to the
Ecole Normale Supérieure de Cachan and to the
Budapest University of Technology and Economics**

by
Noémi FRIEDMAN
in fulfillment of the thesis requirement for the degree of
Doctor of Philosophy

Domain:
Civil Engineering

Title of the thesis:
**INVESTIGATION OF HIGHLY FLEXIBLE, DEPLOYABLE
STRUCTURES: REVIEW, MODELING, CONTROL, EXPERIMENTS
AND APPLICATION**

Supervisors: Prof. György FARKAS / Prof. Adnan IBRAHIMBEGOVIC

Thesis to be presented and defended in Cachan, in the 9th of december, in front of the jury members:

Mr. Jean-Marc ROELANDT	Professor	President
Mrs. Anikó CSÉBFALVI	Professor	Opponent
Mr. Luc DAVENNE	MDC, HDC	Opponent
Mr. Antal LOVAS	Professor	Examiner
Mr. Adnan IBRAHIMBEGOVIC	Professor	Supervisor of the thesis
Mr. György FARKAS	Professor	Co-supervisor of the thesis

Laboratory name: LMT de Cachan
ENS CACHAN/CNRS/UMR
61, avenue du Président Wilson, 94235 CACHAN CEDEX (France)

**INVESTIGATION OF HIGHLY FLEXIBLE, DEPLOYABLE
STRUCTURES: REVIEW, MODELING, CONTROL, EXPERIMENTS
AND APPLICATION**

**(MECANIQUE ET APPLICATION D'INGENIEUR DES
CONSTRUCTIONS ELANCEES, NOTAMMENT DES STRUCTURES
DEPLOYABLES)**

by
Noémi FRIEDMAN

LMT de Cachan
ENS Cachan
61, avenue du Président Wilson, 94235 CACHAN CEDEX (France)

Budapest University of Technology and Economics (BME)
Department of Structural Engineering, Faculty of Civil Engineering
Rakpart 3. Budapest, Hungary, H-1111

PREFACE AND ACKNOWLEDGEMENT

This work presented in this thesis was carried out at the Department of Structural Engineering, Faculty of Civil Engineering, Budapest University of Technology and Economics (**BME**) and at the Laboratory of Mechanics and Technology (LMT-Cachan) at the École Normale Supérieure de Cachan (**ENS de Cachan**) in a ‘cotutelle’ program.

First I thank both my supervisors Prof. Adnan Ibrahimbegovic and Prof. György Farkas for their constant encouragement and guidance. A debt of gratitude is owed to prof. István Hegedűs for valuable theoretical discussions and guidance.

I also would like to express my appreciation to dr. Gyula Greschik and dr. Mihály Weiner for taking their time to help me get along with some difficulties, and for sharing forward-going ideas.

I owe a grateful thank to Prof Tibor Tarnai for lending me valuable technical papers and books on the subject and encouraging me to prepare some physical models, and to Flórián Kovács for his profound revision of the thesis and useful advises for correcting.

The enormous help of Antal Schuchmann should be also herein acknowledged for his technical support in building the physical models.

I would like to thank all of the colleges at the Department of Structural Engineering in Budapest and also the ones at the LMT de Cachan.

The parallel doctoral program could not have been carried out without the scholarship received from the French Government through the French Embassy in Hungary, which I would like to herein appreciate.

Last but not least, I would like to express my grateful thanks to my parents for their continuous encouragement and support in my whole life without which I could have hardly get to the level where this PhD thesis could be born and acknowledge my family; my husband Gabor Schuchmann and my two beautiful daughters Hanna and Hédi, their continuous love and enormous patience during working on this thesis.

This work is connected to the scientific program of the ‘Development of quality-oriented and harmonized R+D+I strategy and functional model at BME’ project. This project is supported by the New Hungary Development Plan (Project ID: TÁMOP-4.2.1/B-09/1/KMR-2010-0002).

DECLARATION

The author declares that, except for commonly understood and accepted ideas, or where specific reference is made to the work of other authors, the content of this dissertation are his own work, and includes nothing that is the outcome of work done in collaboration. This dissertation has not been previously submitted in part or in whole, to any University or institution for any degree, diploma, or other qualification. This dissertation is presented in 198 pages.

ABSTRACT

In the following thesis, an extensive review on different transformable systems used in architecture and civil engineering is given. After the review, structures undergoing large displacements and instability phenomenon were highlighted. The main goal of the dissertation was to investigate the general behavior of a specific, immature self-deploying system, the antiprismatic structure proposed by Hegedűs. The emphasis was mainly taken to the analysis of the packing behavior. First, a simplified planar model was identified sharing similar, highly nonlinear packing behavior. For both the 2D and the 3D structures numerical simulation of the packing was performed with different type of controls and the results were confirmed by analytical investigations. The research clarifies the mechanical behavior of the chosen system, provides tools to simulate the packing of the structure, options for control, and gives very simple approximations for main mechanical characteristics of the antiprismatic system in order to facilitate preliminary design and verification of the numerical results. The significance of snap-back behavior, occurring at the force-displacement diagram during packing was analyzed. Within the framework of the thesis a novel type of system, slightly deviating from the original one was also investigated. For the specific systems, small physical models were built and presented in this work, which led to the proposal of a novel type of expandable tube. An attempt was given to provide ideas for application of antiprismatic structures by combining the investigated system and different learnt existing systems from the architectural review.

Keywords: *deployable structures, retractable structures, antiprism, yoshimura pattern, snap-through analysis, post-critical analysis, transformable, pop-up structure*

RESUME

Dans cette thèse, nous nous intéressons d'abord à de possibilités d'application des structures déployables en architecture et dans l'industrie de construction. Le thème principale de la recherche a été l'étude des structures subissant de grandes déformations et en passent par état d'instabilité au cours d'un programme de chargement. Le but était la description générale du comportement mécanique d'un système modèle d'une structure anti prismatique, auto-déployable proposée par Hegedus. La plus grande importance a été mis sur exploitation du comportement de la structure au cours de son emballement, de qui a été examine en considérant différentes possibilités de contrôle de procédure. Dans la première étape de l'étude, la structure spatiale a été remplacée par les études au cours d'emballement d'une structure planaire se comportant d'une manière semblable. En utilisant des simulations numériques, dont les résultats ont été vérifiés par les approches analytiques, on a clarifié le comportement mécanique du système anti prismatique, et on a donné des formules simple permettant d'évaluer de principaux paramètres géométriques et mécaniques pour facilité le pré-dimensionnement de la structure. L'importance de l'influence de l'intensité et de la fréquence du déplacement relatif interne généré brusquement au cours d'emballement a été également étudiée. Dans le cadre de la thèse on a analysé également les caractéristiques mécaniques d'une système différent de la structure d'origine. Pour les deux différent systèmes structuraux on a préparé des modèles physiques expérimentaux, dont les résultat ont conduit aux nouveaux types des structures, lesquelles sont les structures spatiales pliables à plat. On a proposé alors quelques idées et schémas pour la possibilité d'application architecturale de systèmes treillis anti prismatiques.

Mots-clé : *structures déployables, antiprisme, yoshimura pattern, analyse postcritique, grandes déformations, grands déplacements*

ABSZTRAKT

A disszertáció a nyitható-csukható szerkezetek építészeti és építőmérnöki alkalmazásáról írt áttekintéssel kezdődik. Az áttekintett szerkezeti típusok közül, a nyitás/csukás közben nagy elmozdulást szenvedő és instabil állapotban átmenő szerkezeteket választottam fő kutatási témaként. Célként a még gyerekcipőben járó, antiprizmatikus, síkba hajtható kipattanó szerkezeti rendszer mechanikai viselkedésének leírását tűztem ki. A legnagyobb hangsúlyt az összecsomagolás közbeni viselkedés feltárása kapta, amelyet különböző vezérlési lehetőségek esetén is vizsgáltam. A térbeli szerkezet mechanikai vizsgálatát egy síkbeli, hasonlóan viselkedő modell összecukási elemzésével kezdtem. Analitikus vizsgálatokkal is igazolt, numerikus szimuláció segítségével tisztáztam az antiprizmatikus rendszer mechanikai viselkedését és a tervezési fázis megkönnyítésére közelítő képleteket adtam a legfontosabb mechanikai és geometriai jellemzők becsléséhez. Megvizsgáltam a csomagolás közben fellépő, hirtelen közbenső relatív elmozdulások intenzitását és gyakorlati jelentőségét. A disszertáció keretein belül egy, az eredetitől eltérő szerkezeti rendszer mechanikai jellemzőit is elemeztem. A különböző rendszerekhez fizikai kísérleti modellek is készültek, amelyek egy új típusú, táglással síkba hajtható térbeli szerkezethez vezettek. Az antiprizmatikus rácsszerkezet alkalmazási lehetőségeire vázlatokat, ötleteket mutattam be.

Kulcsszavak: nyitható-csukható szerkezetek, antiprizma, yoshimura hajtogatási pattern, átptattanás, poszt-kritikus vizsgálat, kipattanó szerkezet

CONTENTS

Preface and acknowledgement.....	3
Declaration	4
Abstract.....	5
Absztrakt.....	6
Contents	7
1 Introduction	11
2 Architectural background: Transformable Structures in Civil Engineering and Architecture	14
2.1 The history of architectural transformable structures	14
2.2 Transformable structures by the movement of rigid panels or structural segments	17
2.3 Transformable lattice structures.....	22
2.3.1 Transformable structures by pantographic systems.....	22
2.3.2 Deployable structures folding into a bundle	22
2.3.3 Retractable pantograph structures.....	26
2.3.4 Pantadome erection	31
2.4 Tensegrity structures.....	33
2.5 Other deployable lattice designs and mixed systems.....	36
2.6 Soft, membrane structures.....	39
2.7 Foldable membrane structures.....	40
2.8 Pneumatic structures.....	42
2.9 Pneumatic systems for the erection of spatial structures	43
2.9.1 Formwork for thin concrete shell structures.....	43
2.9.2 Erection of segmented concrete or ice domes.....	44
2.10 Summary of architectural background.....	45
3 Analysis of a simplified planar model.....	47
3.1 Aims and scope	47
3.2 Analytical investigation	48
3.2.1 Mechanical analysis of the basic segment.....	48
Kinematical equations.....	48
Equilibrium equation	50

Constitutive equation	50
Equilibrium path	50
Calculation of critical state – nonlinear instability problem.....	52
3.2.2 Mechanical analysis of multi-storey, ‘alternately stiffened’ structures.....	53
Tracing equilibrium paths: uniform and bifurcated packing.....	53
Snap-back behavior of bifurcated packing.....	58
Packing path with ‘post-packed phenomenon’	63
Stability analysis.....	65
Taking self-weight into account.....	66
3.2.3 Mechanical analysis of masts without intermediate stiffening	69
Tracing equilibrium paths.....	69
Stability analysis	75
3.3 Numerical analysis.....	76
3.3.1 Methodology	76
3.3.2 Software description	77
3.3.3 Simulation of the packing of the basic unit.....	77
3.3.4 Numerical analysis of ‘alternately stiffened’ multi-storey masts.....	79
Unrestricted simulation.....	79
Restriction of ‘post-packed phenomenon’	84
3.3.5 Numerical analysis of multi-storey masts without intermediate stiffening	88
Unrestricted simulation.....	88
Restriction of ‘post-packed phenomenon’	95
Investigation of packing pattern and the critical force	97
3.4 Summary of the investigation of simplified planar models	98
4 Analysis of packing antiprismatic deployable lattice structures.....	100
4.1 General characteristics.....	100
4.2 Mechanical characteristics – analytical investigation.....	101
4.2.1 Analysis of the basic unit	101
Kinematical equations.....	101
Equilibrium equation	105
Constitutive equation	106
Equilibrium path	106

Calculation of critical state	108
4.2.2 Analysis of ‘alternately stiffened’ multi-storey structure.....	113
4.2.3 Analysis of a ‘non-stiffened’ k-storey structure.....	116
4.3 Mechanical characteristics – numerical analysis.....	117
4.3.1 Numerical analysis of the basic unit, parameter analysis.....	117
Basic assumptions, numerical model	117
Parameter analysis	118
4.3.2 Numerical analysis of ‘alternately stiffened’ multi-storey structure	121
4.3.3 Numerical analysis of a ‘non-stiffened’ multi-storey structure	126
4.3.4 Dynamic analysis of antiprismatic structures.....	137
4.4 Summary of investigating antiprismatic deployable structures.....	143
5 Realization— experiments by physical models, ideas for control and applications	145
5.1 Physical models	145
5.2 Ideas for control and application	148
6 Summary, further research perspectives.....	152
6.1 Summary.....	152
1. Parametric analysis of basic antiprismatic and planar segment, proposal for approximations of main mechanical parameters for preliminary design.....	153
2. Analysis of the complex alternately stiffened planar and antiprismatic structure ..	153
3. Non-smooth packing of the alternately stiffened structure	154
4. Analysis of non-stiffened antiprismatic structures.....	154
6.2 Further research perspectives.....	155
Appendix A: Static and kinematic determinacy of antiprismatic structures	156
Appendix B: Analysis of the snapping-through of a shallow truss.....	158
Quasi static analytic and finite element formulation for tracing equilibrium path and for finding critical points.....	158
Numerical examples.....	161
Appendix C: Analysis of the basic unit of a snap-through type pantographic deployable structure.....	163
Appendix D: Energetical approach for the calculation of planar and antiprismatic self-deployable structures.....	164
DI. Calculation of the planar structure with energetic approach.....	164
DI.1 Analysis of basic segment.....	164

D1.2 Analysis of ‘alternately stiffened’ multi-storey structures	165
Equations	165
Methodology	167
D1.3 Analysis of ‘non-stiffened’ multi-storey structures	168
Equations	168
Methodology	171
D2. Calculation of the antiprismatic mast with energetic approach	173
D2.1 Analysis of basic segment.....	173
D2.2 Analysis of ‘alternately stiffened’ multi-storey structures	174
D2.3 Analysis of ‘non-stiffened’ multi-storey structures	176
Annex E: Choosing constitutive laws in small and large displacement domain.....	180
List of Figures	182
List of Tables	190
List of References.....	191

I INTRODUCTION

Observing nature, several transformable structures can be found, like the extensible worm, deployable leaves and wing of insects [Vincent, 2001], expanding virus capsid [Kovács et al., 2004], not to mention the movable structure of our own, human body. For centuries several small-scale man-constructed deployable structures have been constructed too, such as umbrellas, chairs, fans etc. For the last four-five decades, advanced man-made structures have appeared mainly for spatial engineering applications like for booms, solar arrays, antennas, reflectors (e.g.: [Gantes, 2001; Pellegrino, 2001; Wada et al, 1988]), as the volume and the weight of a structure to be transported to space is crucial. On earth, until recent times, only smaller structures like tents, yurts and shelters had been constructed for architectural purposes. Confirming to the novel conceptions of the 21th century and due to available numerical and robotics technologies, advanced transformable structures are already applied in civil engineering and architecture. Structures used for off-shore industry and light deployable structures used for modern architecture can be mentioned among these.

These structures are designed to undergo very large displacements and remain fully operational [Ibrahimbegovic, 2003]. Often the structures of that kind can integrate a multibody system (e.g. [Ibrahimbegovic and Taylor, 2003] or [Ibrahimbegovic and Schiehlen, 2001] which facilitates a construction phase before being integrated in a structural assembly (e.g. [Gant, 1996]. Modeling of the component of 3D frame-type flexible structures of this kind is nowadays under control thanks to the geometrically exact beam model [Ibrahimbegovic and Taylor, 2002]; [Ibrahimbegovic and Mamouri, 2000] capable of representing large displacements and rotations, and solving the pertinent instability problems [Ibrahimbegovic and Al Mikdad, 2000].

With the help of these tools, the deployable structures undergoing instability phenomenon were investigated. First the analytical and numerical resolutions of some basic snap-through type lattice structures were carried out, starting with the static and dynamic analysis of a shallow truss and followed by the deployment analysis of the basic unit of the snap-through type structure of Zeigler which was scrutinized by Gantes. The behavior of these structures has been already examined before by several researchers, but it was a good start to familiarize with structures undergoing large displacements and instability phenomenon.

Finally a specific system, namely the deployable antiprismatic lattice structure has been chosen for investigation, because its mechanical behavior has not yet been thoroughly analyzed. This cylindrical structure, derived from the well known yoshimura origami pattern and proposed by Hegedűs, is characterized by its pop-up deployment due to the energy accumulated from lengthening some bars during packing. Zero deployment-load corresponds both to the fully deployed and the compact configuration, the latter being an unstable equilibrium state corresponding to the maximal internal energy. It is true that the antiprismatic pop-up system has been proposed almost two decades ago, but due to the lack

of popularity no practical application has been offered yet. The main goal of the dissertation was to investigate the general behavior of the specific system to blaze a trail towards the architectural application of this system by providing designing tools, profound analysis of packing behavior, ideas of applications.

The first step is already a challenge, to fully master the construction phases of a flexible, deployable structure which takes any structural component from initial (unstressed state) to a `deformed` yet equilibrium state. Naturally, the popping up of the structure requires a thorough dynamical analysis and vibration control. However, the packing of the structure — even by smoothly controlling boundary displacements — may also cause inertial effect that cannot be ignored due to intermediate snapping of the structure.

The following thesis was organized in four larger blocks.

In the first block (*Chapter 2*) an extensive but not exhaustive review on different transformable systems — retractable roofs, deployable and retractable pantographic lattice systems, tensegrity structures, soft membrane structures and pneumatic systems — used in architecture and civil engineering will be given. Though the main research topic of the authors within the theme of transformable structures is just a small slice, this study was carried out to explore earlier and current researches and technologies to demonstrate the wide range of available systems, their historical background and their potentials in the future.

The second block (*Chapter 3*) introduces the problem of investigating packing behavior of the antiprismatic deployable structure through a simplified 2D structure possessing similar packing properties to that of the chosen specific system. The equilibrium paths of packing and the concerning difficulties (bifurcation of the path, snap-back phenomenon, singular configurations etc.) as well as the packing sequences will be revealed through analytical and numerical research.

The third block (*Chapter 4*) deals with the same problem but already for the targeted 3D problem. The same analysis presented for 2D structures is carried out for two different type of antiprismatic systems. After analyzing the original structure offered by Hegedűs (further called as *non-stiffened antiprismatic structure*), a different system, slightly deviating from the original one (further called as *alternately stiffened antiprismatic structure*), was also investigated. The antiprismatic system proposed by Hegedűs is constructed from identical double antiprisms with an elastic middle polygon and rigid polygons in the boundaries. The modified model eliminates the rigid internal polygons; the pop-up column is constructed from continuously rotating elastic polygons with two rigid polygons on the top and on the bottom. In this chapter approximations for main mechanical characteristics were also provided from the analytical investigation that can serve as a tool for preliminary design and verification of the numerical results.

Finally, in the fourth block (*Chapter 5*), an attempt is given to provide ideas for application of antiprismatic structures by combining the ideas and characteristics of the available systems in *Chapter 2* and the topology of the antiprismatic structure investigated in *Chapter 5*. The small physical models built for experimenting were also presented in this block. In this chapter, different applications and control systems were sketched without aiming to give detailed solutions.

In the last chapter the thesis is summarized, highlighting the remarkable results of the thesis that can be considered as new scientific achievements. In this chapter the further research perspectives are also outlined.

In the *Annex* the review on the kinematic determinacy of antiprismatic structures, methodologies used in the numerical calculations, investigation of snapping-through structures (shallow truss, and the basic unit of a snap-through type system), auxiliary calculations for investigated structural systems and some mentions on choosing constitutive model is attached to the dissertation.

2 ARCHITECTURAL BACKGROUND: TRANSFORMABLE STRUCTURES IN CIVIL ENGINEERING AND ARCHITECTURE

'If architects designed a building like a body, it would have a system of bones and muscles and tendons and a brain that knows how to respond. If a building could change its posture, tighten its muscles and brace itself against the wind, its structural mass could literally be cut in half...'

Guy Nordenson, Ove Arup and Partner [Fox]

2.1 The history of architectural transformable structures

The history of transformable structures goes back to centuries before [Walter]. Though possibly everybody is familiar with the light deployable nomad Indian tepees (Fig. 2.1a) that could be transported by animals, only very few know that a part of the auditorium of the Roman Colosseum (Amfiteatro Flavio) (Fig. 2.1b-c) built in the first century had a convertible textile roof [Ishii, 2000]. The structure of the umbrella is an ancient structure as well, but its principle is used in modern adaptive architecture.

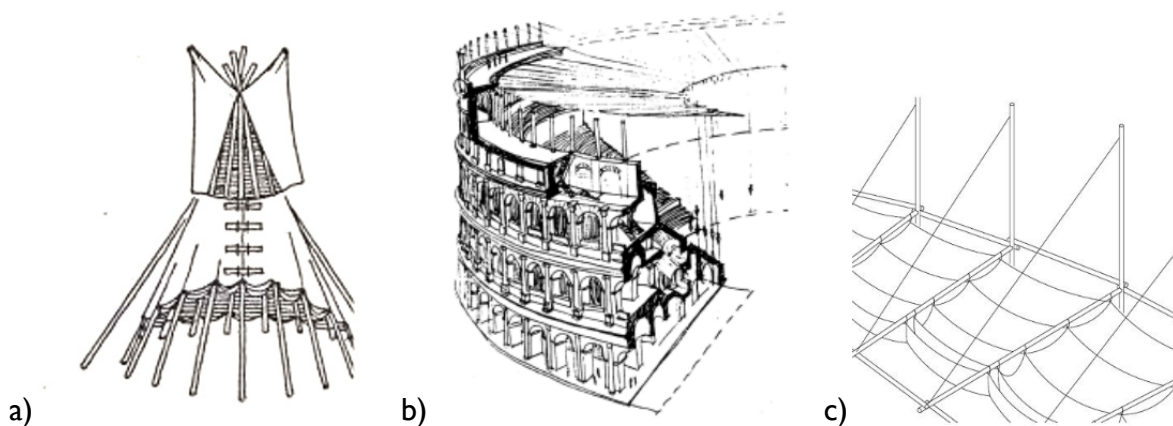


Fig. 2.1: Early movable roof structures: a) Tepee tent from the Sioux Indians [Otto, 1971] (cited by [Walter]); b) Roman Colosseum [Escrig and Brebbia 1996] (cited by [Jensen, 2001] and c) the reconstruction of its convertible roofing system [Gengnagel, 2001] (cited by [Walter])

Obviously, higher scale transformable roof structures appeared only in the 20th century. With the growing demand of hosting sport venues, starting from the 1930s an increasing trend towards building retractable roofs can be observed. As cranes were already common at that time and standards were available for transport tracks, control and drive, the first constructions stem from the principles of crane technology [Ishii, 2000]. Thus, early designs mainly run on rails. The first retractable large span roof is said to be the Pittsburgh Civic Arena (see Fig.2.5 in Chapter 2.2) that was opened in 1961.

After the World War II — parallel to the appearing of retractable roofs opened with rigid body movements — significant pioneer works have to be mentioned regarding deployable/retractable lightweight structures. B. Fuller's reinvention of the geodesic dome (Fig. 2.2a) and his lectures on 3D geometrical forms for architecture, space frames and structural efficiency [Fuller et al, 1975] inspired several researchers to further elaborate his ideas. The tensegrity system invented by K. Snelson [Snelson, 2009] and B. Fuller in 1949 is still the main topic of several ongoing research work that try to widen the application possibilities of these systems and to adapt them to deployable structures [Motro et al, 2001]. Furthermore the systematic research work of F. Otto on deployable and retractable structures [Otto et al, 1971] and his works in the field of tensile and membrane structures [Otto, 1973] led to a big variety of retractable membrane roof structure designs in the second half of the century (e.g. retractable roofs of Montreal Olympic Stadium, bullfighting arena in Zaragoza). Membrane structures can be combined with scissor-like deployable structures. E. P. Pinero's movable theatre (Fig. 2.2b) presented in 1961 can be mentioned as pioneer work of this type [Pinero, 1961]. Though his deployable trellis design had major structural drawbacks, he motivated further pantographic deployable designs like Escrig's deployable swimming pool [Escrig et al, 1996/1] and Zeigler's pop-up dome [Zeigler, 1976, 1977].

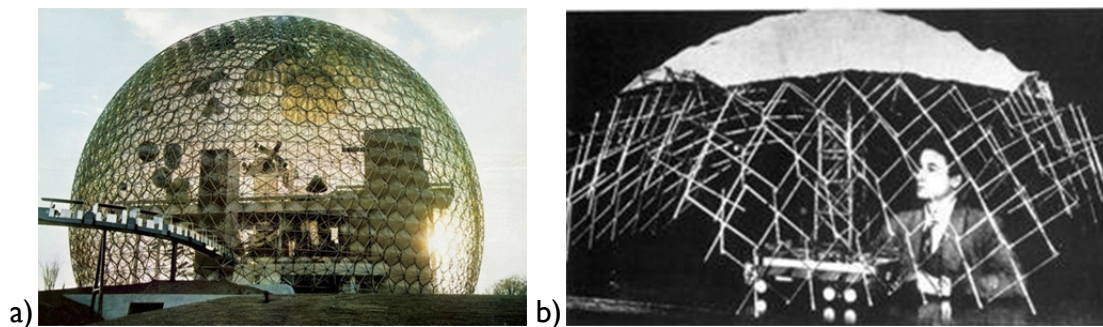


Fig. 2.2: a) *The US Pavilion for the 1967 World's Fair, Montreal by B. Fuller [Hienstorfer, 2007]; b) Pinero with his movable theatre [Robbin, 1996]*

Transformability can be used not just for lightweight structures. In the last decades promising experiments were made with constructions using transformable systems to combat the main problem of concrete shell structures, namely the expensive, difficult and time-consuming production (e.g.: [Roessler and Bini, 1986]; [van Hennik and Houtman, 2008]; [Dallinger and Kollegger, 2009]).

In the second half of the 20th century, regarding deployable and inflatable structures developments were in first place achieved in spatial engineering [Pellegrino, 2001; Gantes, 2001] for booms, solar arrays, antennas, reflectors, as the volume and the weight of a structure to be transported there is crucial.

Current trends show a re-increasing interest in kinetic architecture due to the growing demand on provisory architecture [Kronenburg, 2008] and the need for sustainable technologies [Kibert, 2007, Friedman et al, 2011]. The rapidly decreasing natural resources, the global variation of the climate and the continuously incrementing population are all

insistent problems that are pushing structural development in a new direction that keeps not only economical but environmental and social aspects and development in mind (Fig 2.3) as well. This leads towards a sustainable engineering: towards a development that 'meets the needs of the present without compromising the ability of future generations to meet their own needs' [United Nations, 1987]. Adequately, some very new issues were introduced in structural engineering and architecture, just a few of them are listed here: reducing environmental impact, recycling, reusability, material and energy efficiency, employment of inexhaustible energy resources, operation and maintenance optimization, minimal impact on human health, indoor environmental quality enhancement, waste and toxic reduction etc.

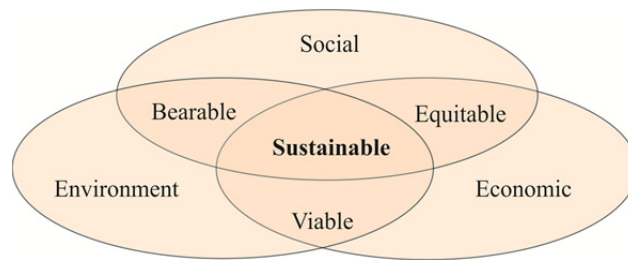


Fig. 2.3: Scheme of sustainable development: at the confluence of three constituent parts [Friedman et al., 2011/1]

Aiming sustainable architecture there is a remarkable tendency towards adapting seminal ideas of the 60s and 70s [Sadler, 2005; Zuk and Clark, 1970] (cited by [Rosenberg, 2010]) to create an indeterminate architecture that can conform to uncertainty and emergent situations, changing in occupant demand and energetic considerations [Rosenberg, 2010].

Though not being a novel idea, involving motion systems to structural design seems to be a currently improving segment of civil engineering thanks to the available technologies that are just catching up with these ideas of the 1960s and 70s.

More precisely, the recent actuality of research of transformable structures is due to the continuously improving computer, robotic and nanotechnologies, the ameliorated numerical methods (e.g. [Ibrahimbegovic, 2009]) and the progressive properties of novel and conventional building materials.

2.2 Transformable structures by the movement of rigid panels or structural segments

As mentioned in the introduction, first designs for retractable covering of sport stadiums stem from the crane technology. F. Otto classified these convertible roofs by a movement matrix (Fig. 2.4).

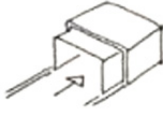
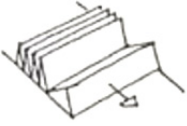
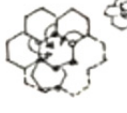
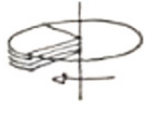
type of movement	direction of movement			
	parallel	central	circular	peripheral
sliding				
folding				
rotating				

Fig. 2.4: Classification of rigid retractable structures: the movement matrix [Otto et al, 1971]

Fig. 2.4 shows that the retraction can be obtained by sliding, folding or rotating the panels in different directions. The panels can overlap while retracting or move independently. The first retractable dome structure is said to be the circularly sliding retractable roof of the Pittsburgh Civic Arena (Fig. 2.5) opened in 1961 and closed in 2010. The 127 m-span roof consists of eight 300 ton sections, six of which are able to rotate by five motors per panel. All panels are fixed on the top to a gigantic, 80 m tall steel truss cantilever. The roof could be opened in about two minutes [Ishii, 2000].

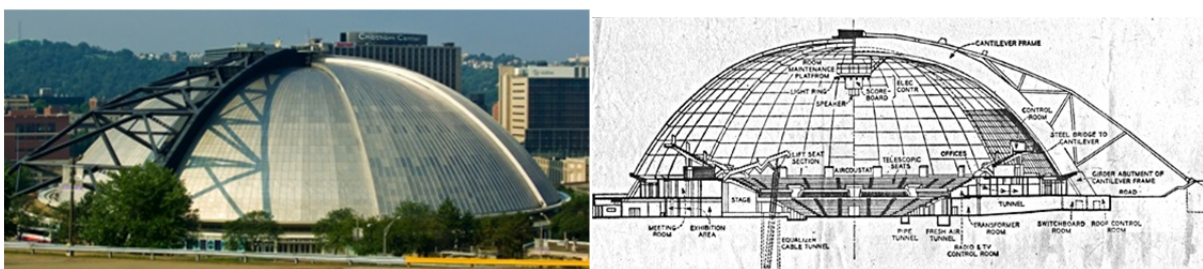


Fig. 2.5: Pittsburgh Civic Arena (architect: Mitchell and Ritchey) photo [Lorentz, 2008] and original blueprint [Helvenstone, 1959]

The structural form of the civic arena is initially optimal as bending moments are minimal due to geometry. Unfortunately for retractability this optimal shape had to be sliced in parts, thus the cost was the huge cantilever that supports the panels, and the bigger structural height. A similar geometry was achieved by a more recent construction that did not apply an external structure to hold the panels. The Fukuoka stadium in Japan (Fig. 2.6) opened in 1993 spans 222 m. The three parts of the roof — two of which are rotatable — are independent

frameworks, with remarkable bending moments. Though careful shape correction was performed for the geometry of individual parts (Fig. 2.7a) to avoid singularities in reaction forces at the inclination lines [Ishii, 2000], the structural height is still gigantic. Each panel is four meters thick, and the total roof weighs 12 000 tons. The sliding rotation of the two panels is enabled by 24 bogie wheel assemblies (Fig. 2.7b-c). It takes approximately 20 minutes to open the roof.

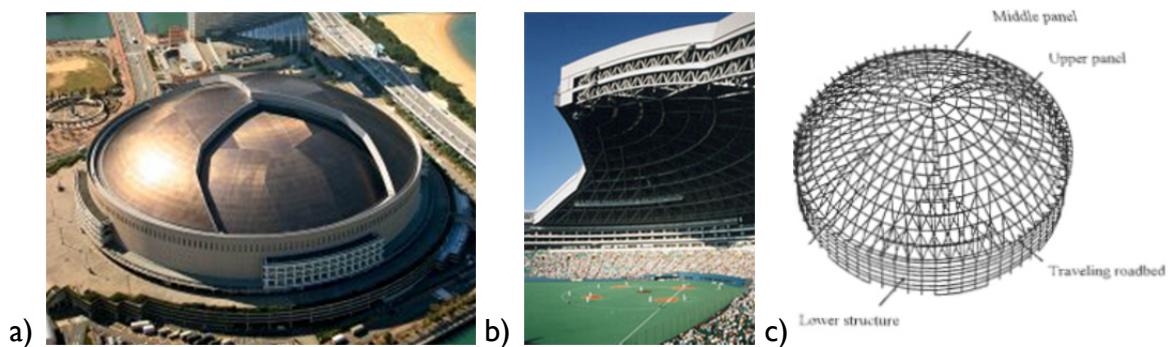


Fig. 2.6: Fukuoka stadium (architect: Takenaka Corp.) a) photo with closed [Yahoo, 2010] and b) with opened roof [Japan Atlas] c) structure [Ishii, 2000]

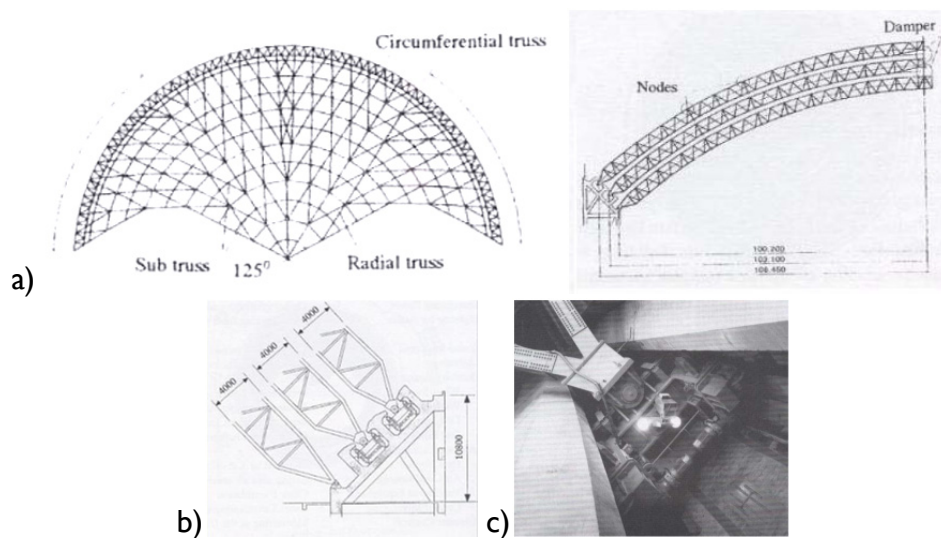


Fig. 2.7: Fukuoka stadium a) geometry of a roof panel b) roadbed section c) driving device [Ishii, 2000]

A much more slender retractable structure was constructed in Oita, Japan, in 2001 called the Oita Stadium or more commonly the “Big Eye” (Fig. 2.8). A large part of the 274 m diameter spherical roof is fix (Fig. 2.8b), only the top two panels are retractable that slide parallel on seven rails to the periphery of the dome. The sliding panels are covered with a special membrane containing a Teflon film that provides better transparency, thus even on rainy days natural lighting is provided [Ishii, 2000].

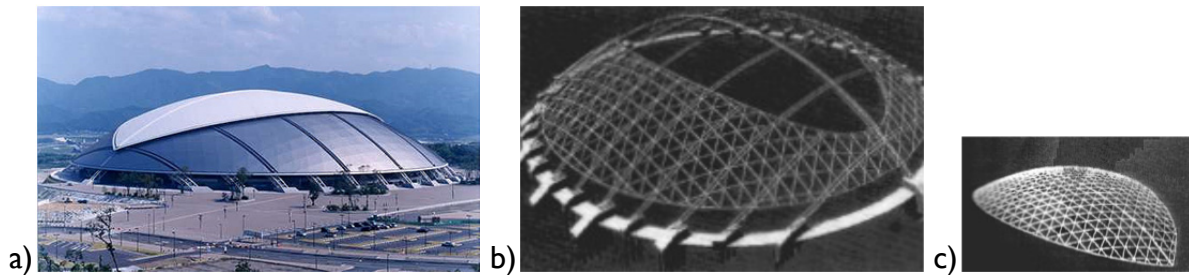


Fig. 2.8: Oita Stadium (architect: Kisho Kurokawa) a) photo [Ezinemark, 2010]; b) fix structural part [Ishii, 2000] and c) retractable top section [Ishii, 2000]

To mention other motion systems for rigid retractable structures briefly just three different examples are shown. A parallel overlapping system was used for the 40 m span retractable roof of the Komjádi swimming pool in Budapest (Fig. 2.9.a), built in 1976. A more complex system of rigid systems is the roof of the Qi Zhong stadium in Shanghai (Fig. 2.9.b) that opened in 2005. The roof resembles to an opening flower, the eight sliding steel “petal” rotates to towards the perimeter in 8 minutes. Of course not every retractable roof can be clearly classified to the categories of the motion matrix shown in Fig. 2.4. For example, the roof of the Toronto Skydome (Fig. 2.10) is a nice example of a mixed system. The 213 m diameter roof is made up of 4 sections, one remains stationary while the two panes slides parallel and one circularly to achieve a high rate of retractability.

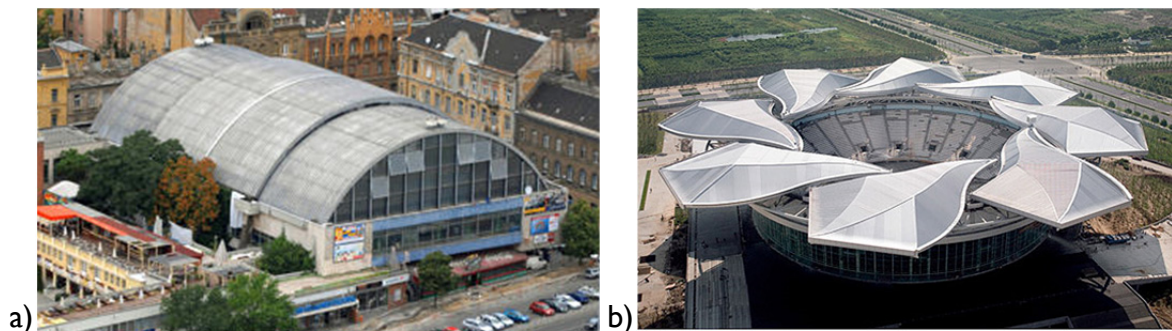


Fig. 2.9: a) Retractable roof of the Komjádi swimming pool [Komjádi]; b) Qi Zhong stadium (architect: Mitsuru Senda), [Ezinemark]

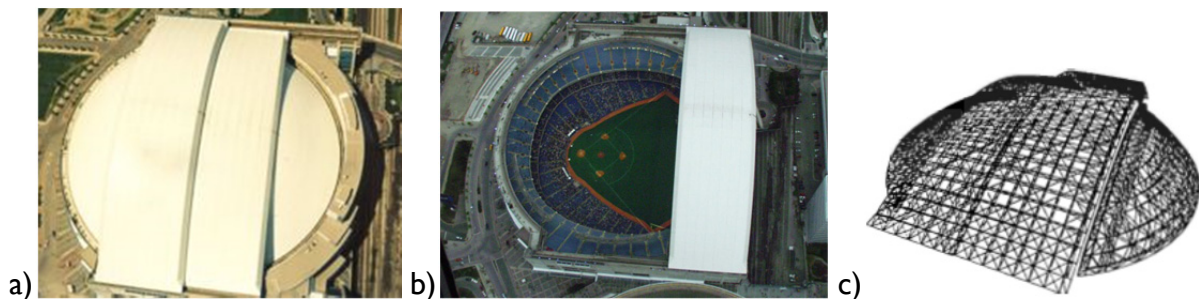


Fig. 2.10: Toronto Skydome (architect: Rod Robbie) a) photo of closed and b) opened roof c) the structure of the retractable roof [Ishii, 2000]

Deployability can be achieved with more complex movements stemming from natural folding patterns like the ones of the leaves or of the wings of the insects [Vincent, 2001; Hachem et al., 2004] or stemming from Origami, the traditional Japanese art of paper

folding. It is true that Origami's history goes back to the 17th century AD, it has not just evolved into a modern art form, but also a challenging geometrical research topic and interesting chance of structural implementation (Fig. 2.11). Folding and packing patterns are primarily used for space structures like deployable solar cell arrays or reflector antennas (Fig. 2.12). Moreover, a remarkable tendency can be observed to apply these patterns for architecture, too (Fig. 2.13).



Fig. 2.11: Foldable tube (exhibition object) and dome (paper model) with the Yoshimura pattern [Yoshimura]

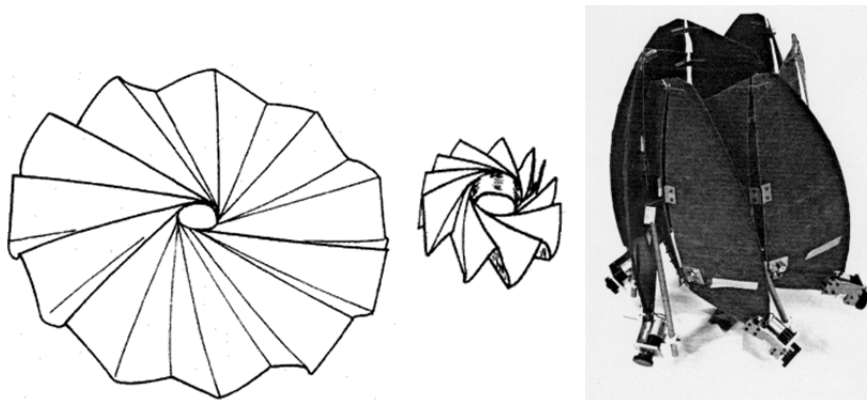


Fig. 2.12: Solid Surface Deployable Antenna and its wrapping fold pattern by the former Deployable Structures Laboratory by Guest and Pellegrino [DSL]

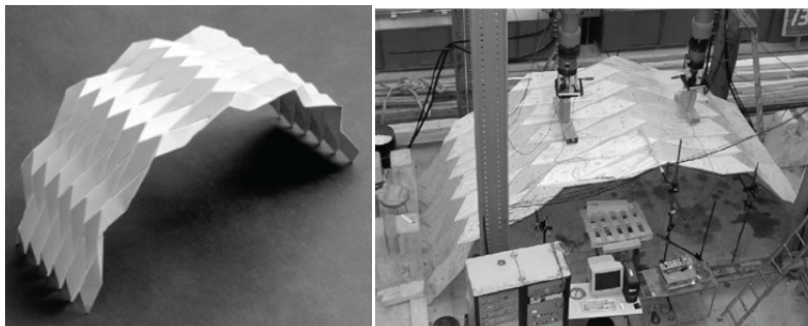


Fig. 2.13: Cylindrical paper and laminated timber model with the Miura pattern [Buri and Weinand, 2008]

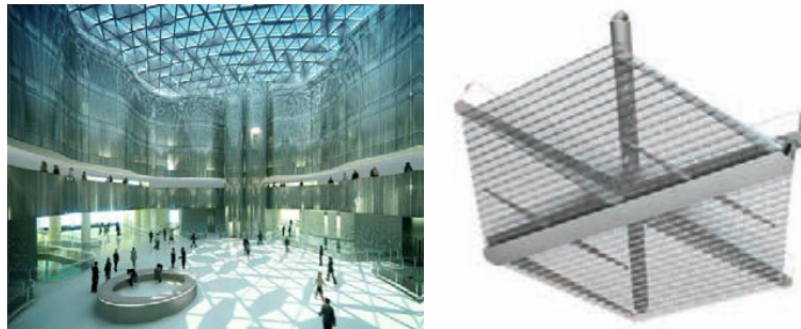


Fig. 2.14: Adaptive shading system of the Audencia Provincial, Madrid (by Hoberman and Fox+Partners) and the model of a hexagonal retractable panel [Hoberman]

More and more recent architectural designs try to apply transformable systems only for achieving the variability of a shell or an envelope of the permanent structure. Though the motion of the building might not be as spellbound as those where whole massive structural parts are in motion, but can offer a nice solution for integrating structural efficiency and the adaptation to external excitation. This was the case with the adaptive sun shading system of the Audencia Provincial, Madrid (Fig. 2.14) designed by Hoberman. The hexagonal shading cells can completely cover the roof, but disappear when retracted into the structural profiles of the structure. The algorithm that controls the movement combines historic solar gain data with real-time sensing of light levels [Hoberman]. Hoberman designed several adaptive shading systems in accordance with his new patented technology using thin plates sliding on each other [Hoberman et al, 2009] (Fig.2.15) to enhance the architectural design of Foster + Partner's buildings. Another example is the convertible shell design of the Aldar Central Market in Abu Dhabi (Fig. 2.16).

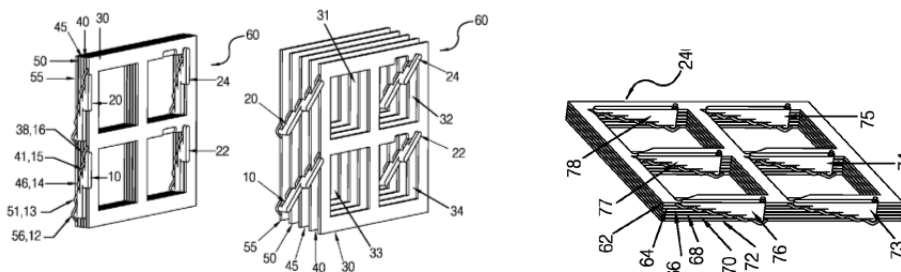


Fig. 2.15: Details of patented adaptive shading system by Hoberman and Davis [2009]



Fig. 2.16: Adaptive shading system of the Aldar Central Market in Abu Dhabi, 2010, Madrid (design by Hoberman and Fox+Partners) [Hoberman]

2.3 Transformable lattice structures

2.3.1 Transformable structures by pantographic systems

A large number of structures that can be opened and closed are based on the well-known concept of the lazy tong system. The minimum component of this system is the so-called scissor-like element (henceforth SLE). The SLE consists of two bars connected to each other with a revolute joint. By the parallel connection of SLEs the simplest 2D deployable structure, the lazy tong is constructed. Connecting at least three of SLEs through complete pin joints a ring is formed, providing a secondary unit of this frame structure (Figs 2.17a-d). By the further connection of secondary units almost all kind of 3D-shapes can be formed folding into bundle (Fig. 2.17e-h). Adding tension components like wire or membrane to its developed form, it becomes a 3D-truss and gets effective strength, thus towers, bridges, domes and space structures can be rapidly constructed [Atake, 1995].

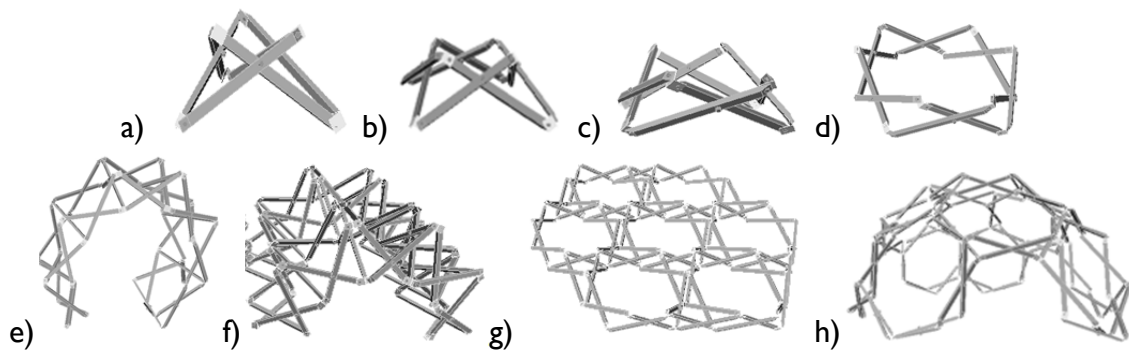


Fig. 2.17: Some secondary units of scissor like deployable structures: a-b) pyramid type units and c-d) skew types; e-h) foldable shapes [Atake, 1995]

2.3.2 Deployable structures folding into a bundle

Pioneer works: movable theatre, deployable roof structure

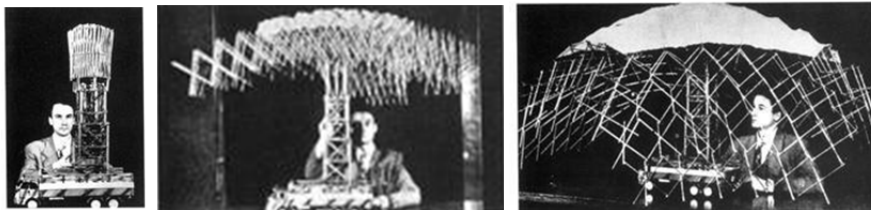


Fig. 2.18: Photo of Piñero with his movable theatre [Hunter]

Using scissor-like deployable structures for architecture was pioneered by the Spanish engineer, E. P. Piñero. He presented a foldable theatre (Figs. 2.18-9) in 1961 [Piñero, 1961], and elaborated several other deployable designs. The biggest drawbacks of his designs were the relatively heavy and big joints due to eccentric connections (Fig. 2.19) and necessary temporary support as the structure was stiffened by intermediate bars or tension elements that were added after the structure was deployed into the desired configuration [Gantes, 2010]. Despite of all the disadvantages of his structures, Piñero inspired several

researchers. This was the case with Professor F. Escrig, who designed the 30 m×60 m deployable roof for a swimming pool in Seville [Escrig, 1996] (Fig. 2.20).

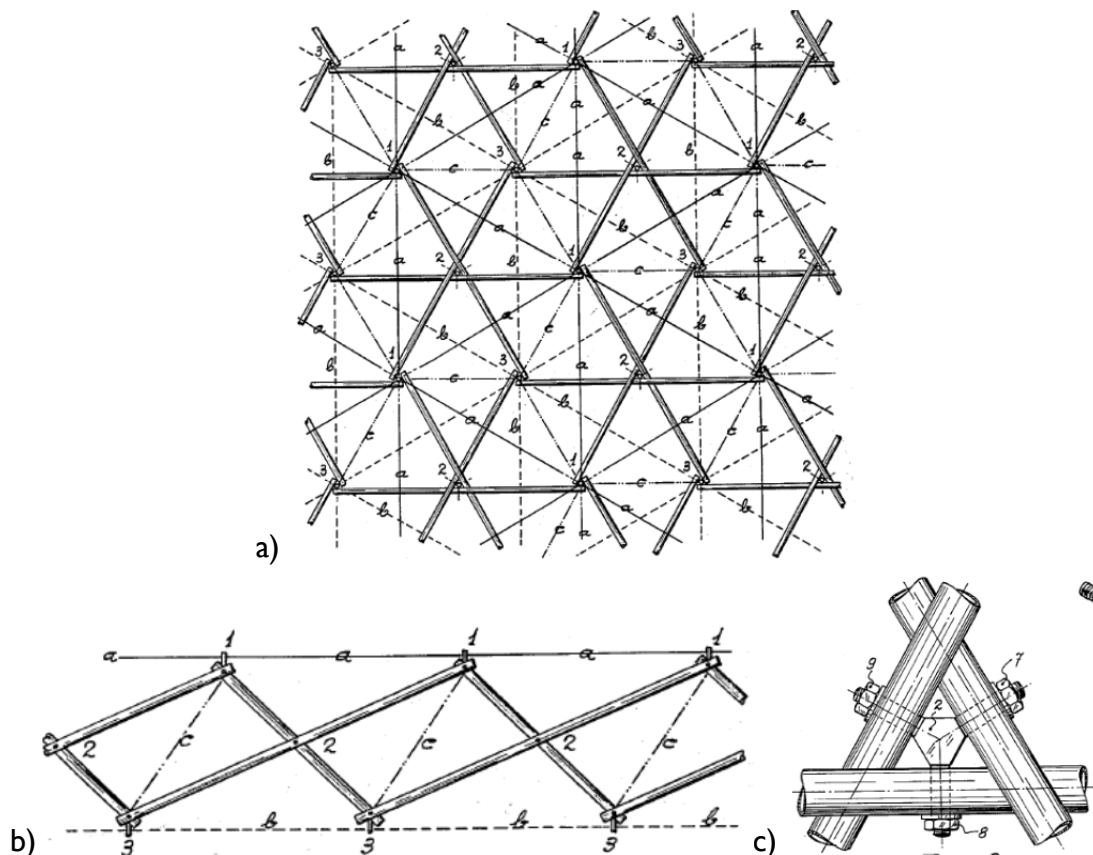


Fig. 2.19: Details of Pinero's reticular 3D structure patent: a) plan view of opened structure; b) fragmentary view; c) connection of three rods of the structure to an intermediate coupling [Piñero, 1965]



Fig. 2.20: Deployable swimming pool (architect: Prof. Felix Escrig) [Escrig, 1996/2]

Deployable structures stiffened by cables

By piling up pyramid type structural units vertically (e.g. Fig. 2.21a-b) a basic pantographic structure is formed: a three-dimensional mast [Atake, 1995]. The only internal degree of freedom of the deployable mast developed in the former Deployable Structures Laboratory is controlled by a single, continuous cable which runs over pulleys connected to the joints of the pantograph [Pellegrino et al., 1993] (Fig. 2.21a). One end of this cable is connected to a drum driven by an electric motor, and its route through the structure is in a manner that winding the cable onto the drum causes the structure to deploy. A series of short (initially loose) cables linking neighboring joints of the pantograph become taut when

the pantograph is fully deployed, and in this configuration, the continuous cable imparts a global state of pre-stress onto the whole structure.



Fig. 2.21: a) Deployable mast controlled by active and passive cables by the former Deployable Structures Laboratory; b) foldable bridge and c) deployable dome by ATAKE Space Design Lab. Co. in the Hanamizuki Park, Japan [Atake]

With the application of this vertical connection horizontally a foldable bridge can be formed, which is useful for its rapid construction [Atake, 1995]. Fig. 2.21b shows an example realized in the Hanamizuki Park, Japan.

The Fig. 2.21c shows the upper half of a semi-regular 32-polyhedron (soccer ball) providing foldable double layer dome. This is constructed by the horizontal connection of sliced octahedron units (48 identical scissors) and was also installed in the same Park [Atake, 1995].

Self-locking deployable structures

While pantograph structures discussed above all need additional stabilizing elements like cables or other locking devices, it is possible to design deployable structures that are self-stable in the erected configuration without any additional member with the application of a special geometric configuration [Gantes, 2001]. This can be achieved by adding inner SLEs to the initial secondary units shown in Fig. 2.17. These units are shown in Fig. 2.22. The inner SLEs deform while unfolding due to geometric incompatibilities resulting a self-locking, self-stabilizing mechanism that locks the structure in its opened configuration [Clarke, 1984] (cited by [Gantes, 2001]). The first dome structure of this type was introduced by T. Zeigler in 1974 [Zeigler, 1976]. Several pop-up displays and pavilions are constructed in accordance with his patents (e.g. Fig. 2.23).

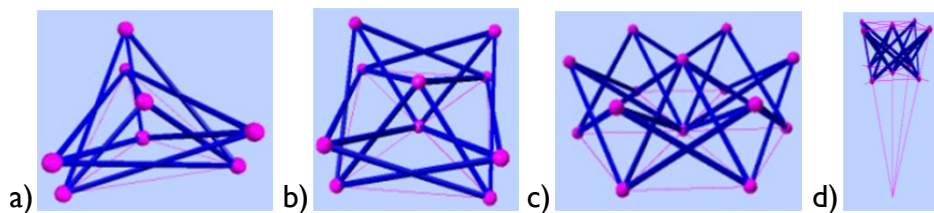


Fig. 2.22: a-c) Self-stable deployable structures: secondary units for the planar and d) for spherical structures [Friedman et al., 2008]



Fig. 2.23: Photo of pop up display and schematic presentation of its installation by Nomadic Display Corp. [Nomadic]

Possible shapes with Zeigler's first pop-up dome patent [Zeigler, 1976] are strongly limited because of strict geometric restrictions. However, the major disadvantage of the structure is that in the final configuration some members are not stress-free and remain curved. This residual stresses and the bent form leads to a decrease of load bearing capacity and makes these structures more susceptible to catastrophic failures due to member buckling [Gantes, 2001]. Zeigler improved his initial structure by introducing sliding joints for some intermediate nodes and flexible connections at the end nodes by springs [Zeigler, 1977] (Fig. 2.24).

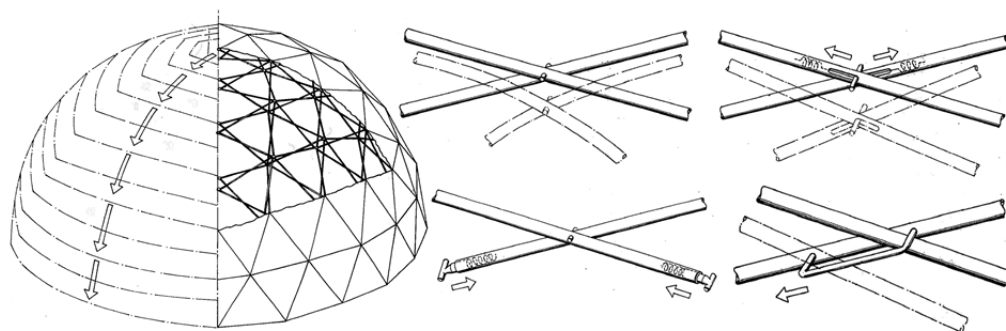


Fig. 2.24: Zeigler's patent for collapsible self-supporting structure: dome and scissor details [Zeigler, 1977]

For the elimination of both of the above-mentioned problems — namely external stabilization and residual stresses in the deployed configuration — improved self-locking structures were investigated by A. Krishnapillai at the MIT [1985, 1986] (cited by [Gantes, 2001]) and patented [1992]. By the satisfaction of certain geometric constraints, these structures can be stable in the deployed configuration having straight and stress-free members, except for dead weight and live load effects. During deployment, however, geometric incompatibilities result in the development of second order strains and stresses and a snap-through type of behavior that 'locks' the structure and assures its stability in the deployed configuration. About self-stable structures of this kind a practical and detailed design guide was published, written by Gantes [2001].

2.3.3 Retractable pantograph structures

The application of structures that can fold into bundle when continuous transformability needed could be difficult to get. The American engineer, C. Hoberman made a considerable advance in the design of retractable roof structures by the discovery of the simple angulated element [Hoberman, 1990, 1991]. By the refraction of the two straight rods of a single SLE the angulated element is formed (Fig. 2.25). This element is able to open and close while maintaining the end nodes on radial lines that subtend a constant angle [Pellegrino, 2001].

Considering a classic SLE (Fig. 3.9a) — consisting of two identical straight rods, hinged together with a cylindrical joint at E — the relationship between α , the angle subtended by the lines OP and OQ defined by the endpoints of the rods (A, D and B, C) and γ , the angle between the two rods (deployment angle):

$$\tan \frac{\alpha}{2} = \frac{\overline{CE} - \overline{AE}}{\overline{AC}} \tan \frac{\gamma}{2} \tag{2.1}$$

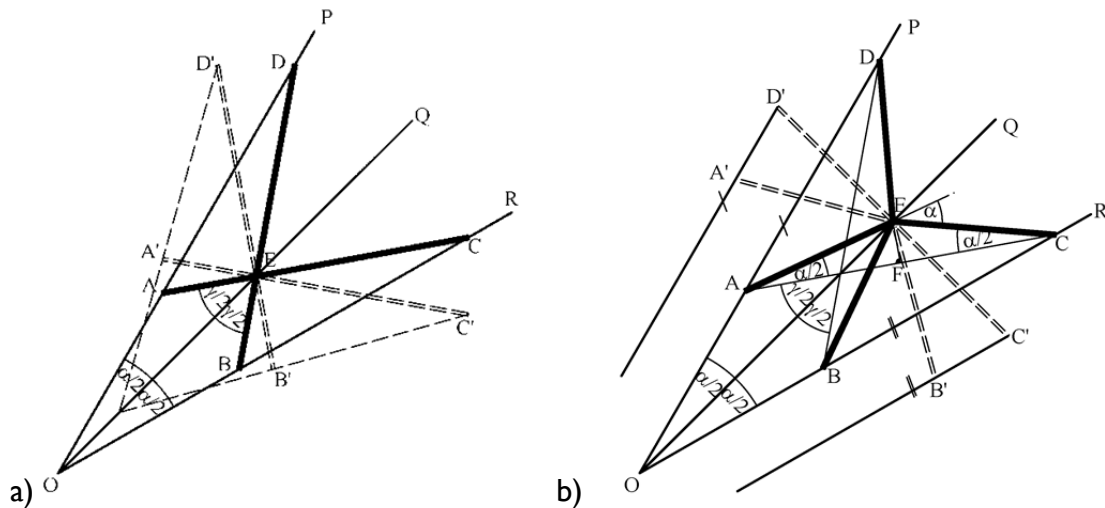


Fig. 2.25: a) Classic SLE and b) the simple angulated element (illustrated in accordance with [You and Pellegrino 1997])

Thus α varies with the deployment angle γ . By the refraction of the two straight rods the angulated element is formed (Fig. 2.25b). The simple angulated element consists of two identical angulated bars ($\overline{AE} = \overline{BE} = \overline{CE} = \overline{DE}$). The connection between the deployment angle γ and α the above equation (1) will take the following modified form for Hoberman’s angulated element [You and Pellegrino, 1997]:

$$\tan \frac{\alpha}{2} = \frac{\overline{CF} - \overline{AF}}{\overline{AC}} \tan \frac{\gamma}{2} + 2 \frac{\overline{EF}}{\overline{AC}} \tag{2.2}$$

If the conditions

$$\overline{AF} = \overline{CF}, \quad \alpha = 2 \arctan \frac{\overline{EF}}{\overline{AC}} \quad (2.3)$$

are satisfied, the variation of γ will not effect α . Hence, if the scissor hinge at E can be mobilized along the OQ line, this element is able to open and close while maintaining the end nodes A, B, C, D on radial lines that subtend a constant angle. Hoberman extended the above derivation also for a non-symmetric angulated element still consisting of two identical angulated rods ($\overline{AE} = \overline{BE}$, $\overline{CE} = \overline{DE}$) but \overline{AE} is not necessarily equal to \overline{CE}) [Hoberman 1990, 1991].

Using angulated elements Hoberman created the retractable roof of the Iris Dome, shown in Fig. 2.26 at the EXPO 2000. The exhibition dome was formed by the connection of the angulated elements on concentric circles. Powered by four computer-controlled hydraulic cylinders, the 6.2 m tall and 10.2 m high retractable dome smoothly retracts toward its perimeter and unfolds [Hoberman]. One of the drawbacks of this design is that the structure does not maintain a constant perimeter, thus to connect it to a permanent foundation is quite a challenge especially in the case of a larger scale structure. On the other hand, for the construction of the relatively small span structure required more than 11 400 machined pieces [Whitehead, 2000], which can cause potential problems with reliability and a laborious and expensive manufacturing. The complexity of the hinges is due to the special geometric configuration coming from the implementation of a 2D mechanism into a 3D structure. The main problem is that the angulated elements are arranged on the tangent planes of conical surfaces. Each 'ring' is situated on the tangent planes of different conical surfaces (the rings on the top are on a shallow conical surface while the ones on the bottom lie on a high one, see Fig. 2.27a-b). Each conical surface has its rotational axis coinciding with that of the retractable roof. This means that at the intersection of the neighboring angulated elements all four angulated element lie on different planes (see Fig. 2.27c). As the hinge axes have to be perpendicular to the plane of the scissor, the interconnecting hinges are realized by a rigid body of small extension connected to four simple scissor hinges with four different hinge axes [Kovács, 2004].

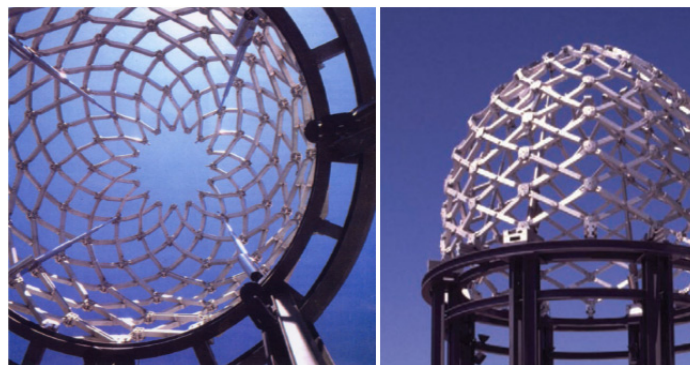


Fig. 2.26.: Iris dome designed by Hoberman, EXPO 2000 [Hoberman]

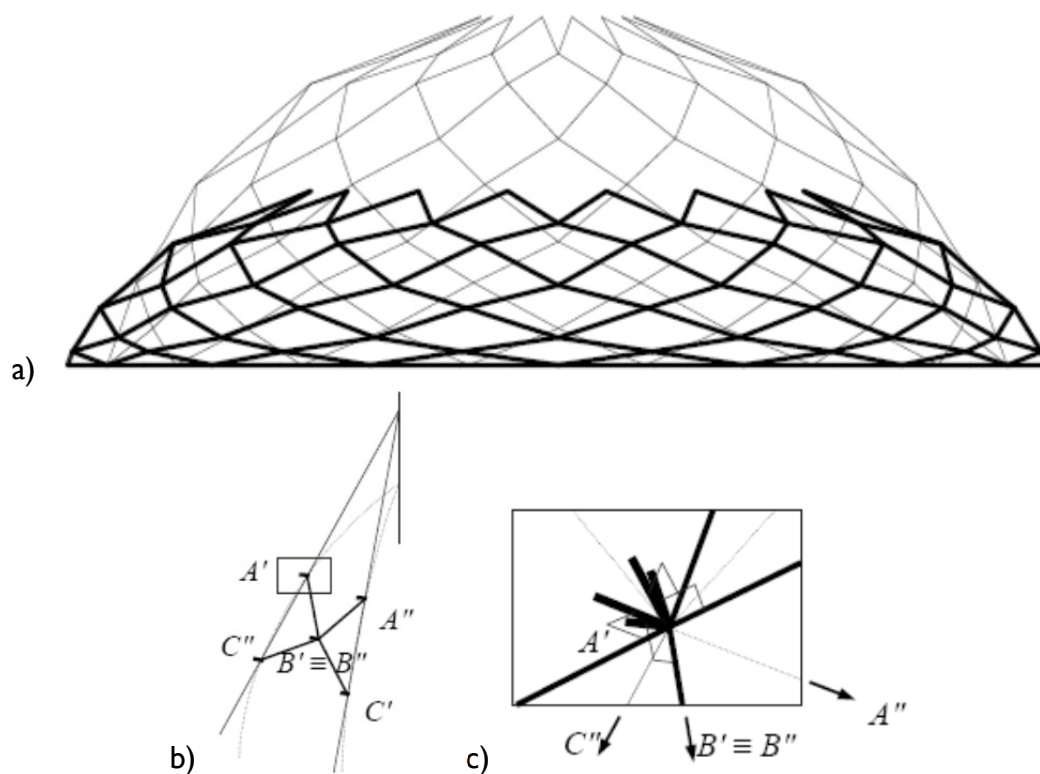


Fig. 2.27: a) Schematic model of Hoberman's Iris dome during deployment; b) angulated element on the tangent plane of a conical surface and c) four non-identical hinge axes at the connection of angulated elements [Kovács, 2004/2]

Further developments were made by Z. You and S. Pellegrino [You and Pellegrino, 1997] by generalizing the angulated elements to a large family of foldable building blocks and by introducing a new type of pantographic structure based on the so-called multi-angulated elements. With multi-angulated elements the number and complexity of elements and joints of retractable trellis structures can be reduced. Each multi-angulated element is composed of a number of bars, which are rigidly connected to each other (Fig. 2.28), instead of separate angulated elements as used by Hoberman.

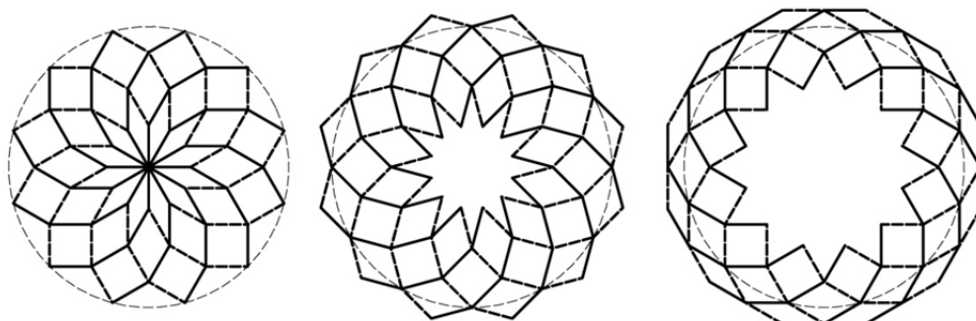


Fig. 2.28: Deployable sequence of a ring structure developed by Z. You and S. Pellegrino

The 3D version of the multi-angulated element can be generated by a vertical projection of all hinges to a hemisphere. An example can be seen on Fig. 2.29. The retractable structure elaborated at the former Deployable Structures Laboratory made from two layers of multi-

angulated elements connected only by cylindrical joints with all hinge axes perpendicular to the plane. Though the projected retractable dome by You and Pellegrino have less complex joints, its opened configuration forms a less aesthetic toroidal-like shape that is more susceptible to wind effects [Kovács, 2004/2].

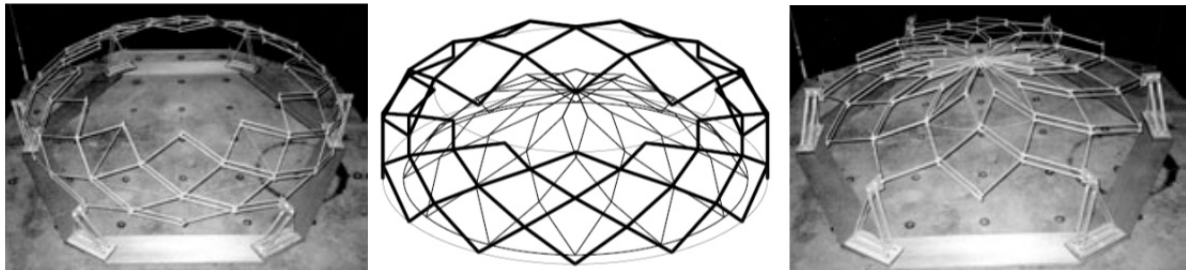


Fig 2.29: 3D model of retractable dome by multi-angulated elements and its physical model at the former Deployable Structures Laboratory [Kovács, 2004/2]

Further developed and very aesthetic retractable dome system was tested by Kokawa [2000], who identified a special geometry that enables all the joints to move on the sphere with scissor hinge axes pointing to the center point of the sphere. Unfortunately with this configuration during retraction there is a slight difference in the direction of hinge-axes and the hole axes thus either a loose hole or an embedded spherical roller bearing is needed [Kokawa, 2000] (Fig. 2.30).

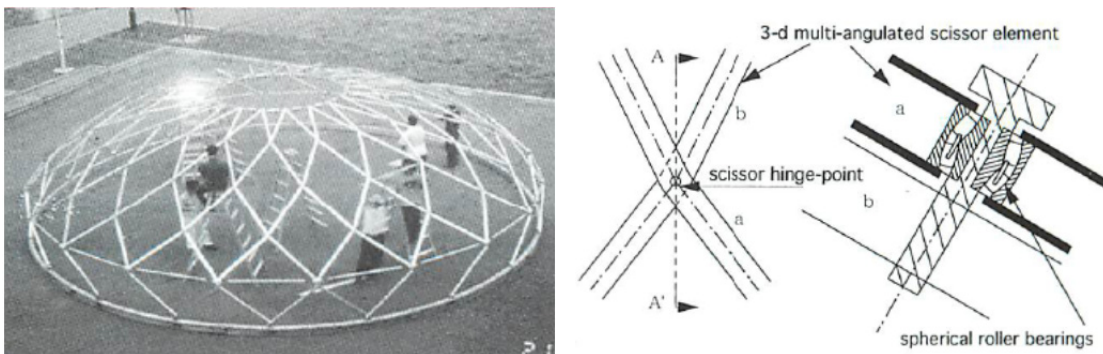


Fig. 2.30: Retractable dome opening on the spherical surface with telescopic ring, plan view and section of its scissor hinge [Kokawa, 2000]

All the above-mentioned retractable dome models have the problem of variable perimeter radius. While Hoberman overcame this difficulty by supporting his Iris dome with a wide annulus on which the dome's joints on the edge can slide radially, the model of the Deployable Structures Laboratory and the one by Kokawa is supported with a secondary mechanism, a pin jointed support.

P. E. Kassabian succeeded to change the geometry of the Iris dome's structure by rigid body rotation, so that the motion of each angulated element is a pure rotation about a fixed point, and thus allows the application of fixed support points [Kassabian 1997, 1999].

F. Kovács identified a new type of retractable iris dome combining simple scissor hinges and common hinges that has a fix outer ring as well [Kovács, 2000/2].

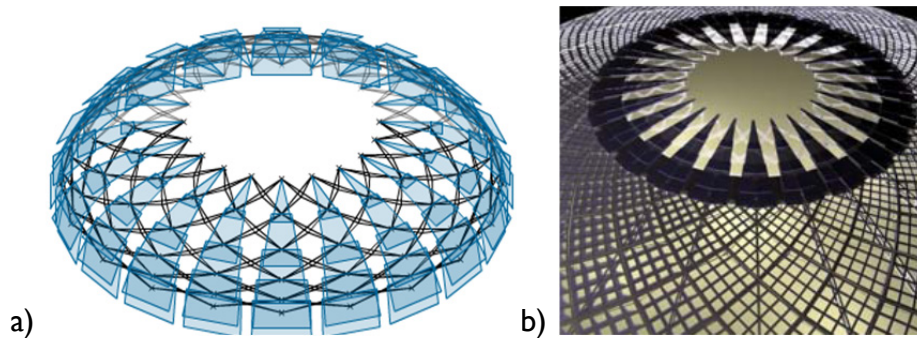


Fig. 2.31: Cover of retractable structures with sliding panels by Hoberman: a) schematic model for covering the iris dome (Happold and Hoberman) and b) model of the dome of Abu Dhabi's international airport, United Arab Emirates, 2006 (Kohn Pedersen Fox Architects) [Hoberman]

the second biggest difficulty regarding retractable domes is the problem of covering the lattice mechanism. An enclosure can be created by elastic/folding membrane or rigid plates, which are allowed to overlap in the retracted position. Several different designs have been proposed by Hoberman [Hoberman, 1991, 2004]. One example is the central part of the responsive dome (Fig. 2.31) that covers a major central courtyard of Abu Dhabi's international airport. The large operable oculus is covered by panels sliding towards the perimeter. The dome's permanent structural part has an envelope that is also transformable varying its permeability. The system performs environmentally both to control light levels and air flows in the space [Hoberman]. Another cover is realized for the 10.7 m tall and 21 m wide transforming curtain of the Olympic Medals Plaza (Fig. 2.32).



Fig. 2.32: Cover solutions for retractable structures by Hoberman: transforming Olympic Arch for the 2002 Winter Olympics (Salt Lake City, USA) designed by Hoberman [Hoberman]

For a different solution P. E. Kassabian has suggested a series of rigid cover elements attached to the multi-angulated elements [Kassabian, 1999] in a manner that the cover elements neither interfere nor overlap during motion while providing a continuous, i.e. gap free, covering surface in both the open and closed positions of the structure. Each cover is attached to a single angulated element so the motion of the structure is not inhibited. Several solutions were developed for finding optimal shape for these covers, with straight or curved inclination lines [Buhl and Jensen, 2004].

2.3.4 Pantadome erection

Not taking the construction of them into account, the 3D spatial structures are extremely efficient. However, the difficulties with installation (big amount of scaffolding, labor and time) often highly decrease this efficiency. This drawback can be significantly reduced with the unique structural system called the Pantadome System invented by M. Kawaguchi and will be herein explained in accordance with M. Kawaguchi [2002].

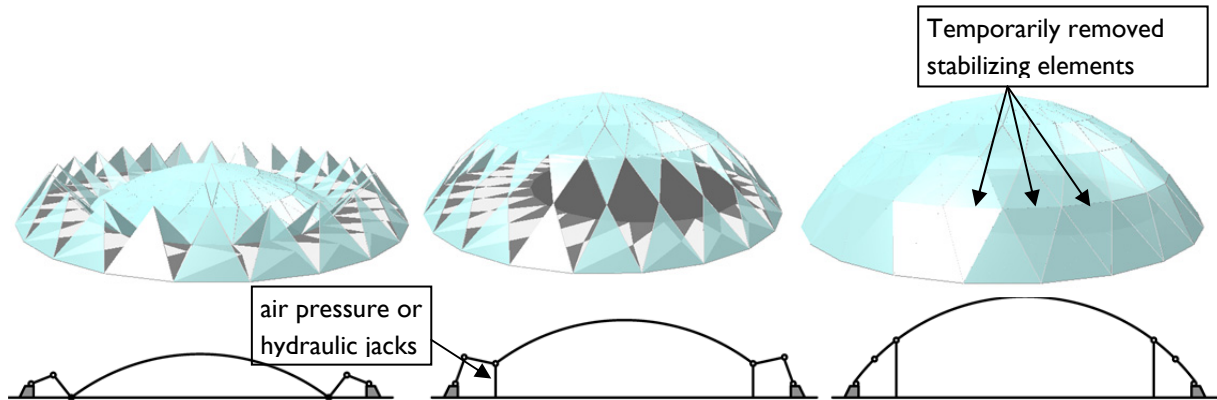


Fig. 2.33: Schema of the of the pantadome erection [Friedman et al., 2011/4] (in accordance with [Kawaguchi, 2002])

The principle of this structural system is to make a dome or a conical space frame kinematically unstable for a period of construction so that it is “foldable” during its erection. This can be done by temporarily taking out the members lying on a hoop circle (Fig. 2.33) then the dome is given a “mechanism”, like a 3D version of a parallel crank or a “pantograph”.

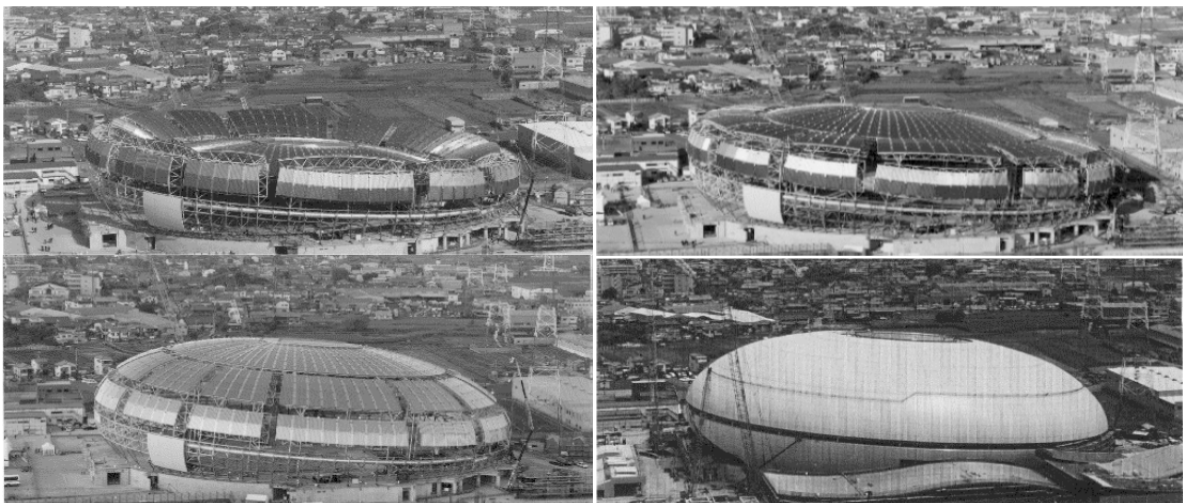


Fig. 2.34: Erection of Namihaya Dome (Showa Sekkei Corp), Osaka, 1997 [Kawaguchi, 2002]

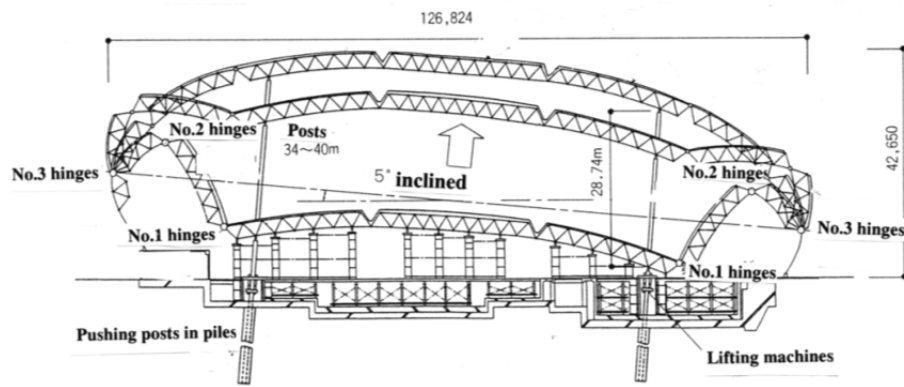


Fig. 2.35: Erection of Namihaya Dome [Kawaguchi, 2002]

Since such a dome is assembled in a folded shape near the ground level and the entire height of the dome during assembling work is very low compared with that after completion, thus the construction can be done safely and economically, and the quality of work can be assured more easily than in conventional erection systems. Not only the structural frame but also the exterior and interior finishings, electricity and mechanical facilities can be fixed and installed at this stage. The dome is then lifted up. Lifting can be achieved either by blowing inside the dome to raise the internal air pressure or by pushing up the periphery of the upper dome by means of hydraulic jacks. The major advantage of this system compared with different lifting solutions is that no guying cables or bracing elements are necessary for lateral stability. This is due to the fact that the mechanism of the system can be controlled with only one freedom of movement in the vertical direction. When the dome has taken the final shape, the hoop members which have been temporarily taken away during the erection are fixed to their proper positions to complete the dome structure. Several designs have been realized in accordance with the pantadome principle. One is the Namihaya Dome with diameter of 127m and 111m, whose erection and its lifting schema can be seen on Figs. 2.34 and 35.

2.4 Tensegrity structures

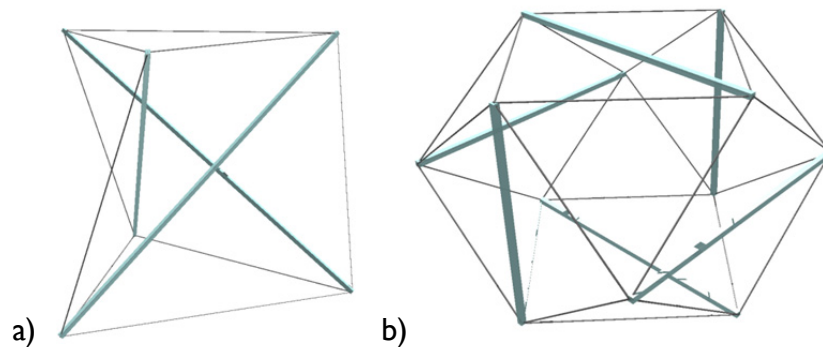


Fig. 2.36: Some tensegrity systems: a) the tensegrity tripod b) expanded octahedron [Friedman et al., 2011/4]

Most of the deployable lattice systems are formed by scissor-like structures. However, there is a trend to apply also tensegrity systems when deployability is needed. This experimental system was born at the end of the 1940s from the artistic exploration of K. Snelson and Fuller's goal of creating maximal efficiency structures [Snelson, 2009]. Snelson called his tensegrity sculptures the "floating compression" system. Nevertheless, it is worthwhile to mention that at the same time exactly the same system was patented by D. G. Emmerich, called the "self-tensioning system" [Emmerich, 1964]. The elements of this spatial truss system can be separated to purely compressed and purely tensile components. With this separation, the tensioned members can be as lightweight as current material technology allows, resulting extremely light, economical and visually less intrusive structures. Just as the authorship of the invention, the exact definition of tensegrity is still disputed [Motro, 2006]. Maybe the first clear definition of this kind of structure is the one that A. Pugh clarified: "A tensegrity system is established when a set of discontinuous compressive components interacts with a set of continuous tensile components to define a stable volume in space" [Pugh, 1976]. Clear definition is further investigated and refined by R. Motro [Motro, 2006]. The simplest tensegrity unit is the tensegrity tripod [Burkhardt, 1994] (Fig. 2.36a) and other tensegrity networks can be derived from geodesic polyhedra [Hugh, 1976] (Fig. 2.36b-c). By the assemblage of these units planar and spherical structures can be created, thus it can be used for walls, floors and roofs, or bridges. Fig. 2.37 shows the spherical assembly of tripods designed by B.R. Fuller, a recent design for a tensegrity roof and a realized, 470 m long tensegrity bridge with 128 m main span in Brisbane, Queensland, Australia.

The idea to have only tendons connected to struts is probably the most innovative concept of this type of structures resulting extremely simple joints. Beyond the difficulty of form finding [Motro, 2006] the main problem of this type of non-conventional structure is the difficulty of manufacturing as the geometry of spherical and domical structures are pretty complex. Other big disadvantage, similarly to all tensile systems, is the poor load response (relatively high deflections and low material efficiency [Hanaor, 1987] as compared with conventional, geometrically rigid structures and the lack of resistance to concentrated loads.

Another big disadvantage is that conventional architectural structures cannot be applied for cladding and connecting structural elements. Consequently, it requires a complete innovation of complementary technologies. A big advance when comparing with other tension systems is that tensegrity structures can encompass very large areas with minimal support at their perimeters, obviating the “heavy anchorage devices” needed for support with some cable-based technologies, or extensive support structures needed by some composite structures, mixing tensegrity systems and non-tensegrity technologies [Motro, 1987]. Deviating slightly from the canonical definition, R. Motro explored and tested many different tensegrity systems for architectural application [Motro, 2006].

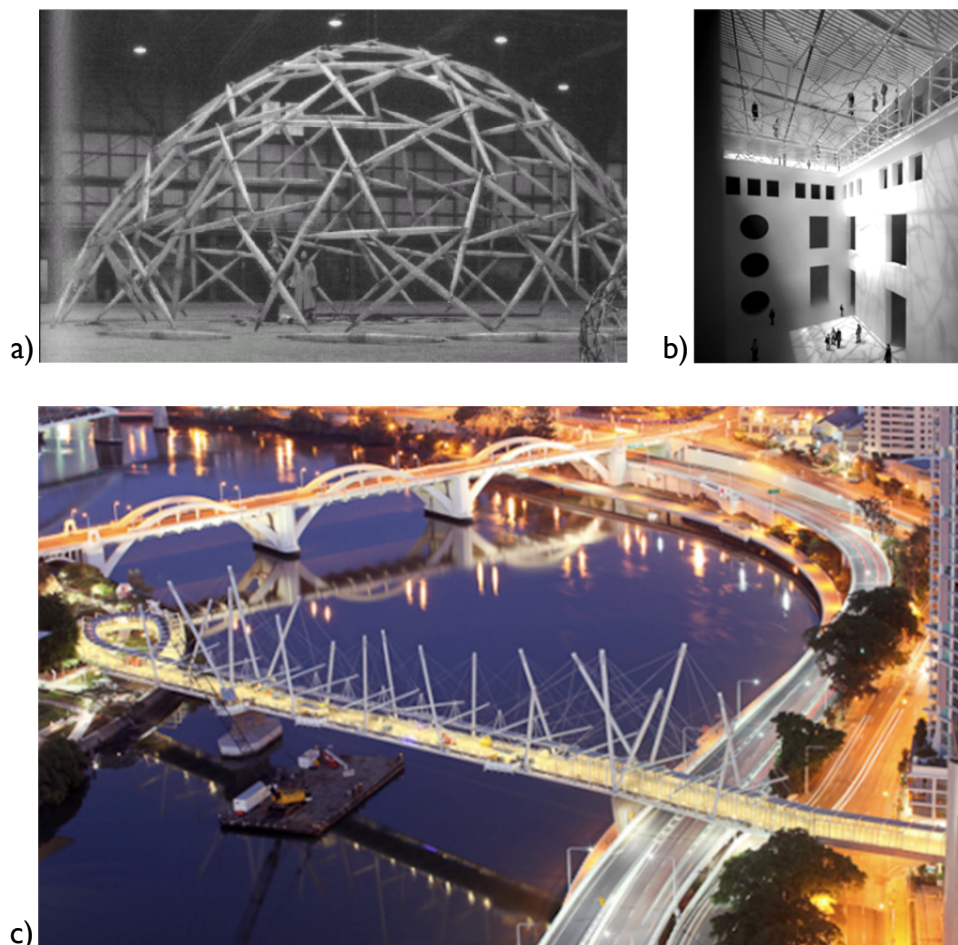


Fig. 2.37: Architectural applications: a) Geodesic tensegrity dome by Fuller, 1953 [Gengnagel, 2002] b) tensegrity roof design of ABDR Arch. Association [ABDR] c) Tensegrity Bridge (Kurilpa Bridge, Brisbane; designer: Cox Rayner Architects and Arup Engineers) [Anupam]

A new type of deployable structure can be created due to the intrinsic property of tensegrity structures. Foldability can be easily obtained by changing the element lengths. This can be either the changing of strut length by using telescopic bars or the folding can be enriched by changing the length of the cable. The main difficulty of the former method is that in the folded configuration the cable is often creates an inextricable tangle, thus unfolding the system is often opposed. The later rather proved to be a usable method concerning assemblies. [Motro et al, 2001]

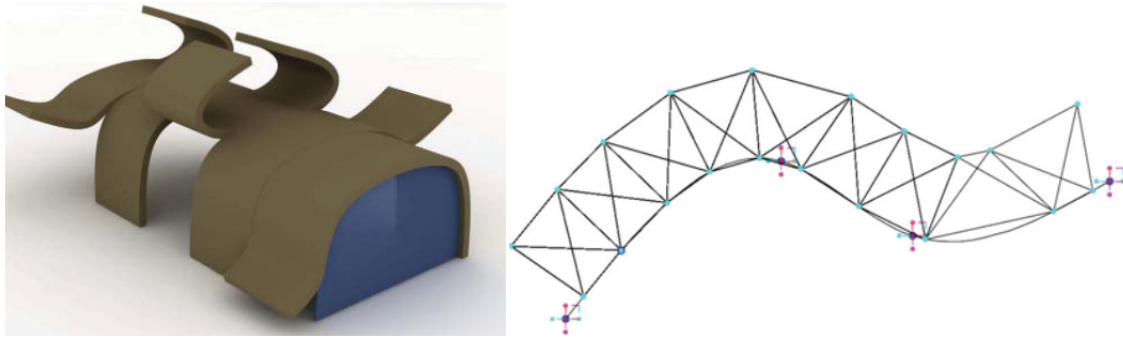


Fig. 2.38: *Single-curved tensegrity grids for responsive architecture by A. Herder [Herder]*

The trend to design adaptive/responsive architectural applications turns the kinematic indeterminacy of tensegrity structures an advantage [Tibert, 2002]. This is due to the fact that only small quantity of energy is needed to change the configuration and thus the shape of the structure. One example of adaptive roof design is the actuated tensegrity of A. Herder [Herder], who used computational design tools to develop a load bearing simple curved tensegrity structure (Fig. 2.38) that is able to change its shape continuously. He used synchronized actuation in a regular tensegrity grid.

2.5 Other deployable lattice designs and mixed systems

For architectural and special applications several deployable lattice systems were invented using ideas differing from the already mentioned pantographic or tensegrity systems and some use a mixture of the mentioned types. The categorization of these lattice systems is quite cumbersome as each invented system is very unique based on ingenious inventions [Pellegrino, 2001]. Herein only a few examples will be presented without scoping an exhaustive list.

For instance, the coilable mast system invented by Mauch [Webb and Mauch, 1969] is derived from the idea that any elastic rod can be pushed to a helical shape [Love, 1944] (cited by [Pellegrino, 2001]). His lattice column is deployed through compressing the longitudinal elastic bars (called longerons) into a helical deformed shape. In the deployed configuration the stiffness is reached by bracing bars (battens) perpendicular to the longerons, and diagonal prestressed cables (Fig. 2.39a).

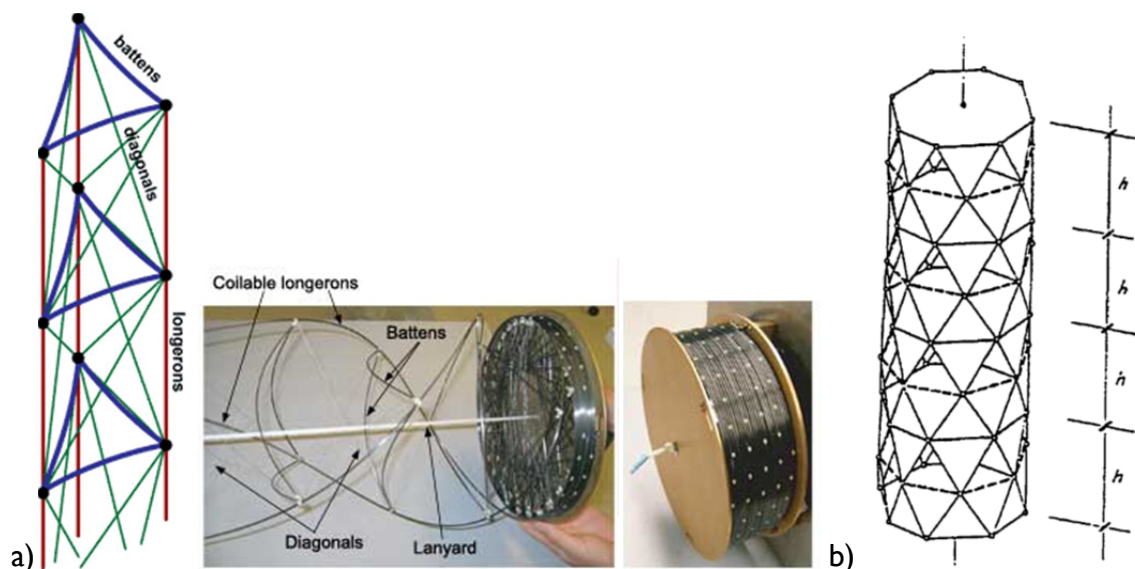


Fig. 2.39: Deployable masts: a) coilable mast by Mauch (Jet Propulsion Laboratory [JPL]) b) foldable mast by Hegedűs [1993]

When released the coiled structure deploys due to the loaded energy in the folded system. Loaded energy can come from special joint configuration, too. This is the case with the deployable structure presented by Fanning and Holloway [1993] where the deployment is due to a spring embedded at the node, forcing the joint to rotate and consequently to deploy when releasing the structure [Raskin, 1998]. The deployment of the foldable column of Hegedűs [1993] also cumulates strain energy with lengthening the horizontal elastic bars while packing (dashed lines in Fig. 2.39b) which results in the structure to pop-up when released. This column consisting of rigid and elastic bars and rigid panels between segments – based on the Yoshimura folding pattern – folds with a snap-through-like behavior.

Folding can be achieved by changing the length of the elements similarly to the examples mentioned at the tensegrity structures. Fig. 2.40 presented by Mikulas et al. [1992]

shows the three possibilities of deploying a planar truss with N bays: by changing the length of the diagonal, the chord or the battens.

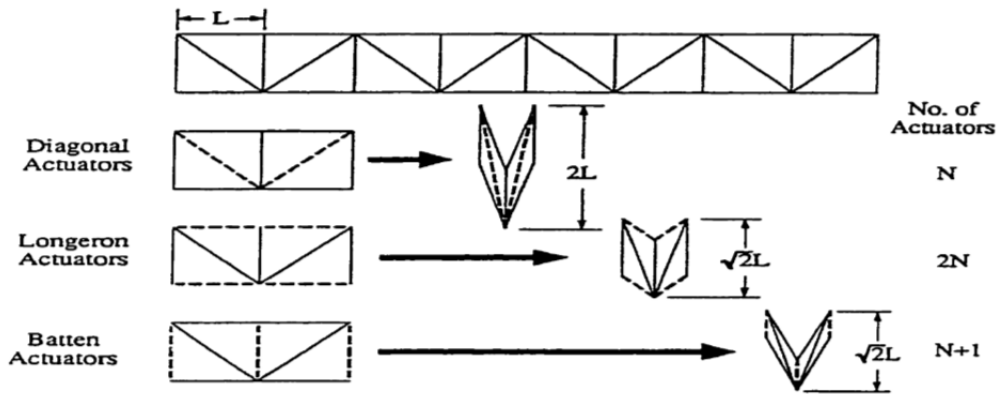


Fig. 2.40: Deployment of planar truss with length-variation [Mikulas et al., 1992]

Other foldable lattice designs use sliding joints for transformation. This is the case with the ancient structure of the umbrella. Similar but more recently published examples are shown in Fig. 2.41 presenting the 3D foldable lattice structure of Onoda et al. [1996] and of Krishnapillai et al. [2004]. The latter is based on the cable-strut systems of Liew et al. [2003].

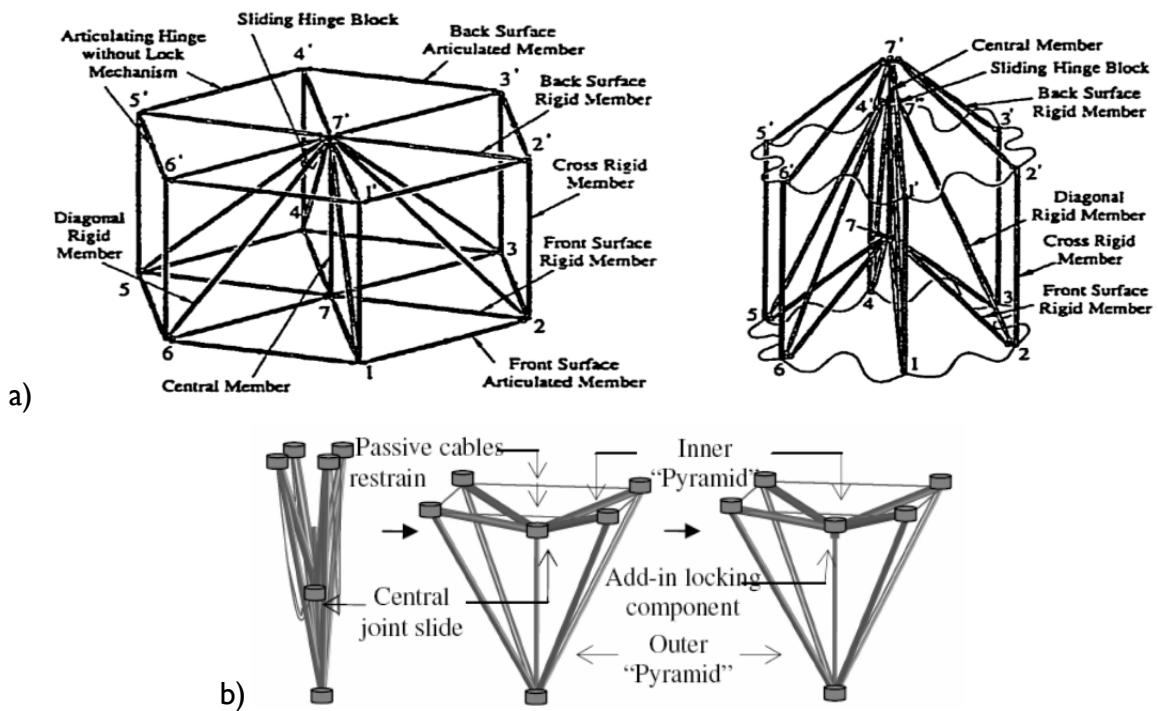


Fig. 2.41: Deployable 3D truss units with sliding node: a) unit by Onoda et al. [1996] (cited by Raskin [1998]) and b) pyramid in pyramid unit by Krishnapillai [Vu et al., 2006/1-2]

For avoiding the defects of instantly deploying, snap-through type deployable structures [Krishnapillai, 2004] a new family of deployable units was introduced combining cable-strut systems with foldability features similar to the deployable tensegrity structures. One example was already demonstrated in Fig. 2.41b. A different category within this family

is the cable-stiffened pantographic systems shown in Fig. 2.42. These mixed systems — based on the ‘deploy & stabilize’ method — is rather applicable for terrestrial use as elements need post-stabilizing and consequently with these units structures cannot be instantly deployed, the on-site assembling is more laborious. The deployable cable truss systems were thoroughly analyzed by Vu et al. [2006/1-2]. Due to his paper the novel system proves a remarkable structural efficiency (calculating from the optimized structure’s total load/structural self-weight and the span/deflection ratios) that is even comparable with conventional non-deployable double layer lattice designs and it is also fast and easy to construct (comparing with conventional double layer structures) while the weight of the structures is still competitive. For an example of architectural application of cable-pantographic elements, a deployable membrane structure was offered by Tran et al. [2006]. The two-wing butterfly membrane structure is supported by two deployable inclined arches (Fig. 2.43), for which parametric studies were carried out by the authors in the case of 30m spanning arches.

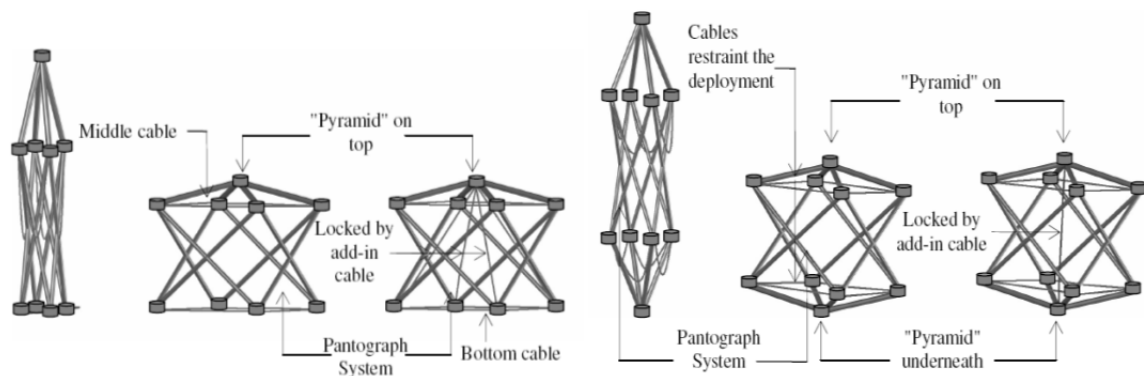


Fig. 2.42: Two types of cable stiffened pantographic system by Krishnapillai et al. [Vu et al., 2006/2]: stowed state, deployed state and the final, ‘locked’ configuration

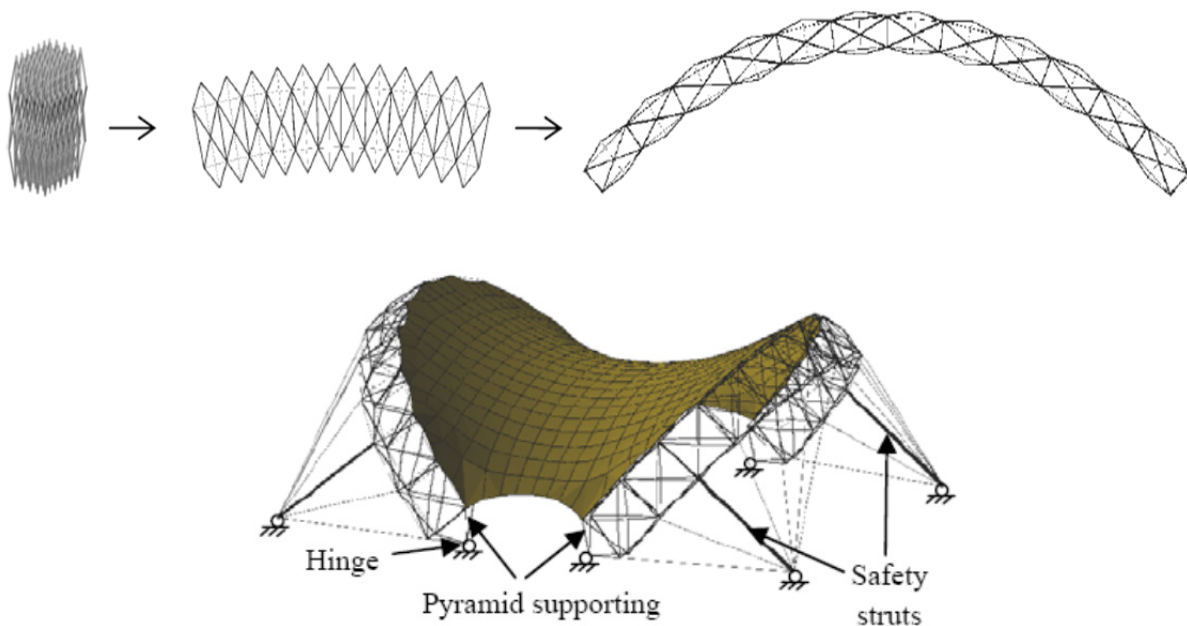


Fig. 2.43: Deployable arches by cable-strut-pantograph elements for a two-wing butterfly membrane structure: deployment of arches and the model of the structure [Tran et al., 2006]

2.6 Soft, membrane structures

Similar to the structures opened by the movement of rigid panels, F. Otto classified the membrane convertible constructions also in a movement matrix (Figs. 2.44-45). He distinguished two different types; one with stationary supporting structure and another with movable supporting structure. Pneumatic structures can also be classified as deployable membrane structures.

As mentioned in the introduction, these types of structures were already in practice in the very past history. However, it was just at the end of the second half of the last century when engineers began to apply textile as building material for large-span constructions. The pioneering works of Frei Otto motivated plenty of membrane designs throughout the world.

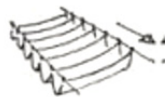
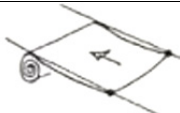
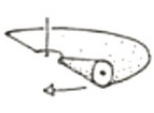
type of movement	direction of movement			
	parallel	central	circular	peripheral
bunching				
rolling				

Fig. 2.44: Classification of membrane convertible constructions: the movement matrix of structures with stationary supporting structure [Otto, 1971]

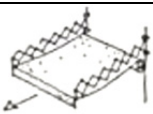
type of movement	direction of movement			
	parallel	central	circular	peripheral
sliding				
folding				
rotating				

Fig. 2.45: Classification of membrane convertible constructions: the movement matrix of structures with movable supporting structure [Otto, 1971]

2.6.1 Foldable membrane structures

The main difficulty concerning deployable membrane structures is the stabilization of the membrane in all the possible configurations (folded, during deployment, opened configuration). In the extended position, the membrane can be secured with pretensioning, which can be achieved either by the drive system itself or by special tensioning devices at the edge of the roof. The flapping wind effect during deployment — causing quite large deformations with small forces — is one of the main difficulties. [Walter]



Fig. 2.46: Olympic Stadium in Montreal (architect: Roger Taillibert) [Tolivero] and its original retractable membrane roof [Barnes, 2000]

This difficulty occurred in the case of the Olympic Stadium in Montreal, Canada (Fig. 2.46). The stadium was to open for the 1976 Olympic Game, but the retractable roof was finished only in 1988. The 20 000 m² PVC/Kevlar folding membrane roof which was to be opened and closed by the 175 m inclined tower, was repeatedly damaged by local failures due to aero-elastic instability. The structure was replaced with a non-retractable spatial steel roof structure.

A similar but more successful design was evolved in 1988, Zaragoza, Spain for the roofing of the bullfighting Arena (Figs. 2.47-48). The roof was separated to a 83 m diameter fixed and a 23 m diameter central convertible membrane roof. For both parts a double spoked wheel system was used. The prestressed outer spokes span between an outer compression ring and two sets of inner tension rings held apart from each other by struts. The membrane of the permanent roof is draped over the lower set of radial cables. The retractable inner roof has similarly two sets of spokes between the inner tension rings and a central hub above the centre of the bullring. The two sets of spokes are connected by an electric spindle. The membrane is suspended to the lower layer of spokes by slides that can be moved by a stationary drive system. When the roof is open, it hangs bunched up in the centre, when is to be closed, 16 electric motors draw the bottom edge of the membrane out to the lower tension rim. Once the edge is secured to the rim, prestress is applied by rotating the top spinder (Fig. 2.48) at the central point, thus the retracted membrane is stabilized [Holgate, 1997; Walter]. Even a 63 m diameter retractable roof was constructed in accordance with this principle over the centre court in Hamburg Rothenbaum [Walter].



Fig. 2.47: The retractable part of the Bullfighting Arena roof in Zaragoza (architect: J. Schlaich) [Sobek, 1999] (cited by [Walter])

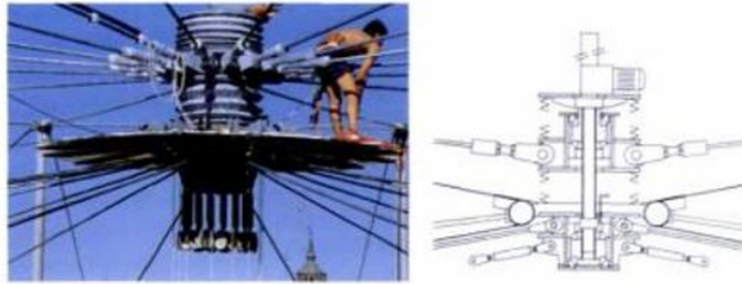


Fig. 2.48: Central spinder for prestressing the cables [Holgate, 1997]

Different membrane folding can be evolved by the umbrella principle. A nice example is the convertible cover of the two courtyards of the Prophet's holy Mosque in Madinah (Fig. 2.49a). The twelve large umbrellas (17 m x 18 m in the open configuration) are stem from the developed system of F. Otto [Otto, 1995]. These umbrellas ensure the shading during the day and the ventilation and cooling during the night.



Fig. 2.49: a) Architectural umbrellas in the courtyard of Mosque in Madinah [Otto, 1995] (cited by [Walter]), Foldable roof in the Rathaus, Vienna [Tillner, 2003] (cited by [Walter])

The openable roof installed in 2000 in the courtyard of the Rathaus, Vienna (Fig. 2.49b) is an example of a different convertible system where the membrane is retracted with sliding the cross-girders [Walter; Tillner, 2003].

The ability to provide numerical simulations for increasingly complex membrane is advancing rapidly due to computer hardware development and the improved computational procedures of nonlinear structural systems. This sweepingly advanced development with the inventions in textile technologies is exploring the further architectural and technical potentials of these structures.

2.6.2 Pneumatic structures

The supporting medium of pneumatic structures is compressed air or gas that creates tension forces on the elastic membrane, thus ensures the strength and the stability of the structure. Probably the balloon is the most well-known classical pneumatic structure. In construction practice the first inflatable structures appeared in the 1950's. These were mainly shelters with single-wall inflatable "bubbles", called air-supported structures constructed from a single layer of pliable material that is supported by the internal compressed air. This internal air pressure slightly has to exceed the external pressure. Consequently, this system requires an air lock, a continuous pressurization system that balances the air leakage, and an anchorage that fixes the structure to the ground or to the substructure.

Other inflatable designs use double-layer inflatable configurations. These air-inflated structures use tubular (air-beam structure) or cellular (air-cell building) shaped membrane skin with an internal pressurization that form together structural elements similar to the conventional ones. The skin takes the tension forces whereas the air is responsible for compression forces in a manner like the reinforced concrete. This new generation of inflatable structures has in general no steel, no aluminium, and no traditional supports and yet can handle large structural loads.



Fig. 2.50: a) Inflatable roof for Heathrow airport central bus station (architect: D5) [Lindstrand, 2006]; b) 19.5 m x 40 m Exhibition Hall with air-inflated elements (architect: Festo AG & Co) in Germany [Festo]

Now, when fabric and computer technology are catching up with this concept, the possibilities of inflatable structures in commercial, military and special applications seem unlimited. Even cubic interior building can be constructed with the air-beam technology (Fig. 2.50b). While more expensive than comparable aluminum structures, inflatable beams save money on transportation and installation because of their small weight and packing size. Proving these facilities, the inflatable roof designed for covering the central bus station of the Heathrow airport (Fig. 2.50a) is an instructive example. The installation of the roof completed in one only night in 2006. Pneumatic design was chosen because the realization of the foundation of a conventional roof would have been run into obstacles as one of the airport's Tube stations is just underneath the site [Lindstrand, 2006].

2.7 Pneumatic systems for the erection of spatial structures

2.7.1 Formwork for thin concrete shell structures

Concrete shells are extremely material efficient structures as uniformly distributed loads mainly cause normal forces appearing in the cross sections while moments are insignificant. Moreover, these structures are also very popular for their attractive architectural appearance. Nevertheless, the time-consuming and expensive production with a conventional formwork is an important drawback of these structures. Similarly to the pantadome system used for lightweight 3D spatial structures, transformability can serve for combating this major problem of concrete shell designs.

Three different pneumatic formwork methods are used for monolithic concrete shell structures [van Hennik, 2008]. If the membrane is inflated first, (Fig. 2.51) the concrete can be sprayed on the inner side or the outer side of the membrane. Evidently the reinforcement has to be placed before spraying the concrete. In the case of the shotcrete on the inside a special layer of polyurethane foam has to be sprayed on the membrane to hold the reinforcement. The membrane can be either taken off/out for reuse after the hardening of the concrete or can be left as a waterproof layer.



Fig. 2.51: a) Inflation of formwork; b) shotcreteing on the inside of the membrane; c) irregular shape structure constructed with pneumatic formwork [Pirs SA.]

The principle of the third method, invented by D.N. Bini, is to do all the constructional work on the ground in plane and then inflating the structure into 3D shape. The pneumatic lifting of the reinforcement and the freshly placed concrete can be achieved with a special sliding reinforcement system (Fig. 2.52a) consisting of conventional steel bars and extensible spirals. As the structure lifts and takes its shape, the spirals stretch and the reinforcing bars slide inside them to reach their final position in the structure [Roessler and Bini, 1986]. For Binishells two layers of membrane is used. The inner layer is attached to the ring beam being part of the foundation and the outer layer is placed after placing the reinforcement and the concrete on the inner layer. The concrete is vibrated after lifting the structure via an equipment that is attached to the centre of the outer membrane (Fig. 2.52b-c). After lifting the outer membrane can be removed and after hardening the inner layer can be deflated and reused for the next construction.

Though pneumatic systems has already been applied for concrete shell structures since the 1960s, these systems seem to regain their popularity due to their aesthetic

appearance, improved technological background and renewed structural concepts. Even irregular shell shapes are constructed with pneumatic formwork [van Hennik, 2008].

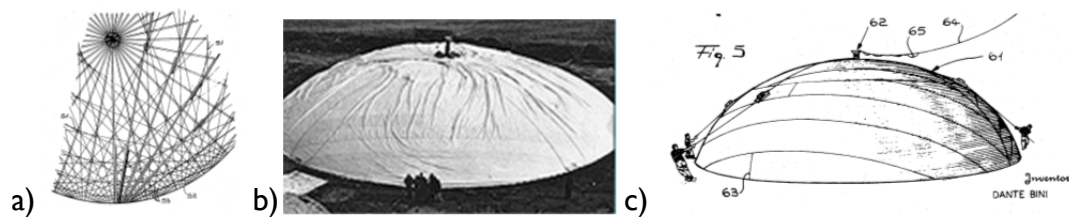


Fig. 2.52: The binishell system: a) expandable reinforcement [Bini, 1972]; b) erection of the dome [Binishell System]; c) vibration of concrete after erection [Bini, 1972]

2.7.2 Erection of segmented concrete or ice domes

Two new and very efficient construction methods for hemispherical concrete shells have been developed at the Institute for Structural Engineering at Vienna University of Technology by J. Kolleger. The novel concepts were tested not just on large scale concrete but as well on ice domes. Both methods start with an initial plain plate that is subsequently transformed into a shell structure [Dallinger and Kolleger, 2009].

The principal step of the first method is to fragment the shell structure into a polyhedron enabling the use of planar precasted parts that can be easily produced at the factory, transported to the site and then quickly assembled. The elements kept together by radial and circumferential steel tendons (Fig. 2.53). The circumferential tendons are tightened through winches and are instrumental for the assembly of the elements. The erection is achieved with a pneumatic formwork that lifts the structure into the desired position. [Dallinger and Kolleger, 2009]



Fig. 2.53: Transformation of precast divided planar segments into a hemispherical dome [Dallinger and Kolleger, 2009]

In the case of the second method the flat plate is divided into segments which are distorted uni-axially and lifted into the final position (Fig. 2.54) [Dallinger and Kolleger, 2009]. The transformation is controlled by one or more active cable(s) and by either a crane positioned in the centre or a pneumatic formwork placed under the structure [Kolleger et al., 2005].

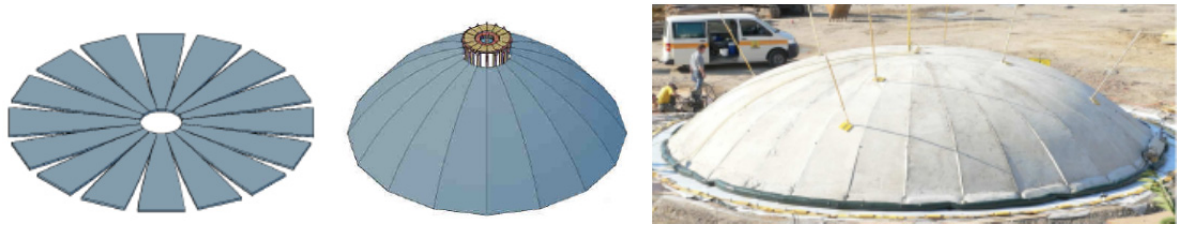


Fig. 2.54: Segment lift method [Dallinger and Kolleger, 2009]

2.8 Summary of architectural background

After a short summary of the historical background, an overview on transformable structures used in civil engineering and architecture have been presented. The feature of transformability in the case of architectural use can arise from two different **motivations**. The first motivation is to create a *fast and/or safe construction method* and in some cases it can be also the need for a *quick demounting process* and the *possibility of reusability*. The second motivation is to *adapt the structure to external excitations like functionality requirement or weather conditions*.

The **motivation to create a fast constructional method** resulted in exotic inventions that can be sub-classed to two categories:

- **Controlled mechanisms** (e.g. by active cables, by pneumatic system)
- **Structures undergoing instability phenomenon**

Pantographic systems like the collapsible movable theatre of Piñero, the deployable mast of Pellegrino or the quickly retractable swimming pool cover of Escrig can be mentioned in the first category. The minimal material use *Tensegrity systems* also offer the possibility of foldability. Ongoing research works try to find a greater variety of possible architectural applications. *Some soft membrane systems* like cable-stiffened textile structures and pneumatic structure can be quickly installed too. F. Otto remarkable systematic study on foldable membrane structures with the recent available material and calculation technologies led to a wide variety of architectural membrane designs even used for big span permanent structures. Pneumatic systems can also serve as a supplementary system for the erection of 3D structures making the installation easier, faster and safer. The “*pantadome*” structural system invented by Momoru Kawaguchi, and some earlier and novel *pneumatic formwork methods* for constructing monolithic and precasted *concrete domes* can be mentioned among these systems.

Self-deploying or self-stabilizing (bi-stable) structures can be constructed involving instability phenomenon during deployment. The pop-up systems like the coilable mast of Mauch or the antiprismatic cylindrical structure of Hegedűs can be mentioned among self-deploying lattice systems. A nice example of a self-stabilized pantographic dome system is the one first offered by Zeigler.

Though these structures mentioned above still attract the military and provisory events in first place, a trend can be observed to apply them for permanent buildings where translucent or extremely light construction is needed.

Structures that can move while in use can be designed, too.

A common example is an off-shore industrial installations where transformability is needed because of functionality requirements. Less familiar structures are those where transformability is coming from energy-saving consideration or from the aim to ameliorate occupant comfort, raise the attraction of the building.

The goal to design dynamic structures that are able to change morphological/mechanical/physical properties and behavior as a response to external excitations and requirements was first addressed in the 1960s and 1970s.

Early transformable designs appeared in first place for housing sport venues. With the currently growing media focus on sport events the demand for *retractable structures* seems to be steadily increasing. Most of these designs use *rigidly moving parts* to retract the roof structure. In most of the cases the slicing of an ideal structural shape results in gigantic structural height, and mechanical instruments enabling retraction further increase the costs of these structures. With new generation roofs like the *retractable pantograph structure* of Hoberman and Pellegrino and the application of a *retractable skin* fixed to the permanent structure can rather count with economical aspects. Several research topics focus on adapting *tensegrity and pantographic structures* to adaptive architecture. Combining transformable structures with a highly distributed control system which is already available in today's technology an intelligent responsive architecture is born. This possibility does not only prospect indoor environmental quality enhancement and better occupant comfort but a better use of natural energy resources and thus a rather sustainable design.

3 ANALYSIS OF A SIMPLIFIED PLANAR MODEL

3.1 Aims and scope

The snap-through type antiprismatic structures were aimed to be investigated. These structures undergo instability phenomenon during packing and deployment. The instability phenomena imply in general that a small perturbation of loading can lead to a disproportional amplification in computed response [Ibrahimbegovic, 2009]. The main challenge for civil engineers of analyzing these structures come from the fact that for conventional engineering structures the stability analysis stops at the calculation of the critical state, at the most, the nature of the post-critical range is needed.

For the first step, basic procedures used for stability analysis, and for structures undergoing instable phases have been investigated. To better familiarize with geometrical instability problems, the analysis of a simple, snapping-through shallow truss and its force-displacement diagram was analyzed with static and dynamical approach. This is presented in Annex B. In the beginning of the research, the investigation and refinement of existing research of the snap-through type lattice design, first presented by Zeigler [Zeigler, 1976], and later on thoroughly analyzed by several researchers [Krishnapillai, 1985, 1986; Gantes, 2001], was targeted as main research field. By profoundly studying the general characteristics (advantages and disadvantages) of the system, and simulating the packing of the structure, the choice of changing the predefined research topic has been made. Nonetheless, a force displacement diagram obtained from the finite element simulation of the packing of a basic segment is also annexed (Annex C).

Similarly to the above mentioned snap-through type deployable structure, the self-deployable (or pop-up) cylindrical structure proposed by Hegedűs undergoes instability problem during packing as well. But this system is rather immature, due to the lack of profound mechanical investigation and of ideas for practical application.

To understand better the behavior of these antiprismatic lattice structures, first a simplified 2D model was identified and investigated manifesting similar properties to the targeted 3D structure. The simplified model consists of elastic horizontal bars of initial length $l_{H0}=2r_0$ and rigid bracing bars shown in Fig 3.1. The bracing is only connected to the horizontal bars with joints allowing free rotations. The bracings are not connected to each other at their crossing point, hence allowing free sliding on each other. The top horizontal bar and every second horizontal bar are rigid. A vertical packing can be obtained by stretching the elastic horizontal bars.

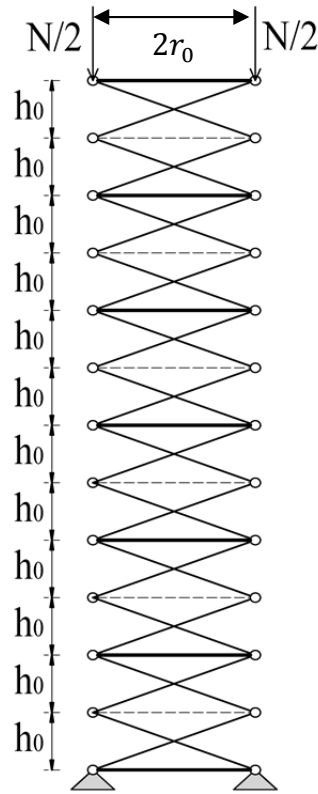


Fig. 3.1: Simplified planar deployable structure

3.2 Analytical investigation

3.2.1 Mechanical analysis of the basic segment

Kinematical equations

The basic unit (segment henceforth) of the planar structure consists of two rigid and one elastic horizontal bars and four rigid bracings shown in Fig. 3.2. If the initial height of the segment is $2h_0$, the length of the bracing is:

$$l_b = \sqrt{(2r_0)^2 + (h_0)^2}$$

When packing the segment by pushing down the top rigid horizontal bar to the height $2h^\varphi$, the middle elastic horizontal bar will stretch out. Assuming that the bracing is rigid enough, that is, incompressible the stretched length can be calculated from the Pythagoras equation as follows:

$$\sqrt{\left(\frac{l_H^\varphi}{2} + r_0\right)^2 + (h^\varphi)^2} = l_b \tag{3.1}$$

$$l_H^\varphi(h^\varphi) = 2\sqrt{(l_b)^2 - (h^\varphi)^2} - 2r_0 \tag{3.2}$$

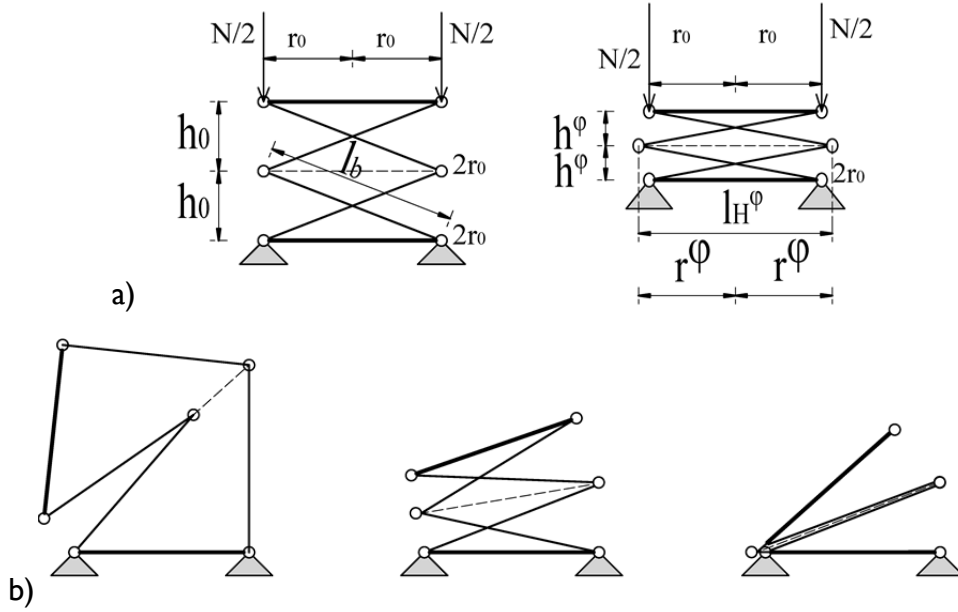


Fig. 3.2: a) Bottom segment of the simplified structure and its packing b) asymmetric freedom of motion of planar structure

And the stretching in function of the changed height (h^φ) or in function of the displacement (u) of the top nodes is:

$$\lambda = \frac{l_H^\varphi}{2r_0} = \frac{2\sqrt{(l_b)^2 - (h^\varphi)^2} - 2r_0}{2r_0} = \sqrt{4 + \frac{(h_0)^2 - (h^\varphi)^2}{(r_0)^2}} - 1 = \sqrt{4 + \frac{h_0 u - u^2/4}{(r_0)^2}} - 1 \quad (3.3)$$

In the packed configuration all the bars lie in the same line, hence the final length and the stretching of the elastic bar (corresponding to the final, packed configuration) is:

$$l_H^\varphi|_{h^\varphi=0} = 2l_b - 2r_0 \quad (3.4)$$

$$\lambda|_{h^\varphi=0} = \frac{l_H^\varphi|_{h^\varphi=0}}{2r_0} = \frac{l_b}{r_0} - 1 = \sqrt{4 + \left(\frac{h_0}{r_0}\right)^2} - 1 \quad (3.5)$$

As presented in Fig. 3.2.b, the structure has non-symmetrical freedom of motions as well, which is to be avoided in the case of a simple deployable mast. In the followings, the analysis will be restricted to movements symmetrical to the vertical symmetry axis of the structure only. It is to be mentioned that this is an important and large restriction. It involves the restriction of global buckling of the structure which should be also investigated in the future.

Equilibrium equation

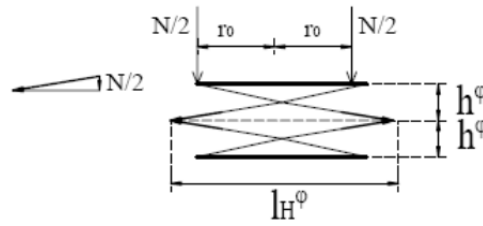


Fig. 3.3: Equilibrium of one segment of planar structure

For packing the structure, applying a vertical force N at the top horizontal bar with keeping the symmetry of the structure (Fig. 3.3), the elastic bar of the analyzed segment is tensioned by the four bracings; two coming from the top and two coming from the bottom. The tension force in the middle horizontal bar will be:

$$S_H(h^\varphi) = 2 \frac{l_H^\varphi(h^\varphi)/2 + r_0}{h^\varphi} \cdot \frac{N}{2} \tag{3.6}$$

As it can be seen from equation (3.6), the equilibrium equation is not linear in the sense that it depends on the geometrical configuration that is on the actual height of the segment.

Constitutive equation

The constitutive equation depends on the actually used material. First, for simplifying the solution and to get a basic understanding of general behavior, for the analytic solution the hypothesis of linear elasticity will be assumed, that is, the connection between strains and stresses can be herein written by Hooke's law. If the axial stress along the bar-length and the cross section A is uniform, this can be written in the form:

$$\varepsilon = \lambda - 1 = \frac{S_H(h^\varphi)}{EA} \tag{3.7}$$

where λ denotes the stretching, that is, the ratio of actual extended length and initial length of the elastic bar.

Equilibrium path

Combining kinematic, equilibrium and constitutive equations the force-displacement diagram can be written in the form:

$$N(h^\varphi) = \frac{S_H h^\varphi}{l_H^\varphi/2 + r_0} = \frac{EA[\lambda(h^\varphi) - 1]h^\varphi}{r_0[\lambda(h^\varphi) + 1]} = \frac{EA}{r_0} \cdot \frac{\sqrt{4 + \frac{(h_0)^2 - (h^\varphi)^2}{(r_0)^2}} - 2}{\sqrt{4 + \frac{(h_0)^2 - (h^\varphi)^2}{(r_0)^2}}} h^\varphi$$

(3.8)

or in function of u ($u = 2h_0 - 2h^\phi$), the vertical displacement of the top nodes:

$$N(u) = \frac{EA}{r_0} \left(1 - \frac{2}{\sqrt{4 + \frac{h_0 u - u^2/4}{(r_0)^2}}} \right) \left(h_0 - \frac{u}{2} \right)$$

(3.9)

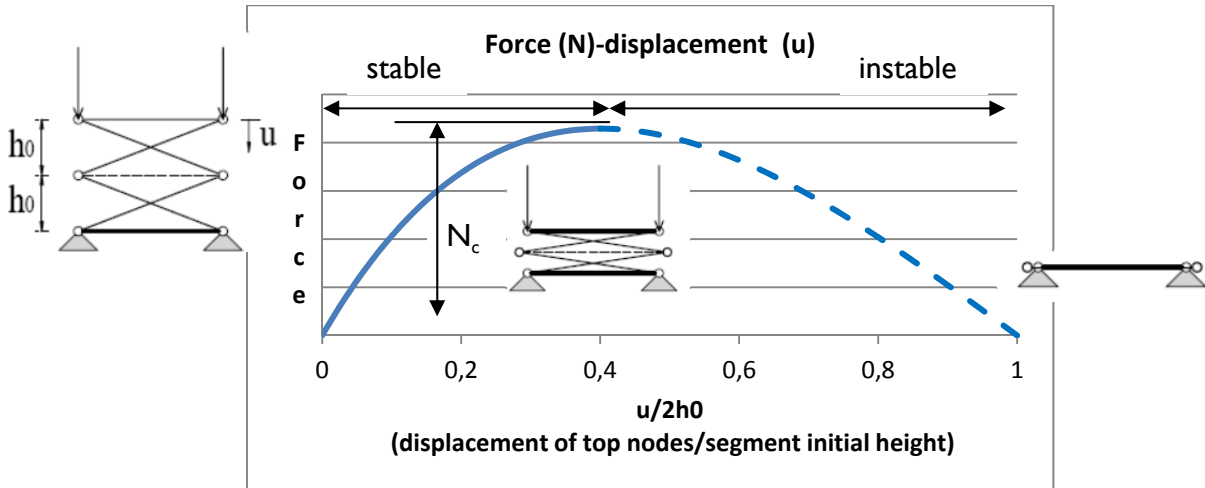


Fig. 3.4: Equilibrium path of basic segment

It can be seen from the plotted equilibrium path of Fig. 3.4 that during packing the structure goes through a critical point. Before this critical point the first state is stable (drawn with continuous line) while the second state is unstable (drawn with dashed line). Both the initial (deployed) and the final (packed) configuration correspond to zero force, but the latter is an unstable equilibrium position. If the bars can cross each other, the equilibrium path continues similarly to the force-displacement diagram of a typical snapping-through structure (like a shallow truss) finding its stable, stress-free position in a downward reflection of the initial one (Fig. 3.5). The closed configuration corresponds to the maximal strain energy (Fig. 3.5), and consequently with a small perturbation the structure will disengage right away from this configuration towards a position corresponding to smaller strain energy.

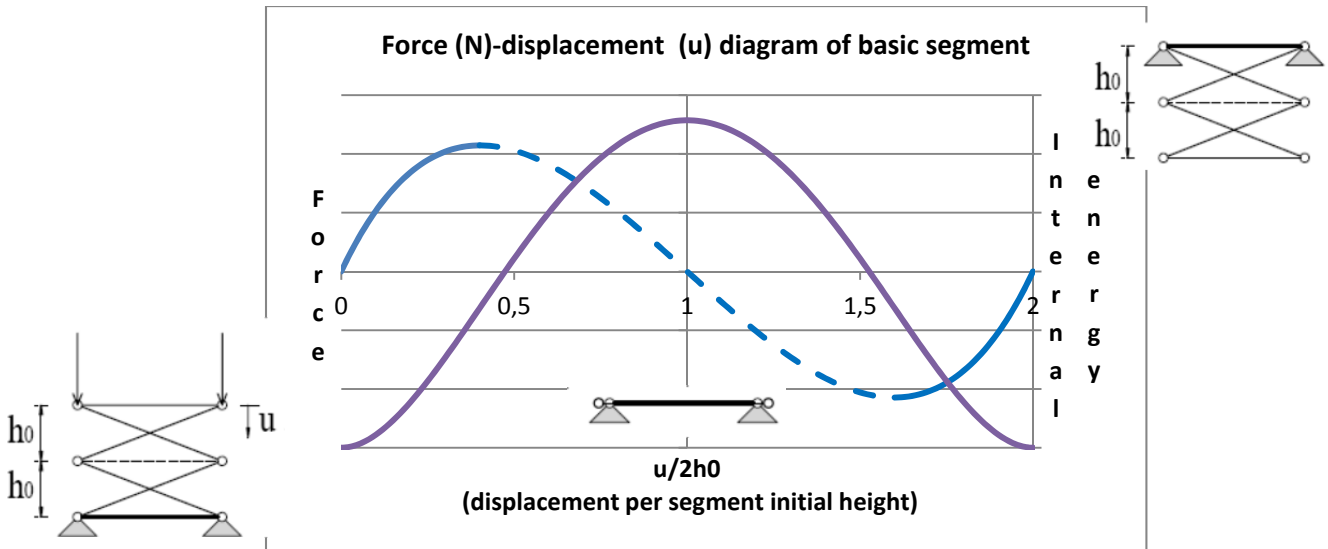


Fig. 3.5: Equilibrium path and internal energy during closure of boundary bars for basic segment with the ‘post-packed phenomenon’

If trying to close a mast consisting of more than one segment and if the segments do not close simultaneously this phenomenon necessarily occurs preventing the structure from a complete packed configuration (see later). When designing packable structures, it is of principal interest that the packed volume is minimal. Consequently, in order to ensure complete closure this phenomenon is to be avoided. Furthermore we will call this behavior after closure a ‘post-packed phenomenon’.

Calculation of critical state – nonlinear instability problem

Assuming cyclic symmetrical folding, the planar structure’s motion can be written with one only geometrical parameter. Let that parameter be u . The critical equilibrium state corresponds to the zero value of tangent stiffness that is:

$$\frac{dN}{du} = 0 \tag{3.10}$$

Introducing the function:

$$g(u) := \sqrt{4 + \frac{h_0 u - u^2/4}{(r_0)^2}} \tag{3.11}$$

$$N(g(u), u) = \frac{EA}{r_0} \left(1 - \frac{2}{g(u)}\right) \left(h_0 - \frac{u}{2}\right) \tag{3.12}$$

$$\frac{dN}{du} = \frac{EA}{r_0} \left[\frac{2}{g^2(u)} g'(u) \left(h_0 - \frac{u}{2}\right) + \left(\frac{1}{g(u)} - \frac{1}{2}\right) \right] = \frac{EA}{r_0} \left[-\frac{1}{2} + \frac{1}{g^3(u)} \left(\frac{h_0 - u/2}{r_0}\right)^2 + \frac{1}{g(u)} \right]$$

(3.13)

where

$$g'(u) = \frac{dg(u)}{du} = \frac{1}{2} \frac{1}{g(u)} \frac{h_0 - u/2}{(r_0)^2} \quad (3.14)$$

Hence the critical values of u can be calculated from the equation:

$$\frac{dN}{du} = 0 \Rightarrow \frac{1}{g^3(u_{cr})} \left(\frac{h_0 - u_{cr}/2}{r_0} \right)^2 + \frac{1}{g(u_{cr})} - \frac{1}{2} = 0 \quad (3.15)$$

Substituting equation (3.11) in (3.15):

$$\left(\frac{h_0}{r_0} \right)^2 + 4 - \frac{1}{2} \left[4 + \frac{h_0 u_{cr} - u_{cr}^2/4}{(r_0)^2} \right]^{3/2} = 0$$

$$\Rightarrow u_{cr} = 2h_0 \pm 2r_0 \sqrt{\left(\frac{h_0}{r_0} \right)^2 - \left[2 \left(\frac{h_0}{r_0} \right)^2 + 8 \right]^{2/3} + 4}$$

(3.16)

For instance, in the case of $r_0 = h_0 = 1$ the results for the vertical displacement of the top joints will be:

$$u_{cr,1,2} = \begin{cases} 0.803 \\ 3.197 \end{cases}$$

3.2.2 Mechanical analysis of multi-storey, 'alternately stiffened' structures

Tracing equilibrium paths: uniform and bifurcated packing

By piling k segments on top of each other we get a deployable mast shown on Fig. 3.1. From now on, we call this type of masts 'alternately stiffened' as every second horizontal bar is rigid (see Fig. 3.1). The above analyzed segment is serially connected, and consequently in any of the horizontal sections of the basic segments the resultant force equals the force applied in the top facet. Hence the equilibrium equation of the complex system will be falling into k separate equations:

$$N(\mathbf{h}^\varphi) = N_i(h^\varphi_i) = N_i[h^\varphi_i, (EA)_i, (h/R)_i] \quad (i = 1..k) \\ N_i = N \quad (3.17)$$

where the functions $N_i(h^\varphi_i)$ correspond to the function given in (3.8). To determine the force displacement diagram of the complex structure the cumulated relative displacements are needed from the segment heights. The relative displacement between the boundary-facets, that is, the displacement of the top facet (if the bottom facet is fixed) is:

$$u = 2 \sum_{i=1}^k (h_0 - h_i^\varphi) \tag{3.18}$$

The force-displacement diagram in the case of uniform packing and $k = 6$ is shown in Fig. 3.6. The uniform packing can be mentioned as an ‘ideal’ and rather irrational equilibrium path as it is only possible when the segments are exactly identical and if the mass of the structure is ignored. In Fig. 3.6 the optional successively controlled deployment path is shown too, which can be realized by controlling the displacement of the end nodes of each rigid horizontal bar.

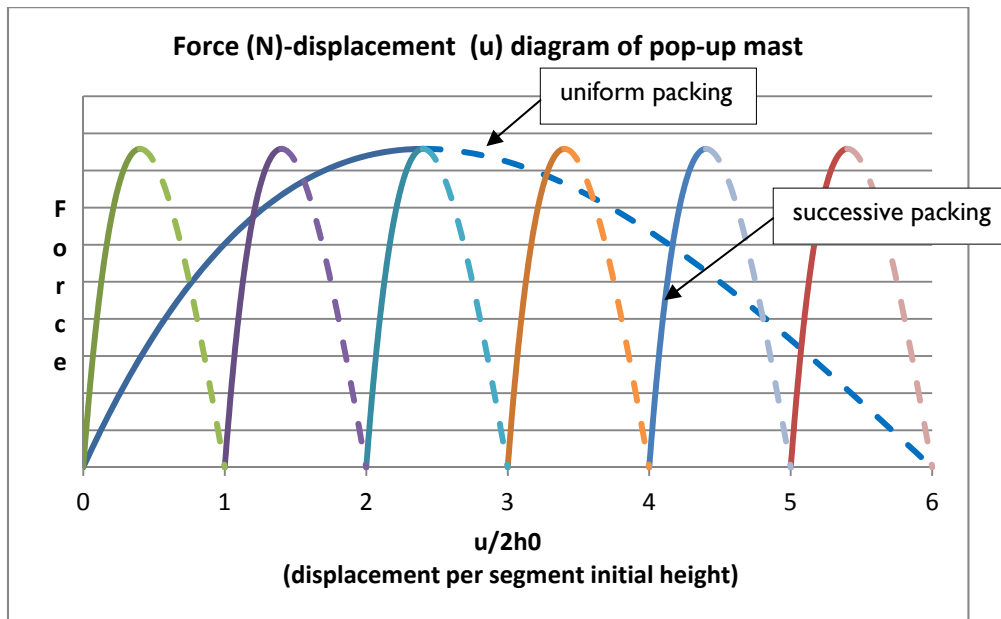


Fig. 3.6: ‘Ideal’ (uniform) and successive packing of planar deployable mast of six segments

The bifurcation of the equilibrium path can be easily visualized for two segments built on top of each other. In Fig. 3.7 the equilibrium equations $N_1(h_1^\varphi)$ and $N_2(h_2^\varphi)$ in (3.17) are plotted for the two segments. Each equilibrium equation has only the actual height of the corresponding segment as variable, and consequently, the equilibrium surfaces in function of h_1^φ and h_2^φ will be cylindrical. The equilibrium path can be plotted from $N_1(h_1^\varphi) = N_2(h_2^\varphi)$, that is, it follows the intersection(s) of the two surfaces. The red line (assigned to path “a” and “b”) in Fig. 3.7 corresponds to the uniform packing when the closure takes effect simultaneously. The paths in black are the optional, bifurcated paths. This later path can be mentioned as typical due to the deviation of the physical and geometrical parameters in reality. In this typical case (e.g. following the paths ‘c’ and ‘d’ on Fig. 3.7) one segment of the structure closes while ‘kicking out’ the other segment to its initial position. After the complete packing of one segment, if the ‘post-packed phenomenon’ (see Chapter 3.2) is restricted, the corresponding $N_i(h_i^\varphi)$ equilibrium equation can be ignored, assuming $h_i^\varphi = 0$ in the further analysis. With this restriction, if the mast is further pushed to closure, the ‘kicked up’ segment can be packed as a single segment following the equilibrium path

calculated for that single segment (paths 'f' or 'e' on Fig 3.7). The restricted packing sequences following the different paths are shown on Fig. 3.8.

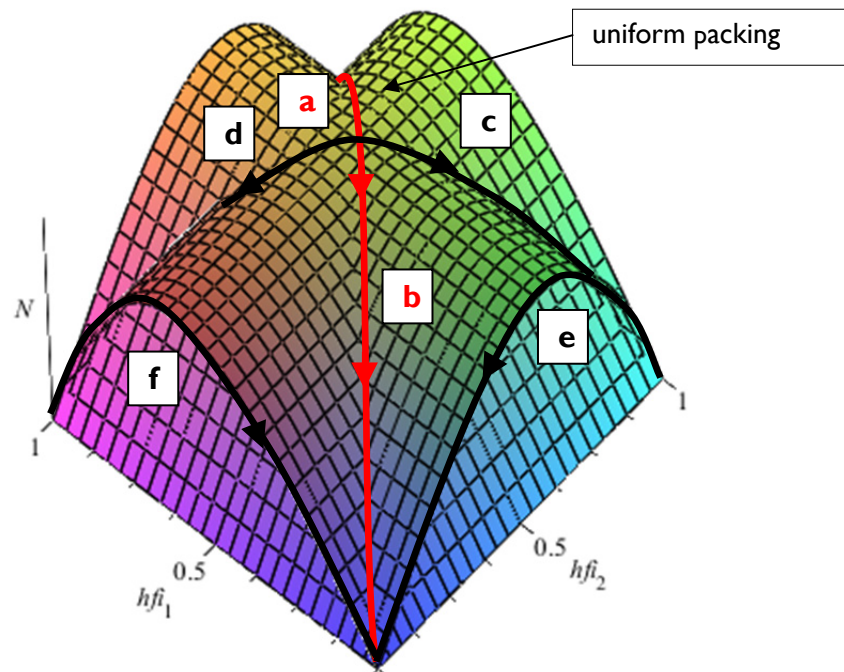


Fig. 3.7: Restricted equilibrium paths in function of the actual height of the segments (h^ϕ) of planar deployable mast consisting two segments

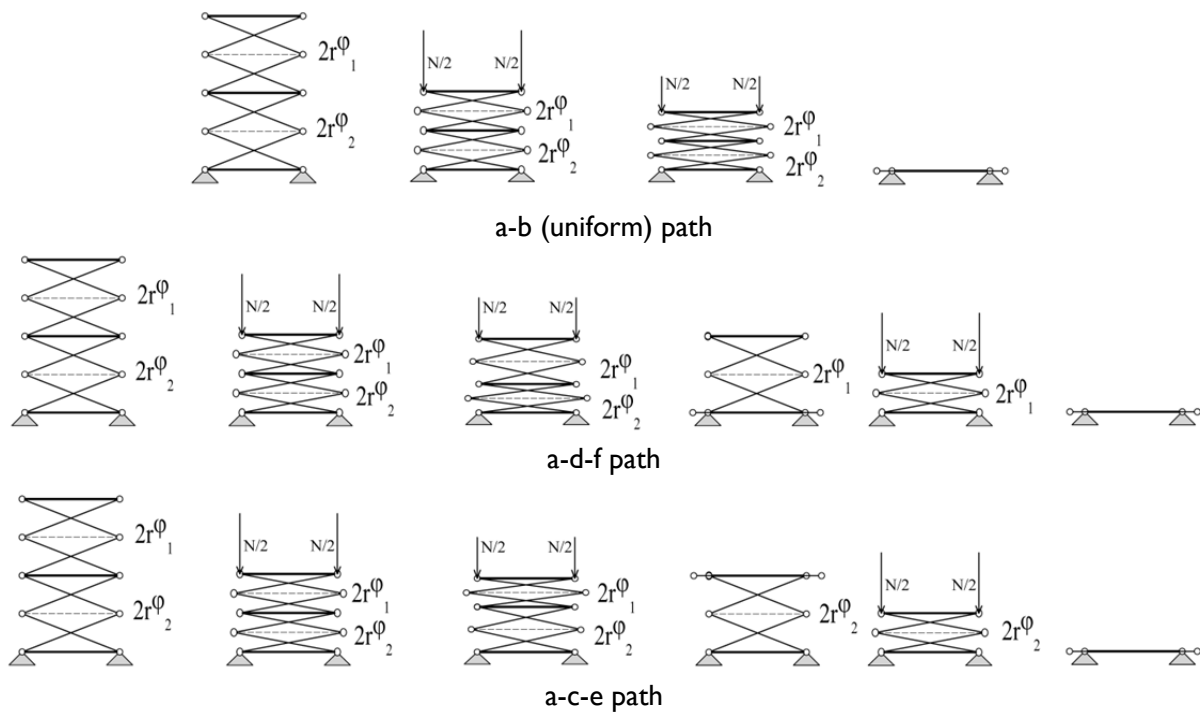


Fig. 3.8: Different restricted packing sequences following different equilibrium paths (path names in accordance with Figure 3.7)

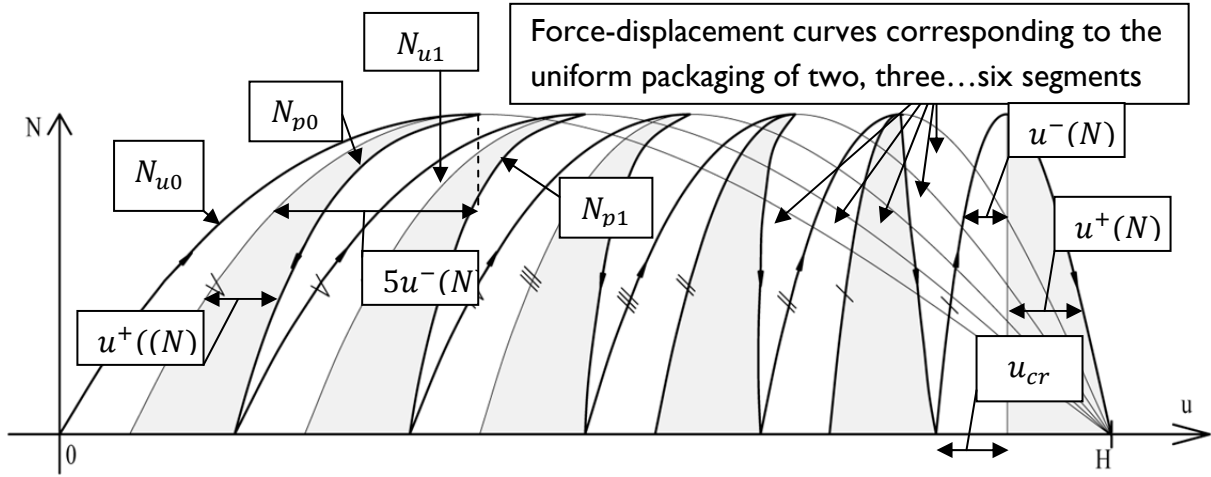


Fig. 3.9: Typical force-displacement diagram — restricted packing of planar deployable mast of six segments (notations: H : total height, u : displacement of the top nodes, N : packing force)

Fig. 3.9 shows the typical force-displacement diagram which is the bifurcated case when no segments close together. As it is presented in this figure, the diagram can be plotted with the help of the curves corresponding to the uniform packing of a mast of 1-6 segments. In the followings the function of the typical force displacement diagram and its general characteristics will be investigated.

Let's nominate the ante-critical phase of the force-displacement function in (3.8):

$$N_u(u) = N: \Omega^+ \rightarrow \mathbb{R} \text{ with } \Omega^+ := \{u | u \leq u_{cr}\} \tag{3.19}$$

and its post-critical phase:

$$N_p(u) = N: \Omega^- \rightarrow \mathbb{R} \text{ with } \Omega^- := \{u | u_{cr} \leq u \leq 2h\} \tag{3.20}$$

with u_{cr} being the critical relative displacement between the top and bottom polygonal facets, which is defined in (3.16).

$$\left. \frac{dN(u)}{du} \right|_{u=u_{cr}} = 0, \quad N(u_{cr}) = N_{cr} \tag{3.21}$$

Let's nominate also the inverse of ante-critical and post-critical parts of the force-displacement function (Fig. 3.10):

$$N_u^{-1}(u + u_{cr}) \Rightarrow u^-(N) \tag{3.22}$$

$$N_0^{-1}(u) \Rightarrow u_a(N) \tag{3.23}$$

$$N_p^{-1}(u + u_{cr}) \Rightarrow u^+(N) \tag{3.24}$$

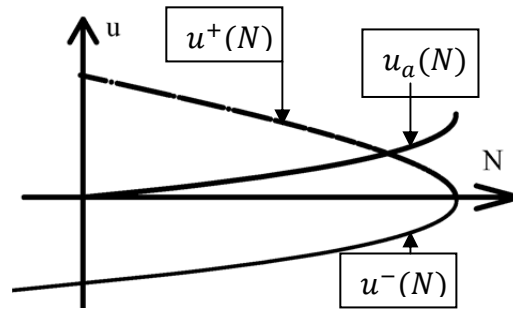


Fig. 3.10: Nomination of inverse functions

The first, uniform packing phase for the six-storey structure corresponds to the function (Fig. 3.9):

$$N_{u0} = N\left(\frac{u}{6}\right) \quad 0 \leq u \leq 6u_{cr} \quad (3.25)$$

The inverse of the function of the force-displacement diagram of the second, post-critical phase is:

$$N_{p0}^{-1}(u) \Rightarrow u_{pj}(N) = 6u_{cr} - 5|u^-(N)| + u^+(N) \quad (3.26)$$

After the complete closure of the segment in the post-critical state the mast begins uniformly packing, which corresponds to the function:

$$N_{u1} = N\left(\frac{u - 2h}{5}\right) \quad 2h \leq u \leq 5u_{cr} + 2h \quad (3.27)$$

This stable phase is again followed by an instable state. The inverse of this part of the force displacement diagram is:

$$N_{p1}^{-1}(u) \Rightarrow u_{p1}(N) = 2h + 5u_{cr} - 4|u^-(N)| + u^+(N) \quad (3.28)$$

In general, a self-deployable structure consisting of k antiprismatic segments the function of the equilibrium path for the alternately repeating stable and instable phases will correspond to:

$$N_{uj} = N\left(\frac{u - j2h}{k - j}\right) \quad j2h \leq u \leq (k - j)u_{cr} + j2h \quad (j = 0..k - 1) \quad (3.29)$$

$$N_{pj}^{-1}(u) \Rightarrow u_{pj}(N) = j2h + (k - j)u_{cr} - (k - j - 1)|u^-(N)| + u^+(N)$$

$$(j = 0..k - 1)$$

$$u_{pj}(N): \Gamma_{pj} \rightarrow E_{pj}$$

$$\Gamma_{pj} := \{N | 0 \leq N \leq N_{cr}\}$$

$$E_{pj} := \{u_{pj} | \min\{[j2h + (k-j)u_{cr}], [(j+1)2h]\} \leq u_{pj} \leq \max\{[j2h + (k-j)u_{cr}], [(j+1)2h]\}\} \quad (3.30)$$

As it has been demonstrated above, the connection of geometrically unstable units typically leads to a successive packing; after the first segment having passed its critical state, the packing localizes to the weakened unit, while the rest of the segments are released. This is a very similar phenomenon to that of material instability. For example, a tension test of a bar with elastoplastic softening behavior serves for a good analogy. Considering a displacement controlled tensile test, the part of the bar, where imperfections cumulate, will be the first to reach its critical, yield stress. The weakened element, which became plastic, will impose the reduction of stress value through softening phase of constitutive behavior in that element. Once the softening starts in the weakened element, reducing the value of stress, the other elements which were still elastic, will simply unload [Ibrahimbegovic, 2009 pp 497-499].

Snap-back behavior of bifurcated packing

The force-displacement diagram of the complex structure not only has descending parts, but also manifests snap-back phenomenon, that is, the typical equilibrium path turns backwards after reaching the critical force. It can be seen from Fig. 3.9, that this phenomenon becomes more emphasized with the increment of segment numbers. If the force-displacement diagram of one segment was symmetrical, that is,

$$|u^+(N)| = |u^-(N)| \quad (3.31)$$

than the last but one instable packing phase would be a vertical line and consequently its inverse would be a constant function:

$$\begin{aligned} u_{p(k-2)}(N) &= (k-2)2h + (k-k+2)u_{cr} \underbrace{-(k-k+1)|u^-(N)| + u^+(N)}_0 \\ &= (k-2)2h + 2u_{cr} \end{aligned} \quad (3.32)$$

Nonetheless, the force displacement diagram of the basic unit is not symmetrical:

$$|u^+(N)| > |u^-(N)| \quad (3.33)$$

To see whether the diagram will manifest a snap-back behavior or not, the sign of the first derivative of the inverse function of the instable phases are needed ($u_{pj}(N)$). If the derivative is positive snap-back behavior will occur. The analytical investigation of the inverse of the function $N(u)$ leads to a root-finding problem of a polynomial of order four. The explicit determination of these roots are quite cumbersome. Instead of doing that let's consider the general characteristics of $N(u)$ in the domain:

$$\Omega := \{u \mid 0 \leq u \leq 2h\} \quad (3.34)$$

Let's shift and mirror the function N (Fig.3.11) by letting

$$f: \Omega_f \rightarrow \mathbb{R}$$

to be the function defined by the formula

$$f(x) = -N(x + u_{cr}) + b$$

on the domain

$$\Omega_f := \{x \mid -u_{cr} \leq x \leq 2h - u_{cr}\} \quad (3.35)$$

Thus

$$f(u) > 0 \text{ for } u \neq 0$$

and

$$f(0) = 0 \quad (3.36)$$

And hence in particular f has a minimum at zero. Of course f is not invertible, but similarly as before, we have two local inverses of f : we have the functions h^+ and h^- defined by the formulas (Fig. 3.11):

$$h^+(y) \geq 0, \quad f\{h^+(y)\} = y$$

and

$$h^-(y) \leq 0, \quad f\{h^-(y)\} = y \quad (3.37)$$

holding for "small enough" positive values of y .

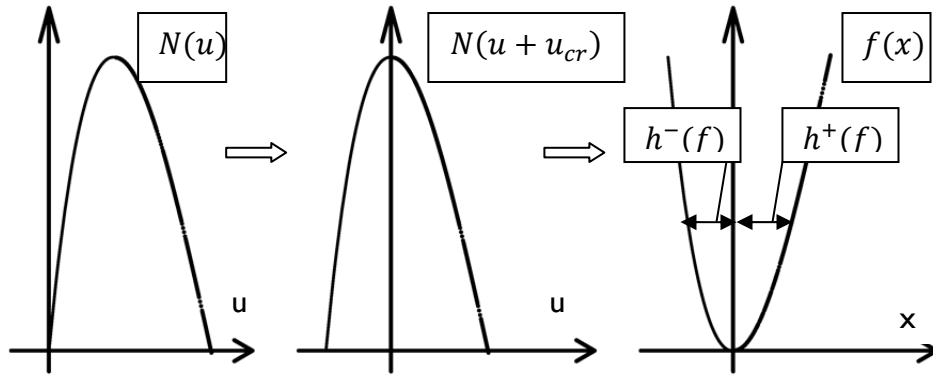


Fig. 3.11: Shifting and mirroring the force-displacement diagram

In what follows we shall compute the limit

$$\lim_{y \rightarrow 0} \left| \frac{h^+(y)}{h^-(y)} \right| \tag{3.38}$$

without entering in particular details regarding the actual form of the function f .

At first it may seem that such a computation is not possible without using our actual knowledge of the function f . Indeed, it is not difficult to see, that if — regarding the function f — only condition (3.36) is known, then the value of the above limit cannot be deduced. Infact, if f was not the shifted version of our force-displacement function N , but the function

$$f(x) := \begin{cases} x^2 & \text{if } x \geq 0 \\ (t x)^2 & \text{if } x < 0 \end{cases} \tag{3.39}$$

where t is a fixed positive constant, then by a straightforward calculation we would have that

$$\lim_{y \rightarrow 0} \left| \frac{h^+(y)}{h^-(y)} \right| = t \tag{3.40}$$

showing that the value of (3.38) can be an arbitrary positive number $t > 0$.

However, the function used for this example, though once differentiable, is not twice differentiable at zero. On the other hand, our actual function, which is the shifted version of our force-displacement function N , is smooth; in fact, it is clearly analytical in a neighborhood of zero (i.e. N is analytical in a neighbourhood of u_{cr}). So let us see what we can deduce instead of using the actual, rather complicated form of f by only taking account of condition (3.36) together with the analytical nature of f .

Let us consider the Taylor expansion

$$f(x) = f(0) + f'(0)x + \frac{1}{2}f''(0)x^2 + \frac{1}{3}f'''(0)x^3 + \dots \quad (3.41)$$

around the point zero. Since $f(0) = 0$, the constant term is zero and actually, by the fact that f has a minimum at zero we must have that the first nonzero term must be an even power of x with a positive coefficient. Thus we must have that

$$f(x) = a x^{2n} + O(x^{2n+1}) \quad (3.42)$$

where n is some positive integer, $a > 0$ is a positive real and O is an ordo-function i.e. that $|O(t)/t|$ remains bounded in a neighbourhood of $t = 0$.

By the definitions of h^+ and h^- , we have that

$$a (h^+(y))^{2n} + O((h^+(y))^{2n+1}) = a (h^-(y))^{2n} + O((h^-(y))^{2n+1}) \quad (3.43)$$

Dividing by both sides with $a (h^-(y))^{2n}$, we obtain

$$\frac{(h^+(y))^{2n}}{(h^-(y))^{2n}} = 1 + \frac{O((h^+(y))^{2n+1}) - O((h^-(y))^{2n+1})}{a (h^-(y))^{2n}} \quad (3.44)$$

where the right hand side clearly tends to 1 as y goes to zero.

Thus

$$\frac{(h^+(y))^{2n}}{(h^-(y))^{2n}} = \left(\frac{h^+(y)}{h^-(y)} \right)^{2n}$$

tends to 1 as y goes to zero, showing that

$$\lim_{y \rightarrow 0} \left| \frac{u^+(y)}{u^-(y)} \right| = \lim_{y \rightarrow 0} \left| \frac{h^+(y)}{h^-(y)} \right| = 1 \quad (3.45)$$

This means that in the infinitesimally small neighborhood of the critical displacement the force-displacement diagram will be heading to be symmetrical. Considering the inverse function of the equilibrium path of the unstable phases in (3.30) in the ε neighborhood of N_{cr}

$$\begin{aligned} u_{pj}(N_{cr}) &= j2h + (k-j)u_{cr} \\ \Delta u_{pj} &= u_{pj}(N_{cr}) - \lim_{N \rightarrow N_{cr}} u_{pj}(N) = \lim_{N \rightarrow N_{cr}} -(k-j-1)|u^-(N)| + u^+(N) \end{aligned} \quad (3.46)$$

For the last but one unstable phase ($j = k - 2$):

$$\Delta u_{pk-2} = \lim_{N \rightarrow N_{cr}} -|u^-(N)| + u^+(N) = 0^+ \quad (3.47)$$

This theoretically means that this descending phase of the force displacement diagram just after the pick is heading to be vertical, that is, its inverse is heading to be a constant. The positive sign in (3.41) the last term is due to (3.33), and means that the first descending part is not snapping back. However, for $j = k - 3$:

$$\Delta u_{pk-3} = \lim_{N \rightarrow N_{cr}} -2|u^-(N)| + u^+(N) \leq 0 \quad (3.48)$$

This result means that **the snap-back behavior of the structure occurs for segment-number more than two.**

Due to fact that the structure undergoes instability phenomenon during packing, displacement control should be applied when smooth packing is targeted. Nonetheless, because of the snapping-back phenomenon, even with an incremental displacement control of the top facet of the column, the structure will manifest sudden internal displacements, resulting in non-negligible inertial and impact effects. In reality this effects get significant if the relative sudden displacement of the internal facets is more than the segment-height. The length of the sudden displacements grows with the increment of the segment-number, and reaches the length of the segment-height when:

$$j2h + (k - j)u_{cr} = (j + 1)2h \quad (3.49)$$

This means that in the descending phase, from the critical state until the complete closure of the currently weakened segment, negative displacements have to be applied, that is, the top nodes have to be displaced upwards to get the next configuration corresponding to zero force. In equation (3.49) $j2h + (k - j)u_{cr}$ represents the displacement of the top facet corresponding to the $(j + 1)^{\text{th}}$ critical state, and $(j + 1)2h$ is the displacement corresponding to the $(j)^{\text{th}}$ zero-force state. From equation (3.49) the critical segment number can be deduced:

$$k_{cr} = \frac{2h}{u_{cr}} \quad (3.50)$$

Consequently the relation $k_{cr} \geq k$ means that snap-back phenomenon necessarily occurs when no segments close together. If not, the structure might be able to be packed without any violent relative displacements if smooth displacement control of the top nodes are effectuated, but small sudden displacements can still occur.

Substituting the equation in (3.16) into (3.50) the critical number of segments is:

$$k_{cr} = \frac{1}{1 - \sqrt{1 - \left[2 \frac{r_0}{h_0} + 8 \left(\frac{r_0}{h_0} \right)^3 \right]^{2/3} + 4 \left(\frac{r_0}{h_0} \right)^2}} \quad (3.51)$$

Equation (3.29) is plotted in Fig.3.12 in function of the ratio of the initial segment height and the length of elastic bars (h_0/r_0). For example if this ratio is less then ~2.5, than in the case of three segments and typical packing path, the snap-back phenomenon will not only occur at the critical state, but the sudden internal displacement will be larger than the segment-height. Nonetheless, for ratios bigger than that, the snap-back phenomenon will still occur when the segment-number is larger than three, but the length of these displacements will not pass the segment-height.

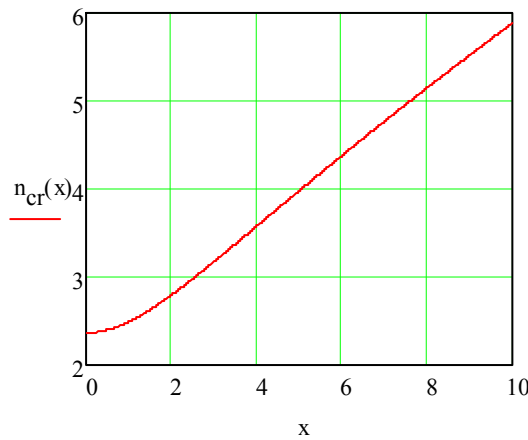


Fig. 3.12: Critical number of segments in function of $x = \frac{h_0}{r_0}$

Packing path with ‘post-packed phenomenon’

When the ‘post-packed phenomenon’ is not restricted, the structure will avoid the completely closed configuration, and disengage from the configuration corresponding to the maximal internal energy. In this case, the segment first to be closed will cross its bottom horizontal bar and pulls out the other segment to an extended configuration. When displacing the top nodes of the mast to the support line the mast will be one segment high (either in a reflected position or not, depending on which segment is the first to close), and consequently no further packing is possible. In order to visualize this behavior, the identical force-displacement diagrams of both units (relative displacement of top and bottom nodes) are plotted on Fig. 3.13 showing the current positions in the associated configurations. The two displacements summed together give the force-displacement diagram of the complex, two-storey structure (last diagrams in Fig. 3.13). One possible sequence in the non-restricted case is shown on Fig. 3.14. The two diagrams for restricted and non-restricted packing can be compared by putting together the last diagram of configuration ‘VIII’ in Fig. 3.11, and the two last loops of the diagram in Fig. 3.9. It can be seen that the first part is identical until the closure of the first segment. Nonetheless, as the packed segment disengages from the closed configuration the structure has to be pulled back in order to smoothly push the top

horizontal bar until the bottom one. And still, the final configuration will not be a packed one; it will stop in a stable configuration corresponding to zero self-stresses and zero external force.

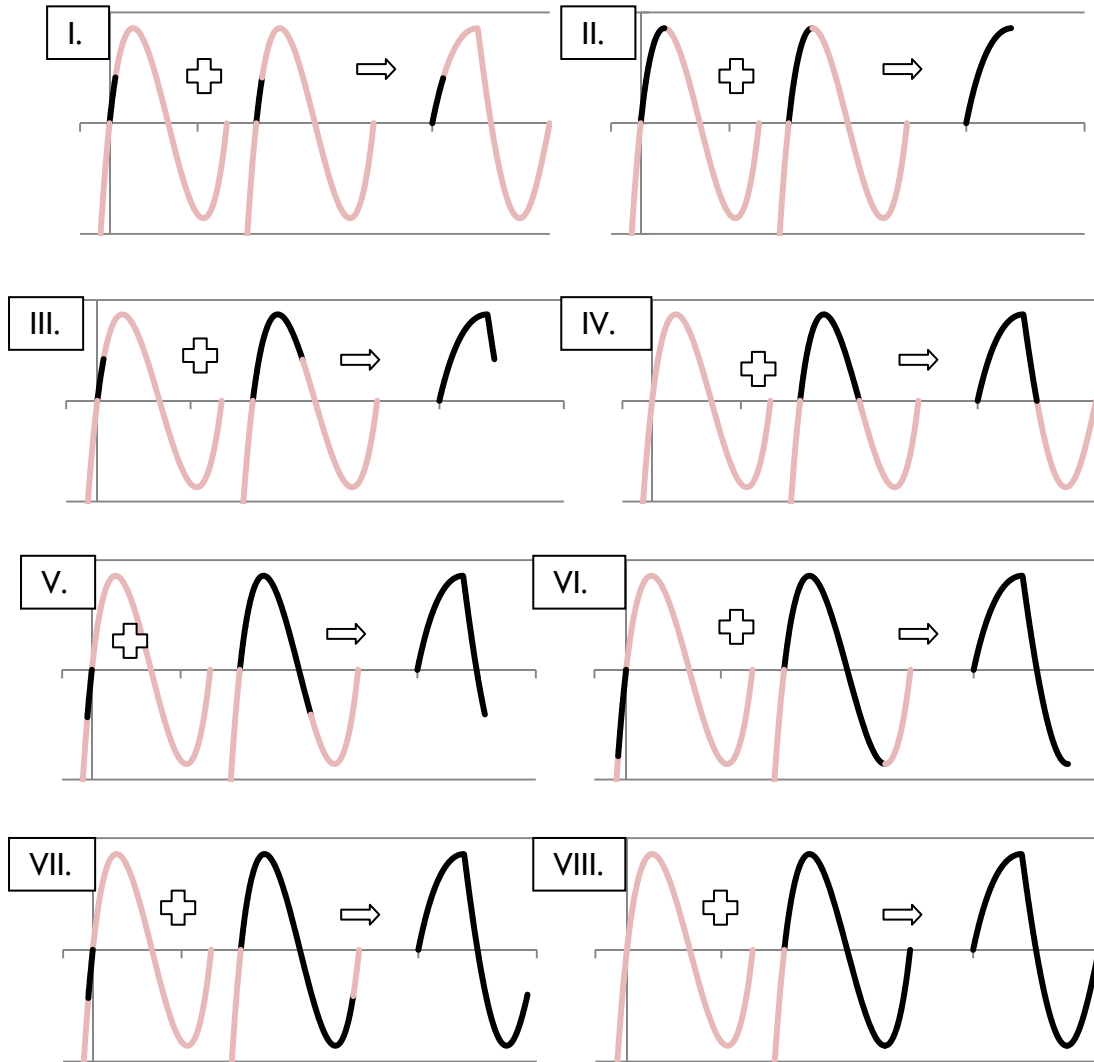


Fig. 3.13: Constructing the force-displacement diagram of deployable mast of two segments from the individual diagrams of separated segments without preventing ‘post-packed phenomena’ (see the packing sequence with the assigned configurations on Fig. 3.12, $h_0/r_0=1$)

Theoretically the restriction means taking out one of the equilibrium equations and fixing its variable to a constant value when the actual height has once reached zero value. To prevent ‘post-packed phenomenon’ physically, the two boundary horizontal bars has to be clicked together, which means additional and variable boundary conditions in the system. However, without this restriction we still have to stick to the already presented intersection paths presented in Fig. 3.7. In order to see the bifurcated paths the part of the equilibrium equation corresponding to the negative segment heights and the ones corresponding to the extended heights has to be also graphed. The non-restricted path is shown on Fig. 3.13.

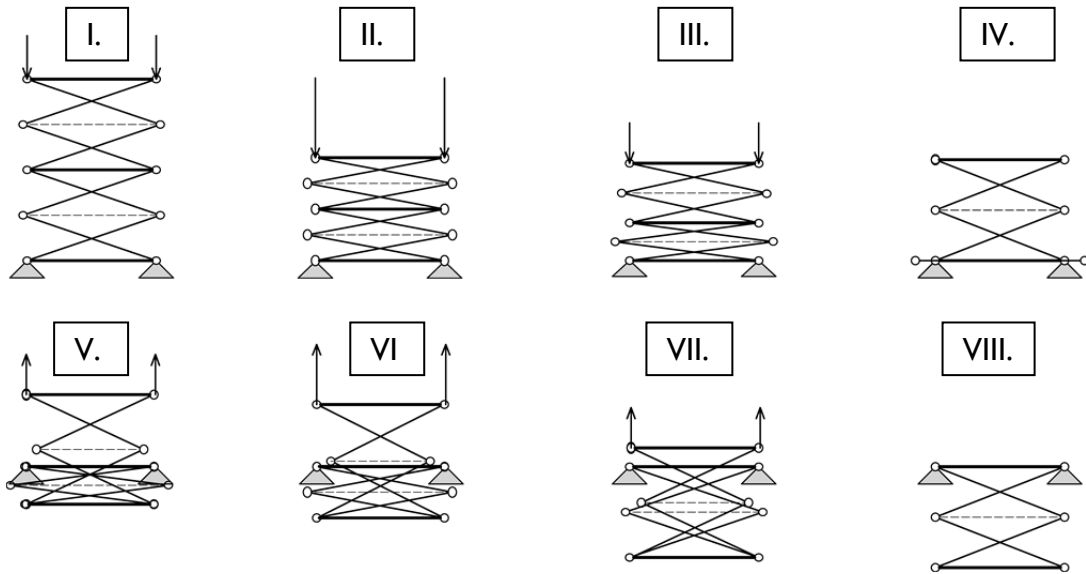


Fig. 3.14: Packing sequence of deployable mast of two segments without preventing ‘post-packed phenomenon’

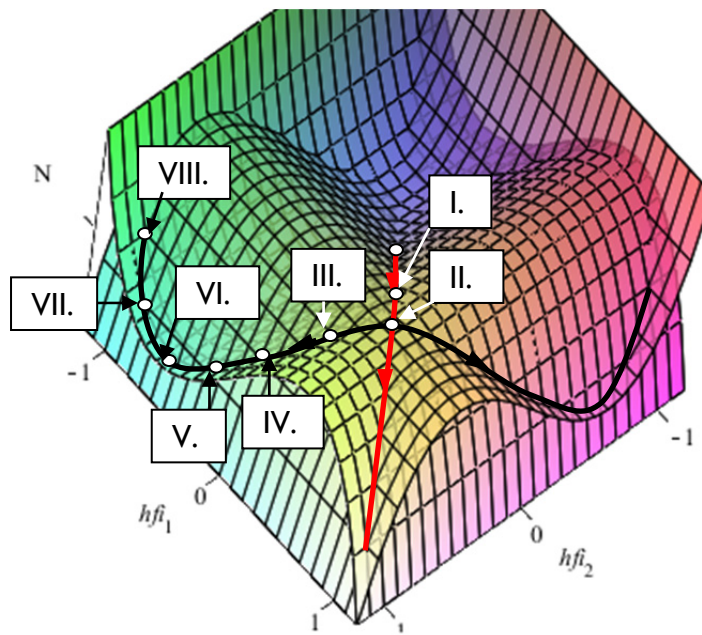


Fig. 3.15: Non-restricted equilibrium paths in function of the actual half-segment heights (h^φ) of the planar deployable mast of two segments

Stability analysis

The paths where the increment of packing force leads to an increment of displacements is stable, the ones where the force has to be decreased in order to pack the structure smoothly is unstable.

Due to the serial connection of the elements the resistant vertical force is the same in each segment, and depends only on the current height of the corresponding segment, consequently the critical state will be defined by the equation already given in (3.16):

$$\frac{dN(\mathbf{h}^\varphi)}{d\mathbf{h}^\varphi} = 0$$

$$\frac{\partial N(\mathbf{h}^\varphi)}{\partial \mathbf{h}^\varphi} = 0 \Rightarrow h_{cr_i}^\varphi = \pm r_{0i} \sqrt{\left(\frac{h_{0i}}{r_{0i}}\right)^2 - \left[2\left(\frac{h_{0i}}{r_{0i}}\right)^2 + 8\right]^{2/3} + 4}$$
(3.52)

And the corresponding critical force is:

$$N_{cr_i} = \frac{EA_i}{r_{0i}} \cdot \left[1 - \frac{2}{\sqrt{4 + \frac{(h_{0i})^2 - (h_{cr_i}^\varphi)^2}{(r_{0i})^2}}} \right] h_{cr_i}^\varphi$$
(3.53)

The structure will get to the critical state at the smallest value of the critical force:

$$N_{cr} = \min(N_{cr_i})$$
(3.54)

If all the mechanical parameters (axial stiffness, height/radius ratio) coincidences the critical state will be reached at the same time by the separate segments of the complex structure. However, in this case, the critical point is not only a limit point but a bifurcation point, as well. When the critical load is reached, the branch-choosing is random. The different branches correspond to different number of segments losing their stable states.

Taking self-weight into account

If the self-weight of the structure is not to be ignored then the vertical force acting on the structure is not identical in the segments, but still the mechanical behavior can be calculated from a separate analysis of the segments.

If we consider only concentrated masses of magnitude m in the end nodes of the rigid horizontal bars (see Fig. 3.16), the equilibrium paths corresponding to the upraising and descending phases have to be modified to functions with the following inverses:

$$N_{u_j}^{-1}(u) \Rightarrow u_{uj}(N) = \sum_{i=j}^{k-1} \{u_a[N + (k-i)nm g]\} - u(knm g) - j2h$$

$$(j = 0..k-1)$$

$$u_{uj}(N): \Gamma_{uj} \mapsto E_{uj}$$

$$\Gamma_{uj} := \{N | (j-k)nm g \leq N \leq N_{cr} + (j-k)nm g\}$$

$$E_{uj} := \left\{ u_{uj} \mid -u(knmg) + 2jh \leq u_{uj} \leq (k-j)u_{cr} - \underbrace{\sum_{i=0}^{k-1} \{u_a[(i-k)nmg]\}}_{U_{uj}} + 2jh \right\} \quad (3.55)$$

$$N_{pj}^{-1}(u) \Rightarrow u_{pj}(N) = U_{uj} - \left| \sum_{i=j+1}^{k-1} \{u^-[N + (k-i)nmg]\} \right| + u^+[N - (k-j)nmg]$$

$$u_{pj}(N): \Gamma_{pj} \mapsto E_{pj}$$

$$\Gamma_{pj} := \{N \mid (j-k)nmg \leq N \leq N_{cr} + (j-k)nmg\}$$

$$E_{pj} := \{u_{pj} \mid \min\{U_{uj}, [2jh - u(knmg)]\} \leq u_{uj} \leq \max\{U_{uj}, [2jh - u(knmg)]\}\} \quad (3.56)$$

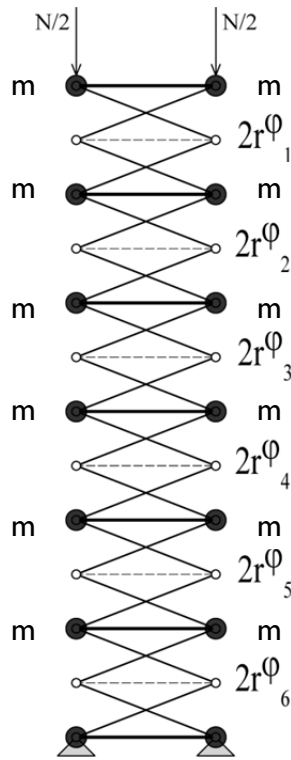


Fig. 3.16: Planar deployable mast with self-weight

It can be seen from the equilibrium equations plotted in Fig. 3.17 that the weight of the structure will eliminate the bifurcation point at the critical state, as the intersecting surfaces are vertically slid with the weight of one segment and consequently eliminating the possibility of uniform packing even in case of arbitrarily small weight. This is a good example to demonstrate that the initial potential energy function, corresponding to identical geometrical and physical constants in the segments, is not structurally stable, that is, by disturbing it with a sufficiently small smooth function will change the number or the type of its stationary points. This phenomenon can be also provoked by a slight deviation of the axial stiffness of the elastic horizontal bars. In both cases the packing will take place successively.

With self-weight, the bottom segment will be the first one to snap to the packed configuration followed from the bottom to the top, one by one (Fig. 3.18). If it is the axial stiffness that deviates, the segment with the weakest horizontal bar will be the first one to close followed by the stiffer segments.

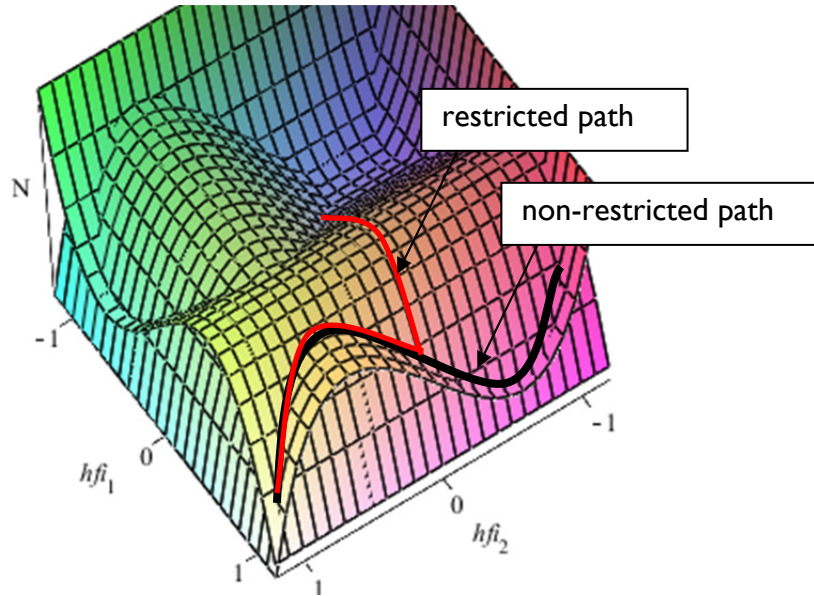


Fig. 3.17: Equilibrium paths in function of the half-heights of the segments (h_1^φ : half-height of top segment, h_2^φ : half-height of bottom segment) of planar deployable mast consisting of two segments taking into account the weight of the structure

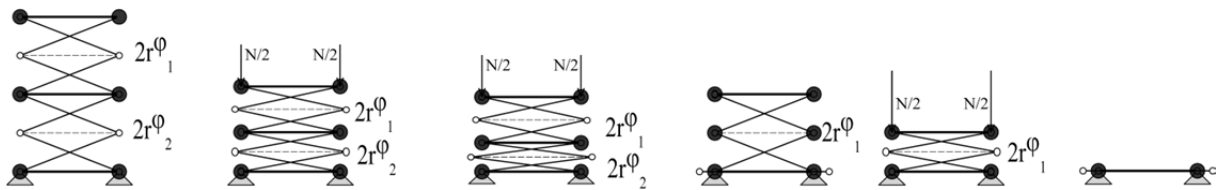


Fig. 3.18: Packing sequences of the planar alternately stiffened mast taking into account the self-weight of the structure (restricted path)

The method of plotting the force-displacement diagram is similar to that one presented for the typical case, where the weights were not taken into account. However, in this case the individual force-displacement diagrams have to be plotted by sliding them vertically with img , that is, with the weight of the segments above. This is shown on the upper drawing on Fig. 3.17. For example the individual force-(relative) displacement diagram of the bottom segment is slid by $6mg$, the one above the bottom by $5mg$ etc. The first part of the diagram can be constructed (lower diagram on Fig. 3.19) by summing all the displacements corresponding to a certain level of packing force read from the slid diagrams. As mentioned above and can be seen from Fig.3.19, the bottom segment will be the first one to reach its critical state and consequently, when further squashed the post-critical behavior of this unit will impose the release of the rest of the structure. When the bottom segment is completely closed the segments above will be somewhat stretched. This stretching is more

intense in the top segment as the compressive force coming from the weight of the structure is less. When further packing the structure, the second segment from the bottom will close next releasing the segments above etc.

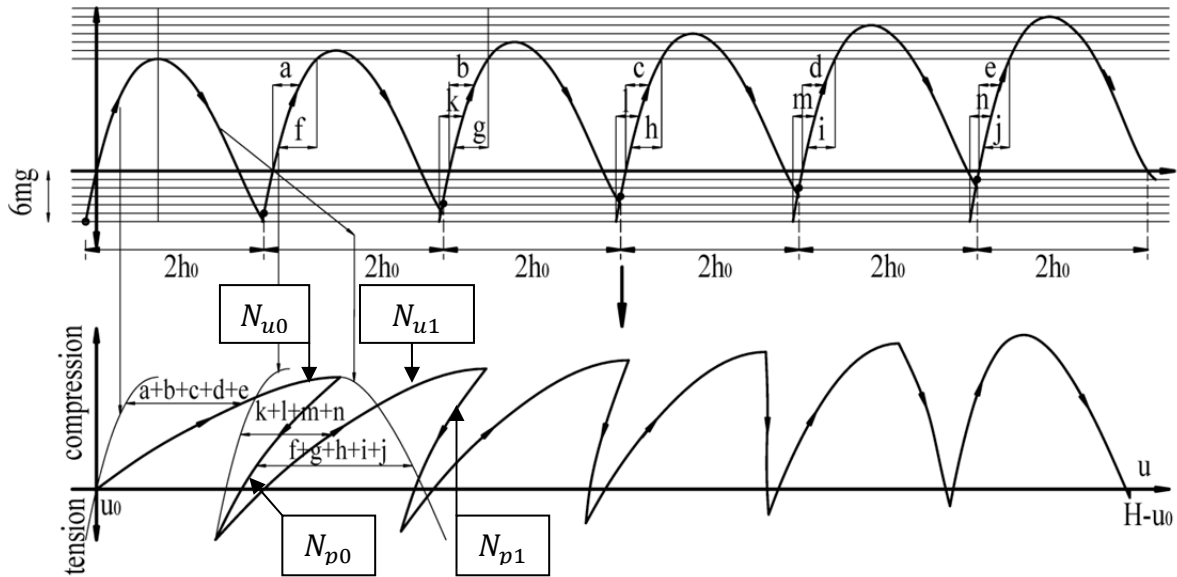


Fig. 3.19: Constructing the force-displacement diagram — restricted packing of planar deployable mast of six segments with self-weight
 (notations: H : total height, u : displacement of the top nodes, u_0 : initial displacement of the top nodes from the weight of the structure)

3.2.3 Mechanical analysis of masts without intermediate stiffening

Tracing equilibrium paths

The behavior of the multi-storey alternately stiffened mast is already interesting to analyze and not perspicuous to understand well its general behavior, but still can be explained transparently from the behavior of one only segment. Now let's consider a more complex structure, where there are no intermediate rigid bars, that is, all the horizontal bars are elastic (Fig. 3.20).

Let us consider such a structure consisting of k segments (the basic segment of pop-up masts without intermediate stiffening is half of the one described for 'alternately stiffened' mast). For the sake of simplicity the equilibrium function will be written in the function of r^φ , that is, in function of the current half-length of the horizontal elastic bars. Here r^φ is a vector of $k + 1$ elements (see Fig. 3.20):

$$r^\varphi = r_i^\varphi \quad (i = 0..k), \quad r_0^\varphi = r_k^\varphi = r_0 \tag{3.57}$$

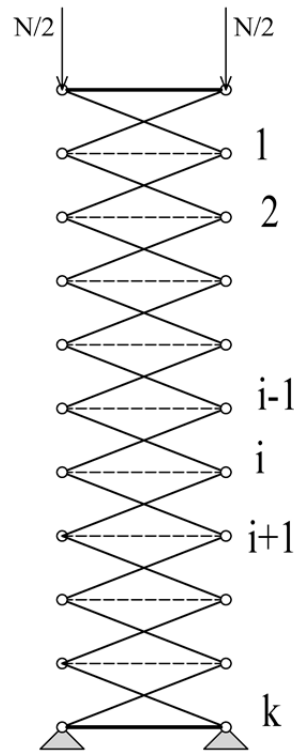


Fig. 3.20: Planar deployable mast without intermediate stiffening

The actual height of the segments in function of the actual half-length of the elastic bars (Fig. 3.21a):

$$h_i^\varphi(\mathbf{r}^\varphi) = h_i^\varphi(r_i^\varphi, r_{i-1}^\varphi) = \sqrt{l_b^2 - (r_i^\varphi + r_{i-1}^\varphi)^2} \tag{3.58}$$

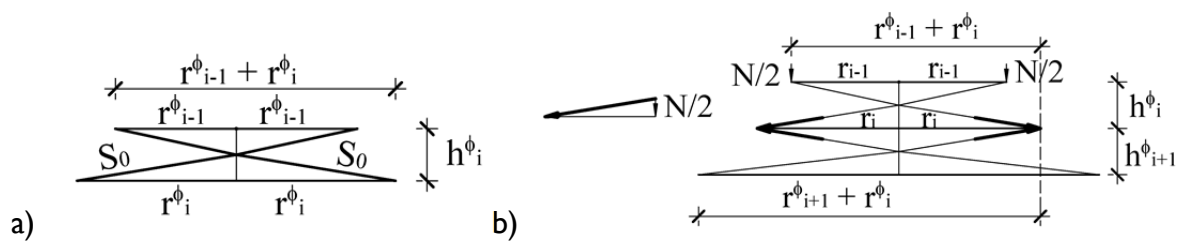


Fig. 3.21: a) Height of the non-stiffened mast from current bar-lengths and b) equilibrium of forces

The stretching of the elastic bars:

$$\lambda_i(\mathbf{r}^\varphi) = \lambda_i(r_i^\varphi) = \frac{r_i^\varphi}{r_0} \tag{3.59}$$

The i^{th} elastic bar is stretched by the forces in the bracings coming from the upper and from the lower segments. This stretching force is (Fig. 3.21b):

$$S_{Hi} = \frac{N r_i^\varphi + r_{i-1}^\varphi}{2 h_i^\varphi} + \frac{N r_i^\varphi + r_{i+1}^\varphi}{2 h_{i+1}^\varphi} \tag{3.60}$$

From (3.59) and from the linear constitutive equation in (3.7) the equilibrium equation:

$$N = N_i(r_{i-1}^\varphi, r_i^\varphi, r_{i+1}^\varphi) = \frac{2EA_i}{r_0} \frac{r_i^\varphi - r_0}{\frac{r_i^\varphi + r_{i-1}^\varphi}{h_i^\varphi} + \frac{r_i^\varphi + r_{i+1}^\varphi}{h_{i+1}^\varphi}} \tag{3.61}$$

The force N can be also written in function of the displacement of the top of the mast, which is:

$$u = \sum_{i=1}^k (h_0 - h_i^\varphi) = \sum_{i=1}^k \sqrt{l_b^2 - (r_i^\varphi + r_{i-1}^\varphi)^2} \tag{3.62}$$

Equation (3.60) is a system of $k - 1$ equations with $k - 1$ unknowns if the value of the force N on the top level is known. The equilibrium equations (3.61) are presented in Figs. 3.22-23 for $k = 3$ and $k = 4$. In the latter case ($k = 4$), symmetrical behavior was assumed, that is, by supposing $r_1^\varphi = r_3^\varphi$.

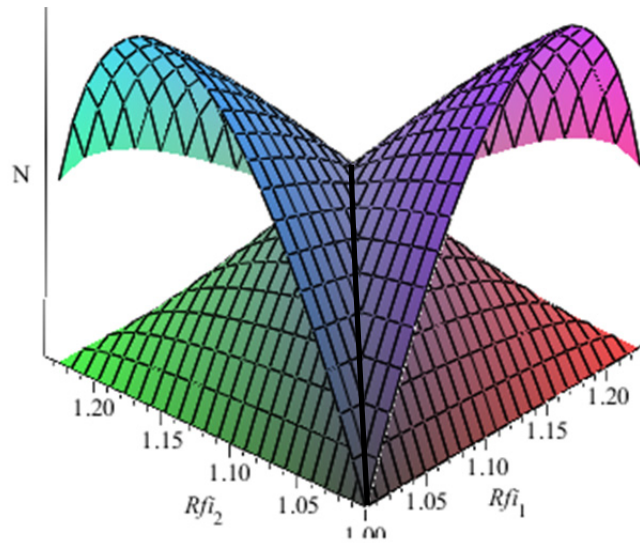


Fig. 3.22: Equilibrium path in function of the half-lengths of the elastic horizontal bars in the case of $k = 3$, initial half-length: $r_0 = 1$

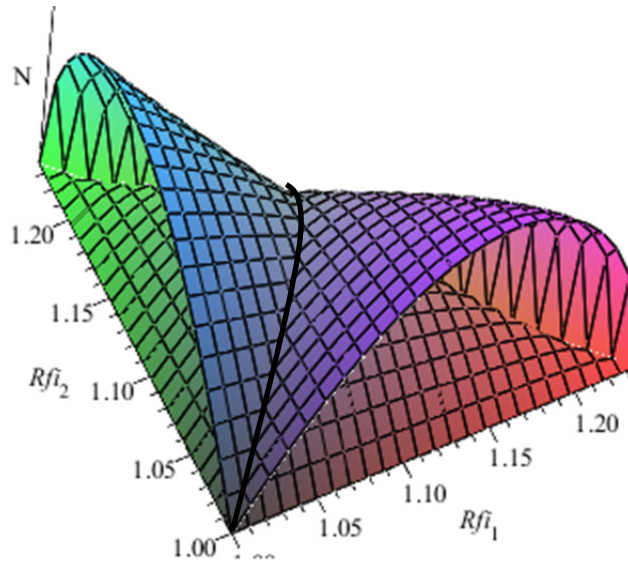


Fig. 3.23: Equilibrium path in function of the half-lengths of the elastic horizontal bars in the case of $k = 4$, initial half-length: $r_0 = 1$

The equilibrium equations in this case will not be cylindrical any longer but doubly-curved, as the tension force in the elastic bars depends not only on its own length but on the length of the neighboring elastic bars as well.

When analyzing mast of three segments the two equilibrium equations will be identical and consequently, Fig. 3.22 will be axis symmetrical. This necessarily means that the equilibrium path will follow the symmetry axis, which results in a uniform extension of the two elastic bars (Fig. 3.24). Though the elastic bars extend uniformly, the middle segment will close first as its bracings are attached to two extending bars while the ones of the top and bottom segment are connected to a rigid and an elastic one.

When analyzing mast of four segments and with the assumption of symmetrical folding ($r_1^\varphi = r_3^\varphi$), the equilibrium equations written for the first and for the second elastic bar will not be the same and thus Fig. 3.23 will not be symmetrical. The upper we climb on the intersection path the more the asymmetry of the intersection-path develops and the faster the middle elastic bar (of length r_2^φ) extends relative to the extension of r_1^φ , the upper bar (Fig. 3.25). The beginning of the packing sequence is shown on Fig. 3.25.

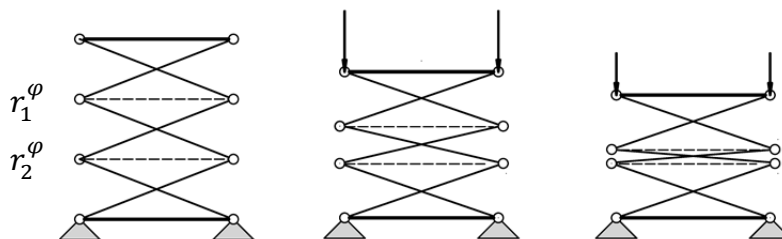


Fig. 3.24: Packing sequence without intermediate stiffening for $k = 3$

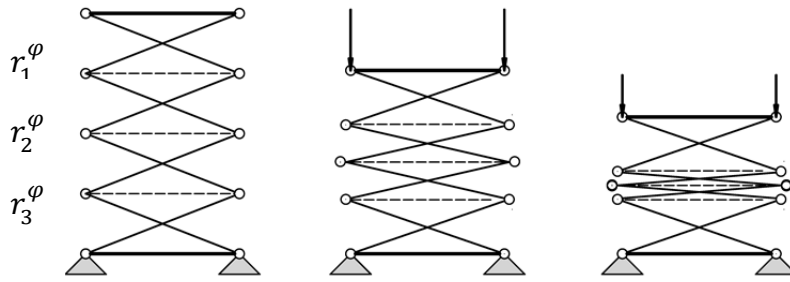


Fig. 3.25: Packing sequence without intermediate stiffening for $k = 4$

This can be presented with the equilibrium equations, too. The three equations assuming horizontal symmetry of the column are:

$$\begin{aligned}
 N_1(r_1^\varphi, r_2^\varphi) &= \frac{2EA}{r_0} \frac{r_1^\varphi - r_0}{\frac{r_1^\varphi + r_0}{h_1^\varphi} + \frac{r_1^\varphi + r_2^\varphi}{h_2^\varphi}} \\
 N_2(r_1^\varphi, r_2^\varphi) &= \frac{2EA}{r_0} \frac{r_2^\varphi - r_0}{\frac{r_2^\varphi + r_1^\varphi}{h_2^\varphi} + \frac{r_1^\varphi + r_2^\varphi}{h_2^\varphi}} = \frac{EA}{r_0} \frac{r_2^\varphi - r_0}{\frac{r_1^\varphi + r_2^\varphi}{h_2^\varphi}} \\
 N_3(r_1^\varphi, r_2^\varphi) &= N_1(r_1^\varphi, r_2^\varphi)
 \end{aligned} \tag{3.63}$$

And the equilibrium will be where:

$$\begin{aligned}
 N = N_1 = N_2 &\Rightarrow \frac{EA}{r_0} \frac{r_2^\varphi - r_0}{\frac{r_1^\varphi + r_2^\varphi}{h_2^\varphi}} - \frac{2EA}{r_0} \frac{r_1^\varphi - r_0}{\frac{r_1^\varphi + r_0}{h_1^\varphi} + \frac{r_1^\varphi + r_2^\varphi}{h_2^\varphi}} = 0 \\
 h(r_1^\varphi, r_2^\varphi) &= \frac{r_2^\varphi - r_0}{\frac{r_1^\varphi + r_2^\varphi}{h_2^\varphi}} - 2 \frac{r_1^\varphi - r_0}{\frac{r_1^\varphi + r_0}{h_1^\varphi} + \frac{r_1^\varphi + r_2^\varphi}{h_2^\varphi}} = 0
 \end{aligned} \tag{3.64}$$

This equation is shown on Fig. 3.26.

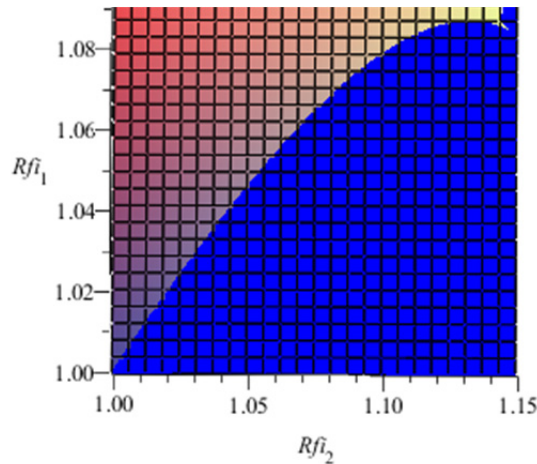


Fig. 3.26: The equilibrium path in the parameter field for $k = 4$ ($h/r_0 = 1$)

Packing the structure further without restricting ‘post-packed phenomenon’ the path can only be seen if the equilibrium paths belonging to the pulling forces (corresponding to negative heights) are plotted too. The analytic identification of the general characteristic of the path gets quite difficult because of complicated surfaces and complicated intersections of paths (Fig. 3.27). Nevertheless, the three-storey structure was analyzed that can be completely packed even without restricting the ‘post-packed phenomenon’ (Fig. 3.28). The equilibrium path will draw a loop during packing and by repeating the first part of the loop the structure completely closes.

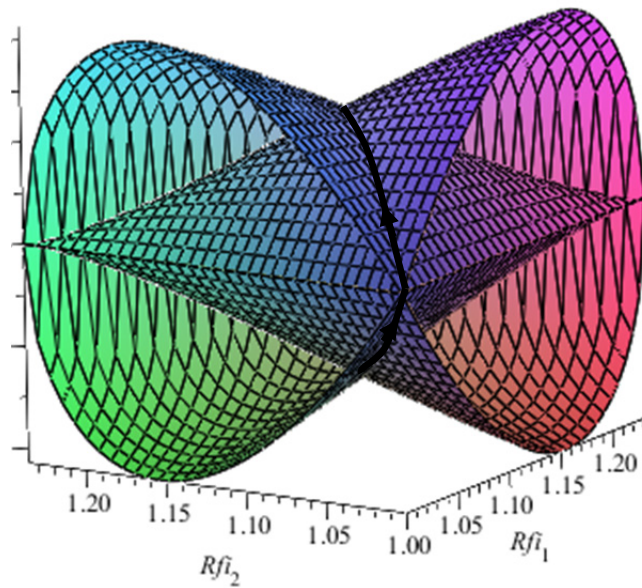


Fig. 3.27: Equilibrium path in function of the half-lengths of the elastic horizontal bars in case of $k = 3$ with the ‘post-packed phenomenon’

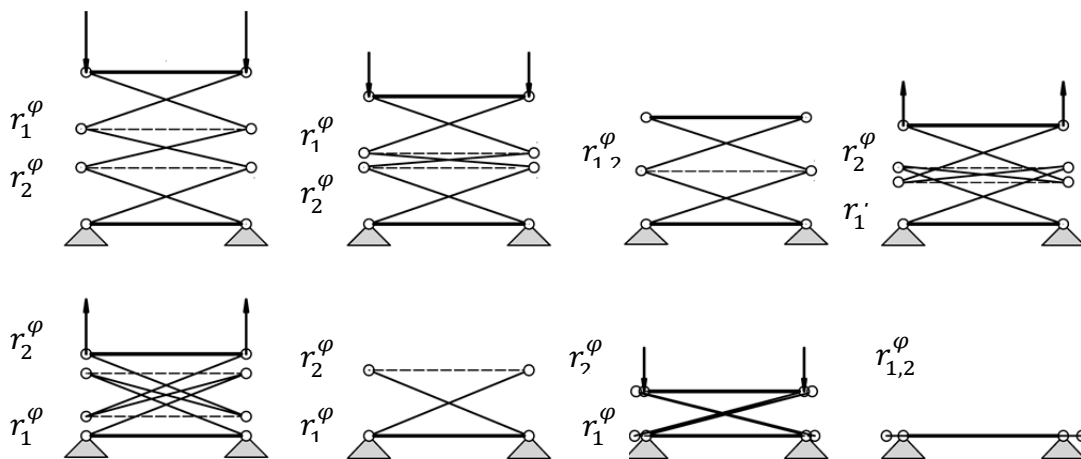


Fig. 3.28: Complete packing sequence of three-storey mast without restricting ‘post-packed phenomenon’

Stability analysis

To decide whether the equilibrium points are stable or not, the derivative of the equilibrium path(s) ($N(u)$) is (are) needed. In the case of the non-stiffened mast, even for smaller number of k , the equations, and to get explicit solution for the critical force as well, get quite cumbersome. Nonetheless, the stability analysis of the non-stiffened mast can be carried out with a numerical analysis. The energetic approach of the problem (see Appendix D) is easier to handle for the numerical investigation. For that, this analysis is later on explained at the numerical analysis chapter.

Fig 3.29 shows the influence of changing the 'alternately stiffened' mast to a 'non-stiffened' one. While the surfaces in blue (light blue and dark blue) are the equilibrium paths (already presented in Fig. 3.23) corresponding to the equilibrium surfaces of the mast with $k = 4$, the reddish (orange and red) surfaces are the ones corresponding to the 'alternately stiffened' mast consisting of two units ($k = 2$)¹. The equilibrium path of the 'alternately stiffened' mast is at the intersection of the two blue surfaces, the one of the 'non-stiffened' structure is at the intersection of the red and orange surfaces. It can be seen the maximum points of the two paths are different; the critical force of the 'alternately stiffened mast' is much larger (almost two times larger) than the one of the 'non-stiffened' one.

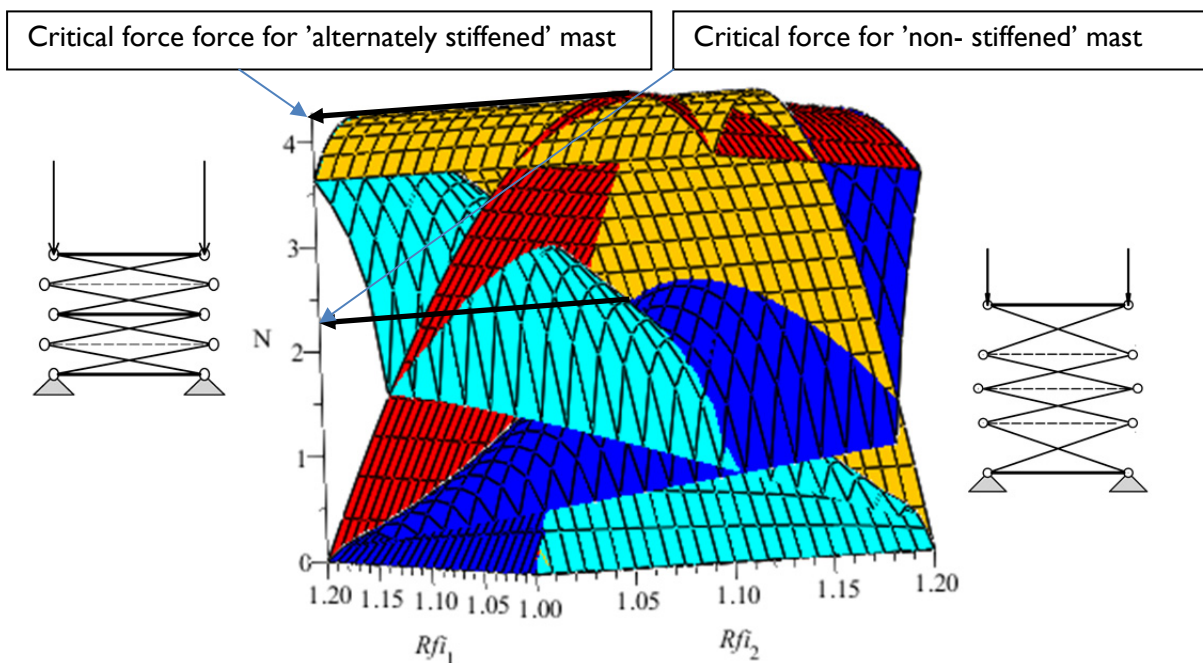


Fig. 3.29: Comparing critical forces of 'alternately stiffened' and 'non-stiffened' structures by plotting equilibrium paths in function of the half-lengths of the elastic horizontal bars (The equilibrium path of the 'alternately stiffened' mast is at the intersection of the light blue and the dark blue surfaces, the one of the 'non-stiffened' structure is at the intersection of the orange and red surfaces, $EA=100$, $h_0 = 1$, $r_0 = 1$, initial total height of the structure: $H = 4h_0$)

¹ Note that the notation k for 'alternately stiffened' and for 'non-stiffened' masts are not identical. The basic segment of the 'alternately stiffened' structure is the double of the one of a 'non-stiffened' structure. Consequently, the compared structures are of equivalent total height.

3.3 Numerical analysis

3.3.1 Methodology

For the numerical analysis of the packing of the different pop-up masts two parallel analyses were carried out. The FEAP finite element software was used to present the general behavior of the structure and to trace the force displacement diagram. As some numerical difficulties were found and the verification of the results was sometimes rather cumbersome and ambiguous, a second, less sophisticated but more transparent simulation of the structure was developed in MAPLE. Fortunately the latter one confirmed the results of FEAP and hence the two programs together provided interesting results concerning the behavior of such structures.

In order to be able graph the complete equilibrium path of the basic segment of the deployable mast a displacement control has to be applied because of the existence of instability phenomenon. In reality, as all the structure has to be kept symmetrical anyway (because of the asymmetrical freedom of motion of the structure), the evident packing procedure of the structure is of this type.

However, in order to trace the complete force-displacement diagram of multi-storey structures, displacement control may not be sufficient if the number of segments is too large. In this case even by controlling smoothly the displacement of the top nodes (by fix incrementing values of ' u ') the structure will 'rattle' down. This is due to the 'snapping-back' characteristic of the force-displacement diagram (Fig. 3.9, 3.17). Displacement control without snapping can be only effective if the displacement of all the nodes is controlled. The aim to trace the force-displacement diagram numerically dictates a different approach than force or displacement control. One of the available procedures is the arch-length method with an inherent additional equation controlling both the increments of displacements and the increments of force, which can be either a positive value or a negative one. This extra condition can be interpreted as a hyper-circle with a chosen radius. The computation in each increment will look for the intersection of this hyper-circle centered at an initial equilibrium point with the force-displacement diagram [Ibrahimbegovic, 2009, pp. 484-486]. The procedure starts with choosing the right parameter for the radius of this hyper-circle and the next step is to solve for both, the increment of the force and the increment of the displacements.

In fact, the equilibrium path is just an abstract diagram as physically controlling both the packing force and the displacements is rather complicated. However, by possessing the complete force-displacement path an attempt can be given to pack smoothly the structure that is without any 'rattle' with the control of the displacement of the top nodes by somewhat pulling back the structure at the snapping-back points. Without doing so, violent internal snapping of the structure can be expected resulting in inertial forces that can damage the structure. Consequently, if the smooth control is not realizable, it is important to know the existence of snap-back phenomenon and if there is so, to put some additional instruments to dump the inertial forces and to control the vibration of the structure when proved necessary.

3.3.2 Software description

The FEAP (Finite Element Analysis Program) is a general purpose finite element analysis program which is designed for research and educational use. The analysis in this thesis was carried out with version 7.4. The FEAP program includes options for defining one, two, and three dimensional meshes, defining a wide range of linear and nonlinear solution algorithms, graphics options for displaying meshes and contouring solution values, an element library for linear and nonlinear solids, thermal elements, two and three dimensional frame (rod/beam) elements, plate and shell elements. Constitutive models include linear and finite elasticity, viscoelasticity with damage, and elasto-plasticity [FEAP, 2011]. Besides the wide range of built-in algorithms probably the best feature of FEAP is that the source code of the full program is available and changeable with a Fortran compiler.

For some verification, the MAPLE mathematical software package was used, using both its symbolic and numerical computational facilities. Some details about the performed simulation are attached in Annex D.

3.3.3 Simulation of the packing of the basic unit

The first step to analyze the planar structure, was to simulate the packing of only one segment. This was executed with a very simple non-linear truss model. Though in FEAP rigid body options with joint interactions are implemented, this option is only available for solid elements within the available version which would just needlessly complicate the mesh generation. For a simpler solution in order to model the rigid rods the axial stiffness of the bracing was defined two orders higher than the axial stiffness of the elastic structure. This can be quite realistic for example in case of using steel for the bracings and a rubberlike material for the elastic bars. If this difference is to be defined much higher the tangent stiffness matrix will be bad conditioned resulting in the augmentation of the numerical errors. Certainly this is to be avoided.

For the constitutive model, the hyper-elastic logarithmic stretch model was used. This model implemented in FEAP calculates the strain from:

$$\varepsilon = \ln(\lambda) \quad (3.66)$$

λ is the vector of principal stretches and ε is the vector of principal strains. In our case, that is, for simple truss model the engineering stress can be calculated from:

$$\sigma = E \varepsilon \quad (3.67)$$

The use of the logarithmic stretch seems to be a good choice, as it can fit well to the force-displacement diagram of a rubber-like material subjected to tensile test, and in the small-strain regime it gives identical results to that one calculated from $\varepsilon = \lambda - 1$ (Fig. 3.30). The fact that this model gives completely fallacious results in the large compression regime

can be ignored now, as the elastic bars of the planar mast are only subjected to tensile forces.

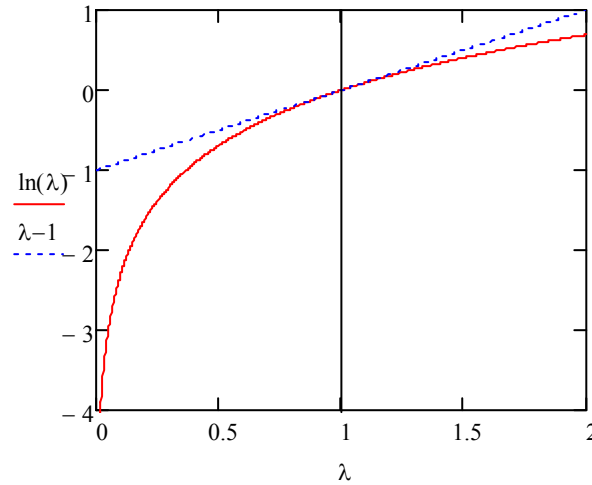


Fig. 3.30: Comparison of logarithmic strain and the one used for small-strain measure for axial force

During packing, the bracings are subjected to high compression loads that can lead to the buckling of these rods. This local buckling phenomenon interacts with the global instability problem during packing. This possibility was ignored in the analysis for practical reasons with the assumption that the stiffness and the cross section of the bracings is such that the Euler critical force of the rods exceeds the maximum of compression force the bracings are subjected to.

The analysis of one segment was carried out with displacement control, by defining vertical boundary at the top two nodes and displacing it with the height of the segment with small increments. For each incremented value of displacement the necessary packing force and the corresponding displacements of the nodes were calculated using the Newton method, sometimes by an additional line search algorithm for better convergence.

The numerical results of the simulation for the force-displacement diagram are presented in *Fig. 3.31*. It can be seen that the difference between the numerical and the analytical results is due to the different constitutive model. The larger the stretching of the elastic bar gets the larger the difference grows. Nevertheless, replacing the constitutive equation (3.7) to

$$\varepsilon = \ln(\lambda) = \frac{S_H(h^\varphi)}{EA} \quad (3.68)$$

and consequently the equilibrium equation (3.8) to

$$N(h^\varphi) = \frac{S_H h^\varphi}{l_H^\varphi/2 + r_0} = \frac{EA \ln[\lambda(h^\varphi)] h^\varphi}{r_0 [\lambda(h^\varphi) + 1]} \quad (3.69)$$

and plotting out the function on the same diagram (Fig. 3.31), it can be seen that this difference excludes large numerical errors, and hence the numerical simulation is more than satisfactory.

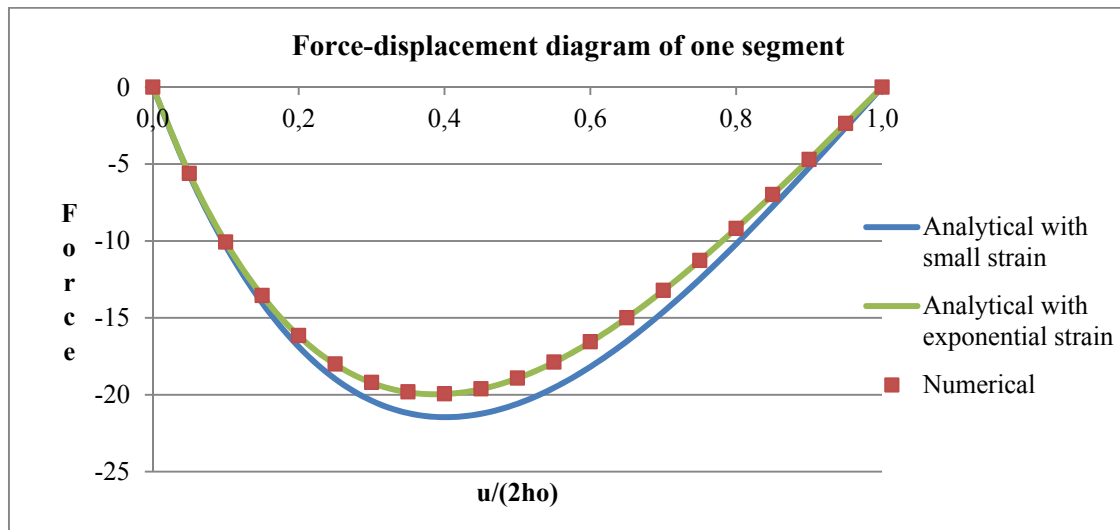


Fig. 3.31: Verifying numerical results with analytical solution – packing of basic segment (numerical results with logarithmic strain, analytical results with small strain formulation and with logarithmic strain $EA = 500, h_0 = 1, r_0 = 1$)

3.3.4 Numerical analysis of ‘alternately stiffened’ multi-storey masts

Unrestricted simulation

The ‘alternately stiffened’ multi-storey mast was modeled with horizontal boundaries at each rigid horizontal bar. These boundaries not only eliminate the possible deformation of these bars but also ensure the assumed symmetrical behavior of the structure. As presented above the uniform packing is not typical and if any physical or geometrical parameter of a segment is deviating from the others it is impossible. In fact the simulation works similar to reality, the only difference is that it is not the imperfections that control the behavior but the numerical errors. However, if a certain behavior is needed to be traced, it is better to ensure the wanted phenomenon by controlling it with predefined imperfections through the input. Accordingly, the following control procedures will be used to trace different paths (Fig. 3.32):

- In order to trace the equilibrium path of the **uniform and successive packing** additional restraints are placed at the end of the rigid horizontal bars. The packing is simulated by controlling the vertical displacement of each horizontal bar with different proportional boundary displacements (Fig.3.32-33);
- In order to trace the **typical path** the axial stiffness of the elastic bars are perturbed with a small imperfection in the finite element simulation. The order of the packing can be controlled by putting the smallest axial stiffness value for the elastic bar belonging to the segment to be closed first (Figs. 3.32, 3.35). In the MAPLE simulation the different bifurcated paths were traced by randomly perturbing the equilibrated variables before using them for the next iteration as initial values (see Annex D)

- **Non-controlled paths** are traced too, which is only governed by the numerical errors of the calculation (Figs. 3.35-36).

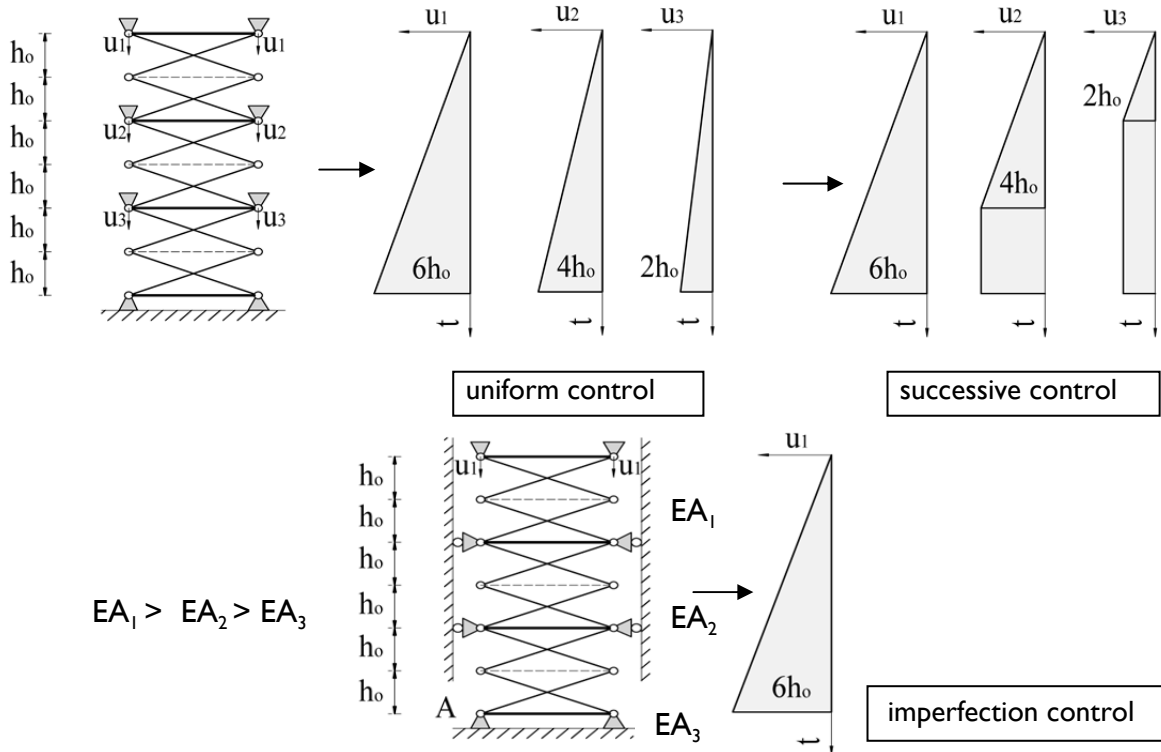


Fig. 3.32: Numerical models with different packing controls (uniform control, successive control, imperfection control, the non-uniform controls pack the segments successively from the bottom to the top) — u_i is the proportional vertical displacement of the i^{th} boundary in function of the pseudo time (t)

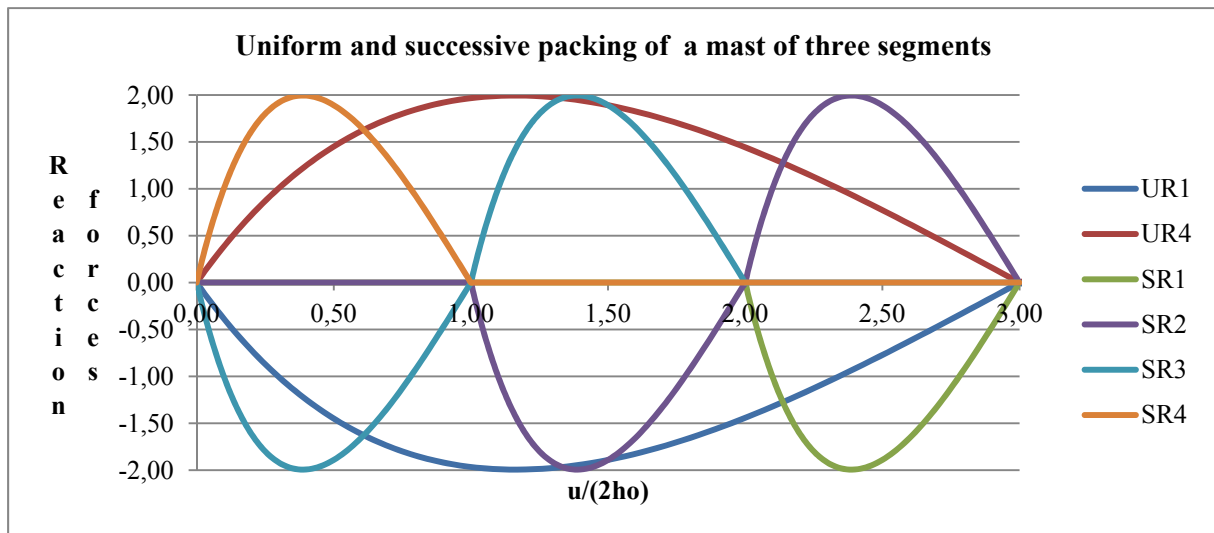


Fig. 3.33: Uniform and successive packing of ‘alternately stiffened’ mast —Reaction forces at the end nodes of the rigid horizontal bars (SR1-SR4: reaction forces from successive control respectively from the top to the bottom, UR1, UR4: reaction forces from the uniform control at the top and at the bottom nodes, downward forces are negative ($EA = 100, h_0 = 1, r_0 = 1$)²)

² Note that for Fig. 3.32 the maximal packing force was ten times higher for the same geometrical configuration. The difference comes from two reasons. First the axial stiffness of the elastic bars is five times greater, second in Fig. 3.32 it is the total packing force that was diagrammed (two times the reaction force), while in Fig. 3.34 it is the reaction force at the top two boundary nodes.

Fig. 3.33 shows that with a successive or uniform control the structure can be closed smoothly without any ‘rattle’ and can be closed completely even without restricting ‘post-packed phenomenon’. However, in practice this is only realizable if all the displacement of all the end nodes of the rigid horizontal bars is controlled. This might be possible for example by connecting them with two vertical telescopic-like devices.

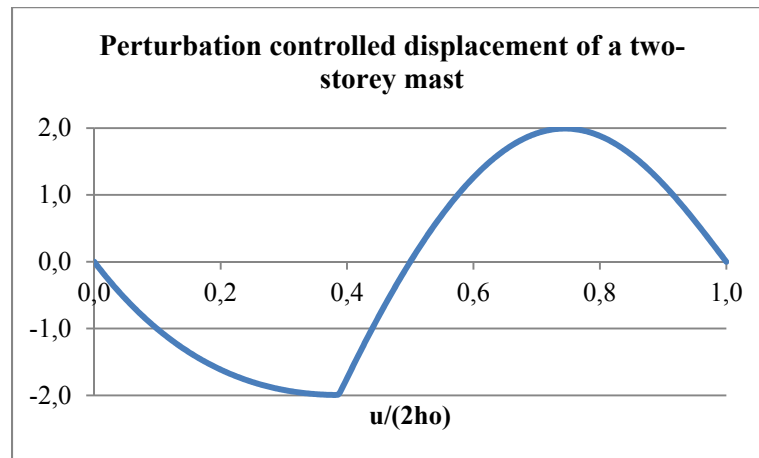


Fig. 3.34: Typical packing simulation of a two-storey planar mast without the restriction of ‘post-packed phenomenon’ controlled by the imperfection of axial stiffness values, downwards forces are negative ($EA_1 = 100$, $EA_2 = 99.8$, $h_0 = 1$, $r_0 = 1$)

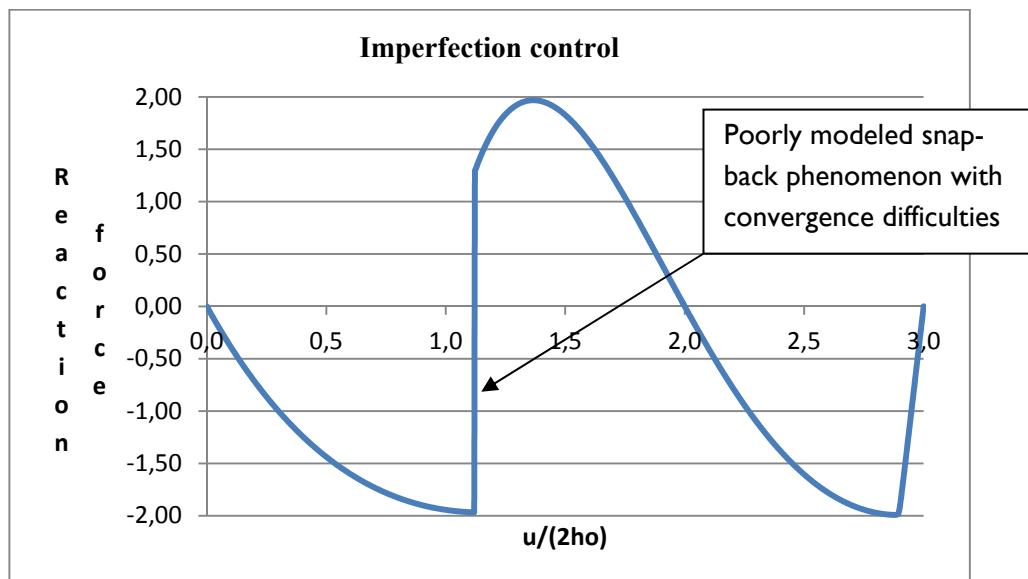


Fig. 3.35: Typical packing simulation of a three-storey planar mast without the restriction of ‘post-packed phenomenon’ controlled by the imperfection of axial stiffness values, downwards forces are negative ($EA_1 = 100$, $EA_2 = 99.8$, $EA_3 = 99.6$, $h = 1$, $r_0 = 1$)

In the case of only controlling the displacement of the top nodes, the typical force-displacement diagram can be traced for instance by perturbing the axial stiffness of the elastic bars. This is presented in Figs 3.34-35 for a two-storey and for a three-storey mast. It can be concluded that the drafted force-displacement diagram calculated from the analytical solution (3.11) and the one originating from the numerical simulations (Fig. 3.34) are in good

accordance and that the packing sequence demonstrated in *Fig. 3.13* confirms the one received from the simulation.

In the numerical examples — for facilitating the verification — the initial height of the half-segment (h_0) and the half-length of the elastic bars (r_0) were chosen of unit length. The critical number of segment belonging to this initial geometry from (3.45) is two ($n_{cr} \approx 2,5$), which explains the large vertical part of the descending (on the figure incrementing) path of the force-displacement diagram of the three-storey structure in *Fig. 3.35*. Because of the poor convergence at the snapping-back part, a line search algorithm was used to be able to find the next equilibrium point after the critical state. This simulation of the three-storey structure demonstrates well that, in case of structures whose packing is characterized by a snap-back phenomenon, the ‘exact’ equilibrium path cannot be plotted by simple displacement control. However, the simulation reflects well the reality; sudden internal snapping of a part of the structure may occur, and related inertial and impact effects should be carefully analyzed before realization.

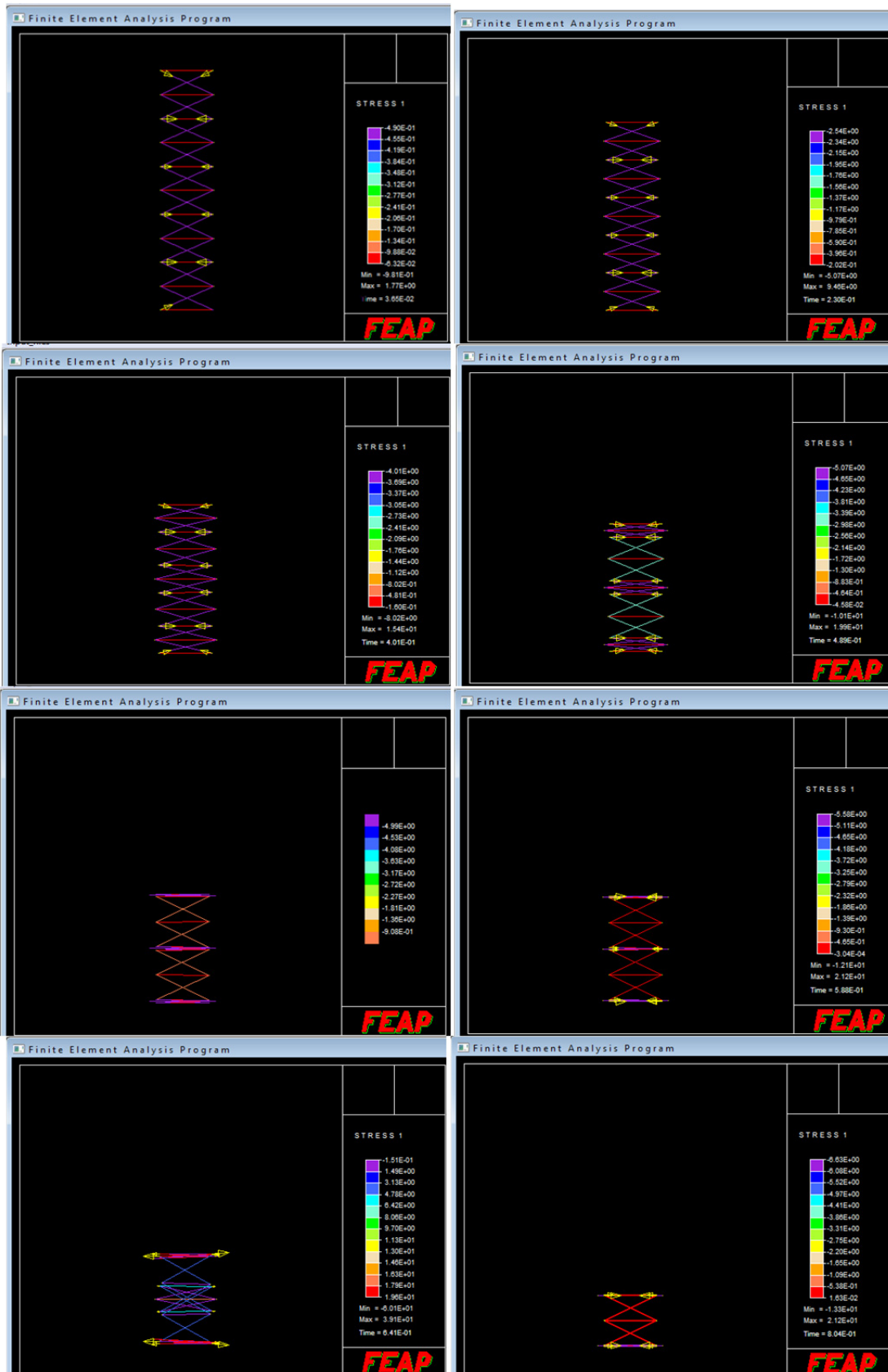
As already mentioned above, the numerical simulation is somewhat similar to realistic behavior. While in case the of a real structure it is the geometrical and physical imperfections that governs the packing sequence, in the case of the numerical simulation it is the numerical errors that decide which segment will be the first one to close. This is demonstrated with the simulation of a five-storey mast, which was only controlled by the displacement of the top nodes, without any implemented imperfections (*Fig. 3.36*). It can be seen from the sequence shown on *Fig. 3.36* that three segments from five close uniformly together

To check whether the structure snaps-back or not in the case of simultaneous closing of several segments, the condition in (3.44) has to be modified to:

$$(k - n_{cl})u_{cr} = (2h_0 - u_{cr})k \Rightarrow \frac{k}{n_{cl}} = \frac{2h_0}{u_{cr}} = k_{cr}$$

(3.70)

with n_{cl} being the number of simultaneously closing segments. In the ‘non-controlled’ simulation $n_{cl} = 3$ and accordingly, $n_{fl}/k = 5/3 \approx 1.67 < k_{cr} \approx 2.5$ and smaller than two, as well. This means that the post-critical paths of the analyzed packing do not possess a snap-back behavior. This can be observed in *Fig. 3.36*. The breaking points on the diagram after the critical points are due to the ‘post-packed phenomenon’ which is manifested after each complete closure of a segment, and may result in sudden pulls of the rest of the structure.



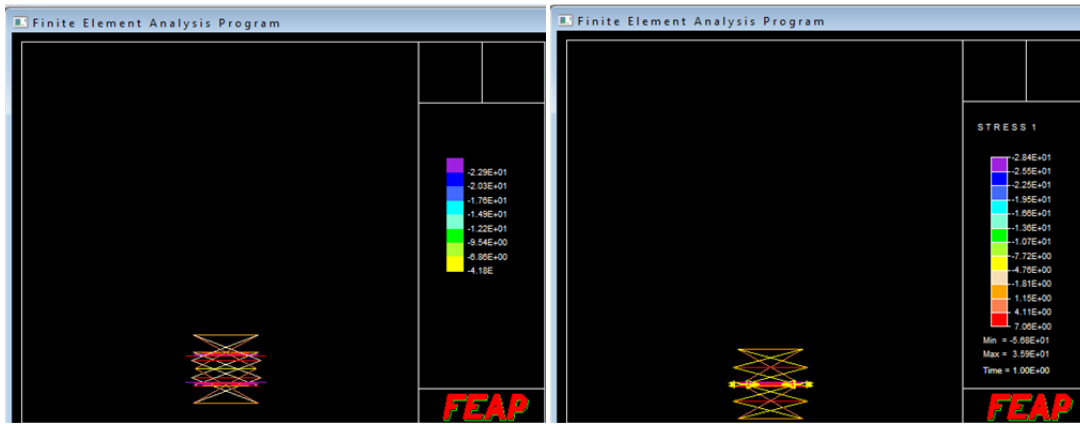


Fig. 3.36: Packing sequence controlled by the numerical errors of planar pop-up mast consisting of five segments, with simulation without the restriction of ‘post-packed phenomena’ ($EA = 100, h_0 = 1, r_0 = 1$)

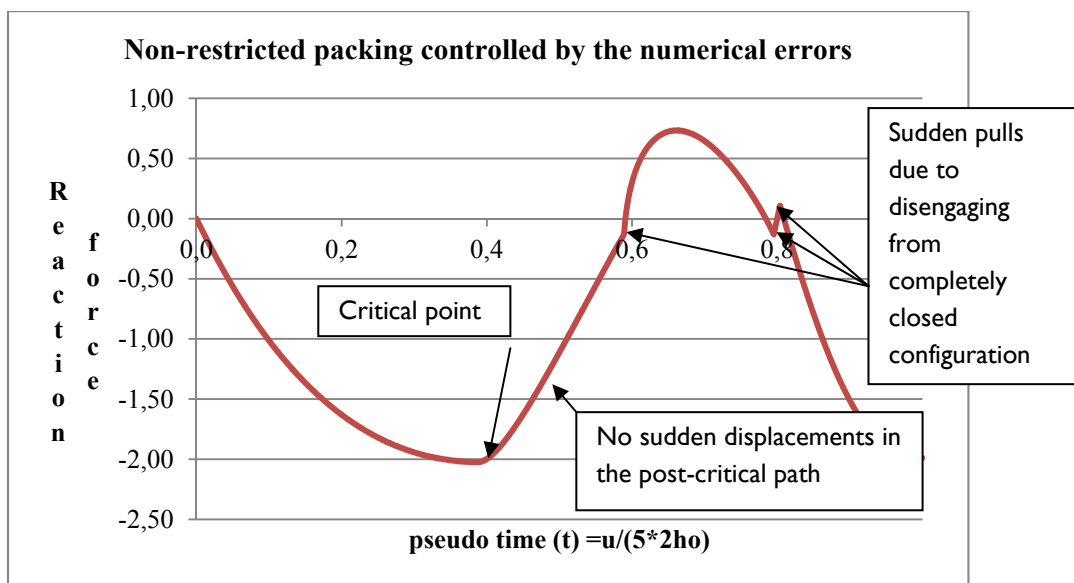


Fig. 3.37: Force-displacement diagram of five-storey planar pop-up mast controlled by numerical errors without the restriction of ‘post-packed phenomenon’ (packing sequence in Fig. 3.36, $EA = 100, h_0 = 1, r_0 = 1$, downward force is negative)

Restriction of ‘post-packed phenomenon’

It have been demonstrated in the previous chapters that the ‘post-packed phenomenon’ may withhold the structure from complete closure. In case of a deployable structure this is to be avoided.

By controlling the displacement of each end nodes of the horizontal bars this phenomenon is intrinsically has no importance. Nevertheless, when trying to close the mast by controlling only the displacement of the top nodes, the closed segments disengage from the closed configuration bringing unwanted sudden responses (see Figs. 3.36-37) into the packing behavior and troublesome geometrical configurations. In order to implement the restriction of the ‘post-packed phenomenon’ into the simulation contact elements have been added between the end nodes of the rigid horizontal bars (Fig. 3.38). A penalty approach was used to enforce the restraint between these nodes. The restraint force is governed by a penalty parameter and the distance in between the end nodes. When the two nodes

approach each other, the contact force increases, and keeps the segment from disengaging from the closed configuration to an upside-down one. If the penalty value is not large enough the restriction of the ‘post-packed phenomenon’ is not captured, and if it is too large, it turns the tangent stiffness matrix bad conditioned. For that, a careful adjustment of this parameter is necessary.

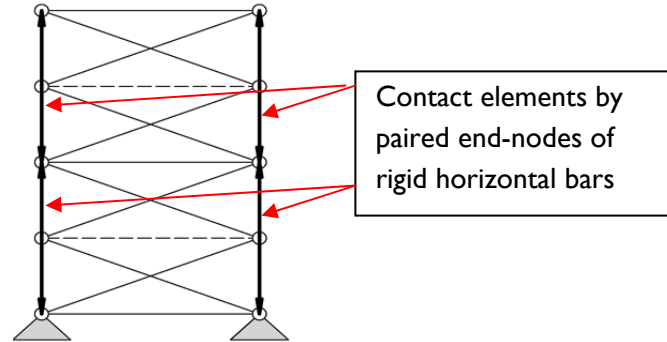


Fig. 3.38: Restricting ‘post-packed phenomenon’ with contact forces

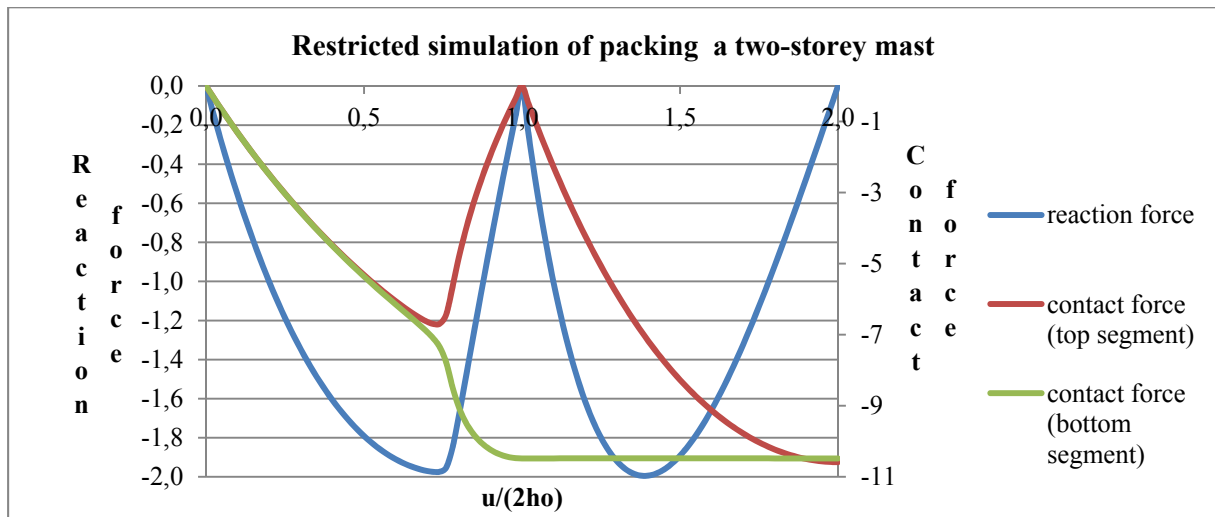


Fig. 3.39: Force-displacement diagram of packing a two-storey mast: restricted simulation with contact forces between the end nodes of rigid horizontal bars and packing control by imperfection of axial stiffness values ($EA_1 = 100, EA_2 = 99, h_0 = 1, r_0 = 1$)

Fig. 3.39 shows that the restricted simulation confirms the behavior deduced from analytical assumptions; the force-displacement diagram from the numerical calculation is identical to the last two loops of the force-displacement diagram constructed in Fig 3.9. It is also presented in the figure that the contact forces between the end points of the horizontal bars are disproportional with the distance between them. Controlling the packing by inducing imperfection of physical parameters (in this case perturbing the axial stiffness) the bottom segment will be the one that closes first ($EA_1 > EA_2$). Parallel to the uniform closing in the first phase the contact forces grow simultaneously. Nevertheless, as the bottom segment reaches its critical height somewhat before the top segment — because of its perturbed elastic bar — it moves apart the boundaries of the top segment, resulting in the decrease of its contact forces. As the structure is further squashed, the extended segment starts closing again until the structures is packed into a completely closed configuration.

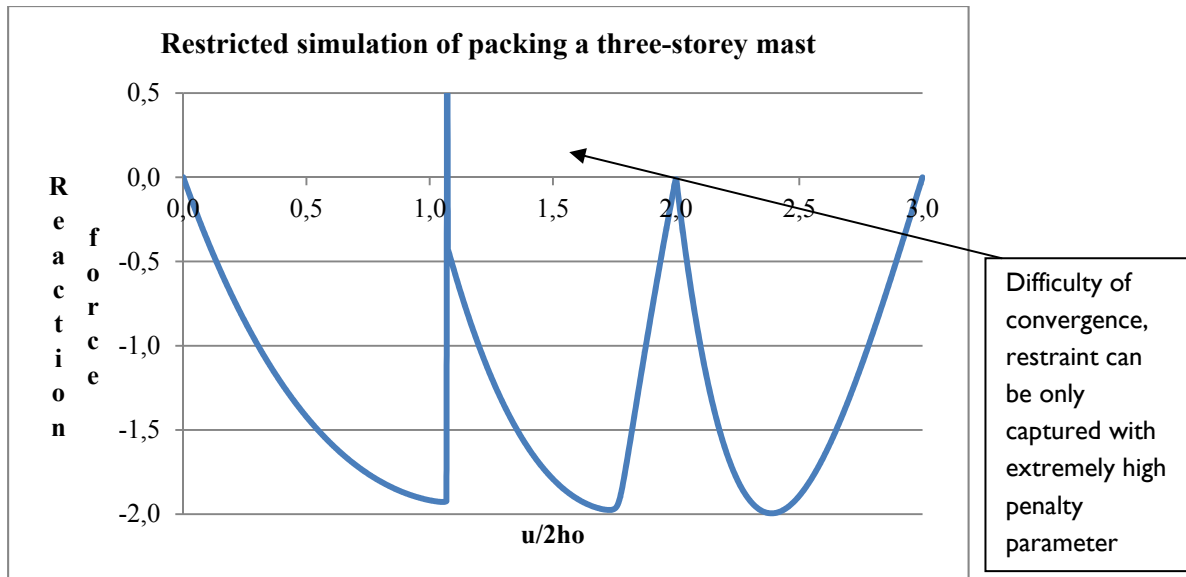
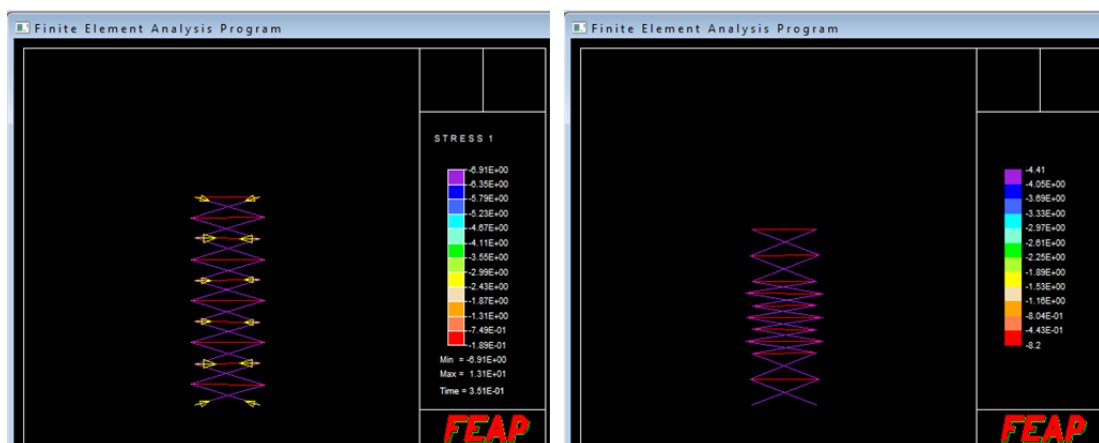


Fig. 3.40: Force-displacement diagram and the associated contact forces between the end nodes of rigid horizontal bars of packing two-storey mast with restricted simulation controlled by imperfection of axial stiffness, ($EA_1 = 100, EA_2 = 99, EA_3 = 98 h = 1, r_0 = 1$)

To capture the restraint for the three-storey structure is much more difficult because of the snap-back phenomenon. The simulation could only result a completely packed structure in case of extremely high penalty parameter. However, other than the bad converging part, after the first critical point (Fig. 3.40), the simulation gave back the expected force-displacement diagram and packing sequence. Despite of the apparent success of tracing the path, it is better to extend the analysis to one that takes the inertial effects into account. The results of the same example of the five-storey uncontrolled mast that was presented in Fig. 3.36-37 with the induced contact forces are shown on Fig. 3.41-42. It can be seen that the restriction of ‘post-packed phenomenon’ smoothes the sudden pull-backs.



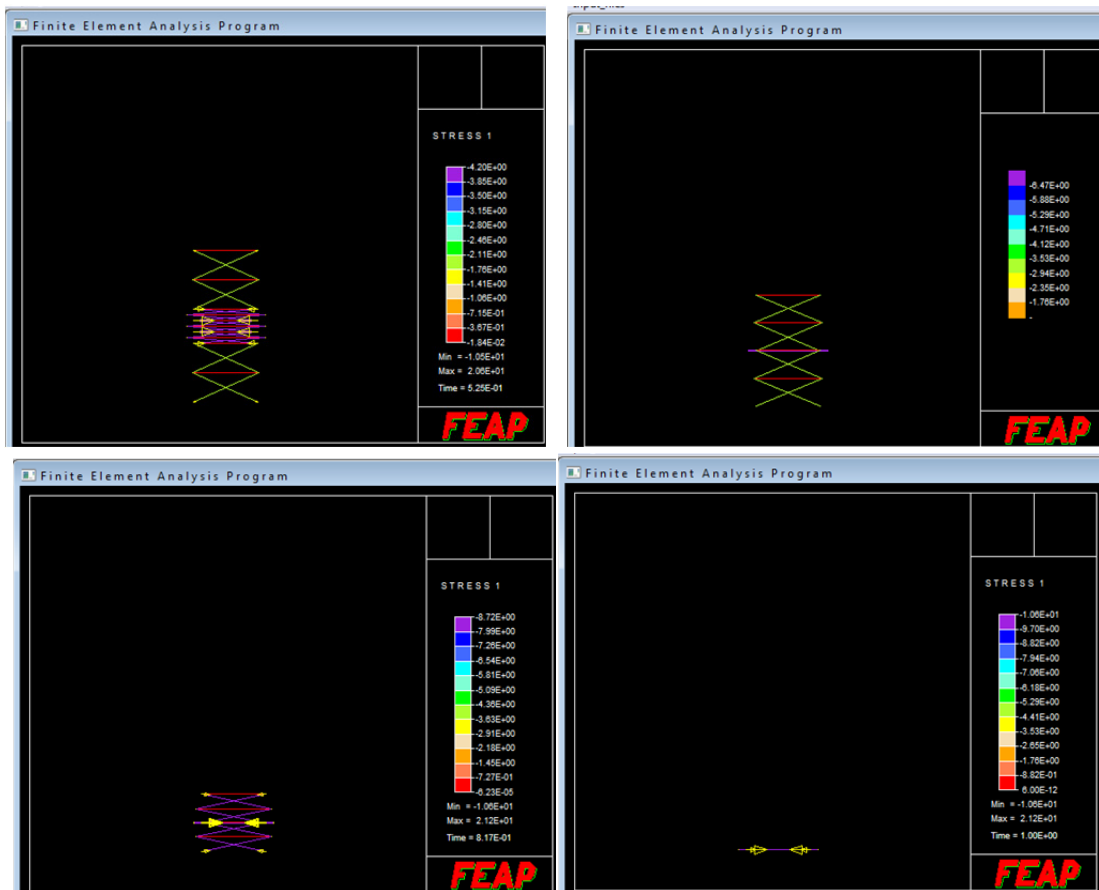


Fig. 3.41: Packing sequence controlled by the numerical errors of planar pop-up mast consisting of five segments, with restricted simulation ($EA = 100, h_0 = 1, r_0 = 1$)

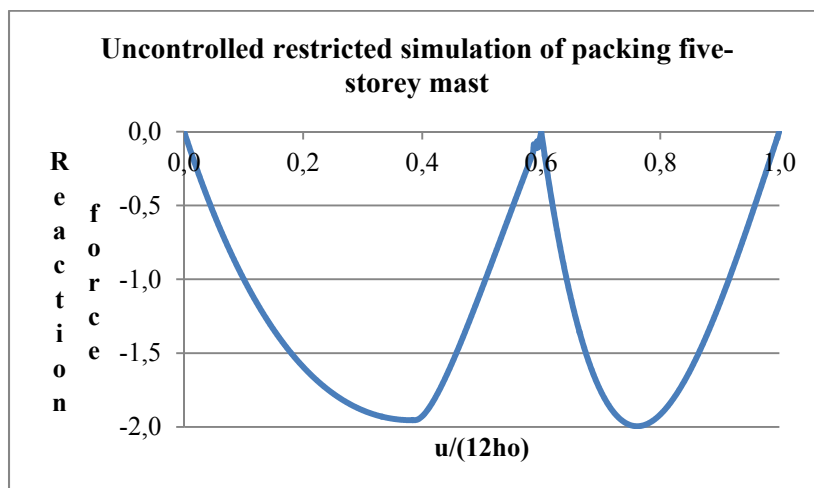


Fig. 3.42: Force-displacement diagram of five-storey planar pop-up mast controlled by numerical errors (packing sequence in Fig. 3.41, $EA = 100, h_0 = 1, r_0 = 1$, downward force is negative)

3.3.5 Numerical analysis of multi-storey masts without intermediate stiffening

Unrestricted simulation

Putting only elastic bars instead of the intermediate stiffen bars, the simulation of the mast is a little more difficult to verify for its less transparent behavior, but a try is given to analyze it in order to prepare further investigation of 3D antiprismatic structures. The three different packing methods explained for the numerical analysis of ‘alternately stiffened’ mast can be similarly applied, with the extinction of horizontal boundaries (Fig. 3.43). In case of the uniform and successive control vertical boundaries were added at each horizontal rod (Fig. 3.44). However, in contrary to the basic segments of the ‘alternately stiffened’ mast, the segments of the non-stiffened mast on top of each other are not identical which makes the successive displacement control being rather abstract.

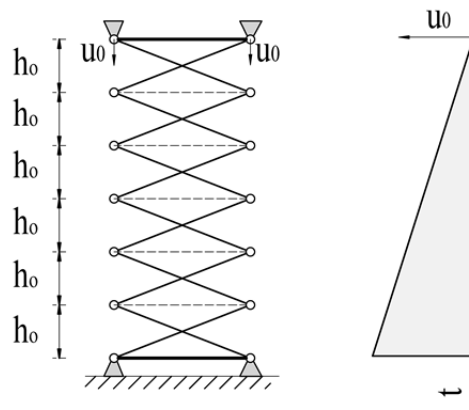


Fig. 3.43: Modeling the packing of non-stiffened mast by controlling only the displacement of the top nodes

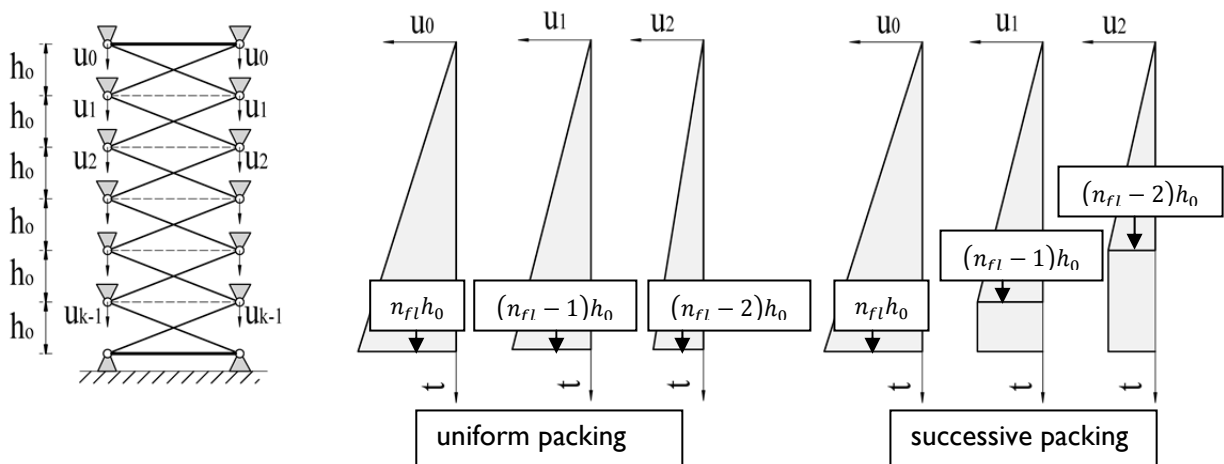


Fig. 3.44: Modeling the uniform and successive packing of a non-stiffened mast by controlling the displacement of every node

Fig. 3.45 and Fig. 3.46 present the uniform packing sequence of a mast of three segments and the associated force-displacement diagram. As the segments are not identical, a uniform closure cannot be effectuated with uniform packing force, consequently, reaction forces equilibrating this difference will appear in the intermediate boundaries. The middle

segment is the less stiff, that is, it would be the first one to close, accordingly, this segment needed to be drawn out in order to get a uniform packing (Fig. 3.45). Though the presented packing sequence shows that such packing is possible, it can be seen from the force-displacement diagram that it takes place under enormous packing forces which are of two times higher order than expected from the stiffness of the elastic bars. This augmentation of packing force means that for the packing the strains in the ‘theoretically’ rigid bars are needed too. If the bracings are assumed to be rigid the uniform packing cannot take place. In the further figures (Figs 3.47-3.49) it is presented that this behavior is characteristic of masts only with odd number of segments.

When geometrical properties analyzed of mast of three segments, it is evident that it is not only the uniform packing but any kind of complete packing is impossible. The boundary segments will be closed only if the two elastic bars extend to the length $2(l_b - r_0)$. But if both boundary segments had been packed, the bracings of the middle segments should have lengthen to this length. Accordingly assuming completely rigid bracings, the boundary and the middle segments cannot close together except in case of $l_b = 2r_0$, that is, a closed initial configuration.

In the case of different odd-storey masts this phenomenon also exists. **Due to the rigid boundaries the completely packed pattern is pre-defined.** This means every first elastic bar has to extend to the length $2(l_b - r_0)$ and every second one should regain its initial length $2r_0$. That is **only possible for even number of segments.**

It can be concluded that the previous analytical investigation of non-stiffened structures ignored a very important detail when presuming packing behavior. This detail was hidden back-stage and the wrong assumption has not been first revealed as the numerical simulation gave back the presumed sequence of packing (Fig. 3.28). However, when analyzing the maximal packing forces, it turned out that the erroneously presumed sequence could be gained only due to the bracings being not rigid in the simulation. This backstage error, the complex domain of the equilibrium functions, can be revealed when rotating the equilibrium surfaces plotted in Fig. 3.27 to the right angle (Fig. 3.50).

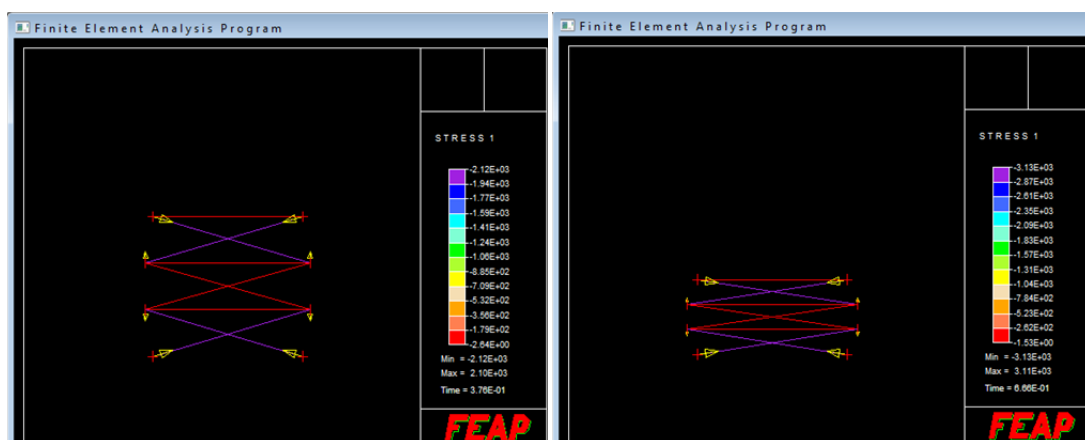


Fig. 3.45: Internal forces during packing: packing sequence of non-stiffened mast of three segments with uniform control ($EA = 100, h_0 = 1, r_0 = 1$)

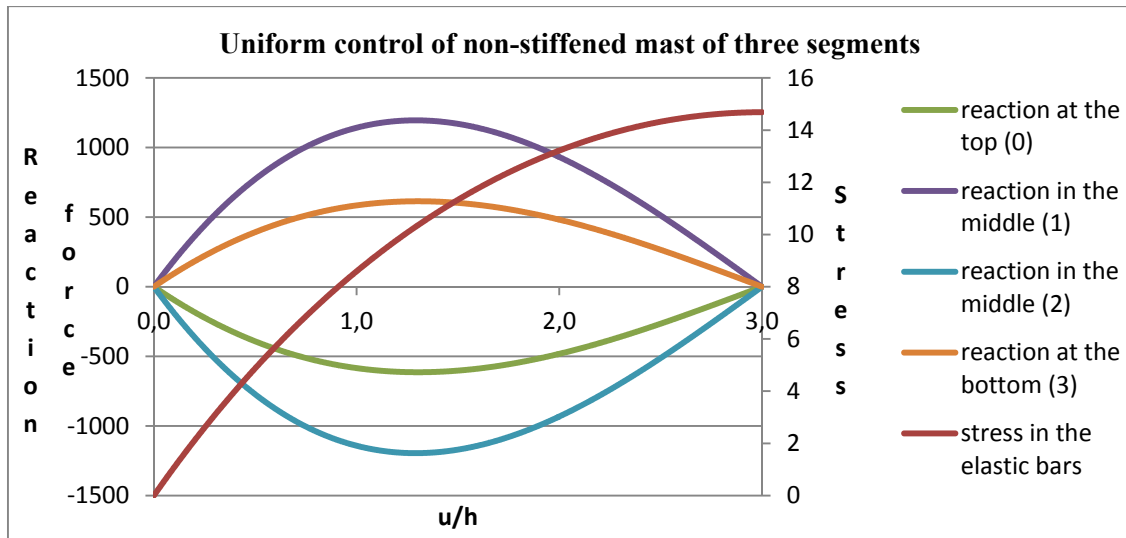


Fig. 3.46: Force-displacement diagram of packing a non-stiffened mast of three segments with uniform control ($EA = 100, h_0 = 1, r_0 = 1$)

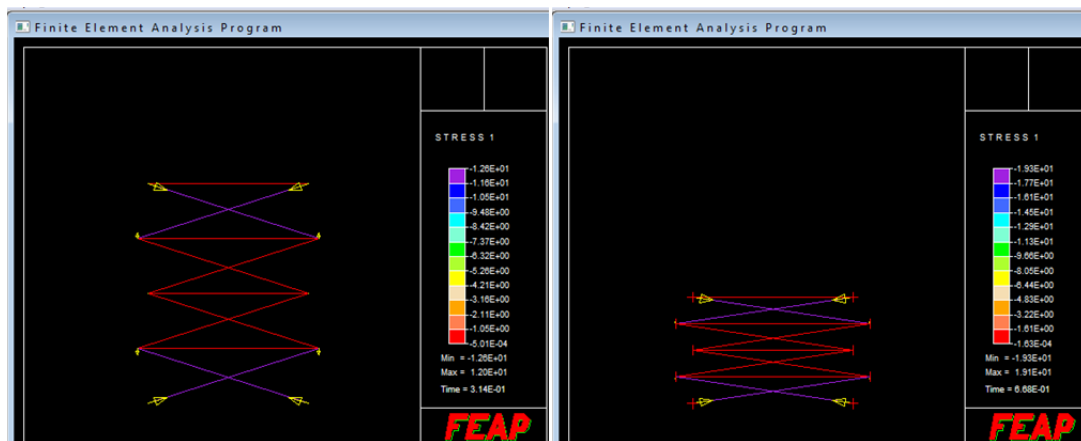


Fig. 3.47: Packing sequence of a non-stiffened mast of four segments with uniform control ($EA = 100, h_0 = 1, r_0 = 1$)

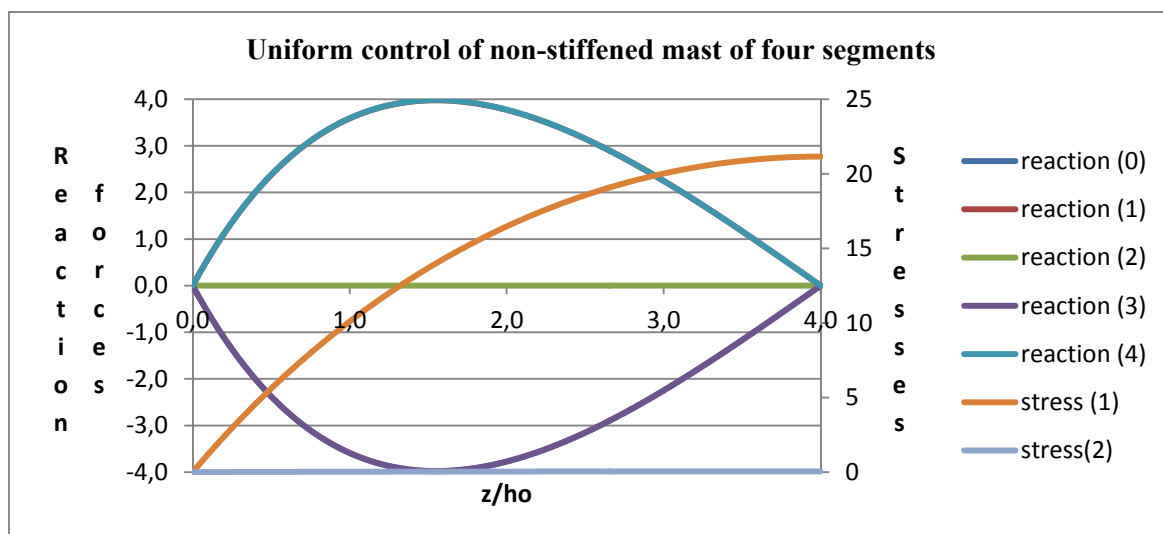


Fig. 3.48: Force-displacement diagram of packing a non-stiffened mast of four segments with uniform control ($EA = 100, h_0 = 1, r_0 = 1$)

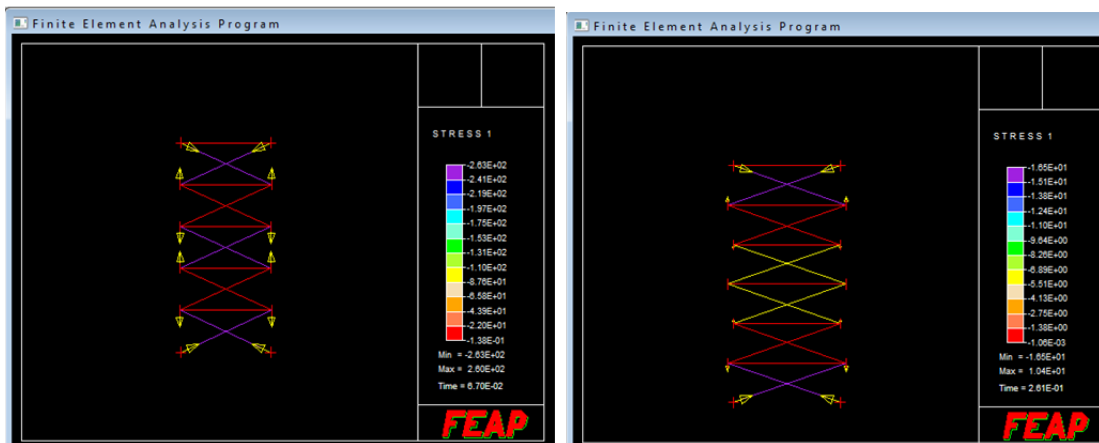


Fig. 3.49: Packing simulation of a non-stiffened mast of five and six segments with uniform control ($EA = 100, h_0 = 1, r_0 = 1$), maximal reaction force at the top in case of five segments is $R_{max}^{n5} = 361$ and the one of six segments is $R_{max}^{n6} = 5,95$

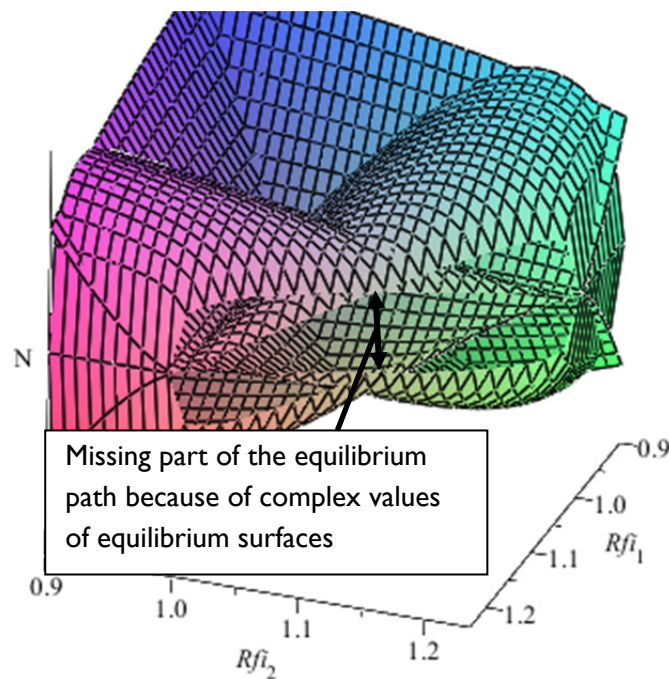


Fig. 3.50: Impossible closure of masts with odd number of segments — equilibrium path in function of the half-lengths of the elastic horizontal bars in case of $k = 3$ with the ‘post-packed phenomenon’

The successive control of such a structure is rather awkward and — due to the same reasons which keep the odd number of segments uncompactable — can be only achieved by changing the length of the bracings (Fig. 3.51). For that it seems a better possibility to control only the displacement of every second elastic bars, especially taking into account the fact that odd number of segments cannot lead to a complete compact configuration (Fig. 3.52).

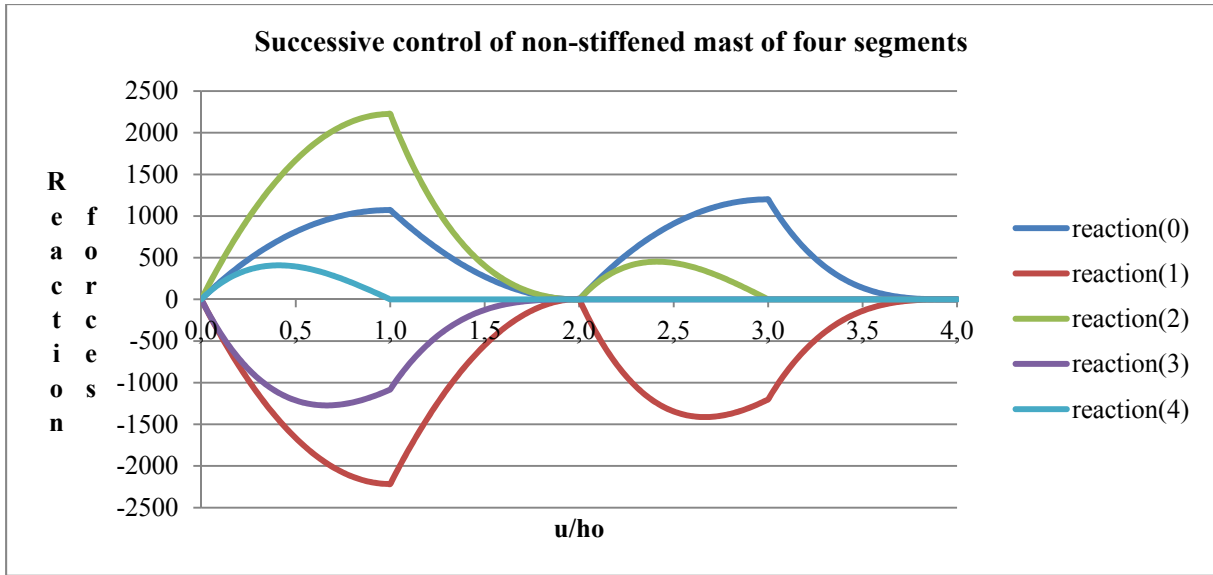


Fig. 3.51: Fallacious packing simulation of non-stiffened mast of four segments with successive control — reaction forces ($EA = 100, h_0 = 1, r_0 = 1$)

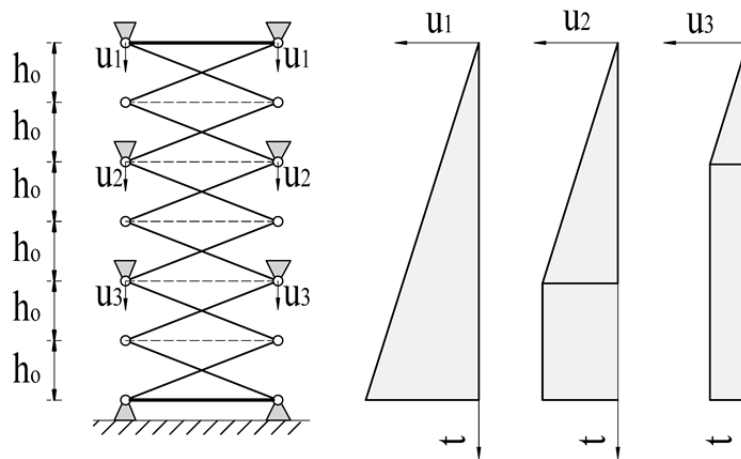


Fig. 3.52: Modeling successive packing of non-stiffened mast by controlling the displacement of every second node

Nevertheless, if only every second elastic bar-ends are controlled then the ‘post-packed phenomenon’ will necessarily occur (Fig. 3.53-54). First, when trying to close the bottom double-segment its middle, elastic bar extends and its upper elastic bar compresses (the compression of the latter results in the extension of the above elastic bar). This way the upper segment of this double unit will close first and when pushing further the upper elastic bar will duck through the middle one and accordingly, all the elastic bars will regain their initial geometry, while the height of the bottom segment turns only h_0 instead of the initial $2h_0$ height. Afterwards, trying to close the upper double segment, almost until the very end of the packing, it will behave as the basic segment of the ‘alternately stiffened’ mast, but at the final stage this double unit disengages from the closed configuration as well. The large values of reaction forces at this final stage reflect that the complete sequence could be only achieved by changing the length of the bracings.

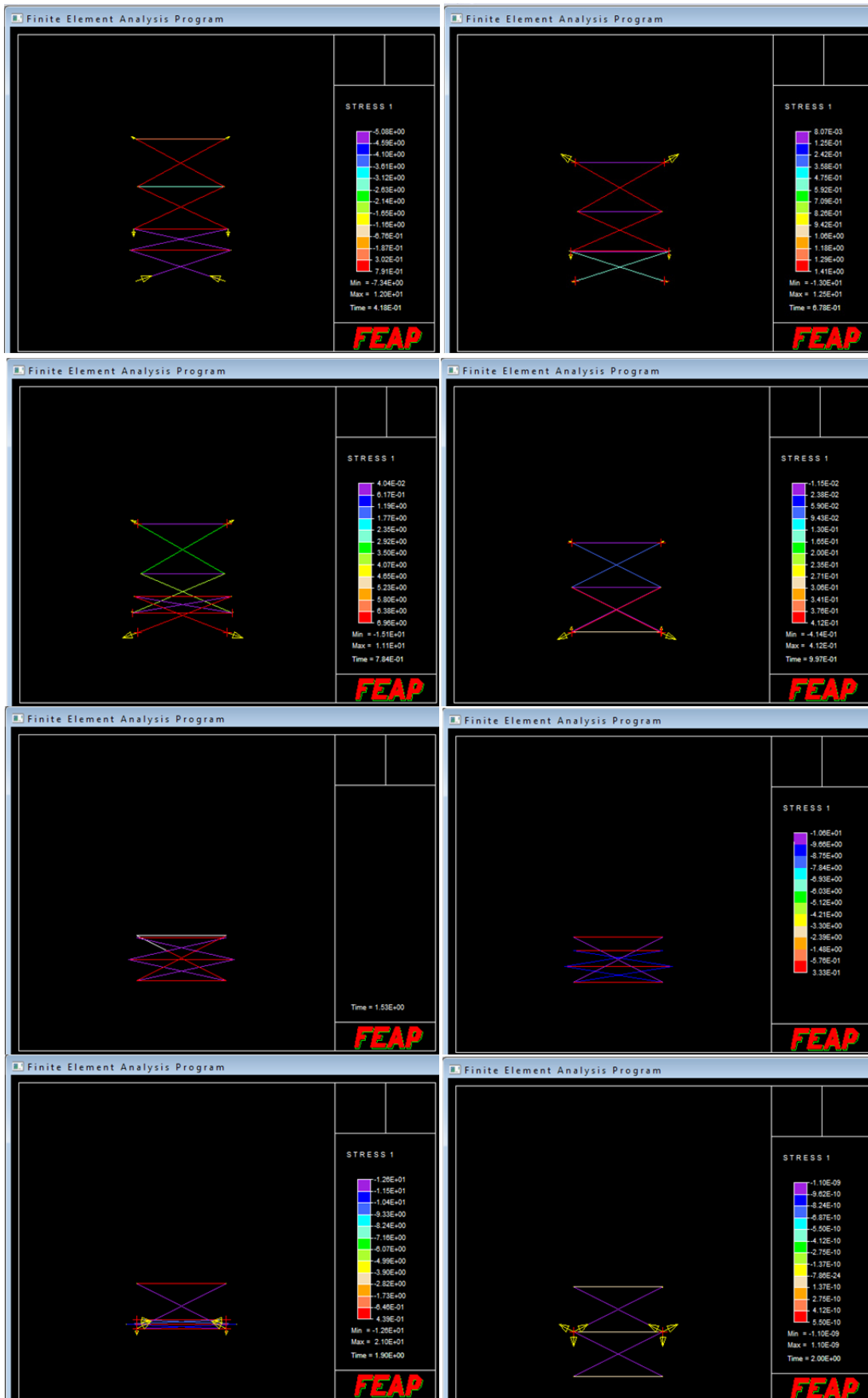


Fig. 3.53: Packing sequence from simulation of non-stiffened mast of four segments by successive control of double segments ($EA = 100, h_0 = 1, r_0 = 1$)

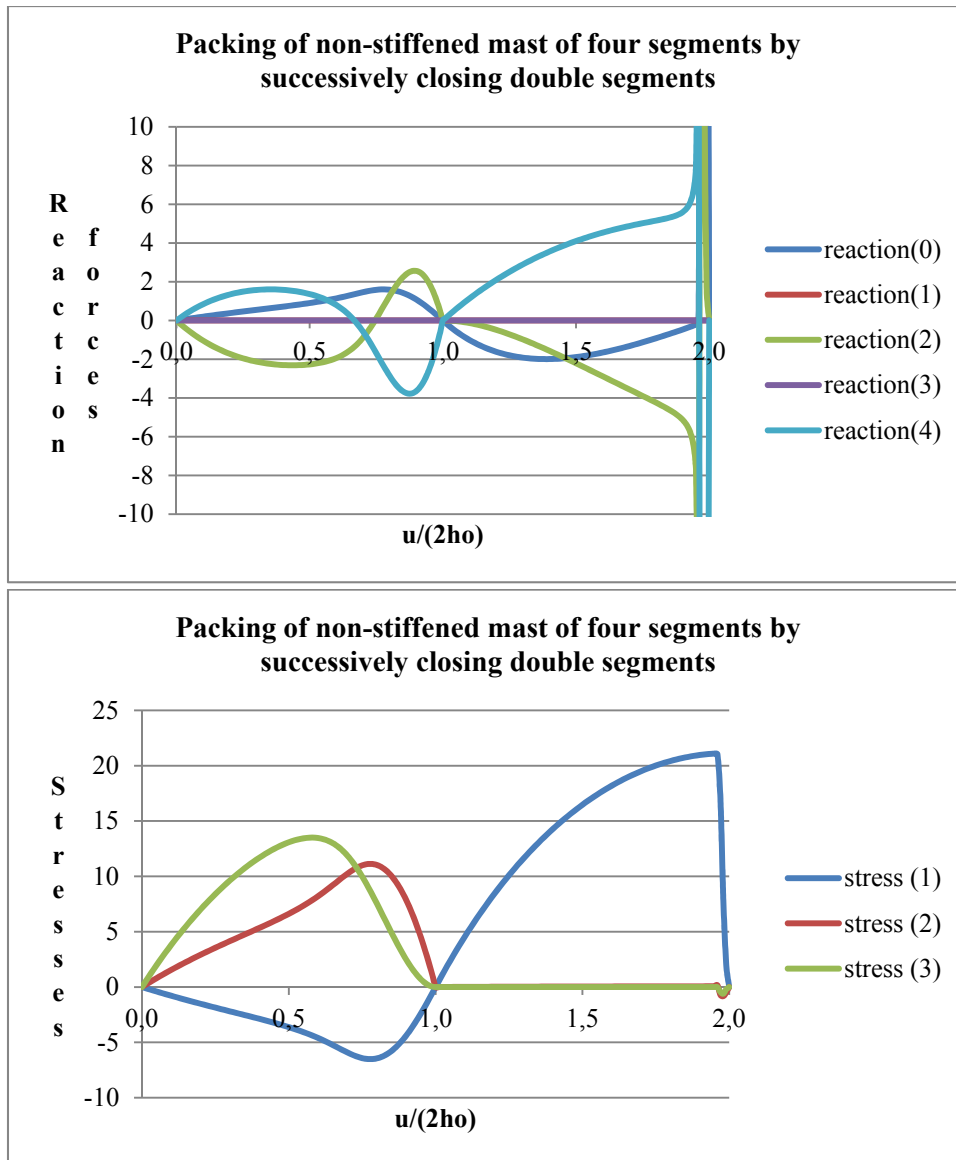


Fig. 3.54: Packing simulation of non-stiffened mast of four segments by successive control of double segments —reaction forces and stresses in the horizontal bars ($EA = 100, h_0 = 1, r_0 = 1$)

Fig. 3.55 shows the force-displacement diagram of packing a mast of six segments from an unrestricted simulation by controlling only the displacements of the top nodes. The nonzero value of the packing force at the final point reflects that no complete packing was achieved. The middle two segments closed first which was followed by the ‘post-packed phenomenon’ resulting in upward reaction forces at the top. If the symmetry (for example the axial stiffness of one of the middle elastic bars) had been violated than probably it would have been only one segment closing in the beginning.

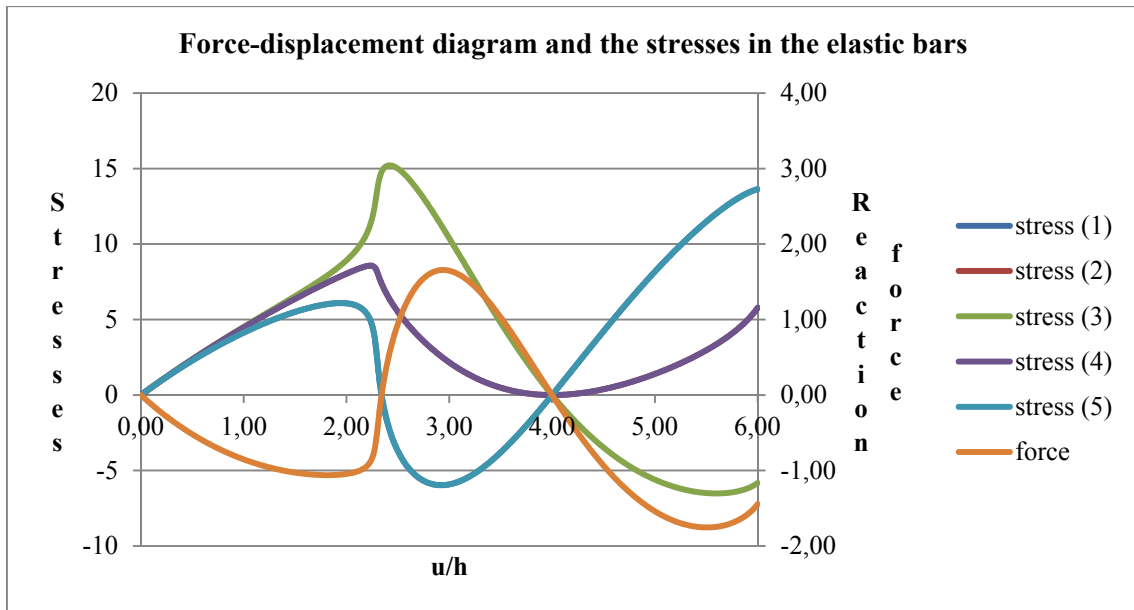


Fig. 3.55: Non-restricted packing simulation of non-stiffened mast of six segments by controlling only the displacements of the top nodes ($EA = 100, h_0 = 1, r_0 = 1$)

Restriction of ‘post-packed phenomenon’

The restriction of the ‘post-packed phenomenon’ was modeled similarly to the case of ‘alternately stiffened’ mast. The difference is that in the non-stiffened mast contact elements have to be introduced between each node (Fig. 3.56). This was proved to be necessary before, in the section above, where the successive simulation controlling only every second node was presented.

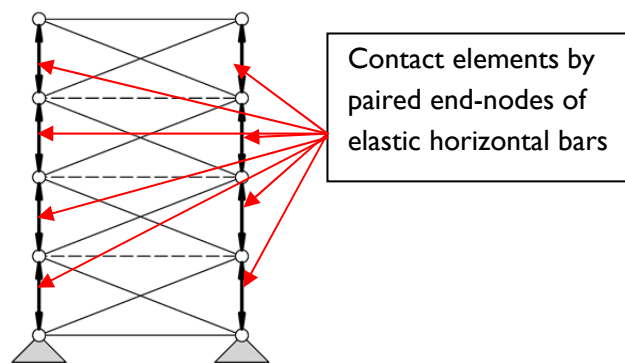


Fig. 3.56: Modeling the restriction of ‘post-packed phenomenon’ for non-stiffened masts

The force-displacement diagram from the simulation of a mast of four segments and the associated stresses in the elastic bars are presented in Fig. 3.57. No perturbations were initialized and consequently the middle two segments could reach its critical height at the same state. These two middle segments closed first followed by the stiffer boundary segments. It is demonstrated in the diagram that contrary to the case of the ‘alternately stiffened’ mast, after the complete closure of a segment, its elastic bar does not stop changing length.

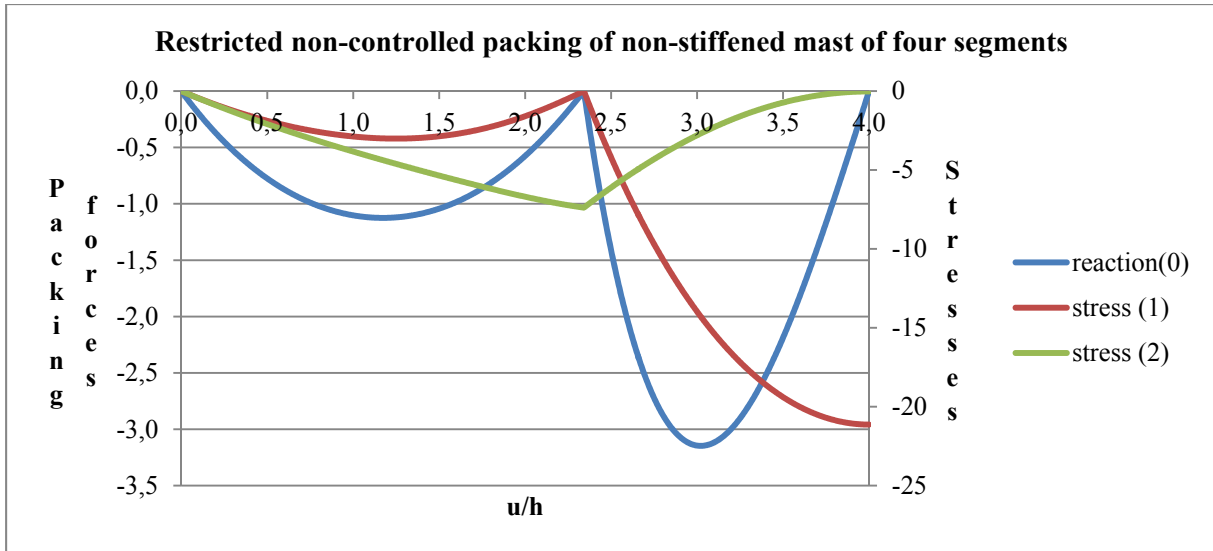


Fig. 3.57: Restricted packing of non-stiffened mast —force-displacement diagram and stresses during packing ($EA = 100, h_0 = 1, r_0 = 1$)

The same simulation, but perturbing the axial stiffness of the bottom elastic bar results in an extra loop in the force-displacement diagram. This is presented with the associated stresses in the elastic bars in Fig. 3.58. It can be figured from the diagram that this perturbation caused a snap-back phenomenon that is after the first critical point some intermediate violent displacements occur.

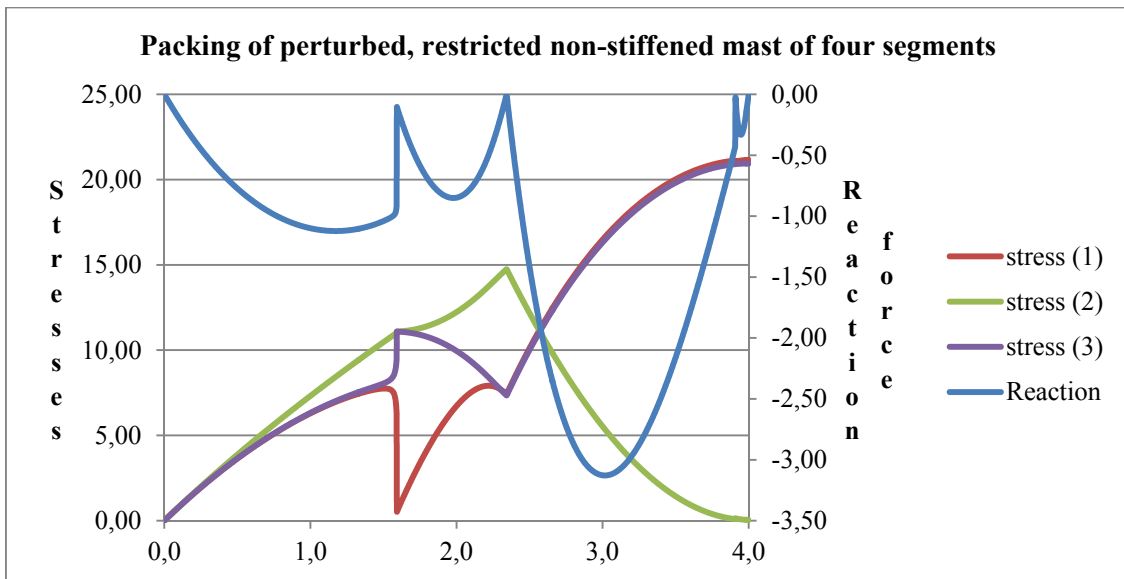


Fig. 3.58: Restricted packing of non-stiffened mast —force-displacement diagram and stresses during packing ($EA_i = 100; i = 1,2; EA_3 = 99; h_0 = 1; r_0 = 1$)

Investigation of packing pattern and the critical force

While the critical force of the ‘alternately stiffened’ mast was very simple to determine, to give the critical force of the alternately stiffened mast can only be numerically investigated. Fig. 59 shows the tendency of the critical force in function of the number of the segments.

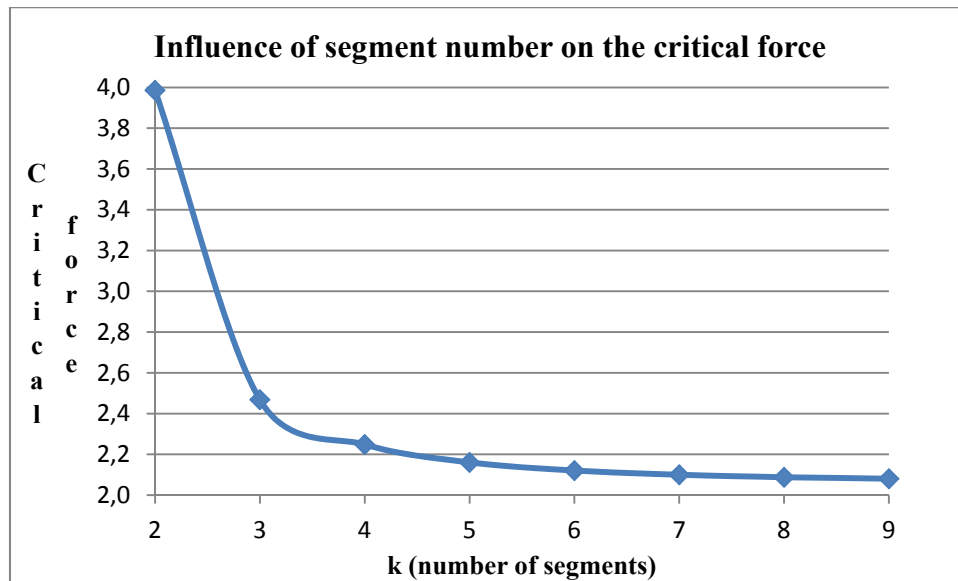


Fig. 3.59: Influence of segment number on the critical force of ‘non-stiffened’ masts for two different ratios of segment height and half-length of elastic bars (with logarithmic constitutive model, by FEAP) ($EA = 100$; $h_0 = 1$; $r_0 = 1$)

The same tendency is calculated with the self-developed MAPLE simulation which calculates with linear, elastic small strain constitutive model (see Appendix D, Fig D3). As presented in these figures, the mast gets softer with the increment of the segment number. By increasing the segment number, the critical value is heading to be the half of the critical force of the ‘alternately stiffened’ mast.

The pattern of the packing can be presumed from the numeric simulation carried out by uniform packing. From the intensity and the direction of the internal reaction forces, the softest segment can be extrapolated; the first segment to close will be possibly the one where the largest tension reaction forces occur. Nonetheless, in practice, the numerical experiments has shown that is it always the middle segments that close first in the simulation.

3.4 Summary of the investigation of simplified planar models

For the preparation of investigating antiprismatic deployable structures, a two dimensional deployable structure having similar packing behavior was identified and analyzed. Firstly the packing of the basic segment of the mast was analyzed. Through the kinematical, equilibrium and constitutive equations the force-displacement diagram was deduced associated with the function:

$$N(u) = \frac{EA}{r_0} \left(1 - \frac{2}{\sqrt{4 + \frac{h_0 u - u^2/4}{(r_0)^2}}} \right) \left(h_0 - \frac{u}{2} \right)$$

The initial and the closed configurations both correspond to zero force. While the former being a stable state the latter is an unstable one. The given diagram exhibits an instability phenomenon, which occurs at the critical height:

$$u_{cr} = 2h_0 \pm 2r_0 \sqrt{\left(\frac{h_0}{r_0}\right)^2 - \left[2\left(\frac{h_0}{r_0}\right)^2 + 8\right]^{2/3} + 4}$$

After clarifying the mechanical behavior, the packing of the multi-storey masts were analyzed. Two different type of mast was defined. One is called 'alternately stiffened' which is constructed by piling the basic segment on top of each other and the other is called 'non-stiffened' which is corresponds to the same topology but all the horizontal stiff bars are replaced by elastic ones.

It was shown that the behavior of the 'alternately-stiffened' mast can be calculated from the behavior of its basic segments. In case of perfectly identical physical and geometrical parameters the mast can be packed with a uniform packing pattern, that is, the segments can close simultaneously. Nevertheless, this hypothesis is not realistic and consequently, the typical equilibrium path corresponds to a bifurcated one. A method to construct the typical force-displacement diagram is provided with and without taking the self-weight into account.

From the construction method of the force-displacement diagram the critical segment number was deduced:

$$k_{cr} = \frac{1}{1 - \sqrt{1 - \left[2\frac{r_0}{h_0} + 8\left(\frac{r_0}{h_0}\right)^3\right]^{2/3} + 4\left(\frac{r_0}{h_0}\right)^2}}$$

If the number of analyzed segments was more than k_{cr} sudden intermediate nodal displacements, exceeding the initial height of the basic segment, is sure to take place during packing, assuming that no segments close simultaneously. However, smaller internal snapping already occurs for segment-number more than two.

The 'post-packed phenomenon' was defined and presented which may withhold the structure from complete packing and consequently it is to be avoided. Packing sequences and equilibrium paths have been presented for both the restricted and the non-restricted case. The restricted simulation means restraining the model from disengaging from the completely closed configuration during packing, that is, with restricted simulation the structure is kept from the post-packed phenomenon.

The basic segment of a 'non-stiffened' mast is half of the one of the 'alternately stiffened' one. It was proved that the 'non-stiffened' mast can only be completely packed in the case of even number of segments.

Numerical simulations of the basic segment and the two types of multi-storey structures were carried out. Different control possibilities have been presented for the investigation of packing behavior.

For 'alternately stiffened' masts, the uniform and the successive control were offered by guiding the boundary nodes of each segment. The typical path can be traced by introducing physical imperfections and controlling only the displacement of the top nodes. In the case of the latter option, restraining the structure from 'post-packed phenomenon' is necessary. This was simulated with a penalty method by pairing the end nodes of the rigid bars one under the other. The induced contact force is disproportional to the distance in between the paired nodes and keeps the segments from disengaging from the closed configuration.

For 'non-stiffened' masts, the uniform packing control can be simulated by guiding all the nodes. This type of control is rather abstract, but served with some valuable results about the behavior of these structures. Firstly, it was revealed that non-stiffened masts can be only packed completely if the number of the segments is even. Secondly, the internal reaction forces can give general idea about the softness of the different segments. The ones, which have to be drowned out during uniform packing is softer, the one that is compressed by these internal forces are stiffer.

It is presented that the successive packing of the structure is only possible, when restraints are put in between each level of elastic horizontal bars.

The influence on the critical force by the segment-number was also investigated. It was shown that by replacing the stiff horizontal bars with elastic bars, the structure is softened, that is, the critical force decreases. With the increment of the segment-number the critical force decreases. This decrement, with the increment of the number of the segments, is heading to a constant value, which is approximately the half of the critical force of the 'alternately stiffened' mast.

4 ANALYSIS OF ANTIPRISMATIC DEPLOYABLE LATTICE STRUCTURES

4.1 General characteristics

An antiprism is a polyhedron composed of two parallel, identical polygons connected by triangles. Antiprisms are similar to prisms except the two polygons are twisted relative to each other and thus the lateral faces are not quadrilaterals but triangles (Fig. 4.1a). A regular antiprism is formed with a $180/n$ degree of twisting angle between the two n -sided polygons. Concerning mechanical behavior of space truss systems generated from the edges of a regular antiprism the results are rather fascinating. Tarnai had shown that a space truss generated from even sided regular antiprism is a finite mechanism while the ones from odd sided antiprisms are rigid forms [Tarnai, 2001]. Nevertheless, by building stable truss units (formed from odd sided antiprisms) on top of each other, forming a cylindrical truss, small displacements of boundary joints at the bottom grow exponentially along the height [Hegedűs, 1986]. Consequently it is rather to be avoided to apply such regular antiprismatic trusses for conventional engineering applications without any additional stiffening. Nonetheless, this geometry can serve for the construction of a very interesting pop-up mast.

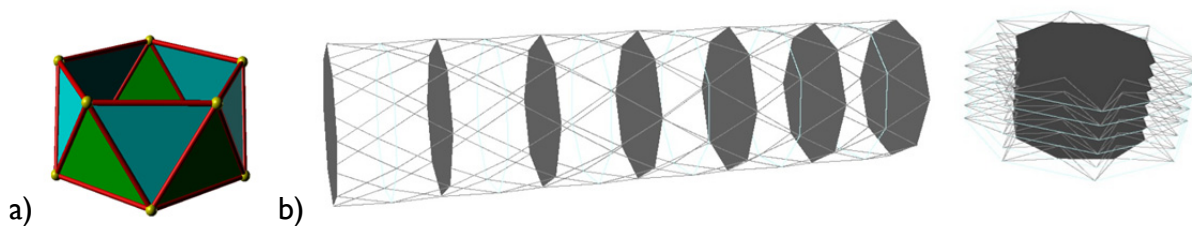


Fig. 4.1: a) Regular pentagonal antiprism; b) deployable mast offered by Hegedűs [Farkas, Friedman et al., 2011/7]

The deployable cylindrical column offered by Hegedűs [1993], shown on Fig. 4.1b, consists of rigid panels (octagonal panels in the figure) and rigid and elastic bars (drawn with continuous and dashed lines respectively). The mast is packed with pushing the top polygonal panel in the vertical direction. With a uniform cyclic symmetric folding the elastic bars are stretching out and the parallel polygonal panels are pushed together. It is true that the structure cannot be controlled by a single axial force [Hegedűs, 1993], but with a careful symmetry control the structure can be packed to a theoretically planar truss. In this packed configuration the structure is in equilibrium without any external forces. This state of self-stress is not a stable position, consequently with a small perturbation the structure can snap back to the initial, deployed, strain-free configuration.

4.2 Mechanical characteristics – analytical investigation

4.2.1 Analysis of the basic unit

Kinematical equations

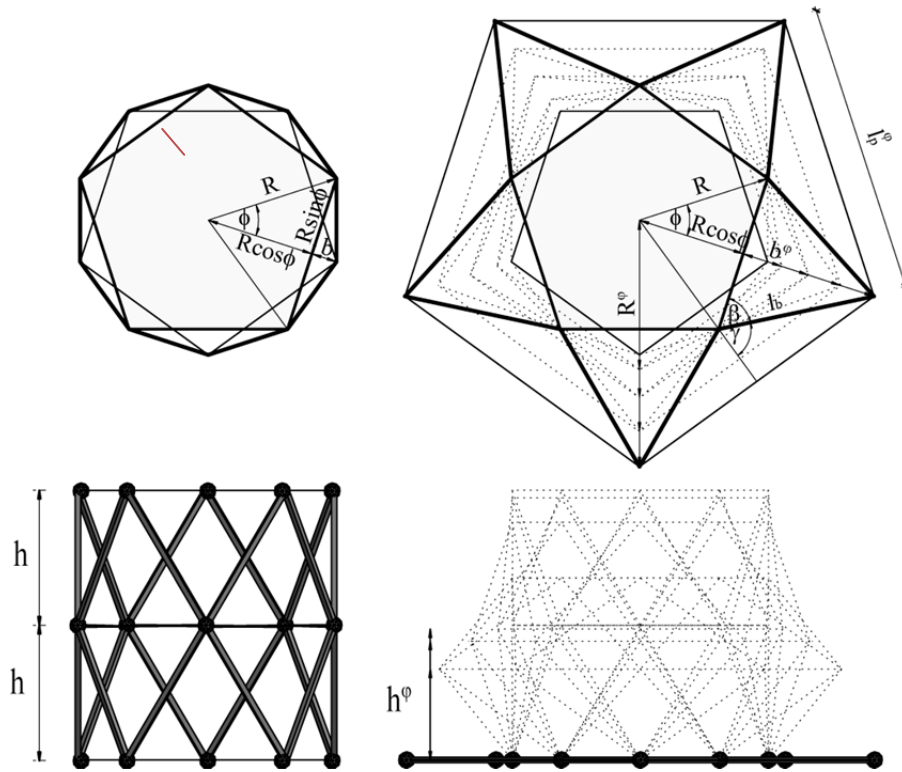


Fig. 4.2: Planar and side view of initial (deployed) configuration (on the left) and final (packed) configuration (on the right)

Let's consider one single deployable unit of the analyzed antiprismatic truss system built from two segments of height h , consisting of three, initially congruent regular n -gons with tangential circle of radius R . The length of each horizontal bar in the reference, deployed state is

$$l_p = 2R \sin \phi \tag{4.1}$$

with

$$\phi = 180^\circ/n \tag{4.2}$$

The length of the rigid bracing bars is:

$$l_b = \sqrt{h^2 + R^2 \sin^2 \phi + (R - R \cos \phi)^2} = \sqrt{h^2 + 2R^2 (1 - \cos \phi)} \tag{4.3}$$

Similarly to the planar model, the antiprismatic structure has an asymmetric freedom of motions as well [Hegedűs, 1993] (Fig. 4.3). Despite this fact, from now on, in the analysis only cyclic symmetrical packing will be considered. However, it is important to mention that

the results deduced herein are only true in case of being able to control the movement of the structure in a way that this assumption is not violated.

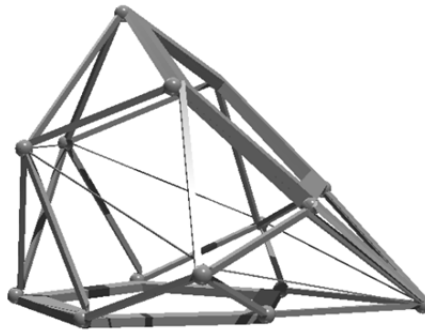


Fig. 4.3: Asymmetric freedom of motion of antiprismatic structures

During packing, the joints of the boundary polygons (the one on the top and the one on the bottom) are horizontally fixed, thus the length of their horizontal bars is constant. Furthermore, if we assume that the bracing bars are perfectly rigid (incompressible) and that the folding is uniform and has cyclic symmetry, the current length of the bars of the middle polygon stretches out during packing to:

$$l_p^\varphi(R^\varphi) = 2R^\varphi \sin \phi \tag{4.4}$$

where R^φ is the actual radius of the tangential circle of the middle, expanding polygon which can be determined with:

$$\begin{aligned} R^\varphi(h^\varphi) &= R \cos \phi + \underbrace{\sqrt{l_b^2 - (h^\varphi)^2 - R^2 \sin^2 \phi}}_{b^\varphi} \\ &= R \cos \phi + \sqrt{h^2 - (h^\varphi)^2 + R^2(1 - \cos \phi)^2} \end{aligned} \tag{4.5}$$

The last term under square root corresponds to the length of bracing bars projected to the radius, and denoted with b_φ in Fig. 4.2.

The stretching during packing is:

$$\lambda(h^\varphi) = \frac{l_p^\varphi(h^\varphi)}{l_p} = \frac{R^\varphi(h^\varphi)}{R} = \cos \phi + \sqrt{\left(\frac{h}{R}\right)^2 - \left(\frac{h^\varphi}{R}\right)^2 + (1 - \cos \phi)^2} \tag{4.6}$$

In the completely packed configuration the bars of the middle polygon stretch out to the length:

$$l_p^\varphi|_{h^\varphi=0} = 2l_b \sin \gamma \tag{4.7}$$

where

$$\gamma = 90^\circ + \phi - \underbrace{\arccos(l_p/2l_b)}_{\beta}$$

The last term refers to the angle between the fixed polygonal bars and the bracing bars (denoted with β on Fig. 4.2) in the completely packed configuration.

Equation (4.7) can also be written from equation (4.4) and (4.5) by substituting $h_\varphi = 0$:

$$l_p^\varphi|_{h_\varphi=0} = 2R^\varphi|_{h_\varphi=0} \sin \phi = 2R \cos \phi \sin \phi + 2 \sin \phi \sqrt{h^2 + R^2(1 - \cos \phi)^2} \quad (4.8)$$

The final stretching of the polygonal bars:

$$\lambda_{max} = \lambda|_{h_\varphi=0} = \cos \phi + \sqrt{\left(\frac{h}{R}\right)^2 + (1 - \cos \phi)^2} \quad (4.9)$$

In practical design, when considering rational values of h/R , equation (4.9) can reasonably be simplified to a linear connection (Fig. 4.4). The value of $(1 - \cos \phi)^2$ is always small, and depends on the angle ϕ that depends further on the number of the sides of the polygon, n (see equation (4.2)). It reaches its maximal value in the case of triangular antiprismatic segment. As for practical consideration triangular and even-sided antiprisms will be avoided, the maximum value is $(1 - \cos \phi)^2 = 0.036$, which corresponds to a pentagonal unit. Let's consider only a reasonable domain of h/R :

$$0,5 \leq h/R \leq 2 \quad (4.10)$$

Even in the case of the minimal value of this domain, $(h/R)^2$ will be one order greater than $(1 - \cos \phi)^2$. Accordingly, for a preliminary estimation the latter one can be neglected, which leads to a simple linear approximation (Fig. 4.4) of equation (4.9):

$$\hat{\lambda}_{max} = \frac{h}{R} + \cos \phi \quad (4.11)$$

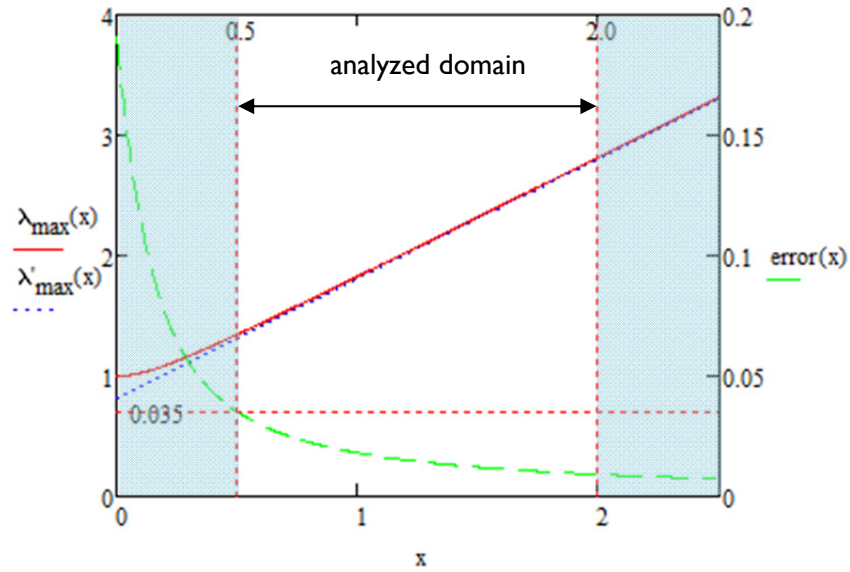


Fig. 4.4: Linear approximation for final stretching of elastic bars ($\lambda_{max} = \hat{\lambda}_{max}$) of pentagonal ($n=5$) antiprismatic unit in function of the height-radius ratio ($x=h/R$) (exact function (4.9) with continuous line ($\lambda_{max}(x)$), approximation of stretching (4.11) with dotted line ($\lambda'_{max}(x)$), error of the approximation with dashed line)

The error of this estimation can be calculated from:

$$error\left(\frac{h}{R}\right) = \lambda_{max} - \hat{\lambda}_{max} \tag{4.12}$$

The maximum value of (4.12) is at the lower boundary of the domain (see Fig. 4.4), that is at $h/R = 0.5$, and obviously the more sides the polygon has the least the error is (see Table 4.1 and Fig. 4.5)

highest error of approximation (at $h/R=0.5$)					
n-gon	λ_{max}	λ_{max} approx	error ($\lambda_{max} - \lambda_{max}$ approx)	error/ λ_{max}	error/ ϵ
5	1.344	1.309	0.035	2.62%	10.235%
7	1.411	1.401	0.010	0.69%	2.365%
9	1.443	1.440	0.004	0.25%	0.817%
11	1.461	1.459	0.002	0.11%	0.355%
13	1.472	1.471	0.001	0.06%	0.179%

Table 4.1: Highest error of the linear approximation for final stretching of elastic bars ($\hat{\lambda}_{max}$) for different odd sided n-gons

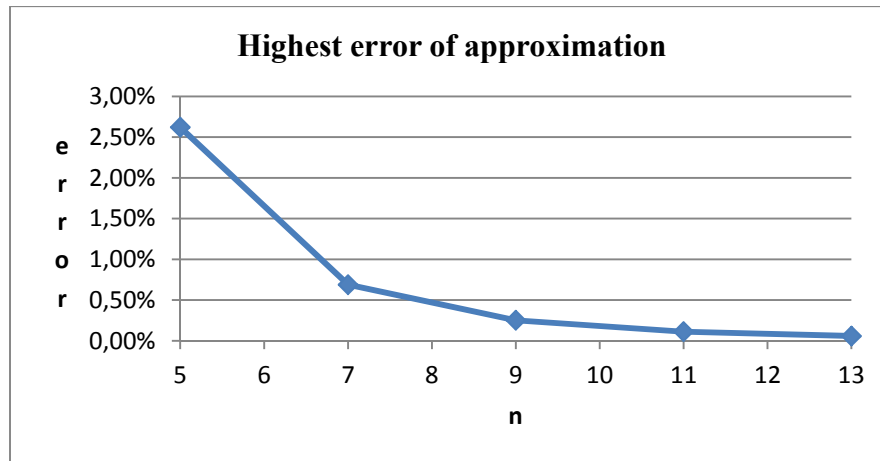


Fig. 4.5: Highest (at $h/R = 0.5$) error of the linear approximation for final stretching of elastic bars ($\hat{\lambda}_{max}$) for different odd sided n -gons

This simplified linear equation can serve for the preliminary stage of design and for a good verification of results coming from the numerical analysis. Nevertheless, using the simplified equation in the case of small h/R ratio (smaller than 0.5) the stretching is highly underestimated. This error in case of pentagonal unit reaches 10% for $h/R = 0.1$ which leads to a completely fallacious result giving compression in the bars instead of stretching.

Equilibrium equation

For packing the structure, a vertical force N is applied at the top horizontal polygon (Fig. 4.6) with a symmetrical distribution, that is, the load is $N_p = N/n$ at each vertex. The elastic bars of the middle polygon are tensioned by the rigid bracings coming from the top and bottom facet of the unit. With the assumption of cyclic symmetrical packing this tension force in the bars will be:

$$S_p(h^\varphi) = \frac{2N}{n} \cdot \underbrace{\frac{R^\varphi(h^\varphi) - R \cos \phi}{h^\varphi}}_{S_r} \cdot \frac{1}{2 \sin \phi} \quad (4.13)$$

Where S_r denotes the horizontal radial projection of the four compression forces coming from the bracings (Fig. 4.6).

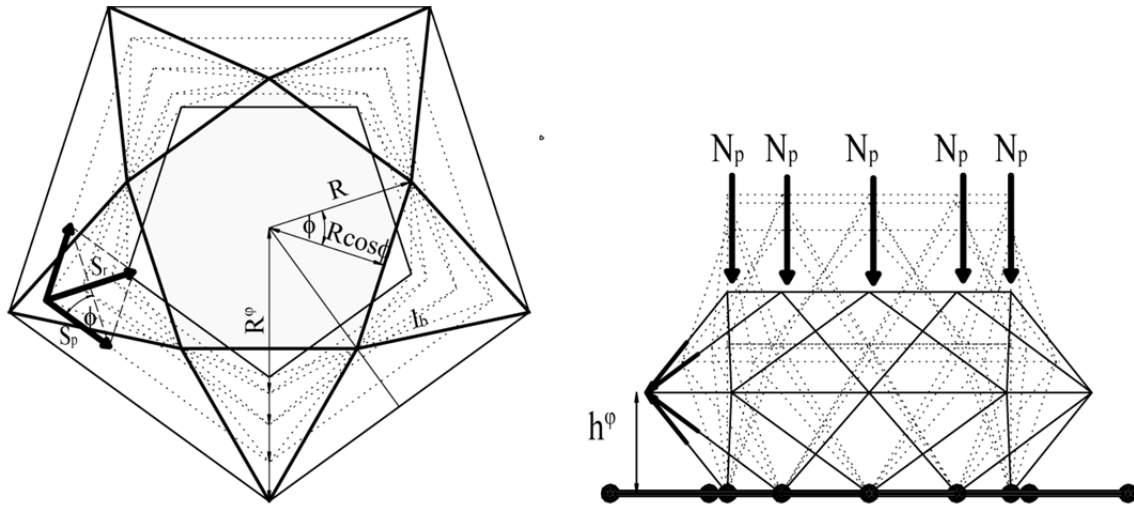


Fig. 4.6: Equilibrium of basic deployable unit

Constitutive equation

Similarly to the methodology for 2D simplified model for the sake of simplicity only the hypothesis of linear elasticity will be assumed in the analytical approach, that is, the strain in the elastic polygonal bars is:

$$\varepsilon(h^\varphi) = \lambda(h^\varphi) - 1 = \frac{S_p(h^\varphi)}{EA} \tag{4.14}$$

where λ denotes the stretching that is the ratio of actual extended length and initial length of the elastic bar.

Equilibrium path

Combining equilibrium (4.13) constitutive (4.14) and kinematic (4.5-6) equations, the force-displacement diagram can be written in the form:

$$N(h^\varphi) = \frac{nS_p(h^\varphi)h^\varphi \sin \phi}{R^\varphi(h^\varphi) - R \cos \phi} = \frac{nEA[\lambda(h^\varphi) - 1]h^\varphi \sin \phi}{R^\varphi(h^\varphi) - R \cos \phi}$$

$$N(h^\varphi) = nEA \frac{h^\varphi}{R} \sin \phi \left[\frac{\cos \phi - 1}{\sqrt{\left(\frac{h}{R}\right)^2 - \left(\frac{h^\varphi}{R}\right)^2 + (1 - \cos \phi)^2}} + 1 \right]$$

(4.15)

Or in function of the displacement of the top nodes:

$$N(u) = nEA \left(\frac{h}{R} - \frac{u}{2R} \right) \sin \phi \left[\frac{\cos \phi - 1}{\sqrt{\left(\frac{h}{R}\right) \left(\frac{u}{R}\right) - \frac{1}{4} \left(\frac{u}{R}\right)^2 + (1 - \cos \phi)^2}} + 1 \right]$$

This equilibrium path is plotted in Fig. 4.7, and the diagram proves that similarly to the simplified 2D model, the 3D antiprism goes through an unstable phase during packing, that is, after reaching the critical force or the critical height the increment of displacement of top nodes corresponds to a decrement of force. In practice this means, if no displacement control is carried out, after the critical force, the structure snaps to the final packed configuration.

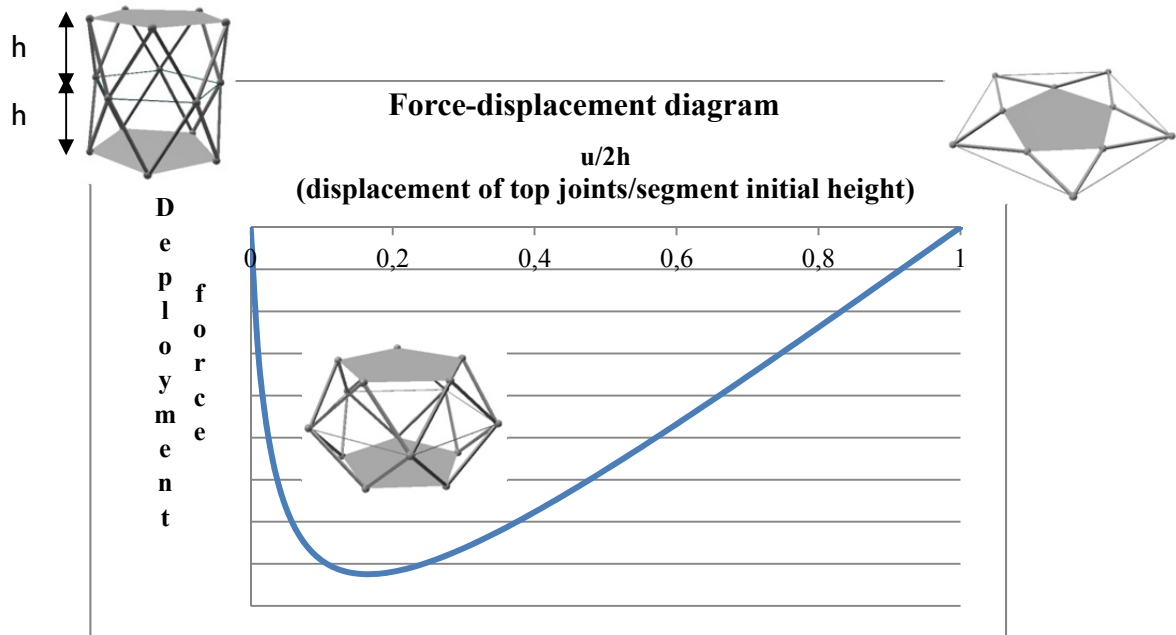


Fig. 4.7: Equilibrium path of basic deployable unit

Similarly to the planar structure the force-displacement diagram of the three dimensional deployable unit could theoretically be continued if the top segment is pushed further. This phenomenon is exactly of the same type as described for the planar structure; the structure ends up in a reversed, upside down version of its initial geometrical configuration which corresponds to zero force and is stable. This phenomenon is to be avoided because of the failure of complete packing. However, this kind of intersection of the elements during packing in practice is not really possible. Nonetheless, in the case of antiprismatic structures another freedom of motion appears at the completely packed configuration. The folded bracings can flip together up [Hegedűs, 1993] allowing the lengthened elastic bars relaxing (Fig. 4.8). This freedom of motion can not only happen theoretically but also in practice, consequently, careful joint design is to be performed to avoid this possibility. Analogously to the definition provided at the analysis of planar structures, these two phenomena (continuing in a reversed configuration and the flipping up of the bracings) will be furthermore called 'post-packed phenomena'.



Fig. 4.8: Post-packed phenomenon: flipping up the bracings

Calculation of critical state

Assuming cyclic symmetrical folding, the 3D structure's motion can be written with a single geometrical parameter. Let that parameter be h^φ . The critical equilibrium state corresponds to the zero value of tangent stiffness that is:

$$\frac{dN}{dh^\varphi} = 0 \quad (4.16)$$

Introducing the function:

$$g(h^\varphi) := \sqrt{\left(\frac{h}{R}\right)^2 - \left(\frac{h^\varphi}{R}\right)^2 + (1 - \cos \phi)^2} \quad (4.17)$$

$$N(g(h^\varphi), h^\varphi) = \frac{nEA \sin \phi}{R} \cdot \frac{[\cos \phi + g(h^\varphi) - 1]h^\varphi}{g(h^\varphi)} \quad (4.18)$$

$$\frac{dN}{dh^\varphi} = \frac{nEA \sin \phi}{R} \left[\frac{[\cos \phi + g(h^\varphi) - 1]g(h^\varphi) - [\cos \phi - 1]h^\varphi g'(h^\varphi)}{g^2(h^\varphi)} \right]$$

where

$$g'(h^\varphi) = \frac{dg(h^\varphi)}{dh^\varphi} = \frac{-h^\varphi}{R^2 g(h^\varphi)} \quad (4.19)$$

$$\frac{dN}{dh^\varphi} = \frac{nEA \sin \phi}{R} \cdot \left\{ \frac{[\cos \phi - 1]g(h^\varphi)}{g^2(h^\varphi)} + \frac{[\cos \phi - 1]h^\varphi^2}{R^2 g^3(h^\varphi)} + 1 \right\}$$

Bringing the first two fractions in the parenthesis to common denominators and substituting equation (4.17) in the nominator:

$$\frac{dN}{dh^\varphi} = \frac{nEA \sin \phi}{R} \cdot \left\{ \frac{[\cos \phi - 1][h^2 + R^2(1 - \cos \phi)^2]}{R^2 g^3(h^\varphi)} + 1 \right\}$$

Hence the critical values of h^φ can be calculated from the equation:

$$\frac{dN}{dh^\varphi} = 0 \Rightarrow (\cos \phi - 1) \left[\left(\frac{h}{R} \right)^2 + (1 - \cos \phi)^2 \right] + g^3(h^\varphi) = 0 \quad (4.20)$$

Substituting equation (4.17) in the last expression the critical height of the structure can be calculated from:

$$x_{cr}^2 = \left(\frac{h_{cr}^\varphi}{R} \right)^2 = x^2 + (1 - \cos \phi)^2 - \{(1 - \cos \phi)[x^2 + (1 - \cos \phi)^2]\}^{2/3}$$

with

$$x = h/R \quad (4.21)$$

Similar to the case of approximating the final stretching we can assume that both $(1 - \cos \phi)^2$ expressions can be neglected. In this case equation (4.21) can be simplified to:

$$\widehat{x}_{cr}^2 = \left(\frac{h}{R} \right)^2 + (\cos \phi - 1)^{2/3} \left(\frac{h}{R} \right)^{4/3} \quad (4.22)$$

For a nicer and still rational approximation (Figs. 4.10-11) of the square root of equation (4.21) the critical height per radius ratio can be approximated with the Taylor formula up to the first order around the point $h/R = 1$ which gives the linear approximation:

$$\overline{x}_{cr} = a + b \frac{h}{R} \quad (4.23)$$

Constants for linear approximation of critical height/radius ratio		
n-gon	a	b
5	-0.1015	0.9362
7	-0.0711	0.9624
9	-0.0522	0.9739
11	-0.0403	0.9802
13	-0.0323	0.9843
15	-0.0267	0.9870
17	-0.0225	0.9890
19	-0.0194	0.9905

Table 4.2: Constants for linear approximation of critical height/radius ratio

The constants a and b depend only on the angle ϕ that is on n , the number of vertex of the polygon and can be calculated from the equation (4.21) and its derivative:

$$a = x_{cr}|_{x=1} - \left. \frac{dx_{cr}}{dx} \right|_{x=1}; \quad b = \left. \frac{dx_{cr}}{dx} \right|_{x=1} \tag{4.24}$$

The values for constants a and b are listed on table 4.2 and plotted on Fig. 4.9.

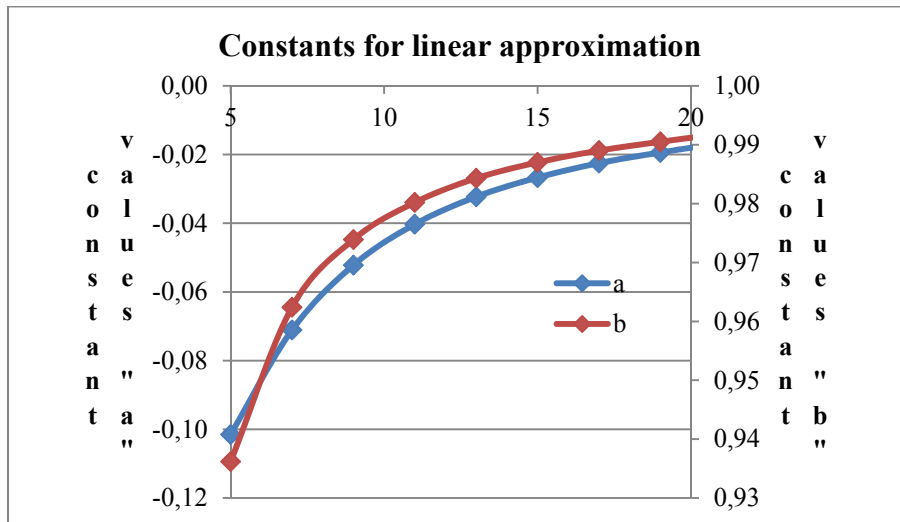


Fig. 4.9: Constants for linear approximation of critical height/radius ratio

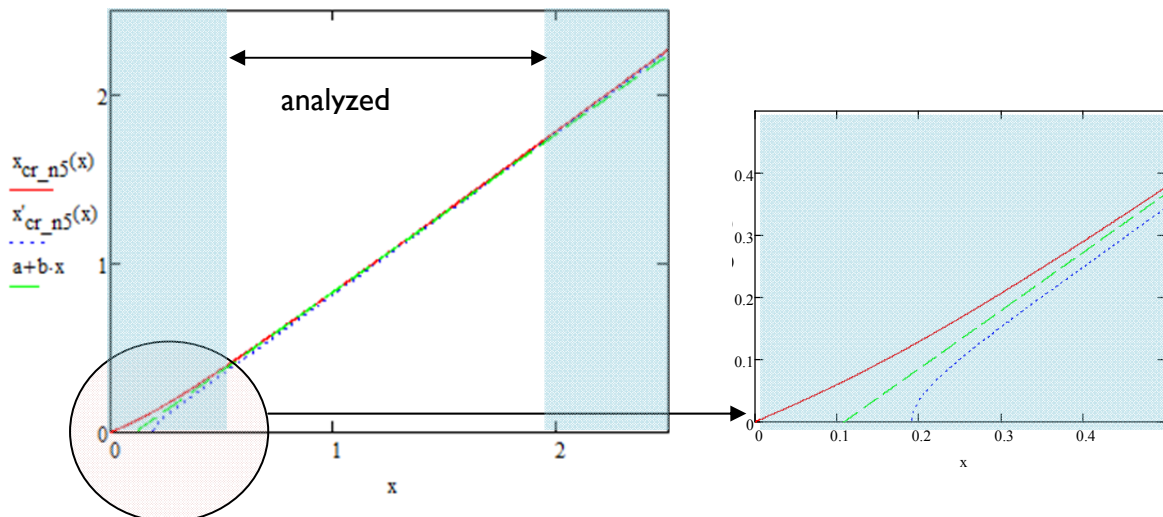


Fig. 4.10: Approximation of critical height: critical height/critical radius ($x_{cr} = h_{cr}/R$) in function of initial height/initial radius ($x = h/R$), for pentagonal segment — exact solution with continuous line, approximation in accordance with (4.22) with dotted line, approximation in accordance with (4.23) with dashed line

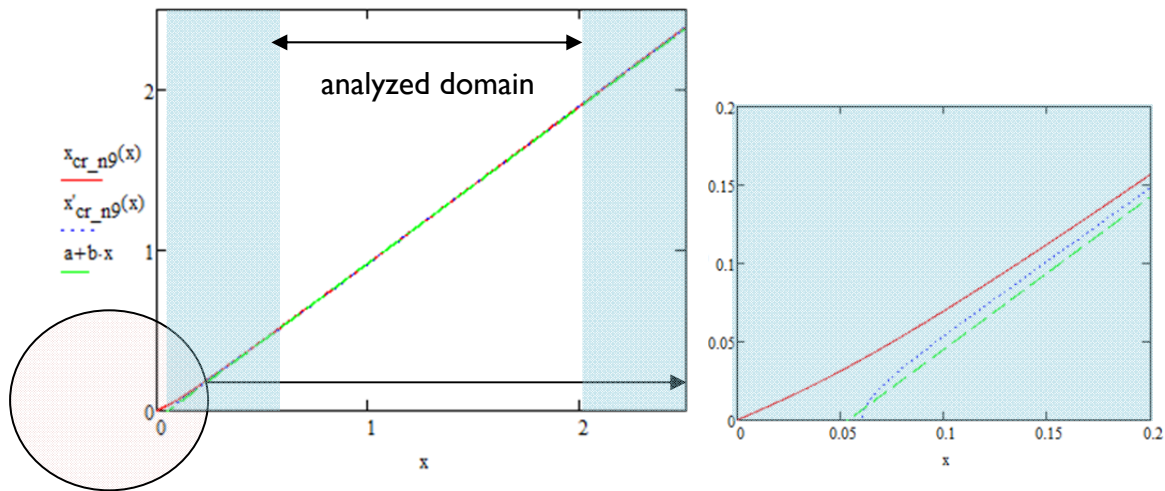


Fig. 4.11: Approximation of critical height: critical height/critical radius ($x_{cr} = h_{cr}/R$) in function of initial height/initial radius ($x = h/R$), for 9-gonal segment — exact solution with continuous line, approximation in accordance with (4.22) with dotted line, approximation in accordance with (4.23) with dashed line

It can be seen from the two diagrams shown on Fig. 4.10-4.11 that depending on the actually analyzed geometry (that is, on n and h/R) in some cases it is the approximation described in 4.22 and in some cases it is the one described in 4.23 that approximates better the exact value. Both equations underestimate the exact value. However, for domains described in (4.10) the offered linear equation gives an acceptable and simple preliminary estimation of the critical height.

The critical force from equations (4.16) (4.17) and (4.19), (4.21):

$$N_{cr}(x, \phi) = nEA \sin \phi \cdot \left(\sqrt[3]{\frac{-c^2}{hc}} + 1 \right) \sqrt{hc - (c \cdot hc)^{2/3}} \tag{4.25}$$

where

$$c = (1 - \cos \phi); \quad hc = (x)^2 + (1 - \cos \phi)^2 \tag{4.26}$$

Plotting equation 4.25 (Fig. 4.12) it can be seen that considering only the domain given in (4.10) the critical force can be also estimated with a linear approximation. Linearizing with the help of the Taylor formula up to the first order around the point $x = h/R = 1$:

$$\overline{N_{cr}} = EA(d + ex) \tag{4.27}$$

The constants d and e depend only on the angle ϕ , that is, on the number of vertices of the polygon (n), and can be calculated from the equation (4.25) and its derivative:

$$d = N_{cr}|_{x=1} - \left. \frac{dN_{cr}}{dx} \right|_{x=1}; \quad e = \left. \frac{dN_{cr}}{dx} \right|_{x=1} \tag{4.28}$$

The values for constants d and e are listed and the error of the approximation at the boundaries of the analyzed domain are given in table 4.3 and plotted on Fig. 4.13.

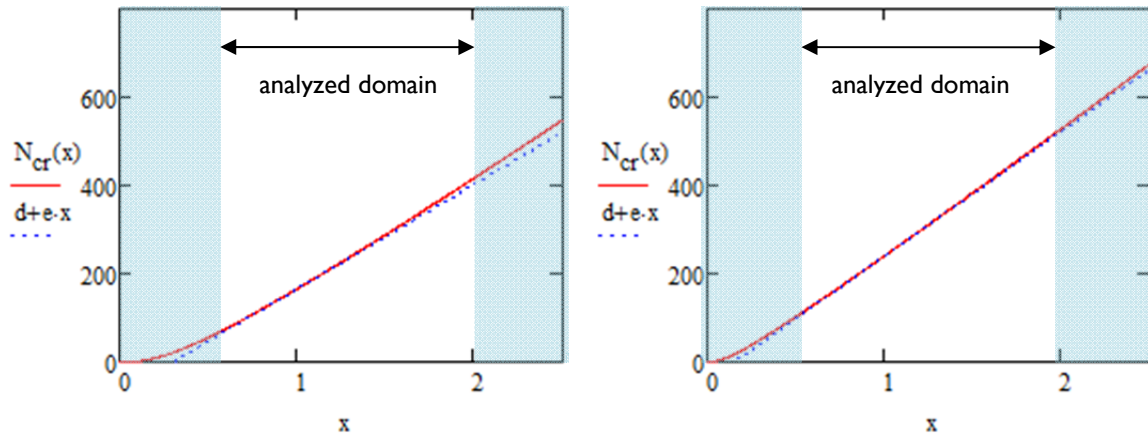


Fig. 4.12: Approximation for the critical force: critical force (N_{cr}) in function of initial height/initial radius ratio ($x = h/R$), for pentagonal (on the left) and for 9-gonal segment (on the right) — exact solution with continuous line, linear approximation with dotted line ($EA=100$)

Constants for linear approximation of critical force				
n-gon	d	e	error at $h/R=0,5$	error at $h/R=2,0$
5	-0.71760	2.36700	15.45%	3.44%
7	-0.55125	2.68066	5.91%	1.74%
9	-0.42549	2.82679	3.26%	1.10%
11	-0.33863	2.90828	2.15%	0.79%
13	-0.27736	2.95922	1.57%	0.61%

Table 4.3: Constants for linear approximation of critical force and the error of approximation at the boundaries

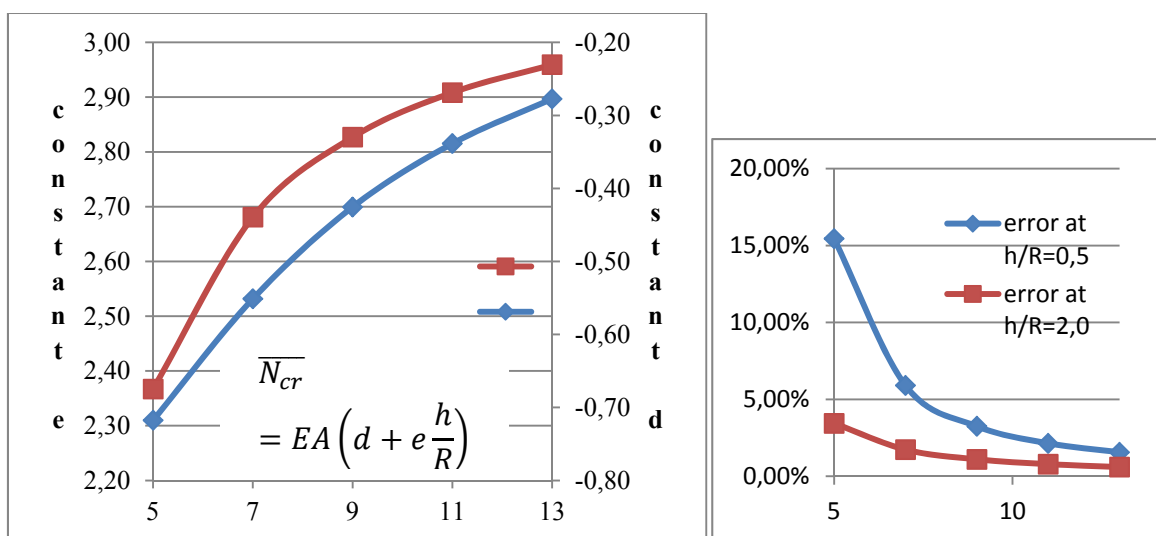


Fig. 4.13: Constants for linear approximation of critical force and the error of approximation at the boundaries

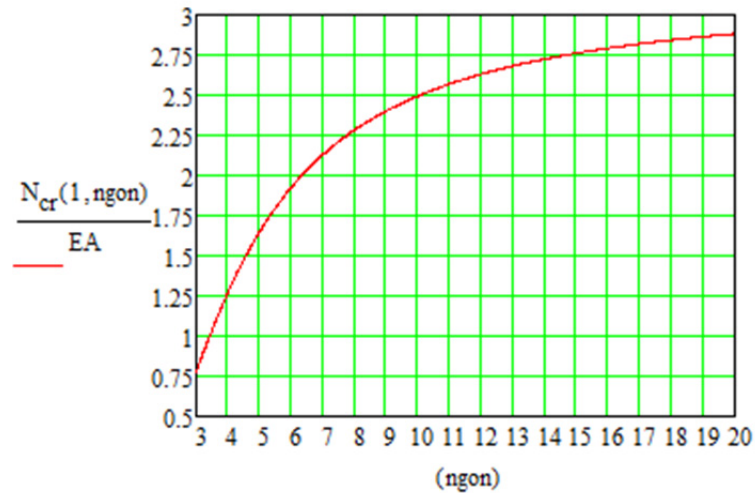


Fig. 4.14: Critical force (N_{cr}) in function of the number of vertex of the polygon for $h/R = 1$

4.2.2 Analysis of ‘alternately stiffened’ multi-storey structure

The ‘alternately stiffened’ mast is built from cascading the basic units analyzed above (Fig. 4.15). The methodology to construct the equilibrium paths of the ‘alternately stiffened’ mast is identical to the one used for simplified planar structure. The force-displacement diagram of the uniform and successive packing is presented in Fig. 4.16 and the associated packing sequences is shown for a two-storey structure in Fig. 4.17.

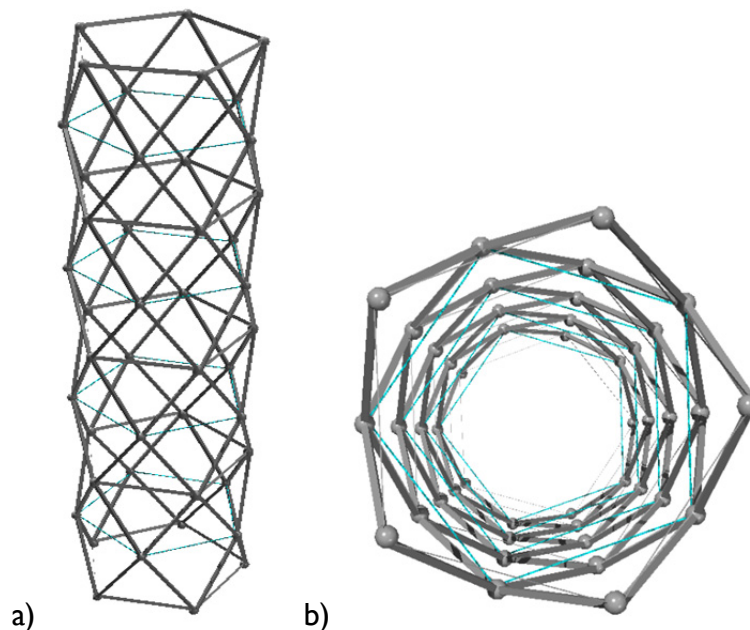


Fig. 4.15: 3D view of ‘alternately stiffened’ antiprismatic mast a) from the side and b) from the top

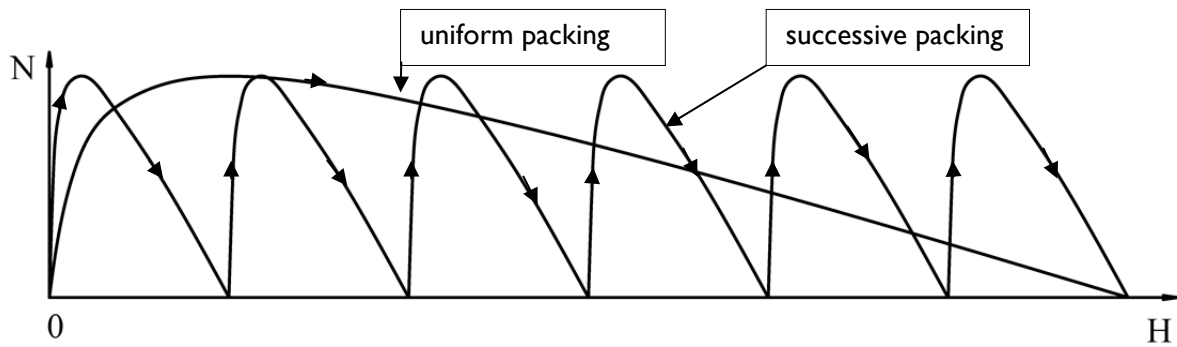


Fig. 4.16: Force-displacement diagram in the case of successive and uniform packing— restricted packing of antiprismatic deployable mast of six segments (notation: H : total height, u : displacement of the top nodes, N : packing force)

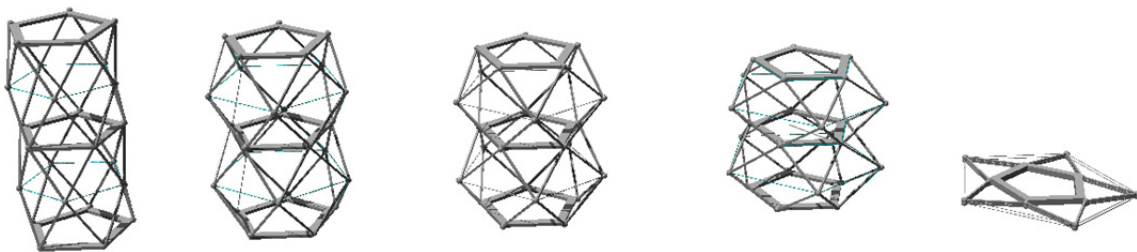


Fig. 4.17: Uniform restricted packing of antiprismatic deployable mast of two segments

The uniform packing is only possible for a perfect structure; the non-simultaneous closure can be mentioned as typical. The bifurcated equilibrium path is constructed in Fig. 4.18 assuming that each antiprismatic unit closes separately.

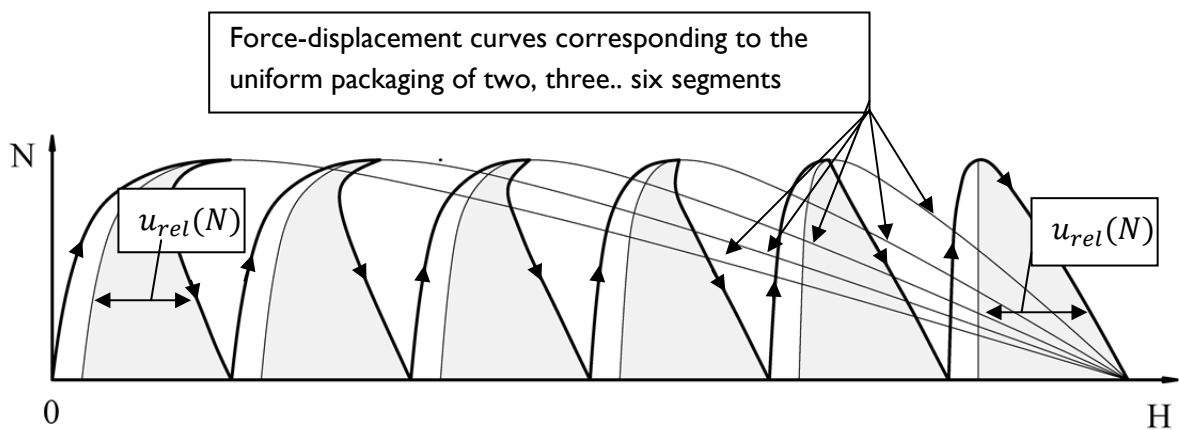


Fig. 4.18: Typical force-displacement diagram — restricted packing of antiprismatic deployable mast of six segments (notations: H : total height, u : displacement of the top nodes, N : packing force)

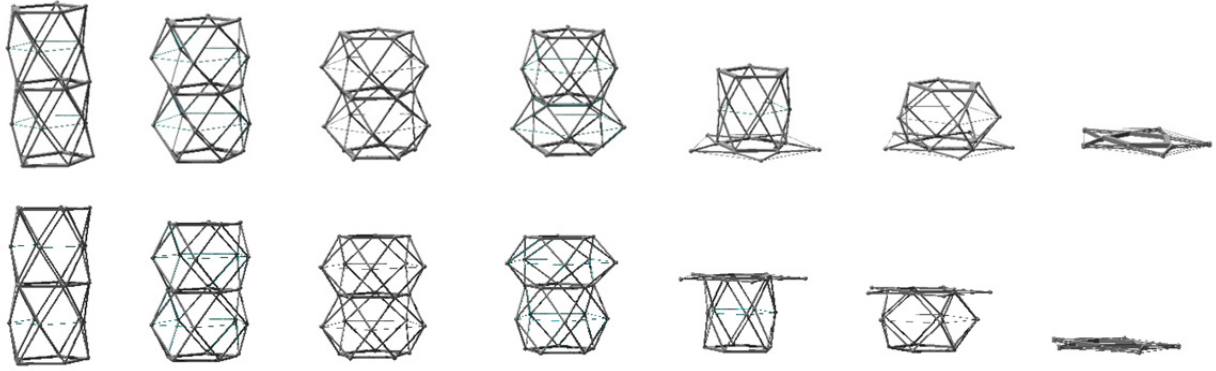


Fig. 4.19: Typical restricted packing sequences of antiprismatic deployable mast of two segments

The typical force-displacement diagram constructed in Fig. 4.18 somewhat differs from the diagram shown in Fig. 3.9 as the asymmetry of the force-displacement diagram of the herein analyzed structure is more emphasized. The already defined critical segment number (see equation (3.50)) can be calculated for antiprismatic structures, too.

$$k_{cr} = \frac{2h}{u_{cr}} = \frac{2h}{2(h - h_{cr}^{\varphi})} = \frac{1}{(1 - h_{cr}^{\varphi}/h)} \quad (4.29)$$

Substituting equation (4.21) in (4.29):

$$k_{cr} = \frac{1}{(1 - h_{cr}^{\varphi}/h)} = \frac{1}{1 - \frac{R}{h} \sqrt{x^2 + (1 - \cos \phi)^2} - \{(1 - \cos \phi)[x^2 + (1 - \cos \phi)^2]\}^{2/3}} \quad (4.30)$$

or using the approximation in (4.23):

$$\overline{k_{cr}} = \frac{1}{1 - \left(a \frac{R}{h} + b\right)} \quad (4.31)$$

which will give an exact value in the case of $h/R = 1$. The constants a and b are given in Table 4.2. For example, for an antiprismatic mast with $h/R = 1$, the critical segment-number is:

$$k_{cr_pent} = \frac{1}{1 - (-0.10377 + 0.9362)} = 5.96 \quad (4.32)$$

This practically means that if the number of the segments of these pentagonal units is more than two (see Chapter 3) than intermediate sudden displacements will take place during packing and if this number is more than five (k_{cr_pent}), that these sudden displacement will be larger than the height of the segment. Namely, the critical segment number only means

that if $k < k_{cr}$, than after pushing through any critical point, upward displacement of top nodes is needed in order to get to the next state which corresponds to zero force.

4.2.3 Analysis of a 'non-stiffened' k-storey structure

Investigating a non-stiffened k-storey³ structure, the set of equations is now written in function of the current radii (R^φ), which is now a vector of $k + 1$ elements:

$$\mathbf{R}^\varphi = R_i^\varphi \quad (i = 0..k), \quad R_0^\varphi = R_k^\varphi = R \quad (4.33)$$

The current height of the segments in function of the current radius of the horizontal polygons is:

$$h_i^\varphi(\mathbf{R}^\varphi) = h_i^\varphi(R_i^\varphi, R_{i-1}^\varphi) = \sqrt{l_b^2 - (R_{i-1}^\varphi \sin \phi)^2 - (R_i^\varphi - R_{i-1}^\varphi \cos \phi)^2} \quad (4.34)$$

The current stretching of the elastic bars:

$$\lambda_i(\mathbf{R}^\varphi) = \lambda_i(R_i^\varphi) = \frac{R_i^\varphi}{R} \quad (4.35)$$

The elastic polygonal bars are tensioned by the rigid bracings coming from the above and from the beneath segment. Still assuming cyclic symmetrical packing, the tension force in the bars are (see Fig.4.6):

$$S_p(\mathbf{R}^\varphi) = S_{pi}(R_{i-1}^\varphi, R_i^\varphi, R_{i+1}^\varphi) = \frac{N}{n} \left(\frac{R_i^\varphi - R_{i-1}^\varphi \cos \phi}{h_i^\varphi(R_i^\varphi, R_{i-1}^\varphi)} + \frac{R_i^\varphi - R_{i+1}^\varphi \cos \phi}{h_{i+1}^\varphi(R_i^\varphi, R_{i+1}^\varphi)} \right) \frac{1}{2 \sin \phi} \quad (4.36)$$

Combining equation (4.36) with the constitutive model in (4.14) and with the function of the stretching in (4.35), the equilibrium equation is:

$$N(R_{i-1}^\varphi, R_i^\varphi, R_{i+1}^\varphi) = 2nEA \sin \phi \frac{R_i^\varphi - R}{\frac{R_i^\varphi - R_{i-1}^\varphi \cos \phi}{h_i^\varphi} + \frac{R_i^\varphi - R_{i+1}^\varphi \cos \phi}{h_{i+1}^\varphi}} \quad (4.37)$$

which corresponds to the equilibrium equation in each level of the mast.

³ Note, that similarly to the planar structure, one storey corresponds to the half of the basic unit of an 'alternately stiffened mast. Consequently with the same h/R ratio, a k-storey 'alternately stiffened mast has the same total height as a 2k-storey non-stiffened mast

The force can also be written in function of the displacement of the top of the mast, which is:

$$u = \sum_{i=1}^k (h_0 - h_i^{\varphi}) \quad (4.38)$$

4.3 Mechanical characteristics – numerical analysis

4.3.1 Numerical analysis of the basic unit, parameter analysis

Basic assumptions, numerical model

For the numerical model truss elements were used. The axial stiffness of the bracings was defined at least of two orders higher than the one of the elastic bars. The logarithmic constitutive model was used for both type of bars. In *Appendix E*, some information are annexed about the optional constitutive models.

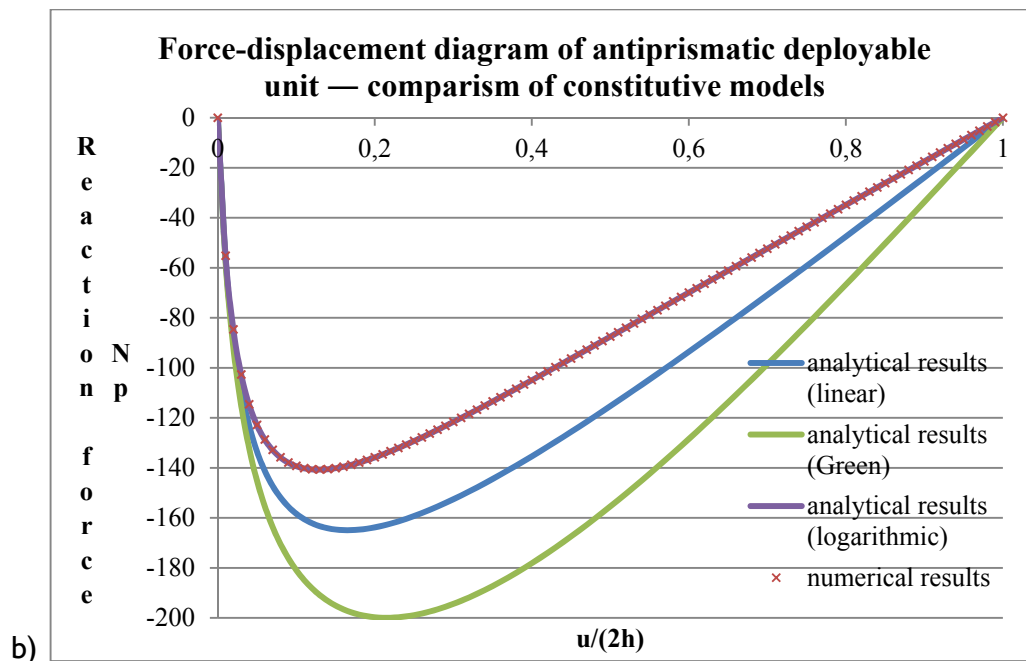


Fig. 4.20: Comparison of different constitutive models: stresses/ E in function of the stretches analytical and numerical results (pentagonal unit, $EA = 500$; $h = 0,5$; $R = 0,5$)

The force-displacement diagrams were calculated analytically with the two different constitutive models too. The results are all plotted from the different analytical solutions in *Fig. 4.20*. With both models, the force-displacement diagram deviates from the one calculated from small strain analysis, especially in the larger strain domains, but the character of the force-displacement diagram is identical to analytical results. It can be seen that the deviation is only due to the different constitutive model, the numerical errors are acceptable. The packing sequence from the simulation is plotted in *Fig. 4.21*.

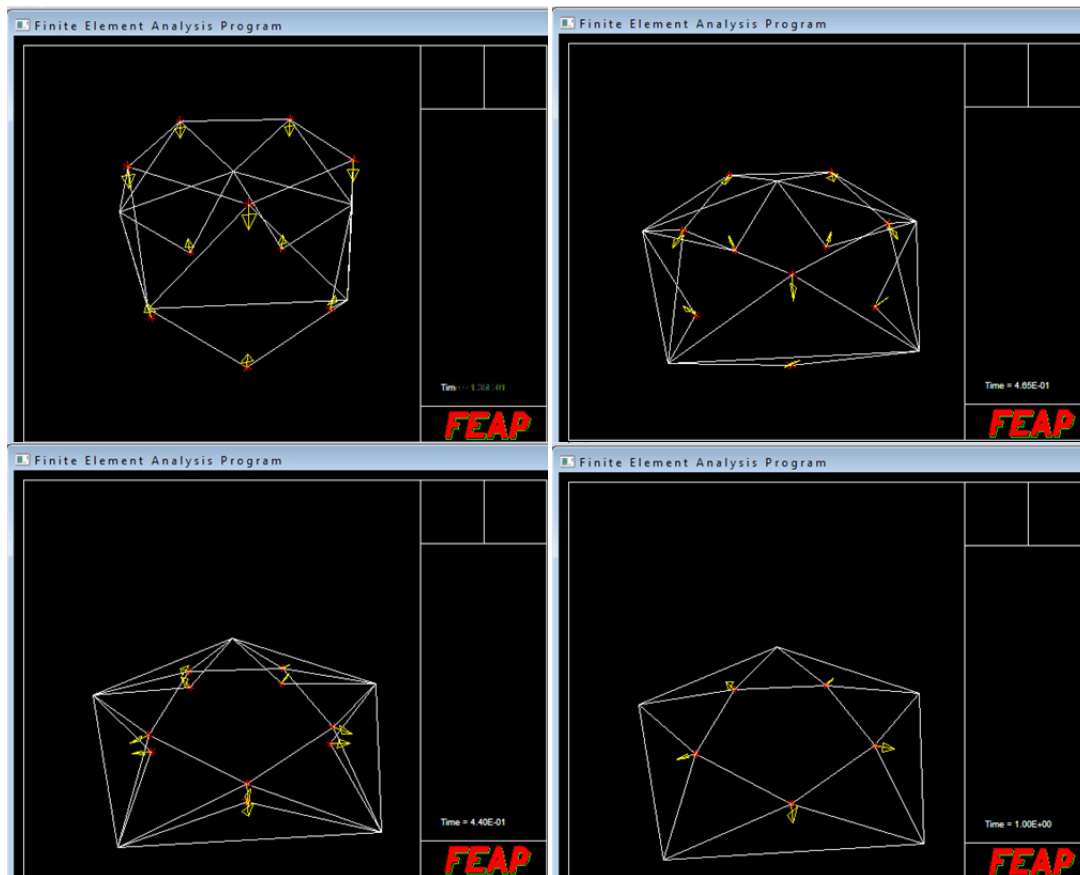


Fig. 4.21: Packing sequence of a pentagonal basic unit

The simulation of the basic unit was carried out with displacement control; the top nodes were proportionally displaced till the bottom nodes with incremental analysis.

Parameter analysis

A parameter analysis was carried out to verify the analytical results. The influence of the geometrical parameters is shown on Figs. 4.22-4.25. Fig. 4.22 shows the force-displacement diagram in the case of different n -gonal antiprismatic basic units. It can be seen from the figure that the asymmetry of the diagram grows with increasing number of vertices. This means that the critical segment number (n_{cr}) increases as well. Fig. 4.23 is in good accordance with the analytical solution plotted in Fig. 4.13. Figs 4.24 and 4.25 analyze the influence of the h/R ratio on the force-displacement diagram and the deployment force. From Fig. 4.25 it can be seen that, as the ratio grows, the asymmetry of the force-displacement diagram gets more emphasized, that is, the higher the critical segment number gets. Furthermore, Fig.4.25 proves that the linear approximation deduced from analytical results (Equation (4.27) and Fig. 4.12) is reliable.

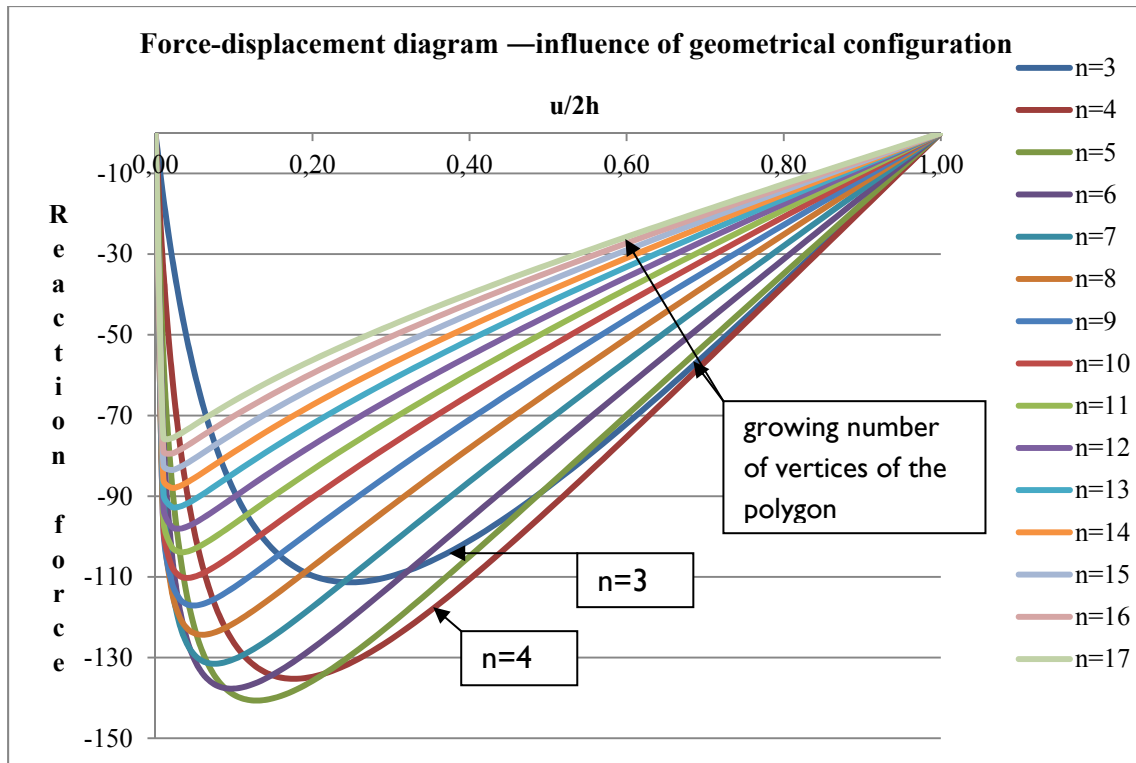


Fig. 4.22: Force-displacement diagram of basic unit in the case of different n -gons ($EA = 500; h = 0.5; R = 0.5$)

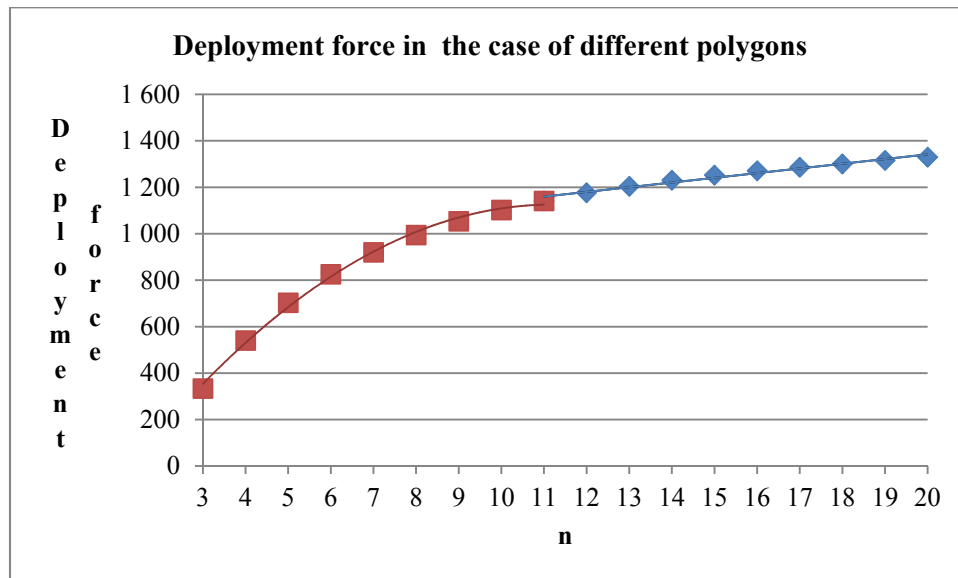


Fig. 4.23: Influence of geometrical configuration — deployment force (maximal reaction force multiplied by the number of vertices) of basic unit in case of different n -gons ($EA = 500; h = 0.5; R = 0.5$)

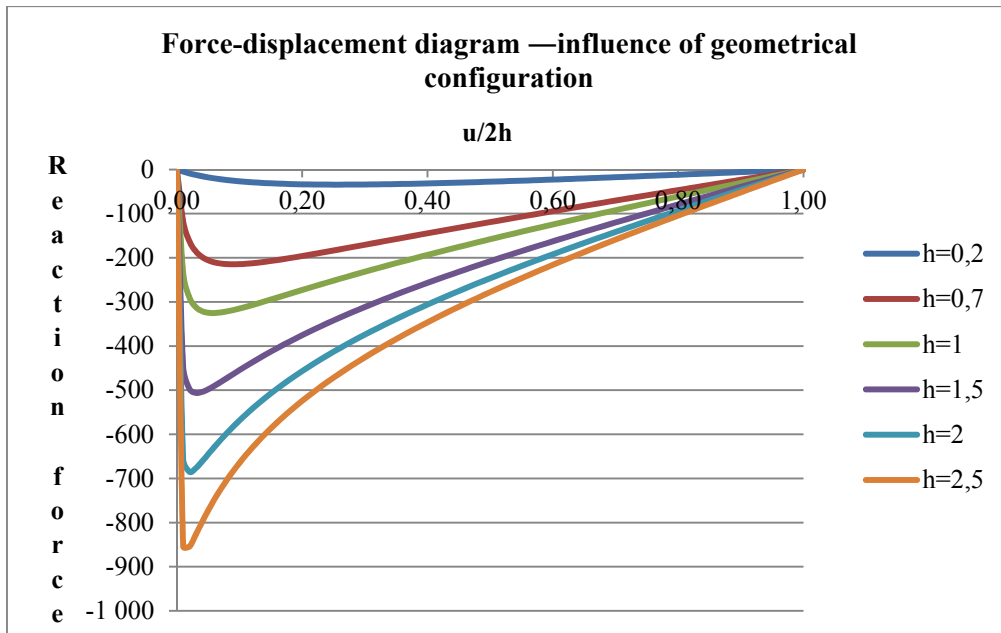


Fig. 4.24: Influence of geometrical configuration — force displacement diagram of basic unit in case of different h/R ratios ($EA = 500; R = 0.5$)

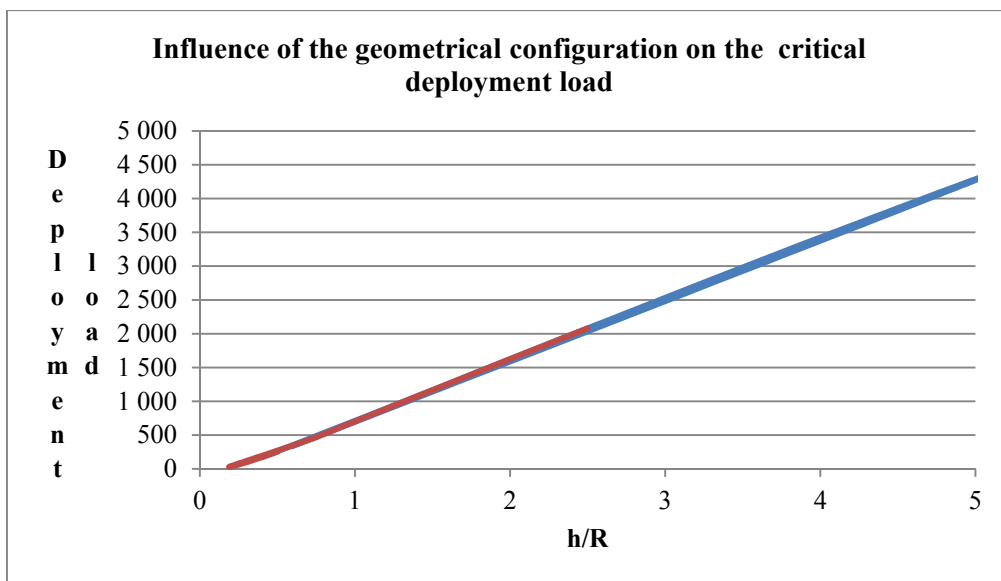


Fig. 4.25: Influence of geometrical configuration on the deployment load in the case of different h/R ratios ($EA = 500; R = 0,5$ (red) $R = 1$ (blue))

4.3.2 Numerical analysis of 'alternately stiffened' multi-storey structure

The packing modeling of the 'alternately stiffened' spatial structure was simulated with the same methodology that was used for planar alternately stiffened models. The deployment sequence of the uniform and the successive packing can be seen in Fig. 4.26.

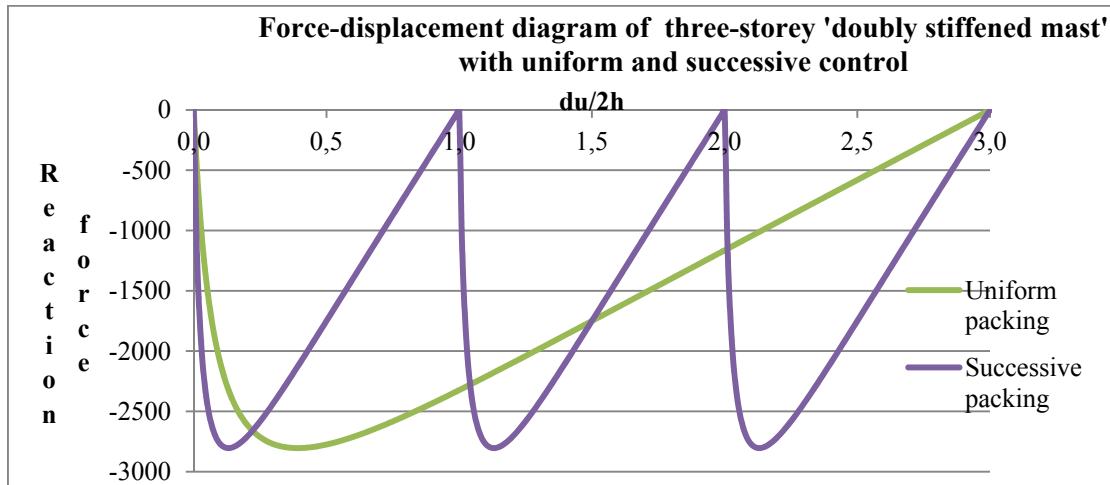
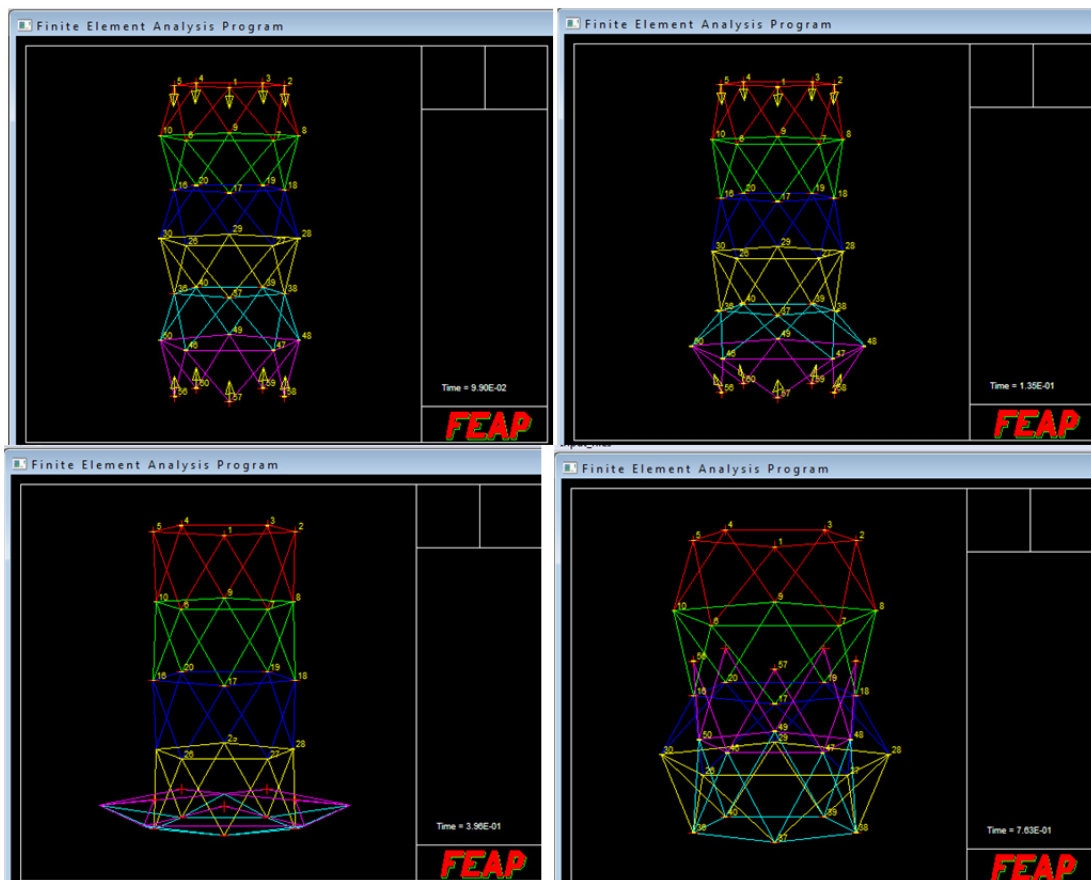


Fig. 4.26: Force displacement diagram of a three-storey 'alternately stiffened' antiprismatic mast



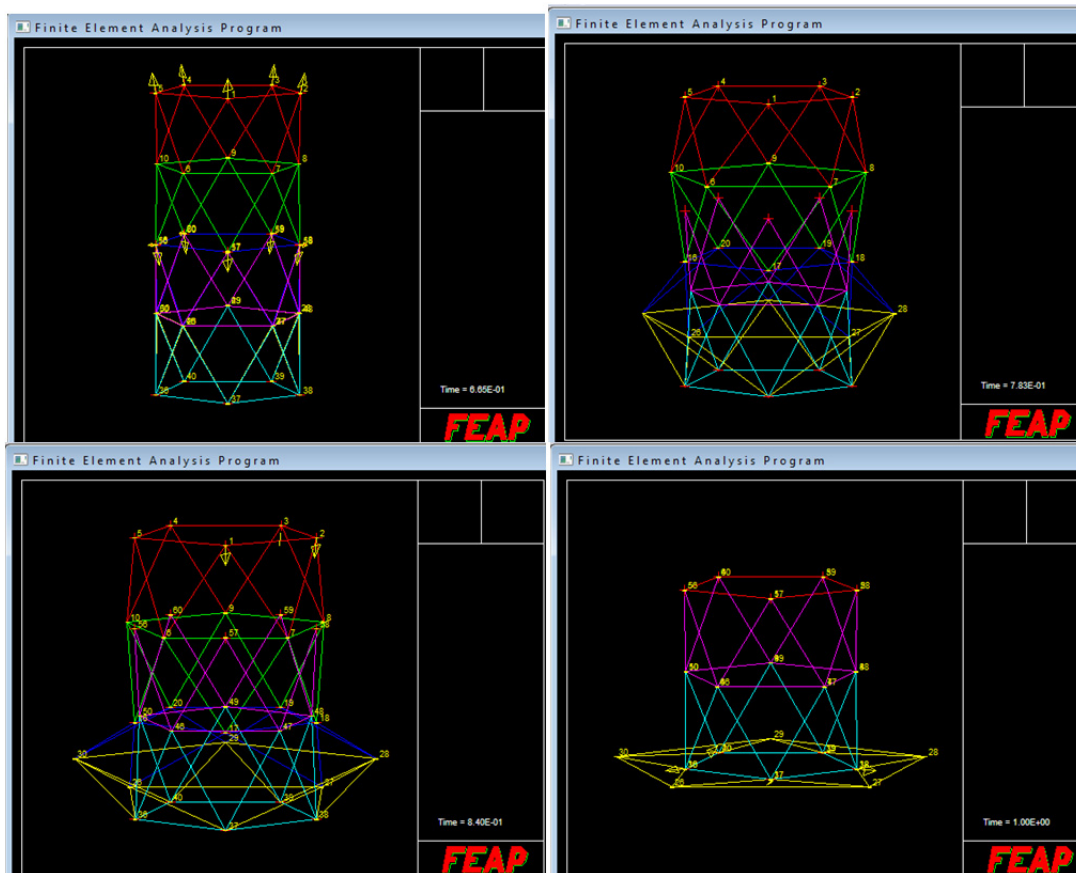


Fig. 4.27: Packing sequence of perturbation controlled unrestricted simulation ($EA_1 = 10\,000$; $EA_2 = 9\,990$; $EA_3 = 9\,980$; $R = 0,5$; $h = 0,5$)

With controlling the displacement of the top nodes only, any equilibrium path is possible. The sequence depends on the numerical errors. To be sure to get a certain behavior, perturbations are to be introduced into the system. For example, Fig. 4.27 shows a three-storey pentagonal antiprismatic mast which was perturbed in a way that leads to a typical equilibrium path. The elastic bar of the bottom segment was defined to be the weakest—that is the bottom one is the chosen part to close first—followed by the middle and finally the top unit. However, without restricting the ‘post-packed phenomenon’, the simulation can give awkward packing patterns. Fig. 4.27 is a nice example for such a phenomenon. The packing sequence obtained from the simulation is the following (Figs. 4.27-28): first the mast begins packing uniformly but the bottom segment slightly overtakes the others (due to the fact that it has the weakest elastic bar), reaches its critical height and, accordingly, starts softening. When the bottom unit reaches its post-critical state, the rest of the mast straightens up and gets back to its initial, undeformed state by the time the bottom segment completely closes. From this point, due to the ‘post-packed phenomenon’, the packing is hard to keep track on. When further squashing, instead of the top segments starting to pack, the bottom segment disengages from its packed configuration and starts turning upside down with pulling the rest of the structure. When regaining its initial, but reversed configuration the whole structure is stress-free and corresponds to a stable equilibrium position. If further displacing the top nodes, the top two segments are squashed

and the reversed bottom unit is stretched. The middle segment reaches first its critical state and starts closing by straightening up the top unit. Further packing cannot be achieved as the top nodes reached the bottom nodes.

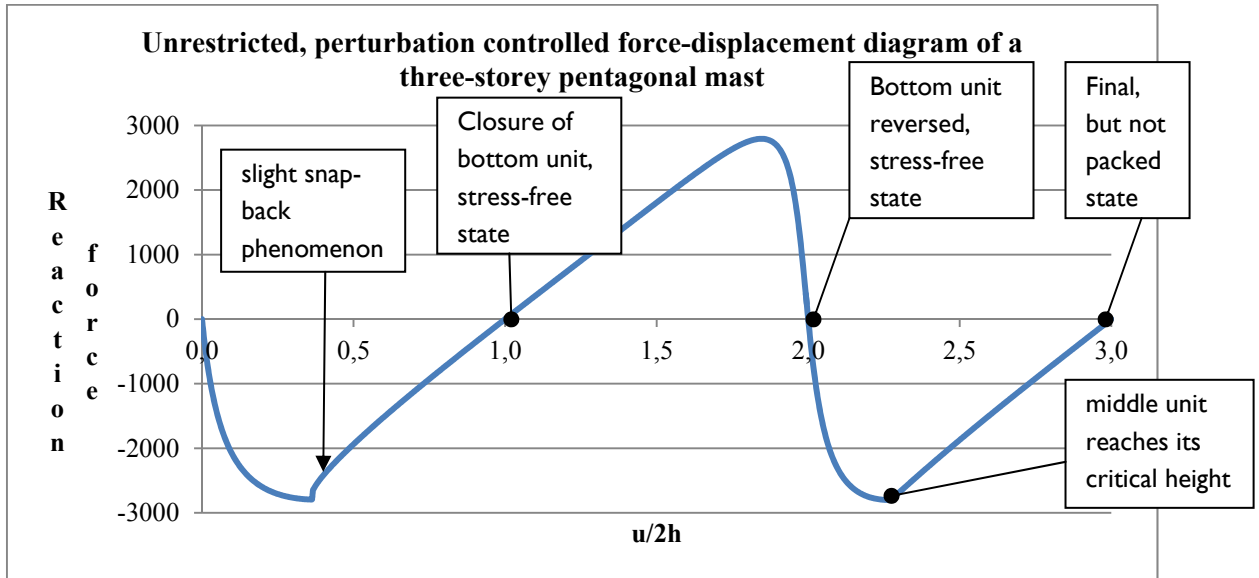


Fig. 4.28: Force-displacement diagram of a three-storey pentagonal mast — perturbation-controlled unrestricted simulation
 ($EA_1 = 10\ 000$; $EA_2 = 9\ 990$; $EA_3 = 9\ 980$; $R = 0.5$; $h = 0.5$)

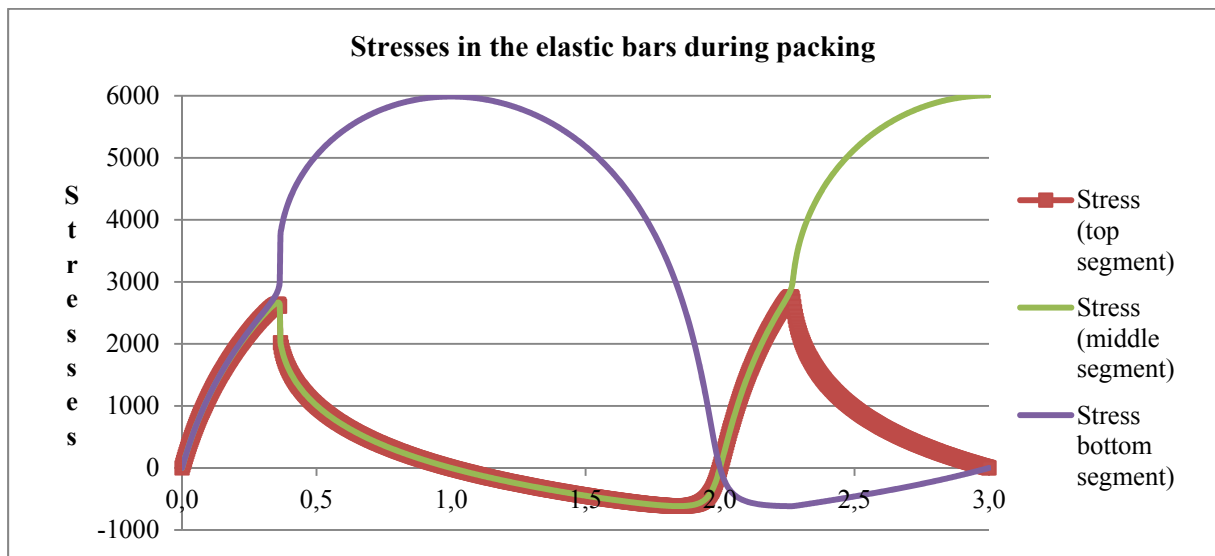


Fig. 4.29: Perturbation-controlled unrestricted simulation of packing a three-storey pentagonal mast — stresses in the elastic bars during packing
 ($EA_1 = 10\ 000$; $EA_2 = 9\ 990$; $EA_3 = 9\ 980$; $R = 0.5$; $h = 0.5$)

The restraint to restrict ‘post-packed phenomenon’ can be modeled with the same contact force induction as used for planar model. However, in the spatial model instead of modeling n paired nodes per units, a different methodology was used. An additional node was defined (Fig. 4.30) in the center of each rigid polygon, fixed horizontally to the axis of the structure. Though there is no element connecting with these nodes, the center points were virtually linked in the vertical degree of freedom to the polygonal vertices of the

associated rigid polygons. The contact forces between the rigid polygons are ensured by pairing these additional nodes. Accordingly, contact forces are induced between the rigid polygons. The more the centers of two rigid polygons are approaching the more intense the contact force gets.

With this methodology the complete packing of the same structure that was presented above can be simulated. This restricted simulation is presented in Figs 4.31-32.

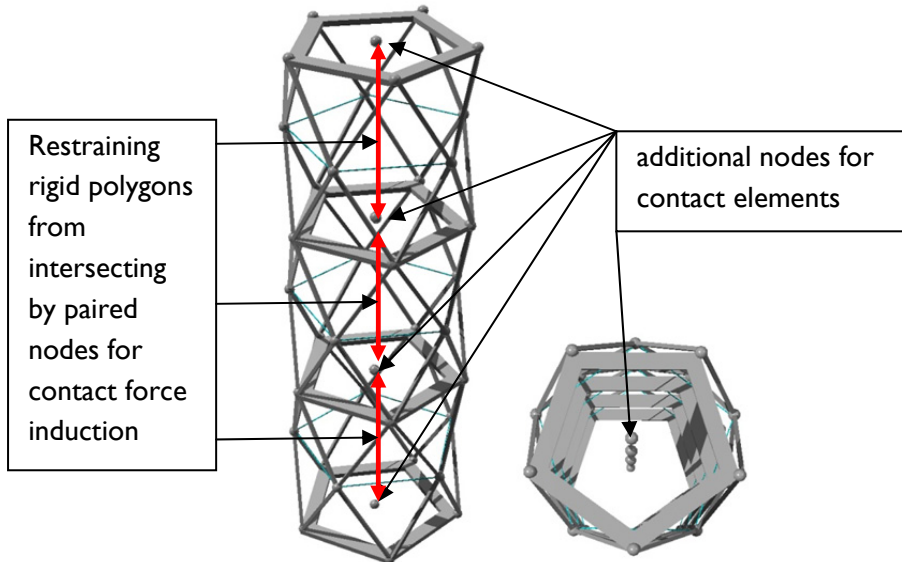


Fig. 4.30: Modeling restriction of 'post-packed phenomenon'

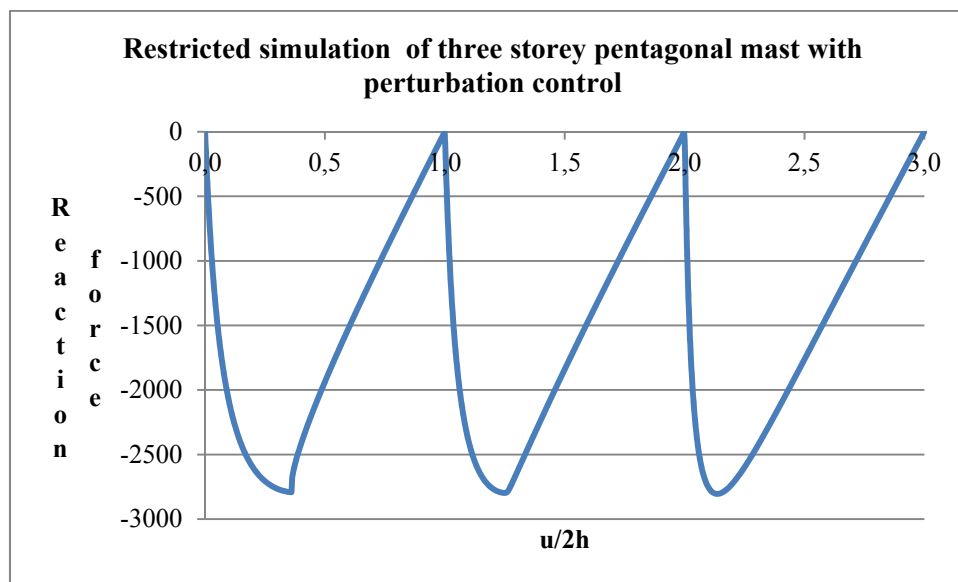


Fig. 4.31: Force-displacement diagram of three-storey pentagonal mast — perturbation controlled restricted simulation

($EA_1 = 10\ 000$; $EA_2 = 9\ 990$; $EA_3 = 9\ 980$; $R = 0.5$; $h = 0.5$)

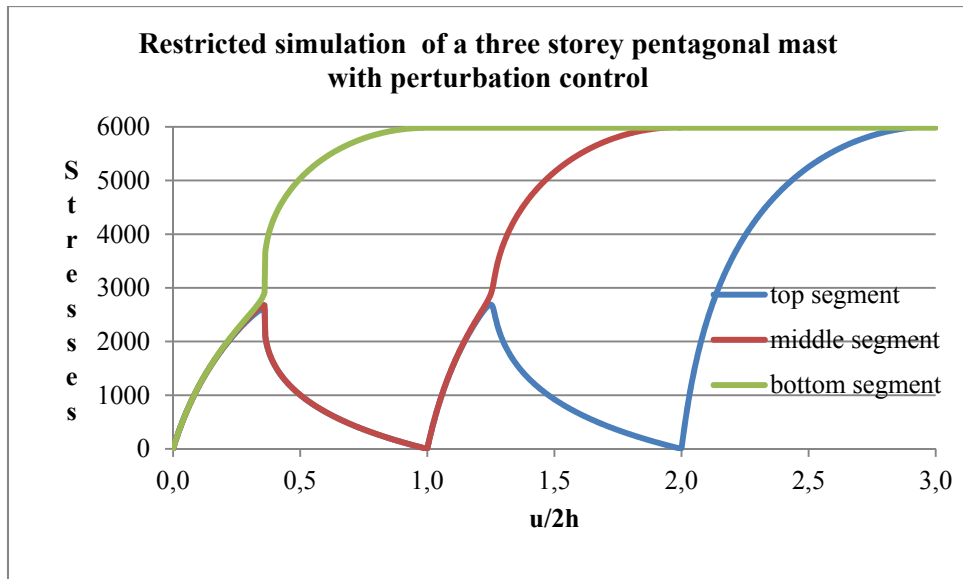
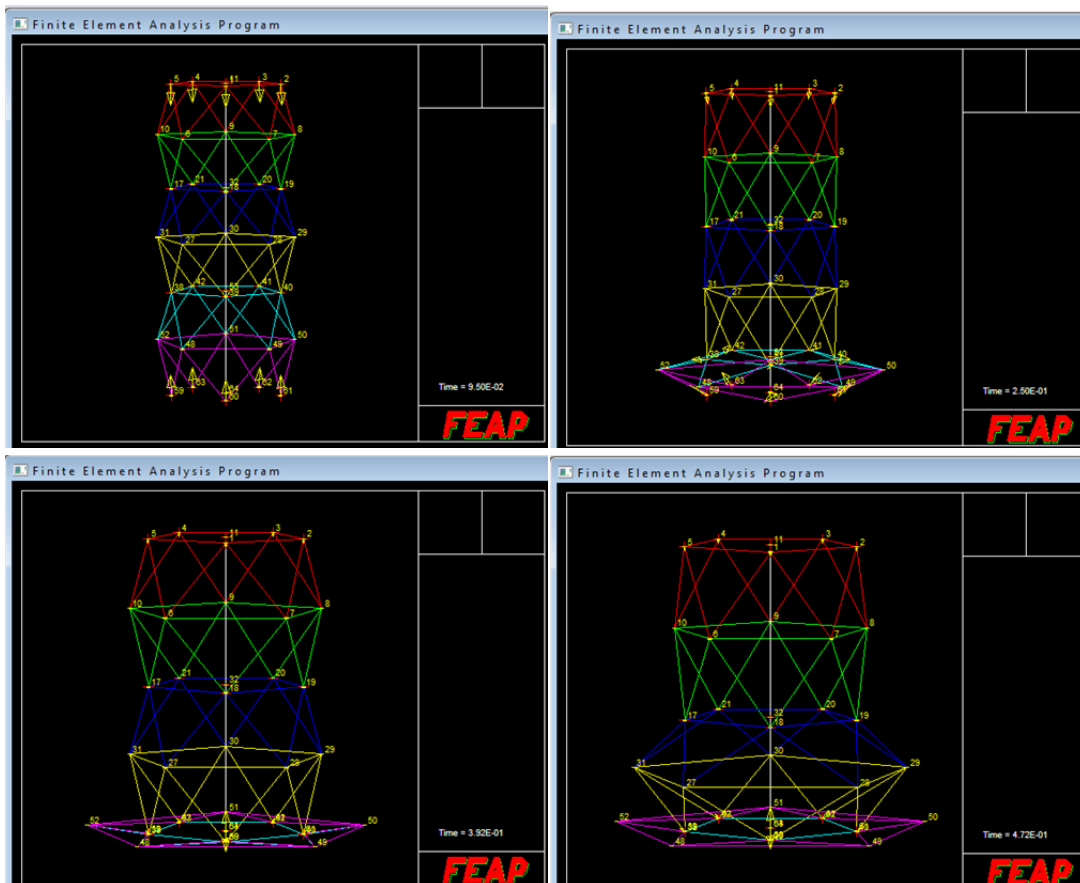


Fig. 4.32: Perturbation controlled restricted simulation of packing a three-storey pentagonal mast — stresses in the elastic bars during packing ($EA_1 = 10\ 000$; $EA_2 = 9\ 990$; $EA_3 = 9\ 980$; $R = 0.5$; $h = 0.5$)



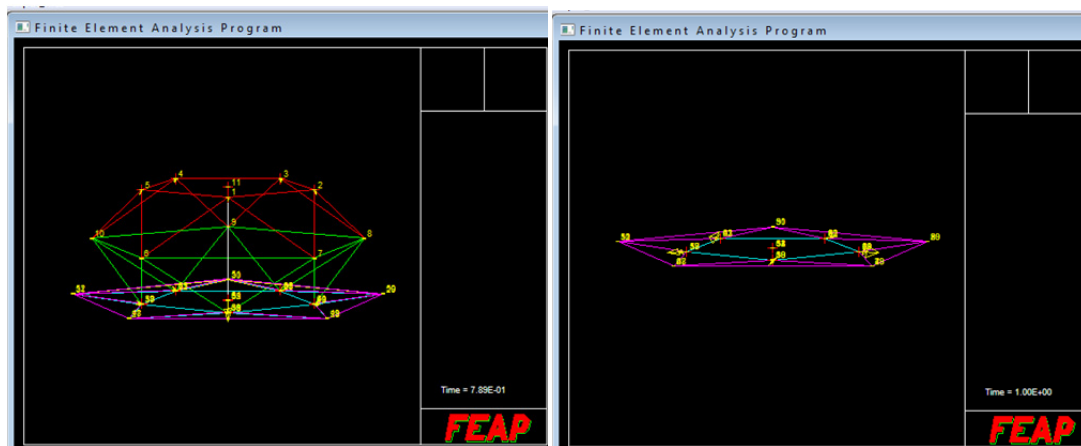


Fig. 4.33: Packing sequence of a three-storey 'alternately stiffened' mast with restricted simulation

4.3.3 Numerical analysis of a 'non-stiffened' multi-storey structure

The packing of non-stiffened multi-storey antiprismatic masts are rather fascinating to analyze. The uniform packing control of the structure was simulated by vertical boundary conditions applied at each node. Similarly to the planar case, the displacement of the boundaries was multiplied by different proportional functions depending on the pseudo time. This proportional function depends on which level the polygonal node is associated to. The functions are identical to the one described for planar structures (Fig. 3.44).

Fig. 4.34 shows the reaction forces at the different levels of the antiprismatic mast. It can be seen on the diagram that each reaction force makes two loops separated by a configuration corresponding to zero forces in the intermediate boundaries. This state is shown in Fig. 4.36. It can be seen from the plan view (Fig. 4.36b) that the disputed configuration corresponds to the one where all the bracings lie exactly in an upright position. While in the beginning, all the polygons start expanding, after a critical force, every odd level (levels 1,3,5) keeps expanding and every even level (levels 2, and 4) starts first relaxing and then shrinking (Fig. 4.35). Consequently, in contrary to the planar structure, the elastic bars of the polygon are not always in tension. From this point, the constitutive model used is an important factor in the analysis. As mentioned before, the logarithmic stretch model gives fake results in the finite compression range. If that was not the case, the polygons on level 3 and 4 would start to compress more. But with logarithmic stretch model it takes lot of energy to compress the elastic bars and, consequently, it is rather the stretching of the bar that assures the closure. It should be mentioned that a linear model would be equally fake, as a realistic elastic bar would deflect before being compressed. Nonetheless, if we assume that around the elastic material a rigid material is installed (see later in next chapter) that doesn't stretch with the material but active only for compression, than the hypothesis of logarithmic stretch behavior can be acceptable to be realistic. It can be concluded from the analyzed structure that the packing behavior of the spatial structure differs from the planar model due to the possibility of compression forces in the polygonal elastic bars. Compression force can occur in these bars if the difference between the expansions of the adjacent polygons is big enough to put the bracings in an upright position.

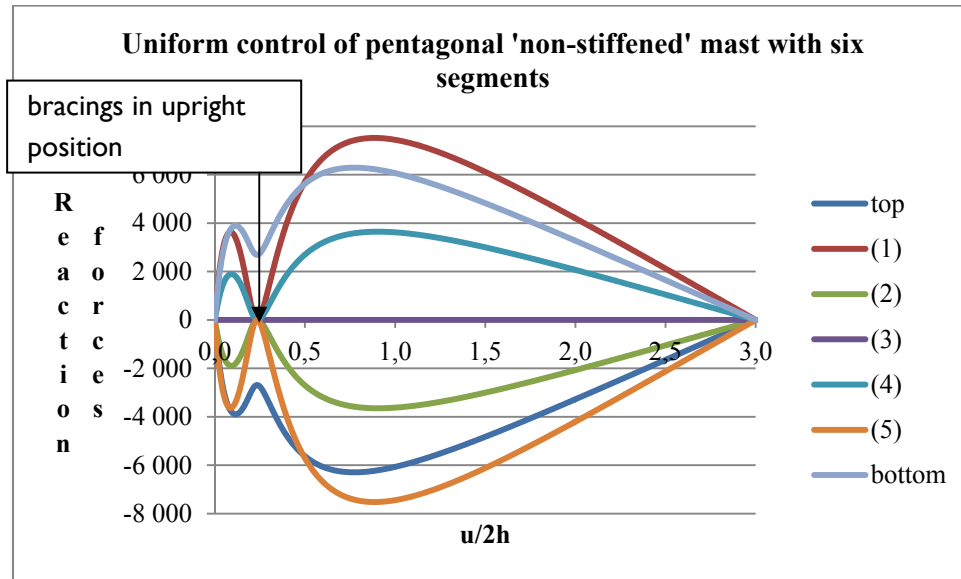


Fig. 4.34: Uniform packing of non-stiffened antiprismatic pentagonal mast with six segments — reaction forces ($EA = 10\,000$; $R = 0,5$; $h = 0,5$)

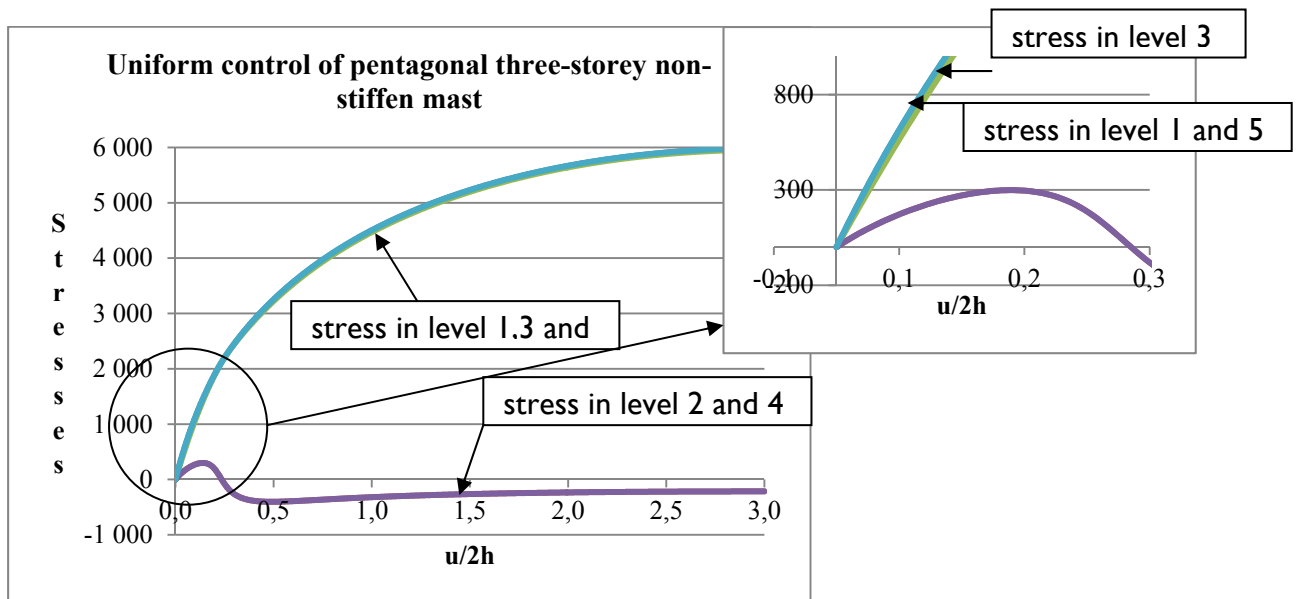


Fig. 4.35: Uniform packing of non-stiffened antiprismatic pentagonal mast with six segments — stresses in the elastic bars ($EA = 10\,000$; $R = 0,5$; $h = 0,5$)

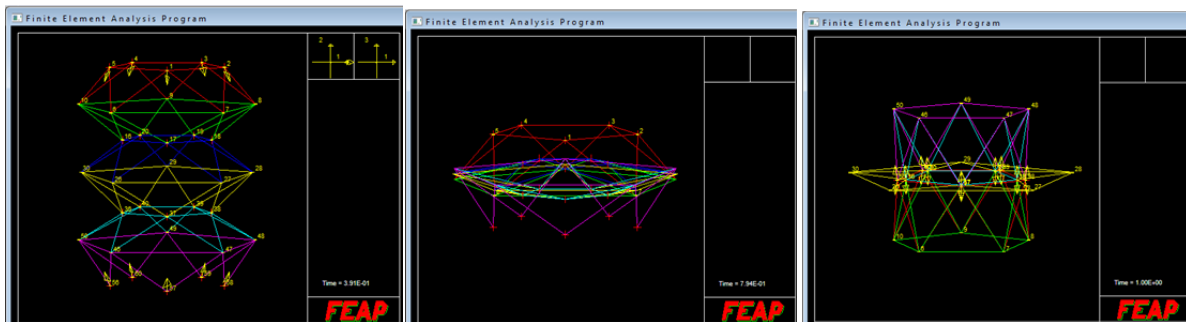
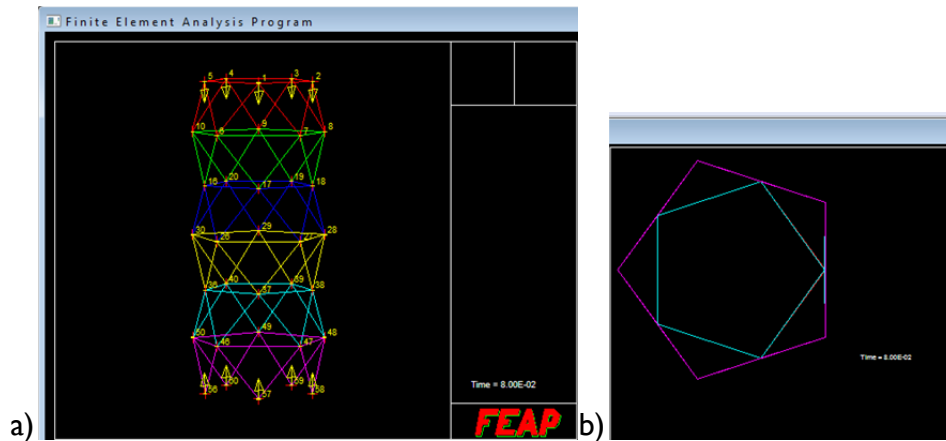


Fig. 4.36: Post-packed phenomenon with controlling only the displacements of every second level

The same analysis used for the uniform packing of ‘alternately stiffened’ masts is not practical in the ‘non-stiffened’ case. Controlling only the displacement of every second level results in a ‘post-packed phenomenon’, namely, the non-controlled pentagons will travel through its adjacent (controlled) polygon and flip up or down the bracings (Fig. 4.36). The uniformly controlled packing simulation is useful for the prediction of packing pattern of only boundary displacement controlled structures; the softest segments of the mast are those that are being tensioned by the intermediate boundary restraints. This tensile force indicates that if the packing wasn’t uniformly controlled this segment would overtake the other segments with closing.

In the analysis of ‘non-stiffened’ planar structures it was shown that the uniform packing in the case of odd number of segments is not possible without lengthening the rigid bars. To see whether an antiprismatic ‘non-stiffened’ mast with odd number of segments is packable, let’s analyze a mast of three segments. The packed geometrical configuration of the bottom and the top segment is predefined. The two boundary segments are drawn in Fig. 4.37. The lengths between the endpoint of the bracings of the top segment and the one of the bottom are:

$$l_{nec} = 2R_{max}^{\phi} \sin\left(\frac{\phi}{2}\right) \tag{4.39}$$

Substituting equation (4.5) into (4.39)

$$l_{nec} = 2 \left(R \cos \phi + \sqrt{l_b^2 - R^2 \sin^2 \phi} \right) \sin \left(\frac{\phi}{2} \right) \tag{4.40}$$

The antiprismatic mast of three segment is packable if $l_{nec} = l_b$, that is, if:

$$pack \left(\frac{l_b}{R} \right) = 2 \left[\cos \phi + \sqrt{\left(\frac{l_b}{R} \right)^2 - \sin^2 \phi} \right] \sin \left(\frac{\phi}{2} \right) - \frac{l_b}{R} = 0 \tag{4.41}$$

and if

$$hcheck \left(\frac{l_b}{R} \right) = \frac{l_b}{R} - 2(1 - \cos(\phi)) > 0 \tag{4.42}$$

It can be seen from the diagram in Fig. 4.38 that the first zero point of (4.41) coincidences with the one of (4.42). This, similarly to the planar case, means the trivial solution: it is packable if the initial configuration is already packed. However, (4.41) has another solution which satisfies the condition (4.42). This means that with a specific geometric configuration, the spatial structure of odd number of segments can be packed in plane.

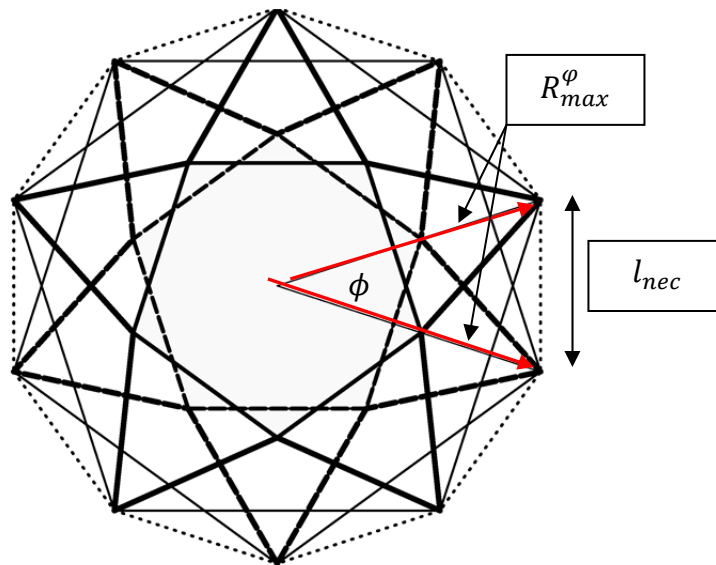


Fig. 4.37: Checking packability of ‘non-stiffened’ antiprismatic masts of odd number of segments (continuous line: bottom segment, dashed line: top segment, dotted line: middle segment)

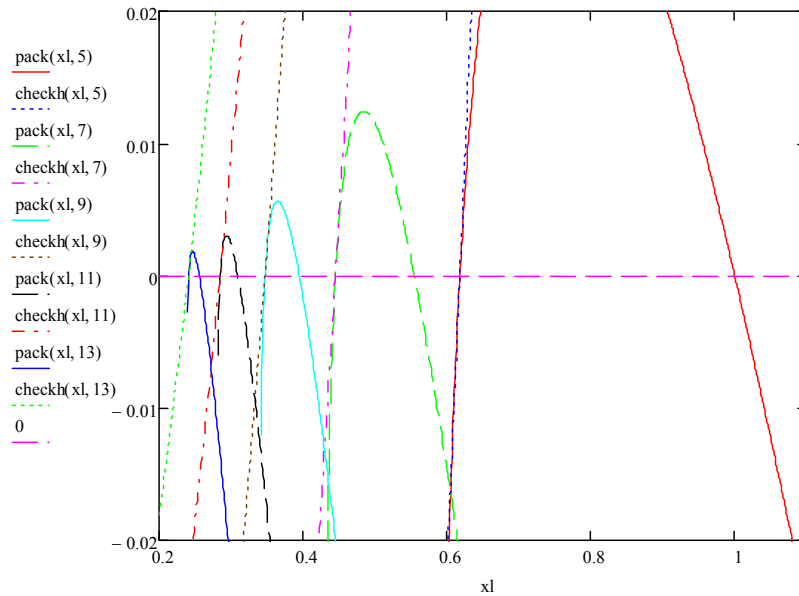


Fig. 4.38: Checking packability of ‘non-stiffened’ antiprismatic masts of odd number of segments in case of $n = 5,7,9,11,13$ (packability functions (4.36 and 4.37) in function of $xl = lb/R$)

Fig. 39 and Fig. 40 show the packing of the pentagonal ‘non-stiffened’ mast with geometrical properties that does not satisfy equation (4.41). It can be seen that the sign of the forces (internal and external) change during packing. On Fig. 4.41 the packing of a three-storey mast satisfying this equation is presented, which can be really packed to plane.

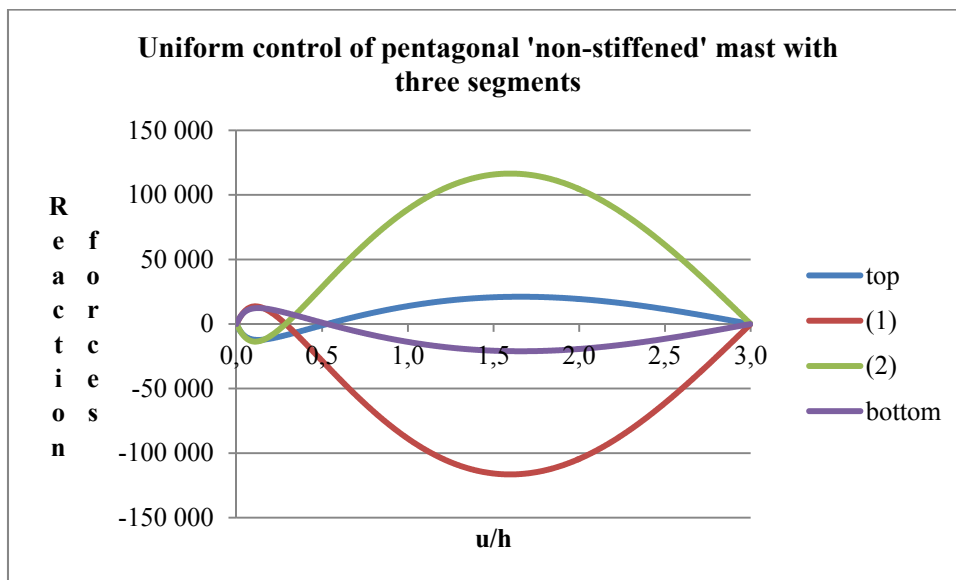


Fig. 4.39: Fallacious packing of non-stiffened mast of three segments ($lb \neq l_{nec}$) ($EA = 10\,000; R = 0.5; h = 0.5$)

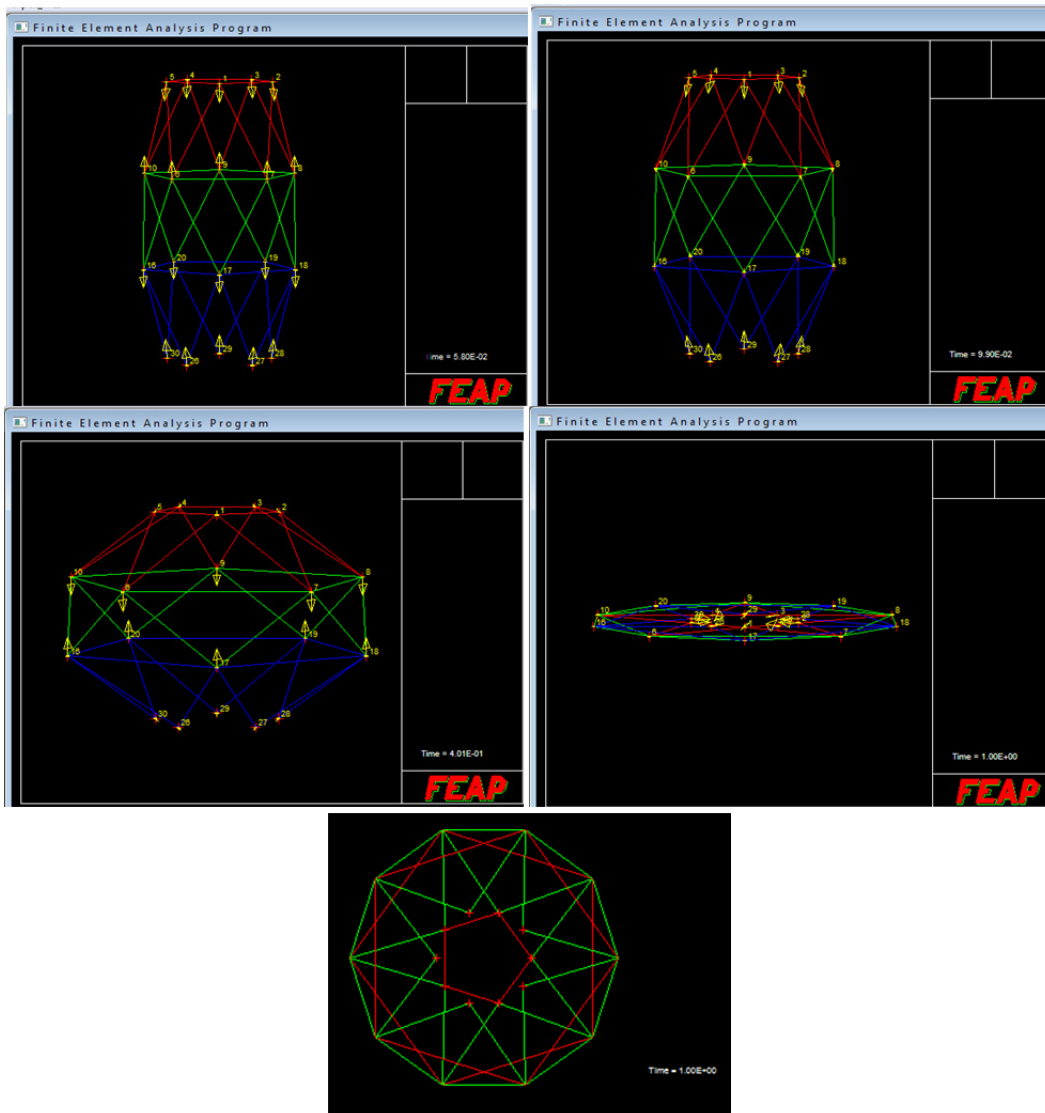


Fig. 4.40: Fallacious packing of non-stiffened mast of three segments ($l_b \neq l_{nec}$)

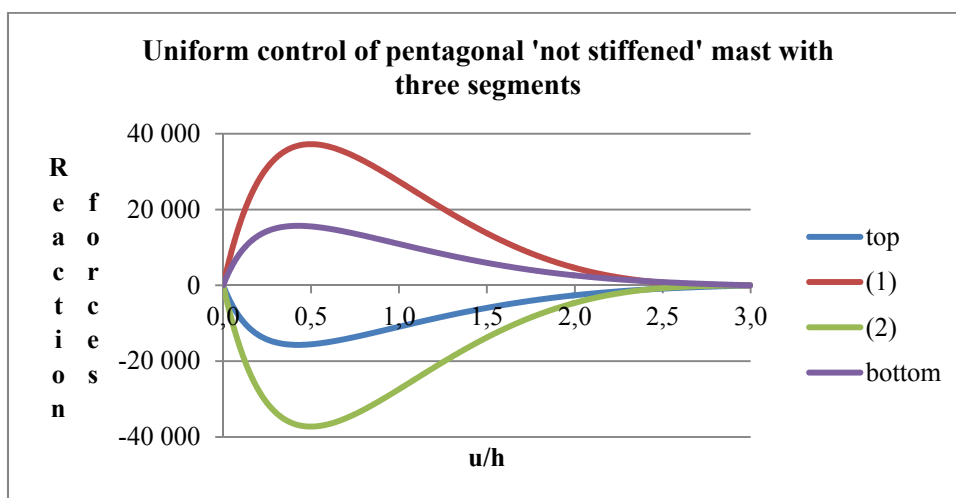


Fig. 4.41: Packing of non-stiffened mast of three segments ($l_b = l_{nec}$)
 ($EA = 10\ 000$; $R = 0.5$; $h = 0.3931$)

Contrary to the mast of even segments, under uniform control, the non-stiffened antiprismatic masts consisting of odd number of segments closes only by expanding its polygons.

The same condition deduced for three segments also stands for masts with 5,7,9..etc. segments. The mast consisting of odd number of segments can be closed by extending all its intermediate polygons to the radius R_{max}^φ if the length of the bracings is l_{nec} . An example is shown for the packing of such structure in Figs. 4.42 and 4.43. Nonetheless this solution is not a unique one if the number of segments is more than three. For example a mast of five segments can be closed in the pattern shown in Fig. 4.44.

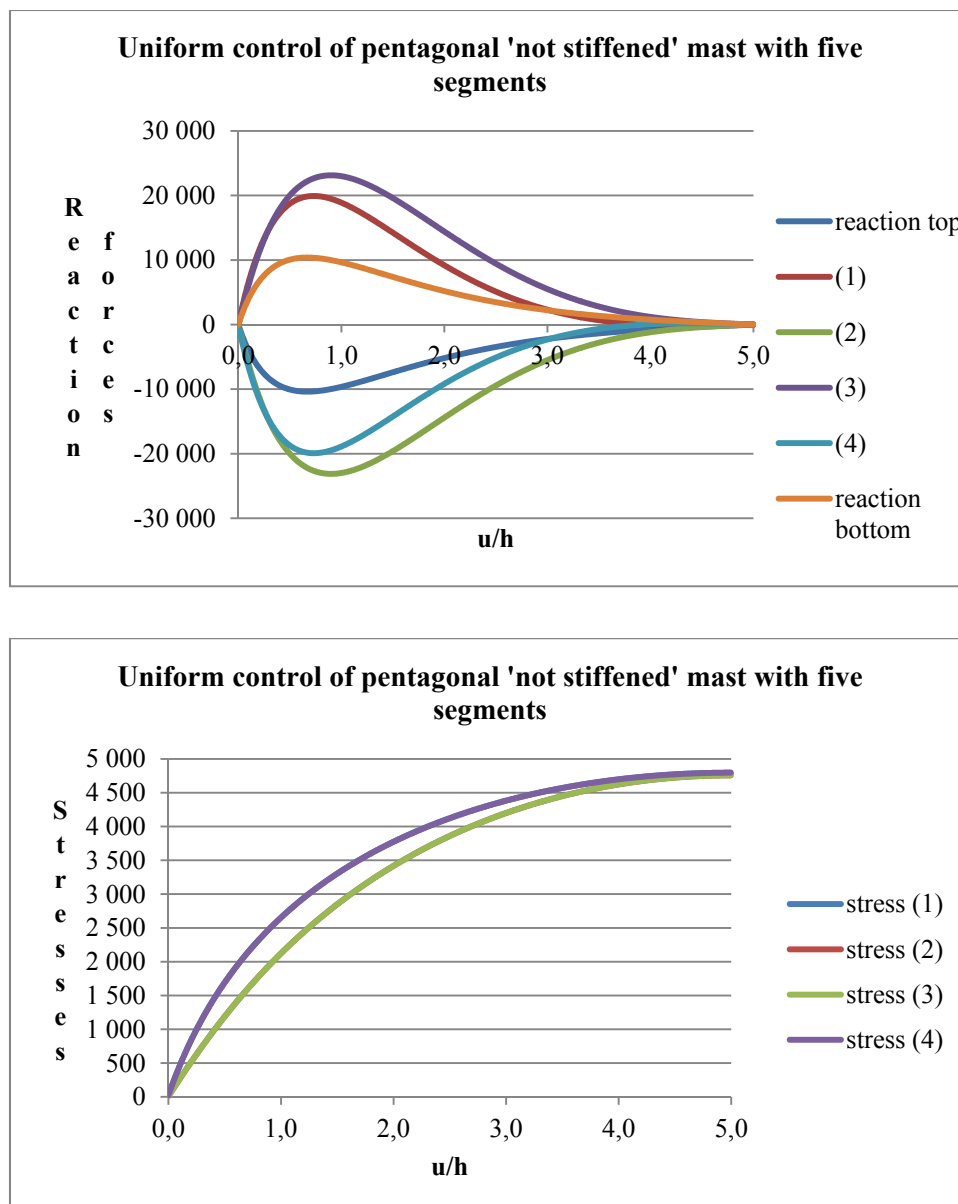


Fig. 4.42: Packing of pentagonal, non-stiffened mast of five segments ($l_b = l_{nec}$), packing sequence in Fig. 4.44 ($EA = 10\ 000$; $R = 0.5$; $h = 0.3931$)

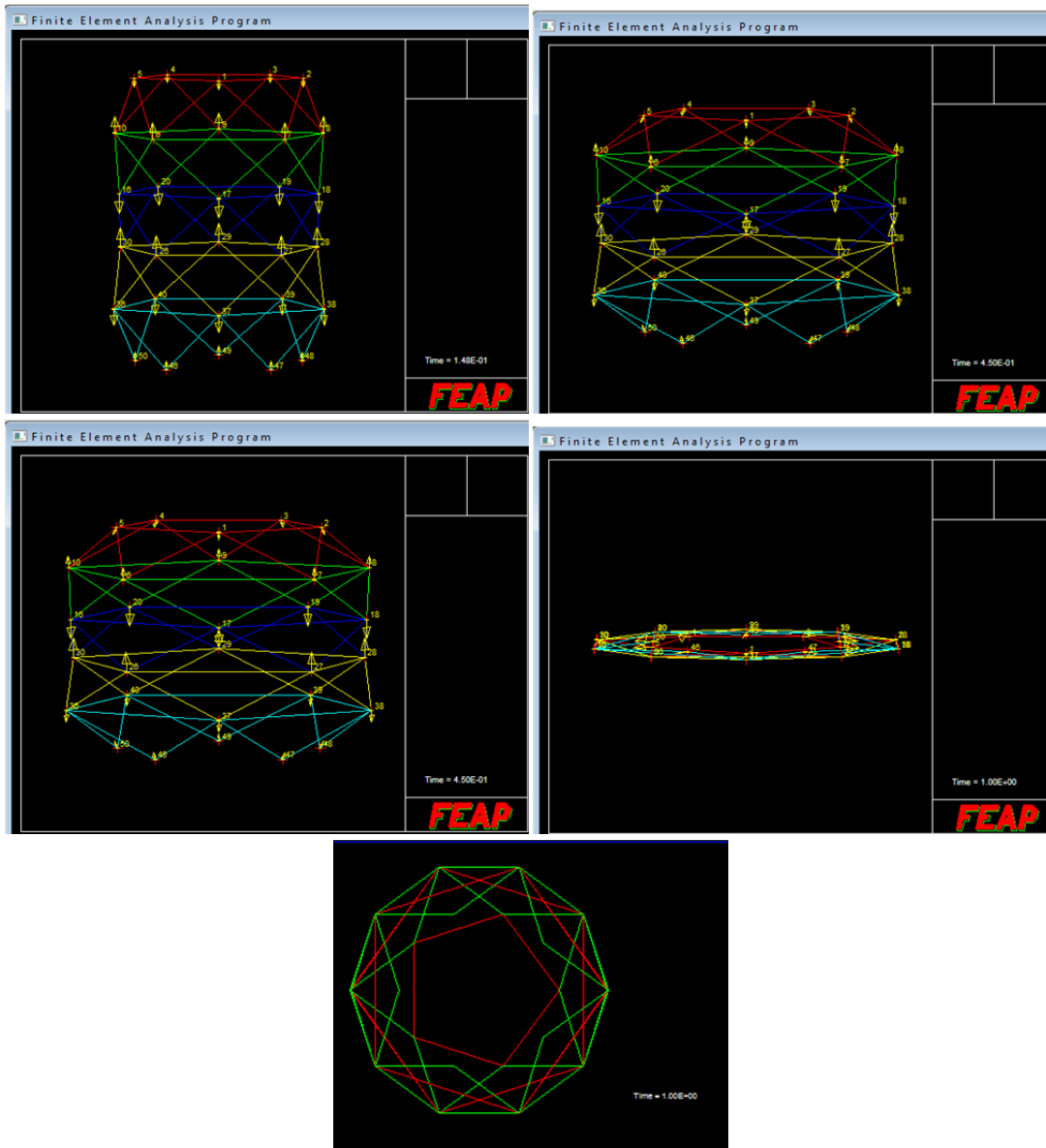


Fig. 4.43: Packing of non-stiffened mast of three segments ($l_b = l_{nec}$)
 ($EA = 10\ 000$; $R = 0.5$; $h = 0.3931$)

This packing pattern is possible if:

$$l_{nec2} = R_2^\phi \sin\left(\frac{\phi}{2}\right) \tag{4.43}$$

with

$$R_1^\phi = R_{max}^\phi \tag{4.44}$$

$$R_2^\phi = R_1^\phi \cos \phi + \sqrt{l_b^2 - R_1^{\phi 2} \sin^2 \phi} \tag{4.45}$$

A simulation of a five-storey antiprismatic mast with bracing-length l_{nec2} is presented in Fig. 4.45

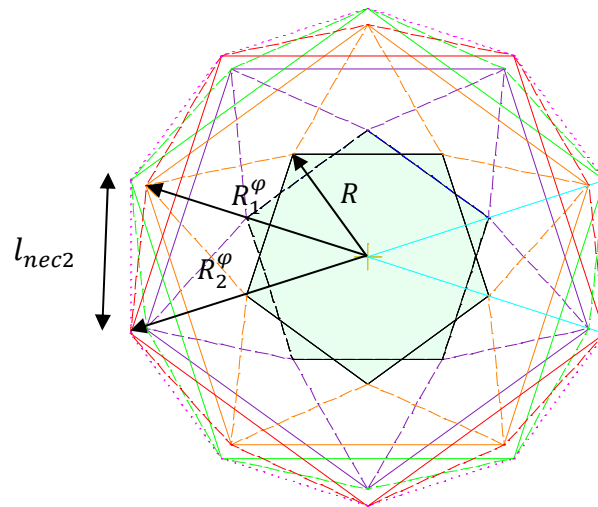


Fig. 4.44: Possible packing pattern of masts consisting of five segments or more (only in the case of odd number of segments)

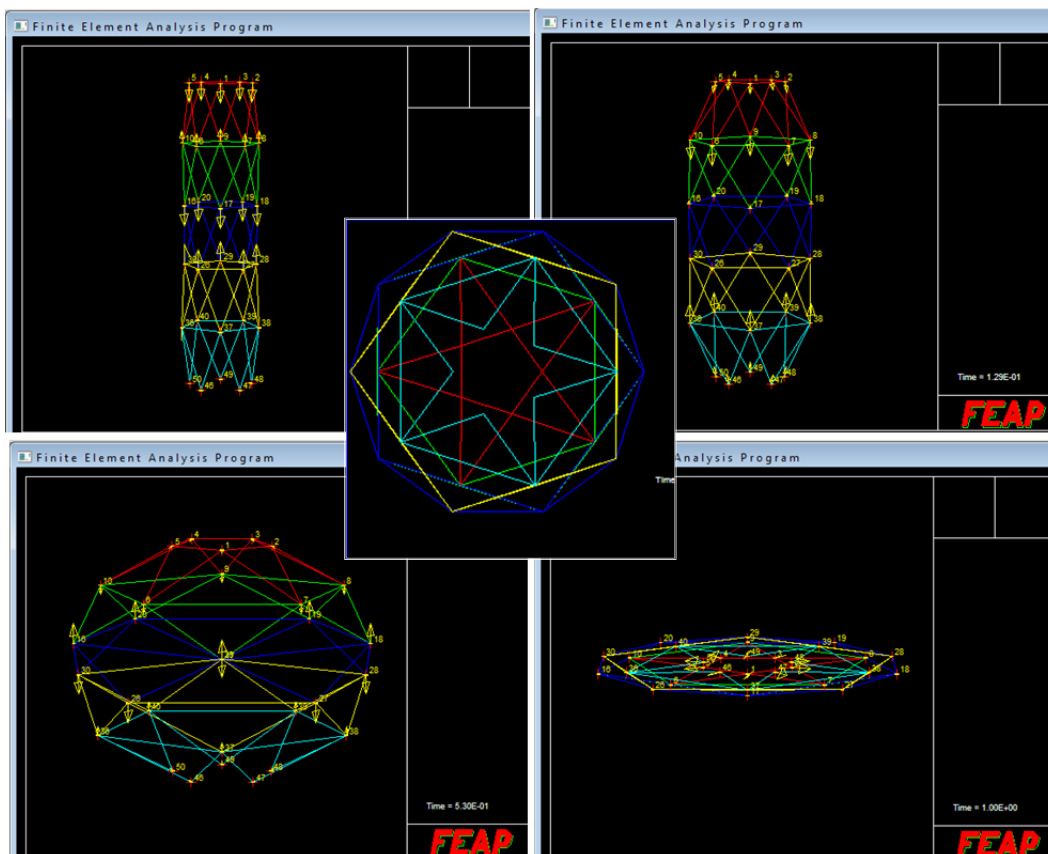


Fig. 4.45: Packing of pentagonal, non-stiffened mast of five segments ($l_b = l_{nec2}$)
 ($EA = 10\ 000$; $R = 0.5$; $h = 0.3931$)

Concerning a non-stiffened mast of seven segments, the mast can be packed to plane in the case of satisfying equation (4.41), but also if the geometry is such that $l_b = l_{nec2}$. On

top of these possibilities, new schemas of packing are conceivable. Some theoretically possible packing patterns are shown on Fig. 4.46.

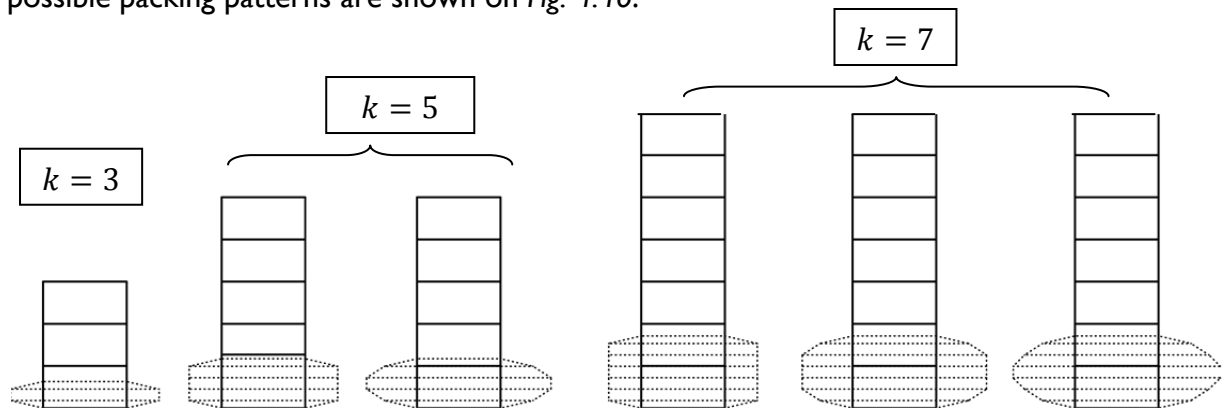
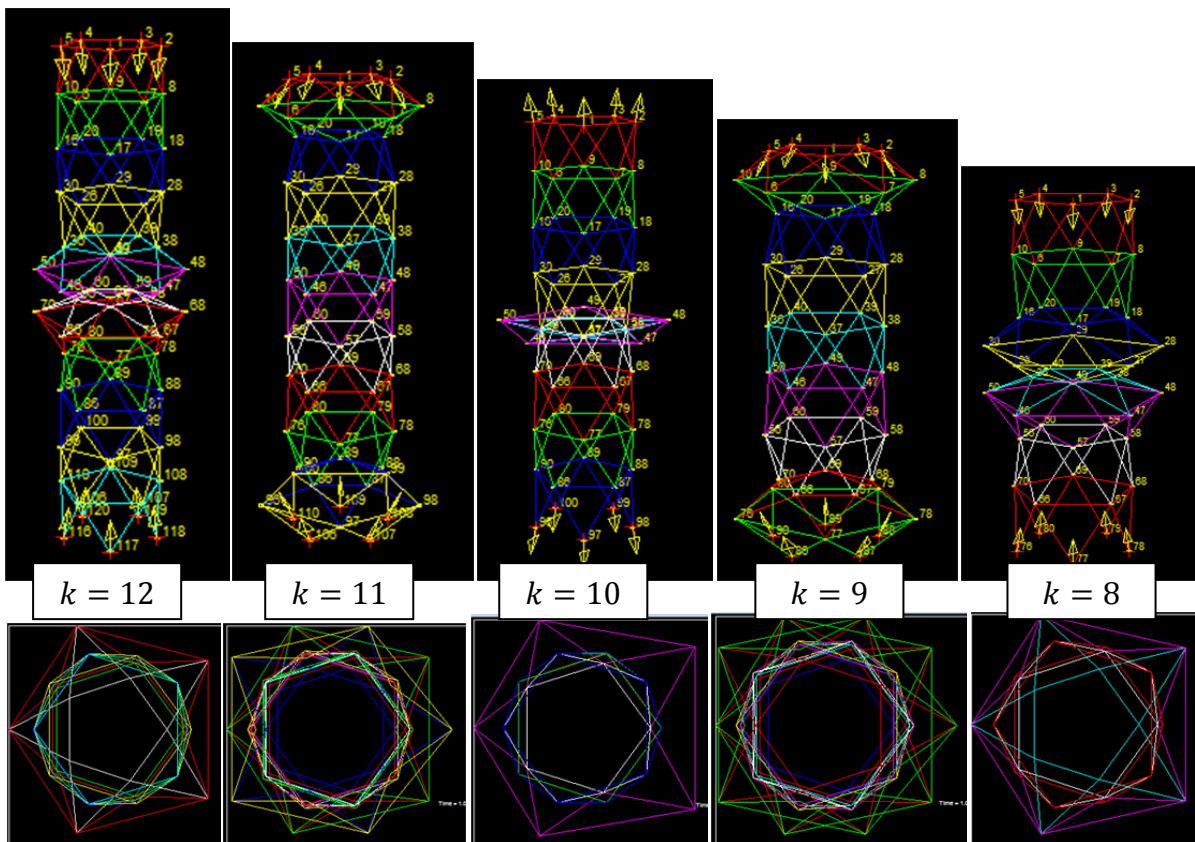


Fig. 4.46: Theoretically possible packing patterns in the case of odd segment number ($k=3,5,7$)

When the structure is only controlled by the displacement of the top facet, the packing patterns show a quite interesting chaotic system (Fig. 4.47). However, the investigations have shown that this pattern is chaotic though, but not completely stochastic. The simulation developed in MAPLE proved that in the case of certain geometrical parameters, there are certain number of possible patterns, among which the numerical errors (or in reality the imperfections) choose. However, these possibilities are not so numerous. The defined parameters were only investigated for a few parameters and segment numbers, but further study would be needed to really clarify the regularities in the system.



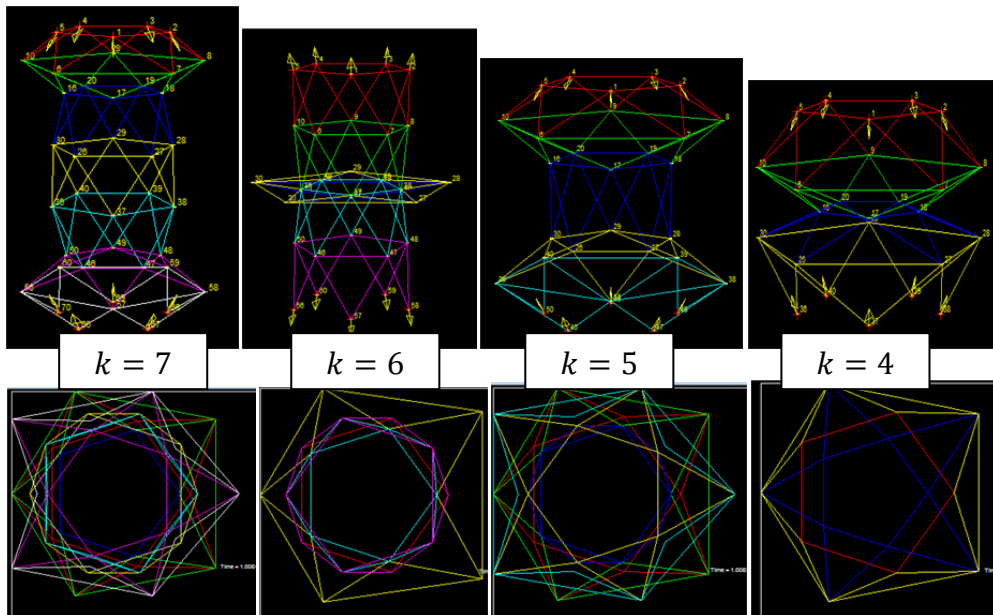


Fig. 4.47: Stochastic packing pattern of non-stiffened antiprismatic mast

Fig. 4.48 shows the influence of the number of segments on the critical force. It can be seen that the difference between the critical force of the masts with odd number of segments (line in green) and the one of the masts with even number of segments (line in red) is getting smaller with the increment of segment number.

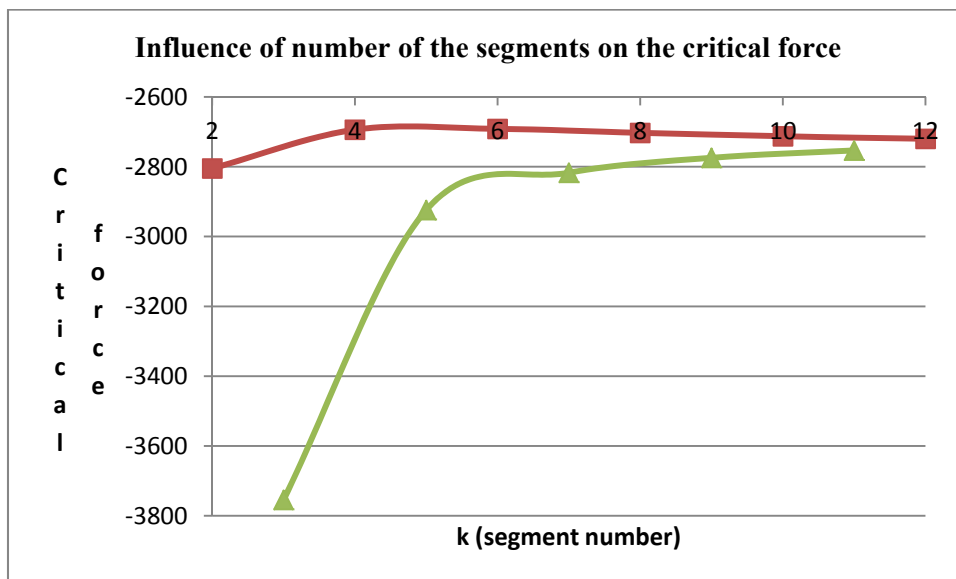


Fig. 4.48: Influence of number of the segments on the critical force

4.3.4 Dynamic analysis of antiprismatic structures

The major advantage of the antiprismatic column, proposed by Hegedűs, is that the structure is self-deployable, and consequently the installation of it can be very rapid. However, it has to be assured that the structure is neither damaged from inertial effects during deployment nor gets stuck in the packed configuration. Furthermore, it was shown above, that when packing, even with the smooth control of the displacements of the boundary facets, the intermediate elements might undergo large snapping. Accordingly, for both, the deployment and the packing, a profound dynamic analysis is inevitable.

The dynamics of the flexible structures imposes several technical and numerical difficulties. First, the right choice of the time-integration schemes which are suitable for handling different deformation modes with potentially large difference in associated stiffness and natural frequencies – or what is referred to the stiff differential equations. The physics of the problem should play an important role in devising any such scheme. The right choice of damping, which can control vibrations and avoid unwanted inertial effects and at the same time is of true nature, is neither evident.

Herein, only a first attempt is given to overcome these difficulties for the dynamic analysis of antiprismatic structures.

The deployment of the antiprismatic mast was simulated with a packed initial configuration. Nonetheless, to avoid singularities, this configuration was not the completely packed one, that is, the initial state was determined with:

$$h_{in}^{\varphi} = 0 + \varepsilon \quad (4.39)$$

where ε is an arbitrary small number. The elastic bars, in this quasi packed configuration are stretched:

$$\begin{aligned} \lambda(h^{\varphi})|_{h^{\varphi}=h_{in}^{\varphi}} &= \cos \phi + \sqrt{\left(\frac{h}{R}\right)^2 - \left(\frac{0 + \varepsilon}{R}\right)^2 + (1 - \cos \phi)^2} \approx \\ &\approx \cos \phi + \sqrt{\left(\frac{h}{R}\right)^2 + (1 - \cos \phi)^2} \end{aligned} \quad (4.40)$$

Accordingly these elastic bars in the initial configuration are pre-stressed. As the dynamic behavior was simulated in the finite element simulation defined by logarithmic stretch model, the prestress has to be calculated from this constitutive model. The logarithmic strain is:

$$\varepsilon(h^{\varphi})|_{h^{\varphi}=h_{in}^{\varphi}} = \ln(\lambda(h_{in}^{\varphi}) - 1) = \ln\left(\cos \phi + \sqrt{\left(\frac{h}{R}\right)^2 + (1 - \cos \phi)^2} - 1\right) \quad (4.41)$$

And the necessary magnitude of prestress in order to achieve self-deployment is:

$$\sigma_{pre_min} = E \varepsilon(h^\varphi)|_{h^\varphi=h_{in}^\varphi} = E \ln \left(\cos \phi + \sqrt{\left(\frac{h}{R}\right)^2 + (1 - \cos \phi)^2 - 1} \right) \tag{4.42}$$

The numerical dynamic simulation was performed by assuming concentrated masses in the joints, and calculating transient solution with the Newmark integrations scheme. Fig. 4.49-4.51 show the first try to simulate the deployment of an ‘alternately stiffened’ mast. It can be seen from the figures that without restricting the segments-crossing, the deployment gets quite messed.

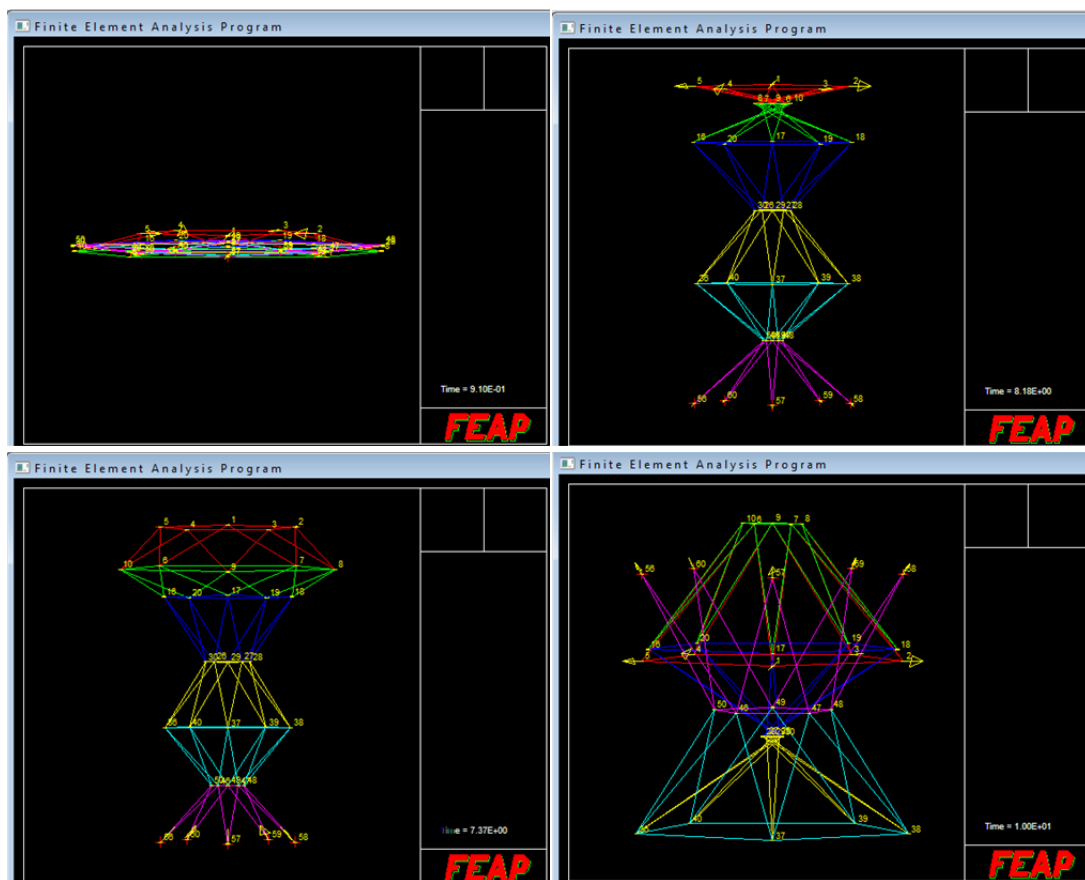


Fig. 4.49: Dynamic deployment of antiprismatic mast: deployment sequence without restriction of post-packed phenomenon

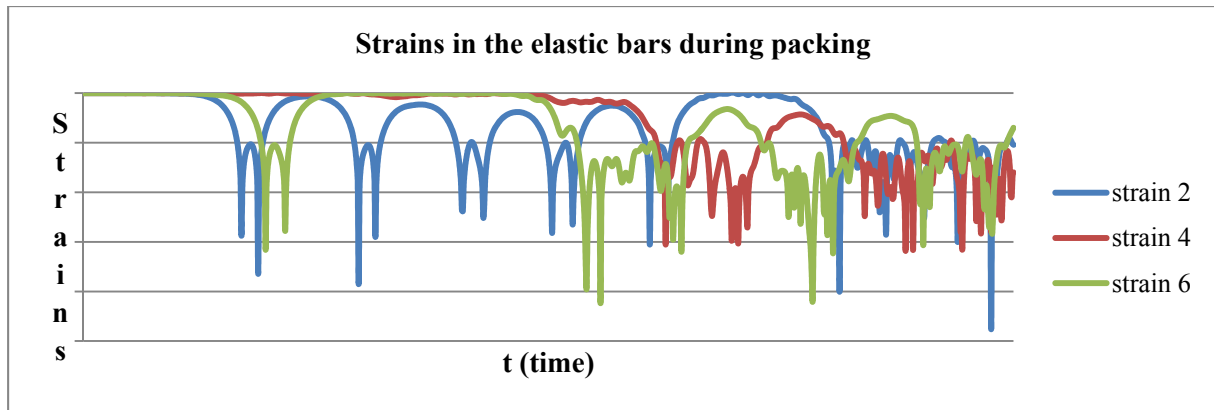


Fig. 4.50: Dynamic deployment of antiprismatic mast: strain in the elastic bars during deployment

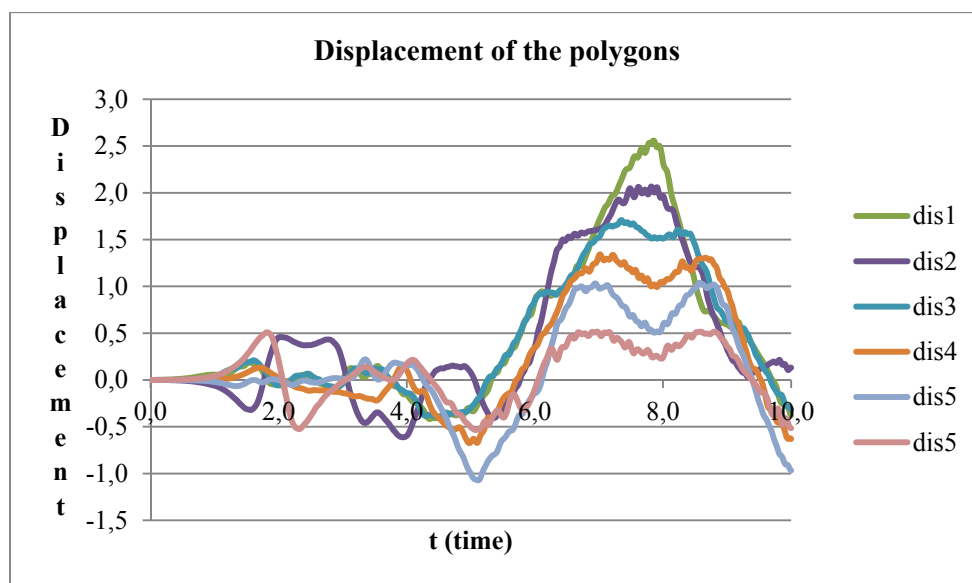


Fig. 4.51: Dynamic deployment of antiprismatic mast: vertical displacement of polygonal nodes ($EA = 10\,000$; $R = 0.5$; $h = 0.5$), packing sequence in accordance with Fig. 4.49

Experiencing the difficulties of the dynamic deployment-simulation and the complexity of verifying results, firstly the analysis of the deployment of a basic segment was carried out. The methodology to carry out the simulations follows the above mentioned methodology (packed initial configuration with self-stress), with the exception that the crossing of the polygons were attempted to be restrained with the penalty method described in *Chapter 4.3.2* (Fig. 4.30). However, deviating from the model, additional node was also defined in the center of the elastic polygon, and consequently two GAP elements were placed in the axis of the basic element. The deployment without any damping can be seen in *Figs 4.52-53*. The third figure in *Fig. 4.52* reflects that the penalty parameter was not always large enough to capture the restraint.

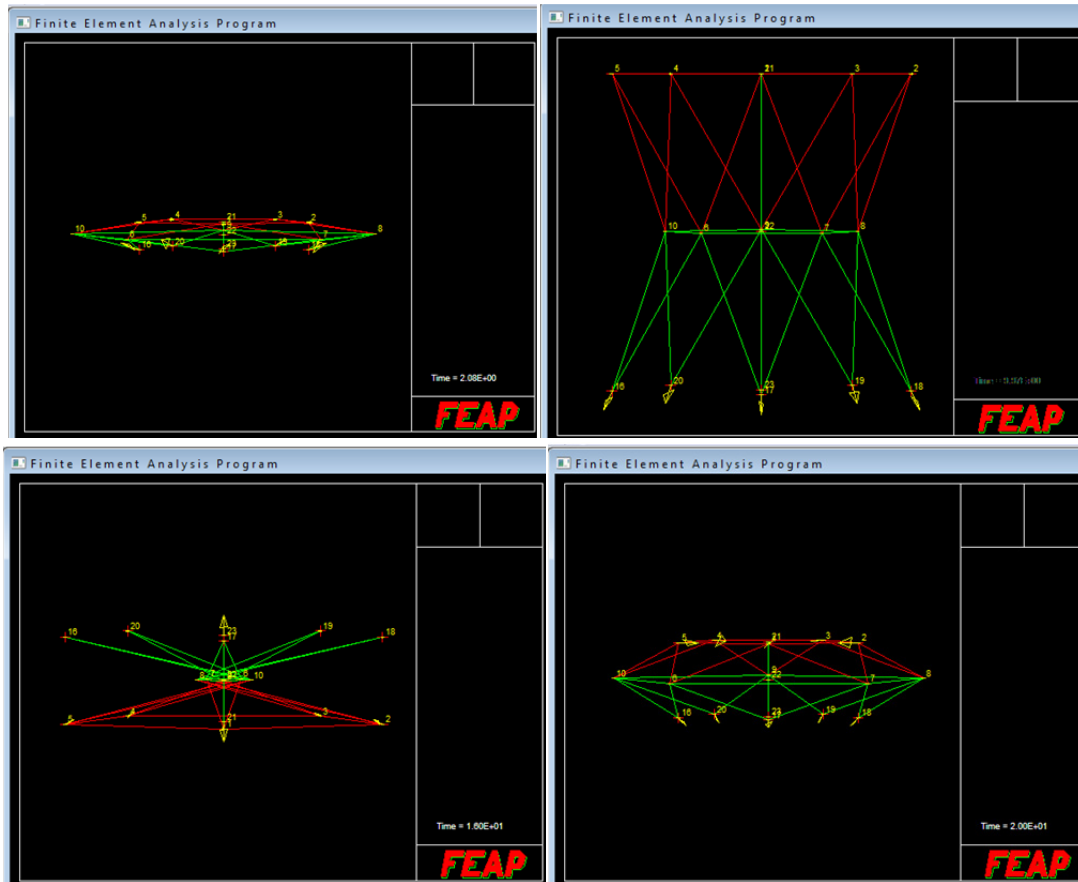


Fig. 4.52: Dynamic deployment of the basic unit of pentagonal antiprismatic mast: deployment sequence with (poorly captured) restriction of segment intersection

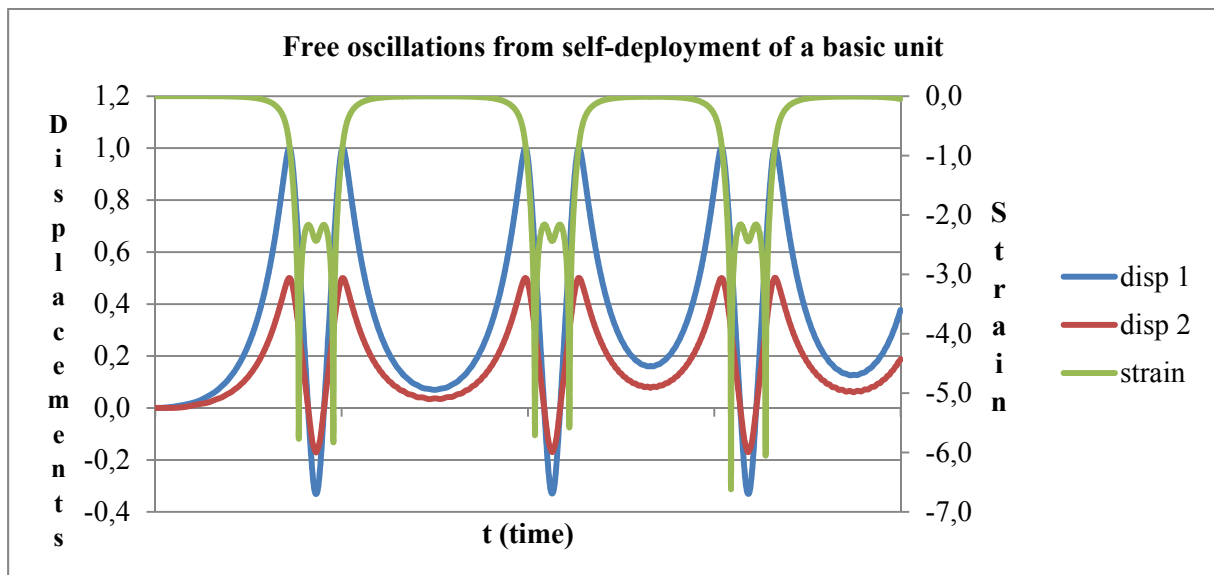


Fig. 4.53: Dynamic deployment of the basic unit of pentagonal antiprismatic mast: deployment sequence with (poorly captured) restriction of segment intersection

initial self-stress ($\sigma_{pre_min} = 5000$) was smaller than $\sigma_{pre_min} = 5989$
 ($EA = 10\ 000$; $R = 0.5$; $h = 0.5$)

For damping the inertial effects and the vibration, two different approaches have been investigated. The most popular, and most importantly numerically easily applicable, damping is the one of Rayleigh.

The solution of second order linear equations by the finite element method leads to the set of equations:

$$\mathbf{M}\ddot{\mathbf{u}}(t) + \mathbf{C}\dot{\mathbf{u}}(t) + \mathbf{K}\mathbf{u}(t) = \mathbf{F}(t) \quad (4.43)$$

Where \mathbf{M} is the mass matrix, \mathbf{C} is the damping, \mathbf{K} is the stiffness matrix, \mathbf{F} the force vector and \mathbf{u} is the vector containing the nodal displacements.

The damping defined as Rayleigh Damping is proportional to the mass and to the stiffness matrix:

$$\mathbf{C} = a\mathbf{M} + b\mathbf{K} \quad (4.44)$$

From this equation it can be deduced that:

$$\Phi^T \mathbf{C} \Phi = a\mathbf{M} + b\mathbf{\Lambda} = 2\zeta\mathbf{\Lambda}^{1/2} \quad (4.45)$$

where Φ is the matrix with the eigenvector of the matrix $(\mathbf{K} - \omega^2\mathbf{M})$ and $\mathbf{\Lambda}$ is a diagonal matrix of the natural frequencies squared, and is the diagonal matrix with the damping ratios. If a specific damping ratio is targeted, the constants a and b in equation (4.44) can be calculated from the equations:

$$\begin{aligned} a &= 2\zeta \frac{\omega_i \omega_j}{\omega_i + \omega_j} \\ b &= 2\zeta \frac{2\zeta}{\omega_i + \omega_j} \end{aligned} \quad (4.46)$$

Consequently, for a specific targeted damping ratio, by numerically checking the natural frequencies (optionally a minimal and a maximal value), the two constants can be determined. The first problem with damping the deployment of the basic segment, that it is only the desired effect that is known, but not the ratio. Further problem opposed from the fact, that during deployment the natural frequencies change. On top of that, numerical problems of simulating deployment with Rayleigh damping has been detected. Disconvergences were found, when (after passing the stress-free configuration) the bracings turn into an upright position. The failure of convergence could be solved by setting b to zero. When the damping matrix is proportional to the mass matrix, though there was no failure of computation at this specific geometrical configuration, but as the bracings rotate inwards, the structure freezes in a position shown in Fig. 4.54. To optimize the damping in a way, that the structure's oscillation around the stress-free position is smaller than the one needed to pass this critical configuration is quite cumbersome.

Ideally the damping of the structure is such, that in the first phase of the deployment it does not make the structure to get stuck in the packed configuration, and allows the fast deployment of the structure. But at the same time, the chosen damping system should also assure that before the deployed configuration the structure smoothly stops.

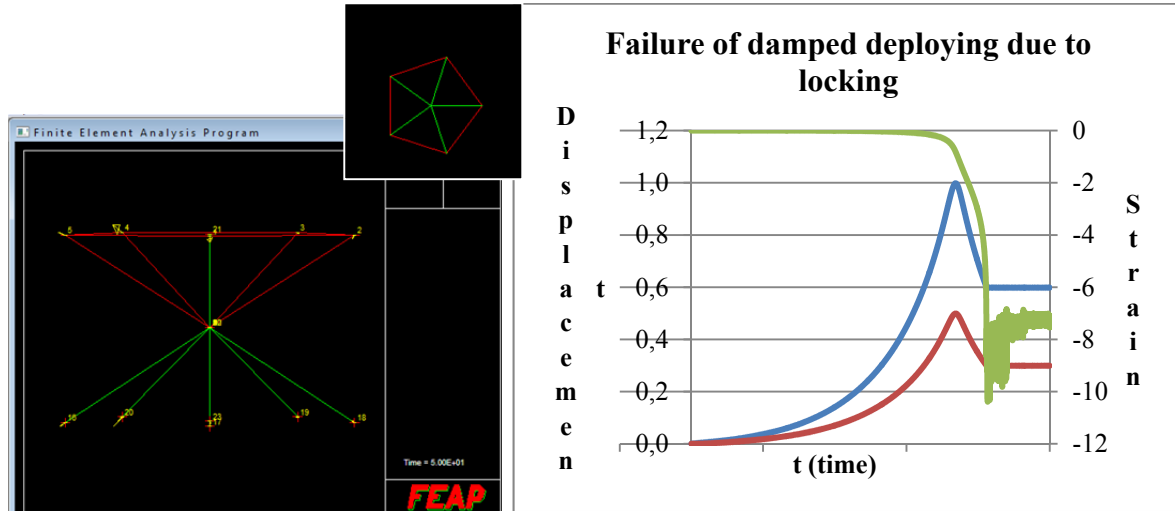


Fig. 4.54: Failure of damped deploying due to locking strain in the elastic bar (in green), nodal vertical displacements of the top facet (in blue) and of the middle polygon (in red)

It can be seen from Fig. 4.55 that choosing a damping that dissipates the energy in function of the horizontal accelerations/or velocities, than the magnitude of the damping will take its maximal value just before the complete deployment of the structure which is ideal for the targeted behavior. In the computation this can be achieved for example by connecting the elastic polygonal nodes to a horizontal bar, that dissipates energy through a linear visco-elastic or plastic constitutive model. However, similarly to the case of the Rayleigh damping, the optimal value of constitutive parameters are not so easy to find because of the locking phenomenon. An even more trivial damping of vibrations and controlling deployment of true nature could be the one controlled by the constitutive model of the flexible horizontal bars. The dissipative behavior of rubber-like materials are nicely presented by the rope, used for bunjy-jumping. The fast damping of oscillations might be of high importance for the investor.

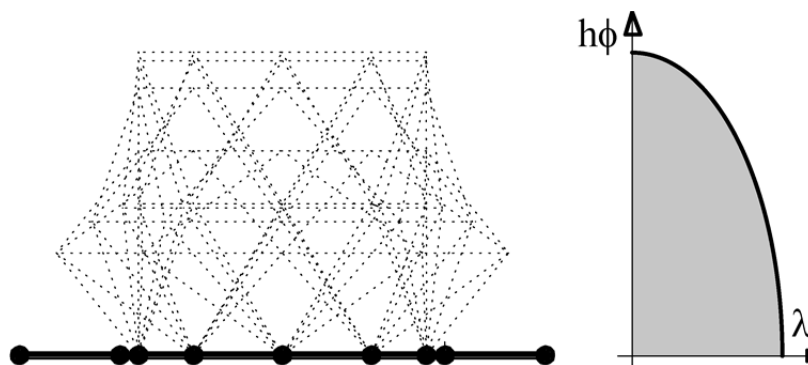


Fig. 4.55: Stretching in function of the current height

4.4 Summary of investigating antiprismatic deployable structures

The analytical investigations were carried out to describe the mechanical behavior of the pop-up column offered by Hegedűs. The results deduced for the basic segment can serve for better understanding the basic characteristics of such structures, as well as for a tool to check numerical results before analyzing more complex structural solutions and for a method of preliminary design of optional architectural solutions (mast, framework, bridge, etc.).

The function of the equilibrium path of the basic unit was defined which manifests instability phenomenon. The critical force and the critical height were explicitly given as well for linear constitutive model. For the representative values of the mechanical and packing behavior, approximations were recommended as a tool for a fast control of numerical results and for preliminary design of architectural applications.

The force-displacement diagram of the multi-storey structure can be constructed from the one of the basic unit with the methodology described for planar structures. Similarly to the planar mast, the typical equilibrium path of the complex antiprismatic structure manifests snap-back phenomenon if the number of the segments is more than two. However, the asymmetry of the force-displacement diagram of the basic unit increases the critical segment number. This means, that though the sudden internal displacements can occur for three-storey structures, these displacements are only significant in the case of larger number of segments. For the critical number, an approximation and the exact explicit form for linear constitutive model has been determined.

For the mechanical characteristics of the basic unit, a parameter study was carried out with finite element numerical simulation. It was shown that the increment of the h/R ratio and the increment of the number of vertices of the polygon lead to a more emphasized asymmetry of the diagram. The more emphasized the asymmetry of the displacement diagram gets, the larger the critical segment number is.

To simulate the packing of the multi-storey structures numerical models were built in FEAP and a self-developed program in MAPLE. The simulation was verified by the comparison of the results with the analytical ones. For the constitutive model of the finitel element analysis logarithmic stretch, for the simulation in MAPLE linear small strains were used.

The finite element simulation of the multi-storey structures was carried out with different displacement controls. After giving examples for the uniform and successive control of the 'alternately stiffened mast' it was shown that by controlling only the displacement of the top nodes the problem of 'post-packed phenomenon' occurs. Two different motions were identified under this definition. The problem of the phenomenon was resolved by defining contact elements between the rigid polygons. This was effectuated by additional nodes placed in the center of the rigid polygons that were linked with a master&slave method to the vertices of the associated polygons. This restricted simulation was performed by controlling the order of the segment-closure with perturbing the axial stiffness of the elastic bars.

In the MAPLE simulation, the typical equilibrium paths were traced by randomly perturbing the last converged solution before each increment of displacement.

For the packing analysis of non-stiffened masts, only uniform control was analyzed. Through the analysis it was shown that if the antiprismatic spatial structure has even sided segments the packing will take effect in two phases; in the first phase every polygon expands, in the second phase every first polygon compresses and every second polygon expands. The transition state is where the bracings turn to an upright position.

For masts consisting of odd number of segments it was shown that in contrary to the planar structure, complete packing might be possible if specific geometry is defined. It was shown, that for a specific radius and n -gon, only one geometric packable configuration exists in the case of three segments. This type of mast is packed only by expanding the polygons. Nonetheless, as the number of the segments is increased, the number of the packable geometric configurations increases as well.

When the non-stiffened mast is controlled only by the displacement of the top facet, the structure's packing pattern for different number of segments is quite chaotic. However, it was found that the system is not completely stochastic. The geometrical configuration of the antiprismatic non-stiffened mast predefines some possible packing patterns. The effect of the number of the segments on the critical force was also investigated.

The biggest advantage of the antiprismatic pop-up mast is the fast deployment of them. However to realize such installation, profound dynamical analysis is necessary. Only the methodology of some possible deployment and vibration controls were presented with emphasizing the problem of possible locking of the structure. This locking phenomenon can be avoided by height- or rotation-limitations in practice.

5 REALIZATION— EXPERIMENTS BY PHYSICAL MODELS, IDEAS FOR CONTROL AND APPLICATIONS

5.1 Physical models

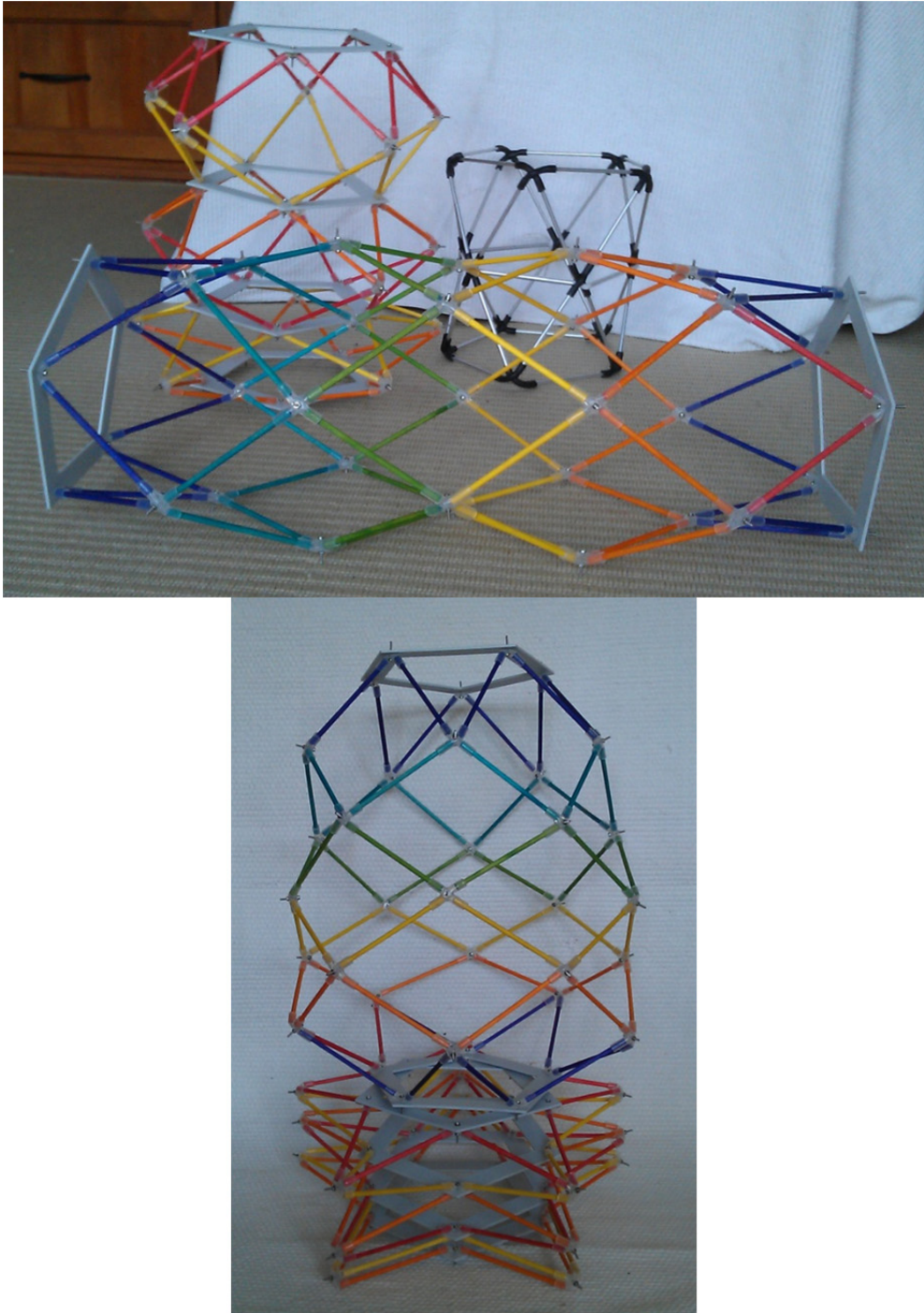


Fig. 5.1: Physical models

For the verification of the results some physical models were built (Fig. 5.1). The rigid bars were either aluminum tubes or timber rods. For modeling the joints, silicon and rubber tubes were used. The stiff polygons were made of plastic. The elastic rods were made of textile covered rubber thread into a tubular stiff bar (Fig. 5.2). The first model confirmed that keeping symmetry, and controlling the displacements to restrain post-packed phenomenon is quite cumbersome without stiffening every second polygon (Fig. 5.2). With the model, the softening behavior was scarcely experimented during packing, which is due to the bending stiffness at the joints. The pop-up behavior even without the elastic bars can also be explained by this behavior. Unfortunately the model of non-stiffened mast was completely un-packable because of asymmetrical motions that locked the structure in a deployed configuration (Fig. 5.4). The asymmetrical freedom of motion is presented in Fig. 5.3

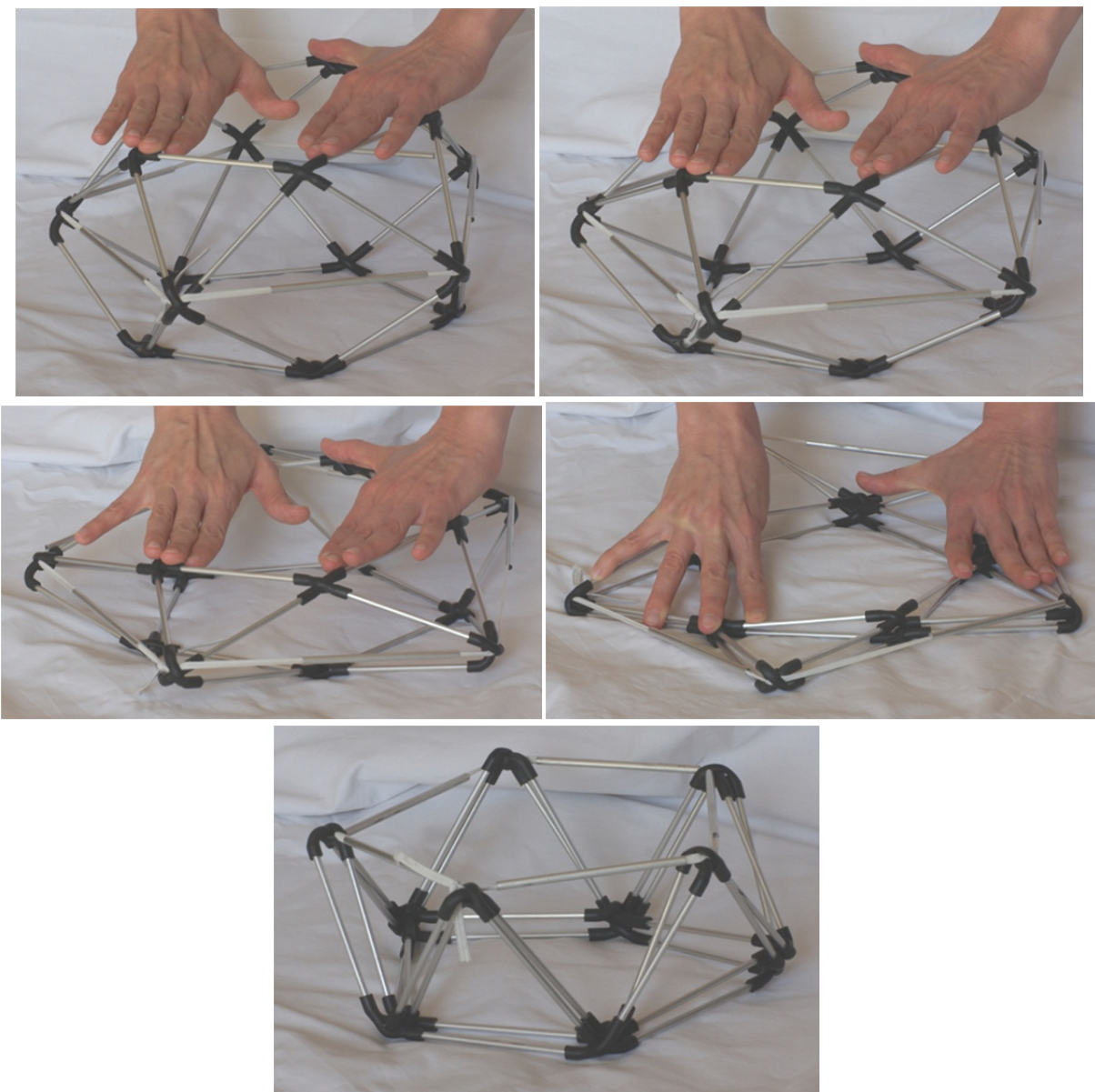


Fig. 5.2: Difficult control of non-stiffened pentagonal unit

Despite the difficulties, with careful joint construction this problem might be handled. During modeling the non-stiffened version of the antiprismatic mast, a novel type of deployable structure was identified (Fig. 5.5). The expandable tube's top and bottom boundaries are rigid polygons, while the resistance of the structure is assured by the bending stiffness of the joint models. This keeps the curved initial configuration. If the two rigid polygons kept parallel, the structure resists to torsional moments very well.

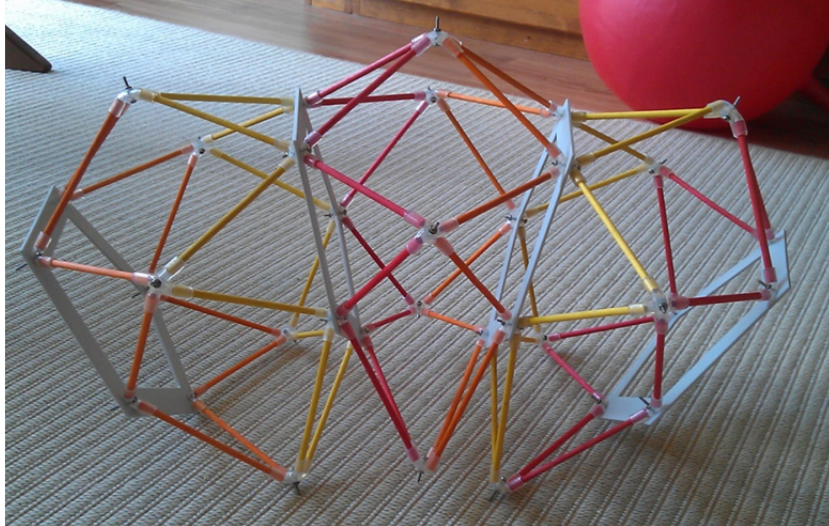


Fig. 5.3: Asymmetrical freedom of motion



Fig. 5.4: Non-stiffened pentagonal structure — locking during packing

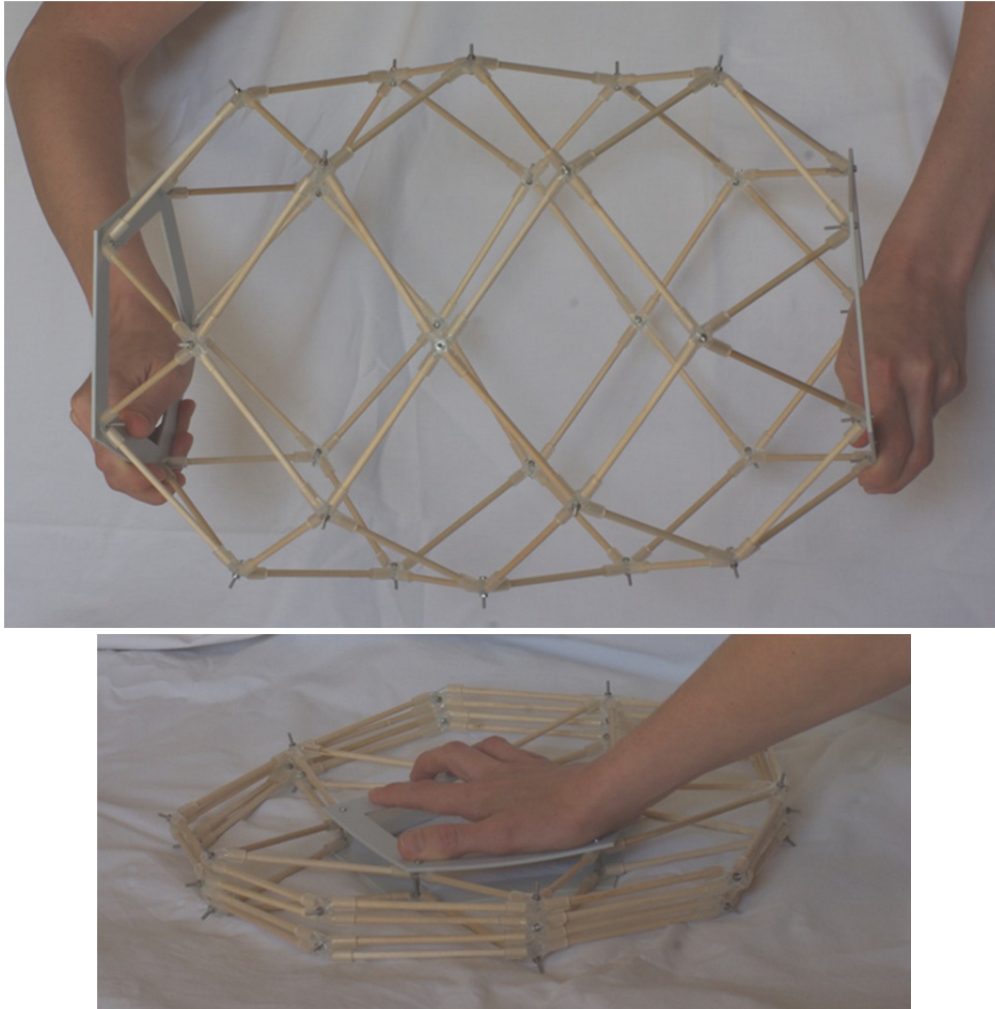


Fig. 5.5: *Non-stiffened pentagonal structure — novel type of deployable structure*

5.2 Ideas for control and application

As a possible application, a pedestrian pop-out bridge application is proposed. The elastic stretchable bars could be of rubberlike material while the rigid bars of a more general stiff, lightweight material. In the deployed configuration the elastic bars should resist to compression forces, too. For that purpose the elastic material could be thread into a tubular stiff bar which is loose and can move freely along the elastic bars in the packed configuration. In the deployed configuration the corresponding joints tighten the stiff bar which has to click into its proper place to be integrated into the structure to ensure the necessary rigidity of the opened bridge. The efficiency of the structure can be raised by keeping it pretensioned in the deployed configuration. The self-stress state can be applied by the elastic bars being still stretched in the opened configuration and by additional longitudinal cables that could be of good help also for the packing control.



Fig. 5.6: Deployable bridge (graphical illustration by E. Kiss)

To build a structure with rubber involved is quite delicate. The biggest problem with rubber is that its relaxation is not to be ignored, its moduli are extremely low and not to mention that with the ozone and UV waves around, its ageing is quite fast. These problems could be somewhat relieved by covering the rubber with a wickered textile that can protect the rubber and limit its lengthening which is also important because of safety considerations. By threading the elastic bars into a rigid stiff tube gives extra protection. However, it is true that these elements can not be prestressed really effectively because of the small moduli of rubber.

The geometry of the antiprismatic masts is attractive even without making them a pop-up structure. If, for example, instead of the elastic bar, a cable is led through the polygon's edges this cable can already effectively stiffen the structure by prestressing it, and at the same time it can serve for deploying the mast. These tensile elements could be either separate ones for each polygon or similarly to the deployable mast designed by Pellegrino, a single cable could be led through the structure that can control the deployment (Fig. 5.7).



Fig. 5.7: Deployment control by one single cable (black stream: active cable, white strings: passive cables)

Unfortunately, the realization of such cable control is very difficult due to the friction at nodes. This was the case with the model in *Fig. 5.7*. Though the deployment was successful, during deploying asymmetrical motions has occurred because of the friction and the non-uniform tightening. Better joint construction and smoother cable surface could have resulted in better performance. Learning from the example of the concrete shell design construction that was mentioned in the second chapter, the cable could be tightened at several, not just one point to keep better the symmetrical conditions.

As mentioned before, all the calculation carried out had the hypothesis of keeping cyclic symmetry of the structure. However, it was shown that even 'alternately stiffened' structures have asymmetrical liberty of motions (see *Fig. 5.3*). Instead of trying to restrain the structure from these motions it could be used as an advantage for adaptive architectural designs. *Fig. 5.8* shows the high flexibility of an 'alternately stiffened' mast, an adaptive arm that can take infinite number of forms.

Finally, some artistic exploration of possible applications of this geometry is presented in *Fig. 5.9*.

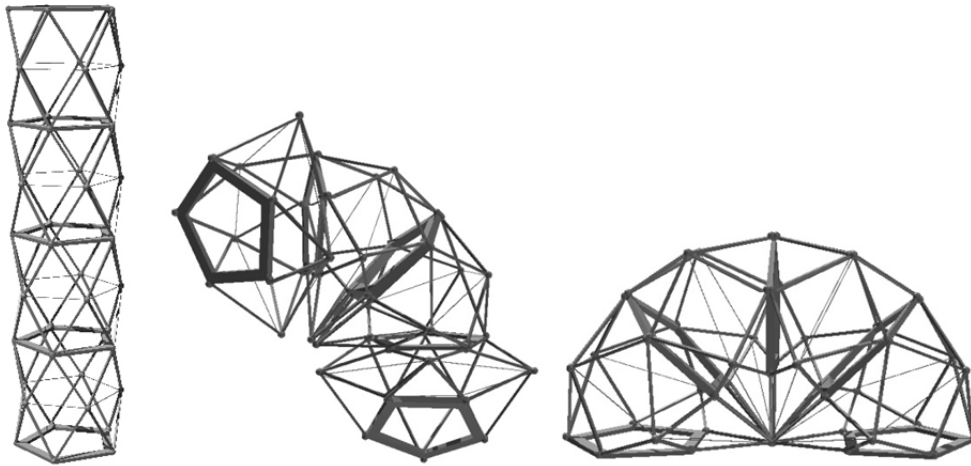


Fig. 5.8: Shape morphing antiprismatic arm [Friedman et al., 2011/4]

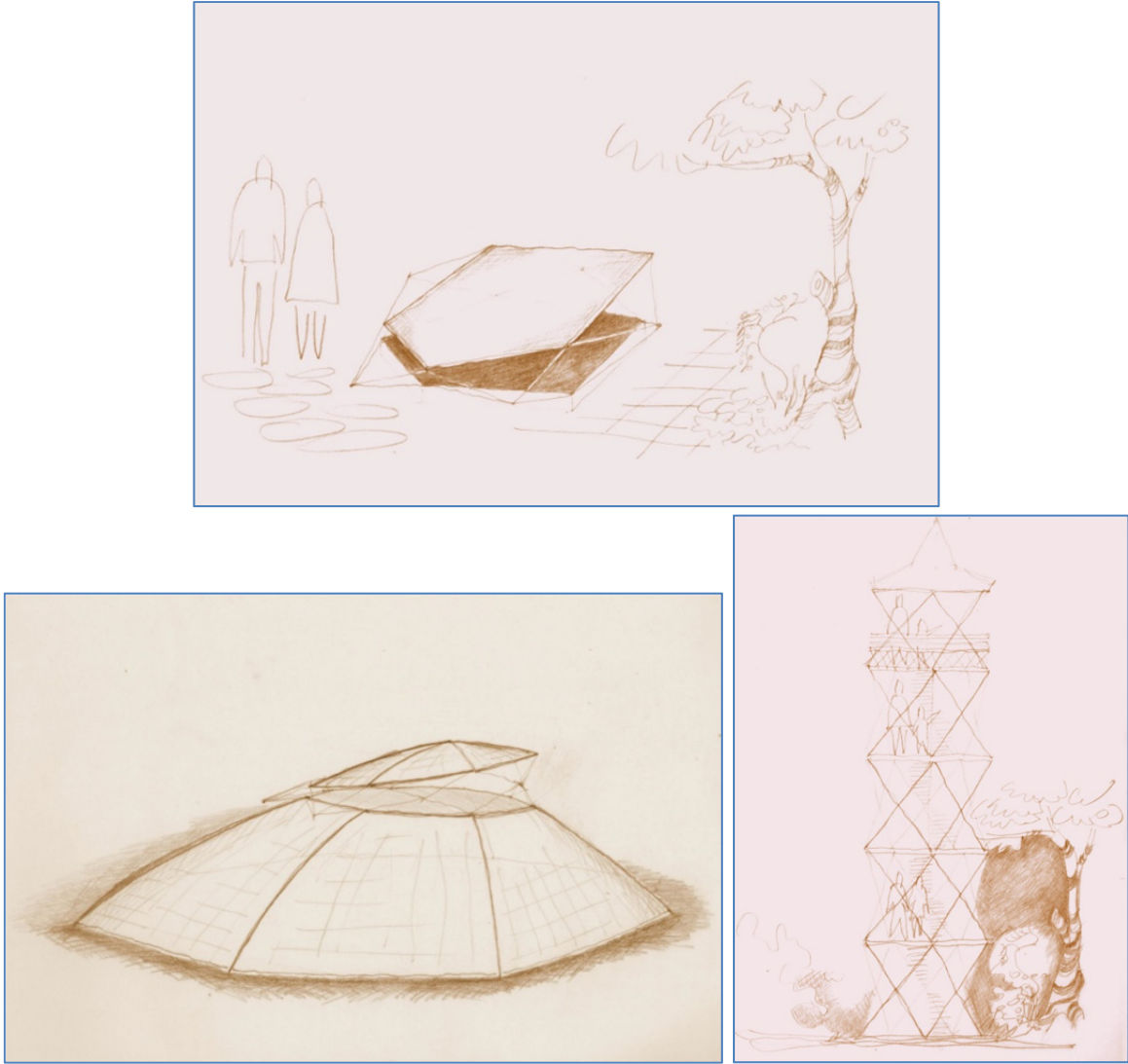


Fig. 5.9: Artistic exploration of possible utilization (transom window, ventilation of dome, look-out tower by E. Kiss)

6 SUMMARY, FURTHER RESEARCH PERSPECTIVES

6.1 Summary

In the following thesis, after a short historical outline an extensive but not exhaustive review on different transformable systems — retractable roofs, deployable and retractable pantographic lattice systems, tensegrity structures, soft membrane structures and pneumatic systems — used in architecture and civil engineering will be given. Though the main research topic of the authors within the theme of transformable structures is just a small slice, this study was carried out to explore earlier and current research and technologies to demonstrate the wide range of available systems, their historical background and their potential in the future in order to prove the actuality of the selected topic.

After the architectural review, structures undergoing large displacements and instability phenomenon were highlighted in the research. First the analytical and numerical resolutions of some basic snap-through type lattice structures were carried out, starting with the static and dynamic analysis of a shallow truss and followed by the deployment analysis of the basic unit of the snap-through type structure of Zeigler which was scrutinized by Gantes. The behavior of these structures has been already examined before by several researchers, but it was a good start to familiarize with structures undergoing large displacements and instability phenomenon. Finally a specific system, namely the deployable antiprismatic lattice structure has been chosen for investigation, because its mechanical behavior has not yet been thoroughly analyzed. This cylindrical structure, derived from the well known yoshimura origami pattern and proposed by Hegedűs, is characterized by its pop-up deployment due to the energy accumulated from lengthening some bars during packing. Zero deployment-load corresponds both to the fully deployed and the compact configuration, the latter being an unstable equilibrium state corresponding to the maximal internal energy.

It is true that the antiprismatic pop-up system has been proposed almost two decades ago, but due to the lack of popularity no practical application has been offered yet. The main goal of the dissertation was to investigate the general behavior of the specific system to blaze a trail towards the architectural application of this system by providing designing tools, profound analysis of packing behavior, ideas of applications.

In this dissertation, the emphasis was mainly taken to the packing behavior. First, a simplified planar model was identified sharing similar, highly nonlinear packing behavior. For both the 2D and the 3D structures numerical simulation of the packing was performed with different type of controls and the results were confirmed by analytical investigations. The research clarifies the mechanical behavior of the chosen system, provides tools to simulate the packing of the structure, and gives very simple approximations for main mechanical characteristics of the antiprismatic system in order to facilitate preliminary design and verification of the numerical results. Within the framework of the thesis a novel type of system (further called as *not-stiffened antiprismatic structure*), slightly deviating from the

original one (further called as *alternately stiffened antiprismatic structure*), was also investigated. The antiprismatic system proposed by Hegedűs is constructed from identical double antiprisms with an elastic middle polygon and rigid polygons in the boundaries. The modified model eliminates the rigid internal polygons; the pop-up column is constructed from continuously rotating elastic polygons with two rigid polygons on the top and on the bottom.

For the specific systems, small physical models were built and presented in this work, which led to the proposal of a novel type of expandable tube.

An attempt was given to provide ideas for application of antiprismatic structures by combining the investigated system and different learnt existing systems from the architectural review. Different ideas for applications and control systems were sketched.

Concluding the remarkable results of the thesis that can be considered as new scientific achievements are herein concluded:

1. Parametric analysis of basic antiprismatic and planar segment, proposal for approximations of main mechanical parameters for preliminary design [Friedman et al., 2011/5]

The general mechanical behavior and parameter analysis of the elementary segment of the alternately stiffened pop-up planar mast and the elementary segment of the alternately stiffened pop-up antiprismatic mast were analytically derived. It was shown that these structures are undergoing instability phenomenon during packing. The force-displacement diagram, the critical force and critical height of the mentioned structures were defined. For the antiprismatic pop-up system approximations were given for the following properties:

- the maximal lengthening of the bars of the middle polygon for complete deployment;
- the critical segment-height;
- the critical packing force;

Numerical parameter analysis was carried out with non-linear finite element simulation to define the influence of the different geometrical and mechanical parameters on the characteristic of the force-displacement diagram by supposing logarithmical strains. It was shown that the asymmetry of the force-displacement diagram depends on the number of the vertex of the polygons and on the ratio of the initial segment height and the radius of the polygons. By increasing the number of the vertex of the polygons or by increasing the ratio the asymmetry will be more significant, that is, the critical height/initial height ratio will decrease.

2. Analysis of the complex alternately stiffened planar and antiprismatic structure [Friedman et al., 2011/6]

The force-displacement diagram of the complex, multi-storey alternately stiffened planar and antiprismatic packable structure was derived from the force-displacement diagram of the elementary segment. These diagrams were investigated in the case of

different control possibilities. It was shown that the **uniform packing** of the analyzed structure **is theoretically possible** by only controlling the displacement of the boundary nodes. However it was also demonstrated that **this path is not typical**, and in reality should be rather mentioned as impossible. The packing of the alternately stiffened deployable structure can be controlled successively as well by closing the elementary segments one after the other. **If only the displacement of the boundary nodes is controlled, the typical packing path is not uniform; the segments close in a random order.** The analytical methodology to construct the typical diagram was determined in the case of ignoring the self-weight of the structure and with taking the self-weight into account as well. The results were confirmed by non-linear finite element simulations and also by a self-programmed numeric simulation based on the minimal energy principal. The main complexity of the numeric simulation is to avoid the segment to turn upside-down after having been completely packed (herein called as post-closure phenomenon. This was modeled by defining contact forces in between the polygons in the finite element analysis and with eliminating the closed segment in the self-developed simulation.

3. Non-smooth packing of the alternately stiffened structure [Friedman et al., 2011/6]

Deriving from the methodology of constructing the force-displacement diagram of the alternately stiffened structure, it was shown that **after a critical number of segments the typical packing of the structure is not smooth** if it is only the displacement of the boundary polygons that is controlled. This is **due to the snap-back phenomenon occurring in the force-displacement diagram of the complex, multi-storey structure.**

A new expression was deduced; namely the **critical segment number**. With the assumption that no segment closes **simultaneously, if the number of the segments is more than critical sudden intermediate snapping will be sure to take place during packing.** If the number of segments is less than critical, the length of the sudden displacement will be smaller than the initial height of the elementary segment.

It is important to lay down that **snap-back phenomenon may occur in the case of fewer segments than the critical number.** It was shown that (independently to the geometry of the antiprism) **this phenomenon already arouses when the number of the segments is more than two** if no self-weight of the structure is taken into account. Nonetheless strong converging problem and, in reality, non-negligible inertial and impact effects occur when the sudden displacements are larger than the segment-height.

4. Analysis of non-stiffened antiprismatic structures

The mechanical behavior and packability conditions of the modified, non-stiffened antiprismatic mast were investigated. It was proven that the **non-stiffened planar structure can be only packed if the number of the segments is even.** In contrary, the existence of packable geometrical configurations was proved in case of odd number of segments for the spatial, not-stiffened antiprismatic **structure.** Deriving from the not-

stiffened structure, **a novel type of deployable structure was identified, a cylindrical lattice structure that can be packed to plane by expansion.**

5. Dynamic analysis of antiprismatic structures

Different numerical and technical possibilities of controlling the deployment and generated vibrations of the basic unit were presented. It was shown that the main problem of deployment control is imposed by the locking phenomenon, occurring after passing the geometrical configuration corresponding to the bracings being in an up-right position. This phenomenon can be overtaken by limiting the rotations of bracings or the complete height of the segment.

6.2 Further research perspectives

The main target of the research carried out was to blaze a trail towards the architectural and industrial application of antiprismatic deployable systems.

General mechanical behavior of the pop-up mast has been explored, but the calculations have been only verified for linear small strains and logarithmic strains. The effect of constitutive models of different realistic and applicable materials on the characteristics of these structures could be interesting to further investigate.

It was shown that the packing of the non-stiffened antiprismatic mast shows a chaotic system, but still regularities can be observed. However, within the confines of the thesis, a compact explanation of the regularity has not yet been found.

The main deficiency of the thesis is the uncompleted dynamic analysis and vibration control of the deployment, as well as of the snap-back phenomenon in the cases of structures with large sudden displacements.

The research has resulted in a novel type of deployable structure, to which mechanical analysis and exploration of possible applications could be carried out.

Another research interest of the author is the further investigation of possible architectural applications and packing/deploying control, and the evaluation of the given sketches by cost-benefit analysis and comparison with similar systems.

During the research of controlling the deployment of antiprismatic structures with continuous, spirally driven cables, the idea to use this control for truss system derived from the inclined yoshimura pattern came up, which might be worthwhile to investigate.

APPENDIX A: STATIC AND KINEMATIC DETERMINACY OF ANTIPRISMATIC STRUCTURES⁴

In accordance with the well-known Maxwell's rule, the condition for stiffness of a spatial truss system is:

$$b = 3j - c \quad (\text{A1})$$

and for planar structures:

$$b = 2j - c \quad (\text{A2})$$

Where b is the number of the bars, j is the number of the joints and c is the number of the constraints.

Let's consider the antiprismatic truss system shown in *Fig. A1*. In accordance to the Maxwell's rule, the antiprismatic structure is rigid, as in the case of an n -gon the parameters are:

$$\begin{aligned} b &= 3n \\ j &= 2n \\ c &= 3n \end{aligned} \quad (\text{A2})$$

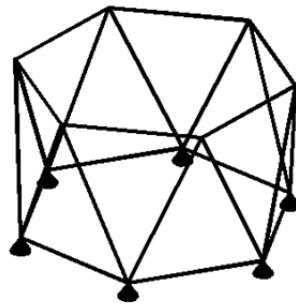


Fig. A1: Antiprismatic truss structure

Nonetheless, in the case of some unfortunate topological or geometrical reasons there can be structures that satisfy though the equation (A1/A2) but still prove to be not stiff. For example, the truss system in *Fig. A2a* satisfies the equation (A2), but by changing its geometry, the truss turns to be both statically and kinematically indeterminate (*Fig. A2b*).

If the equilibrium equation of the antiprismatic truss can be written with the equation:

$$As + q = 0 \quad (\text{A3})$$

⁴ The problem herein is explained on the bases of [Tarnai, 2001]

(where \mathbf{s} is the vector composed of forces in the bars, and \mathbf{q} is the vector of the components of loads at the nodes)

than the static/kinematic determinacy of the structure is defined by the determinant of the matrix \mathbf{A} . The satisfaction of the condition in (A1) assures that the number of the equations and the number of the unknowns are equal. However, this condition does not guarantee yet that these equations are independent and accordingly that the matrix \mathbf{A} is not singular.

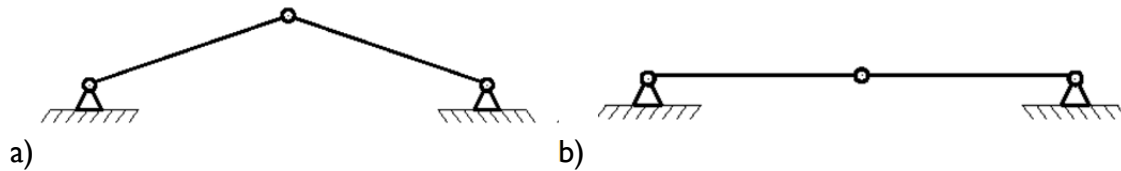


Fig. A2: Changing stiffness with changing geometry

Without going into the details, the determinant of the matrix \mathbf{A} is zero if the number of the vertices of the polygon is even, and non-zero if it is odd. While the structures formed from odd-sided pentagonal antiprisms are stiff, the ones formed from even-sided pentagonal antiprisms are finite mechanisms.

APPENDIX B: ANALYSIS OF THE SNAPPING-THROUGH OF A SHALLOW TRUSS

Quasi static analytic and finite element formulation for tracing equilibrium path and for finding critical points

Let's consider a symmetrical shallow truss with height 'h' and initial bar length 'l' with cross sections 'A' loaded with a vertical force (Fig. B1), and supposing that the elastic constitutive behavior of each bar is described by Saint-Venant-Kirchoff material model with 'E' Young's modulus.

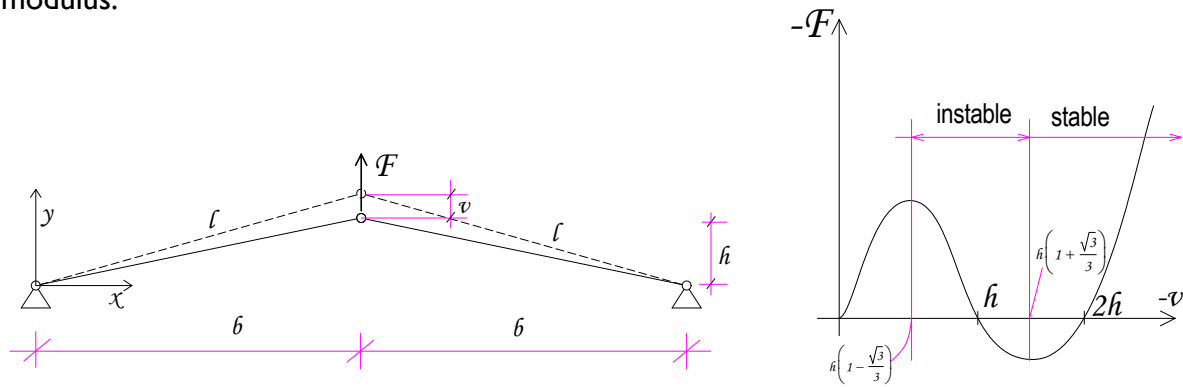


Fig. B1: shallow truss and its force-displacement diagram

Taking into account the symmetry of the structure the compressed (or tensioned) length of the bars in function of the vertical displacement of the middle joint (v) is:

$$l(v) = \sqrt{L^2 - h^2 - (h + v)^2} = \sqrt{L^2 + 2hv + v^2}$$

Thus the kinematic equation:

$$\varepsilon(v) = \frac{l(v)}{L} - 1 = \frac{\sqrt{L^2 + 2hv + v^2}}{L} - 1$$

The constitutive equations:

$$S(v) = S_1(v) = S_2(v) = EA \cdot \varepsilon(v) = EA \left(\frac{\sqrt{L^2 + 2hv + v^2}}{L} - 1 \right)$$

The equilibrium equation:

$$F(v) = (S_1(v) + S_2(v)) \cdot \frac{(h+v)}{l(v)} = \frac{2EA}{L^3} (h+v) \left(hv + \frac{v^2}{2} \right)$$

This gives the equilibrium path shown in Fig B1.b.

The critical equilibrium states correspond to:

$$\frac{\partial F(v)}{\partial v} = 0$$

where

$$\frac{\partial F(v)}{\partial v} = \frac{2EA}{L^3} \cdot \left(hv + \frac{v^2}{2} \right) + (h+v) \cdot (h+v)$$

The zero points of the quadratic equation will be at

$$v_{cr1,2} = -h \left(1 \mp \frac{\sqrt{3}}{3} \right)$$

That corresponds to the maximum and the minimum value of the load:

$$F_{cr,1} = \frac{2EA}{L^3} (h + v_{cr1}) \left(hv + \frac{v_{cr1}^2}{2} \right) = \frac{-2\sqrt{3}EA}{9L^3} h^3$$

$$F_{cr,2} = \frac{2EA}{L^3} (h + v_{cr2}) \left(hv + \frac{v_{cr2}^2}{2} \right) = \frac{2\sqrt{3}EA}{9L^3} h^3$$

Writing the weak form with the non-linear finite element formulation:

$$\mathbf{d} = \begin{pmatrix} 0 \\ 0 \\ 0 \\ v \end{pmatrix} \quad \mathbf{x} = \begin{pmatrix} 0 \\ 0 \\ b \\ h \end{pmatrix} \quad \mathbf{H} = \begin{pmatrix} 1 & 0 & -1 & 0 \\ 0 & 1 & 0 & -1 \\ -1 & 0 & 1 & 0 \\ 0 & -1 & 0 & 1 \end{pmatrix} \quad \mathbf{F} = \begin{pmatrix} R_x \\ R_y \\ F_x \\ F_y \end{pmatrix}$$

$$E_{11} = \frac{1}{L^2} \cdot \underbrace{\begin{pmatrix} 0 \\ 0 \\ b \\ h \end{pmatrix}^T \cdot \begin{pmatrix} 1 & 0 & -1 & 0 \\ 0 & 1 & 0 & -1 \\ -1 & 0 & 1 & 0 \\ 0 & -1 & 0 & 1 \end{pmatrix} \cdot \begin{pmatrix} 0 \\ 0 \\ 0 \\ v \end{pmatrix}}_{\mathbf{h} \cdot \mathbf{v}} + \frac{1}{2L^2} \cdot \underbrace{\begin{pmatrix} 0 \\ 0 \\ 0 \\ v \end{pmatrix}^T \cdot \begin{pmatrix} 1 & 0 & -1 & 0 \\ 0 & 1 & 0 & -1 \\ -1 & 0 & 1 & 0 \\ 0 & -1 & 0 & 1 \end{pmatrix} \cdot \begin{pmatrix} 0 \\ 0 \\ 0 \\ v \end{pmatrix}}_{\mathbf{v}^2} \quad E_{11} = \frac{1}{L^2} \cdot (\mathbf{h} \cdot \mathbf{v} + \mathbf{v}^2) \quad S_{11} = \frac{E}{L^2} \cdot \left(\mathbf{h} \cdot \mathbf{v} + \frac{1}{2} \cdot \mathbf{v}^2 \right)$$

$$f_{\text{int}} = \frac{1}{L} \cdot H^T \cdot (x + d) \cdot S_{11} \quad f_{\text{int}} = \frac{1}{L} \cdot \begin{pmatrix} 1 & 0 & -1 & 0 \\ 0 & 1 & 0 & -1 \\ -1 & 0 & 1 & 0 \\ 0 & -1 & 0 & 1 \end{pmatrix} \cdot \begin{pmatrix} 0 \\ 0 \\ b \\ h+v \end{pmatrix} \cdot \frac{E}{L^2} \cdot \left(h \cdot v + \frac{1}{2} \cdot v^2 \right) = \frac{E}{L^3} \cdot \begin{pmatrix} -b \\ -h-v \\ b \\ h+v \end{pmatrix} \cdot (h \cdot v + v^2)$$

$$F = \begin{pmatrix} R_{x,1} \\ R_{y,1} \\ F_x \\ F_y \\ R_{x,2} \\ R_{y,2} \end{pmatrix} \quad d_1 = \begin{pmatrix} 0 \\ 0 \\ u \\ v \end{pmatrix} \quad d_2 = \begin{pmatrix} u \\ v \\ 0 \\ 0 \end{pmatrix} \quad x_1 = \begin{pmatrix} 0 \\ 0 \\ b \\ h \end{pmatrix} \quad x_2 = \begin{pmatrix} -b \\ h \\ 0 \\ 0 \end{pmatrix} \quad H^1 = \begin{pmatrix} 1 & 0 & -1 & 0 \\ 0 & 1 & 0 & -1 \\ -1 & 0 & 1 & 0 \\ 0 & -1 & 0 & 1 \end{pmatrix}$$

$$E_{11}^{(1)} = \frac{1}{L^2} \cdot \begin{pmatrix} 0 \\ 0 \\ b \\ h \end{pmatrix}^T \cdot \begin{pmatrix} 1 & 0 & -1 & 0 \\ 0 & 1 & 0 & -1 \\ -1 & 0 & 1 & 0 \\ 0 & -1 & 0 & 1 \end{pmatrix} \cdot \begin{pmatrix} 0 \\ 0 \\ u \\ v \end{pmatrix} + \frac{1}{2L^2} \cdot \begin{pmatrix} 0 \\ 0 \\ u \\ v \end{pmatrix}^T \cdot \begin{pmatrix} 1 & 0 & -1 & 0 \\ 0 & 1 & 0 & -1 \\ -1 & 0 & 1 & 0 \\ 0 & -1 & 0 & 1 \end{pmatrix} \cdot \begin{pmatrix} 0 \\ 0 \\ u \\ v \end{pmatrix}$$

For element 1:

$$E_{11}^{(1)} = \frac{1}{L^2} \cdot \left(b + h \cdot v + \frac{1}{2} \cdot u^2 + \frac{1}{2} \cdot v^2 \right) \quad S_{11}^{(1)} = E \cdot E_{11}^{(1)} = \frac{E}{L^2} \cdot \left(b \cdot u + h \cdot v + \frac{1}{2} \cdot u^2 + \frac{1}{2} \cdot v^2 \right)$$

For element 2:

$$E_{11}^{(2)} = \frac{1}{L^2} \cdot \left(-b \cdot u - h \cdot v + \frac{1}{2} \cdot u^2 + \frac{1}{2} \cdot v^2 \right) \quad S_{11}^{(2)} = E \cdot E_{11}^{(2)} = \frac{E}{L^2} \cdot \left(-b \cdot u - h \cdot v + \frac{1}{2} \cdot u^2 + \frac{1}{2} \cdot v^2 \right)$$

The weak form with the finite element formulation:

$$K^{(e)} = K_m^{(e)} + K_g^{(e)} \quad K_m^{(e)} = \frac{A}{L_e} \cdot H^T \cdot (x_e + d_e) \cdot E \cdot \frac{A}{L_e^2} \cdot (x^T + d^T) \cdot H \quad K_g^{(e)} = \frac{A S_{11}^{(e)}}{L_e} \cdot H$$

$$\text{Lin}(r_e(d_e)) = r_e(d_e) + K^{(e)} \Delta u$$

$$K_m^{(1)} = \frac{EA}{L^3} \cdot \begin{pmatrix} 1 & 0 \\ 0 & 1 \end{pmatrix} \cdot \begin{pmatrix} b+u \\ h+v \end{pmatrix} \cdot \begin{pmatrix} b+u \\ h+v \end{pmatrix}^T \cdot \begin{pmatrix} 1 & 0 \\ 0 & 1 \end{pmatrix} = \frac{EA}{L^3} \cdot \begin{bmatrix} (b+u)^2 & (b+u) \cdot (h+v) \\ (b+u) \cdot (h+v) & (h+v)^2 \end{bmatrix}$$

$$K_m^{(2)} = \frac{EA}{L^3} \cdot \begin{pmatrix} 1 & 0 \\ 0 & 1 \end{pmatrix} \cdot \begin{pmatrix} -b+u \\ h+v \end{pmatrix} \cdot \begin{pmatrix} -b+u \\ h+v \end{pmatrix}^T \cdot \begin{pmatrix} 1 & 0 \\ 0 & 1 \end{pmatrix} = \frac{EA}{L^3} \cdot \begin{bmatrix} (-b+u)^2 & (-b+u) \cdot (h+v) \\ (-b+u) \cdot (h+v) & (h+v)^2 \end{bmatrix}$$

$$K_g^{(1)} = \frac{EA}{L^3} \cdot \begin{pmatrix} 1 & 0 \\ 0 & 1 \end{pmatrix} \cdot \left(b \cdot u + h \cdot v + \frac{1}{2} \cdot u^2 + \frac{1}{2} \cdot v^2 \right) \quad K_g^{(2)} = \frac{EA}{L^3} \cdot \begin{pmatrix} 1 & 0 \\ 0 & 1 \end{pmatrix} \cdot \left(-b \cdot u + h \cdot v + \frac{1}{2} \cdot u^2 + \frac{1}{2} \cdot v^2 \right)$$

$$K = K_m^{(1)} + K_g^{(1)} + K_m^{(2)} + K_g^{(2)} = \frac{EA}{L^3} \cdot \left[2 \cdot \begin{bmatrix} b^2 + u^2 & u \cdot (h+v) \\ u \cdot (h+v) & (h+v)^2 \end{bmatrix} + 2 \cdot \begin{pmatrix} 1 & 0 \\ 0 & 1 \end{pmatrix} \cdot \left(h \cdot v + \frac{1}{2} \cdot u^2 + \frac{1}{2} \cdot v^2 \right) \right]$$

Numerical examples

The aim of the analysis of the snapping-through shallow truss was to familiarize with the different procedures of treating instability phenomenon (linear and non-linear instability, direct calculation of critical point, arch-length method.. etc.).

First the force-displacement diagram was traced (Fig. B2b) numerically with an incremental analysis, by controlling the displacement of the top node. For the analysis, a frame model was used, the joint was modeled with a master&slave method. It was shown, that a force-controlled simulation does not give back the equilibrium path because of the snap-back behavior of the structure (Fig. B2b).

In reality, the snap-through occurs suddenly, causing non-negligible inertial effects (Fig B3) and vibration of the structure. For that, a mixed, static-dynamic approach was used for the simulation. Until the critical point, the arch-length method can be applied with an interactive control. When the tangent stiffness matrix turns singular, a switch is applied to dynamic analysis, giving a more realistic modeling of the structure.

Without any damping, the structure keeps oscillating around the equilibrium point (Fig. B2a, pink line Fig. B2b, blue line). The magnitude of the damping controls this vibration after the snapping-through.

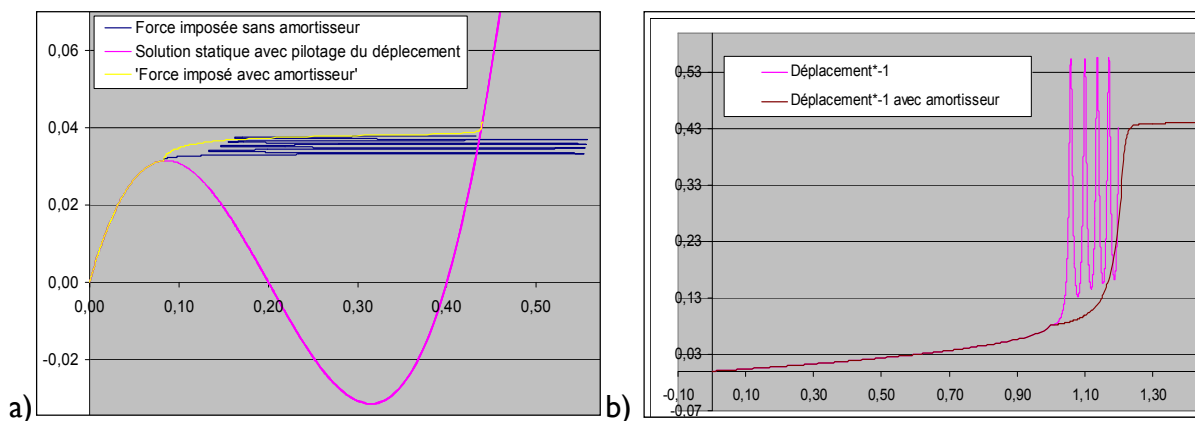


Fig. B2 Force-displacement diagram with displacement control (in pink), with incremental force control (in yellow) and with additional damping (in blue) (a); Displacements in function of the time with (in brown) and without damping (in pink) with force control

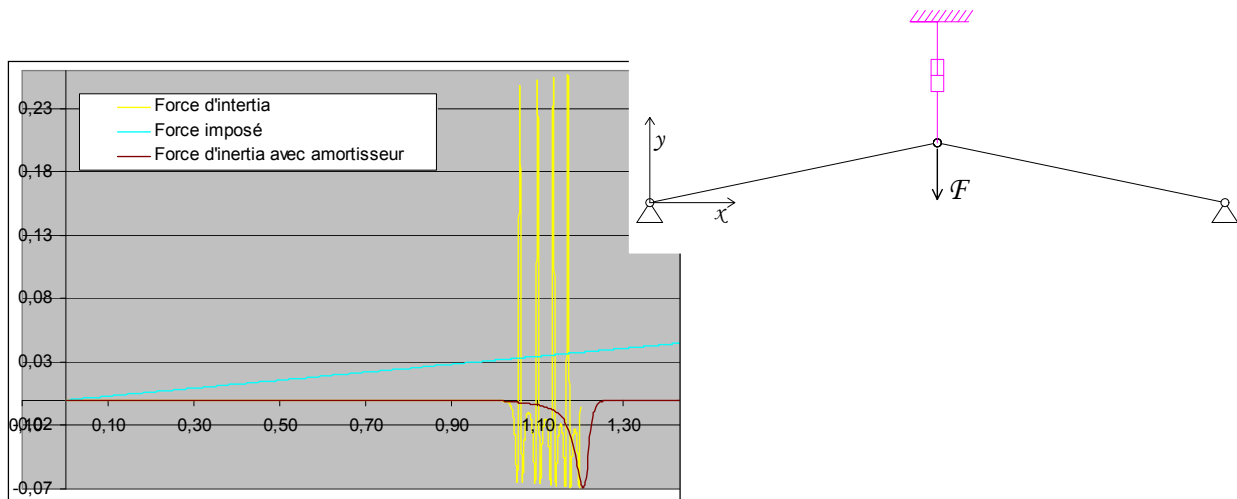


Fig. B3 Inertial effect of snapping through with damping (in brown) and without damping (in yellow) and the imposed increasing force (in blue), and damping model used for the simulation.

For facilitating the complexity of changing analysis during simulation, the snapping-through can be simulated by an only dynamical approach, if the increment of the force imposed is not too large. Fig. B4 shows the force-displacement diagram for forces with different speed of increment.

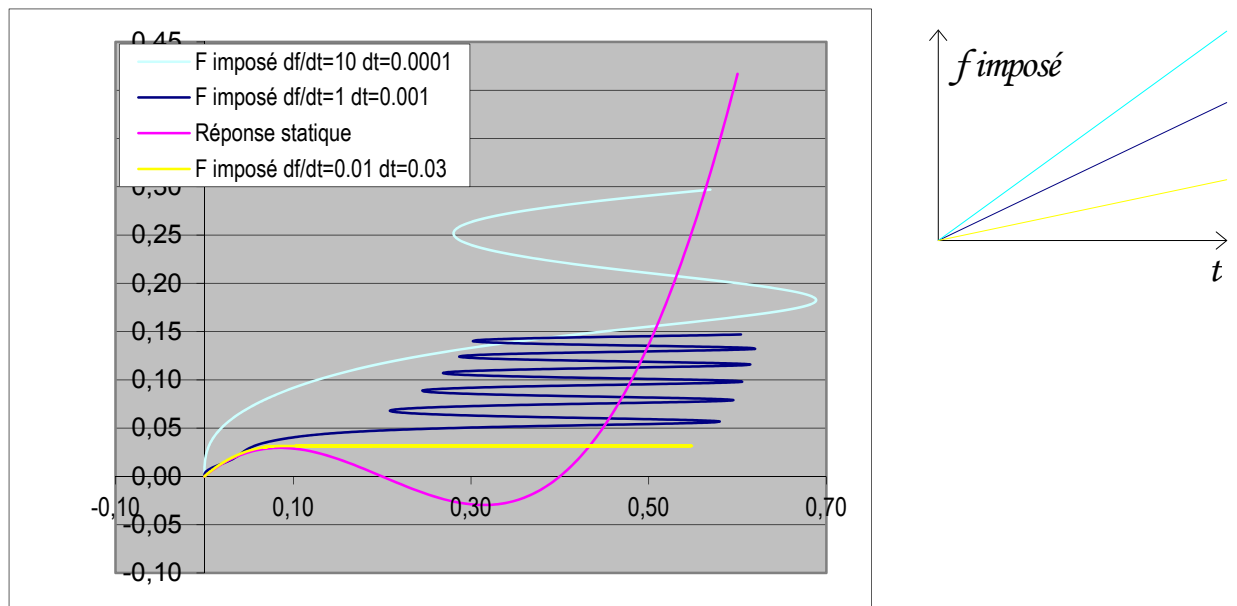


Fig. B4 Force displacement diagram with only dynamical approach: simulation with three different speeds of force increment and the equilibrium path

APPENDIX C: ANALYSIS OF THE BASIC UNIT OF A SNAP-THROUGH TYPE PANTOGRAPHIC DEPLOYABLE STRUCTURE

As an example the force-displacement diagram of the basic element of self-locking deployable structures are herein presented that can be used for planar assemblies (Fig. C1). The outer SLEs would form a simple pantographic mechanism without the inner SLEs. The diagram was plotted from data gained from a numeric simulation (run by FEAP) with displacement control. The center bottom joint was fixed and the center top node was vertically displaced upwards until complete closure. It can be seen from Fig. A1 that no stresses occur in the outer SLEs, and that both, the deployed ($u/h=0$) and the closed ($u/h=1$) configurations correspond to zero force and a stress-free state.

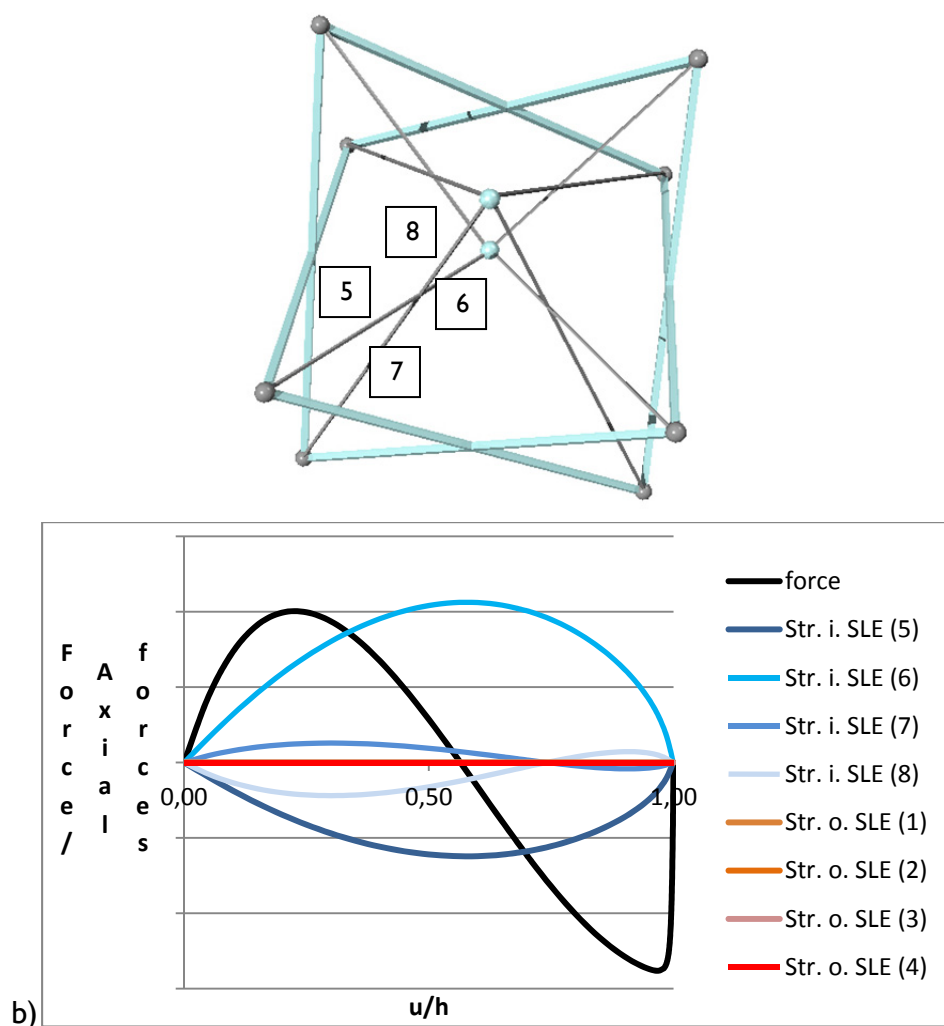


Fig. C1: Packing simulation of self-locking pantographic structures: force displacement diagram and the axial forces in the scissors

APPENDIX D: ENERGETICAL APPROACH FOR THE CALCULATION OF PLANAR AND ANTIPRISMATIC SELF-DEPLOYABLE STRUCTURES

DI. Calculation of the planar structure with energetic approach

DI.1 Analysis of basic segment

The total potential energy of the basic segment can be written in the form:

$$\begin{aligned}\Pi_{\text{ext}}(h^\varphi) &= -2N(h_0 - h^\varphi) \\ \Pi_{\text{int}}(h^\varphi) &= +\frac{1}{2}EA2r_0[\lambda_i(h^\varphi) - 1]^2 \\ \Pi(h^\varphi) &= \Pi_{\text{ext}}(h^\varphi) + \Pi_{\text{int}}(h^\varphi) = -2N(h_0 - h^\varphi) + EA r_0[\lambda_i(h^\varphi) - 1]^2\end{aligned}\quad (\text{D1})$$

The first derivative of the total potential energy:

$$\frac{\partial \Pi(h^\varphi)}{\partial h^\varphi} = 2N + 2EA r_0[\lambda(h^\varphi) - 1]\lambda'(h^\varphi) = 2N - \frac{2EA}{r_0} h^\varphi \left[1 - \frac{2}{\sqrt{4 + \frac{(h_0)^2 - (h^\varphi)^2}{(r_0)^2}}} \right] \quad (\text{D2})$$

where

$$\lambda'(h^\varphi) = \frac{\partial \lambda(h^\varphi)}{\partial h^\varphi} = \frac{1}{\sqrt{4 + \frac{(h_0)^2 - (h^\varphi)^2}{(r_0)^2}}} \frac{-h^\varphi}{(r_0)^2} \quad (\text{D3})$$

At the equilibrium state the total potential energy has stationary point, which is at:

$$\frac{\partial \Pi(h^\varphi)}{\partial h^\varphi} = 0 \Rightarrow N(h^\varphi) = \frac{EA}{r_0} h^\varphi \left[1 - \frac{2}{\sqrt{4 + \frac{(h_0)^2 - (h^\varphi)^2}{(r_0)^2}}} \right] \quad (\text{D4})$$

Equation (D4) corresponds to the equilibrium function already given in (3.8).

To decide whether the equilibrium state is stable or not, the sign of the second derivative of the total potential energy is needed. The second derivative is:

$$\frac{\partial^2 \Pi(h^\varphi)}{\partial h^{\varphi^2}} = -\frac{2EA}{r_0} \left\{ 1 - \frac{2}{\sqrt{4 + \frac{(h_0)^2 - (h^\varphi)^2}{(r_0)^2}}} - \frac{2(h^\varphi)^2}{r_0^2 \left[4 + \frac{(h_0)^2 - (h^\varphi)^2}{(r_0)^2} \right]^{3/2}} \right\} \quad (D5)$$

In the critical point the second derivative turns zero:

$$\frac{\partial^2 \Pi(h^\varphi)}{\partial h_i^{\varphi^2}} = 0 \Rightarrow h_i^{\varphi cr} = r_0 \sqrt{\left(\frac{h_0}{r_0}\right)^2 - \left[2\left(\frac{h_0}{r_0}\right)^2 + 8 \right]^{2/3} + 4} \quad (D6)$$

This gives identical solution to the critical height calculated for one single segment in equation (3.16).

D1.2 Analysis of ‘alternately stiffened’ multi-storey structures

Equations

For multi-storey \mathbf{h}^φ is a vector of dimension k containing the actual half-height of the units, that is, the current height of the mast is:

$$H^\varphi = 2 \sum_{i=1}^k h_i^\varphi \quad (D7)$$

The total potential energy will take the following form:

$$\begin{aligned} \Pi_{\text{ext}}(\mathbf{h}^\varphi) &= -2N \sum_{i=1}^k (h_0 - h_i^\varphi) \\ \Pi_{\text{int}}(\mathbf{h}^\varphi) &= +\frac{1}{2} EA 2r_0 \sum_{i=1}^k [\lambda_i(h_i^\varphi) - 1]^2 \\ \Pi(\mathbf{h}^\varphi) &= \Pi_{\text{ext}}(\mathbf{h}^\varphi) + \Pi_{\text{int}}(\mathbf{h}^\varphi) = -2N \sum_{i=1}^k (h_0 - h_i^\varphi) + EA r_0 \sum_{i=1}^k [\lambda_i(h_i^\varphi) - 1]^2 \end{aligned} \quad (D8)$$

If the axial stiffness of the elastic horizontal bars is not the same, the multiplier EA_i has to be brought into the summing sign in the expression of the internal potential energy. The

stretching of the elastic bars only depend on the height of the segment they take place and accordingly, the equilibrium equation will fall to k separate and identical equations with one only h_i^φ as unknown. The first derivative of the total potential energy:

$$\frac{\partial \Pi(\mathbf{h}^\varphi)}{\partial h_i^\varphi} = 2N + 2EA r_0 [\lambda_i(h_i^\varphi) - 1] \lambda_i(h_i^\varphi) = 2N - \frac{2EA}{r_0} h_i^\varphi \left[1 - \frac{2}{\sqrt{4 + \frac{(h_0)^2 - (h_i^\varphi)^2}{(r_0)^2}}} \right] \quad (\text{D9})$$

where

$$\lambda_i(\mathbf{h}^\varphi) = \frac{\partial \lambda_i(\mathbf{h}^\varphi)}{\partial h_i^\varphi} = \frac{1}{\sqrt{4 + \frac{(h_0)^2 - (h_i^\varphi)^2}{(r_0)^2}}} \frac{-h_i^\varphi}{(r_0)^2} \quad (\text{D10})$$

The stationary point is at:

$$\frac{\partial \Pi(\mathbf{h}^\varphi)}{\partial h_i^\varphi} = 0 \Rightarrow N(\mathbf{h}_i^\varphi) = \frac{EA}{r_0} h_i^\varphi \left[1 - \frac{2}{\sqrt{4 + \frac{(h_0)^2 - (h_i^\varphi)^2}{(r_0)^2}}} \right] \quad (\text{D11})$$

Obviously we get to the trivial solution that pushing the top segments down will result in a uniform packing with $h^\varphi = h_i^\varphi$ where the equilibrium path will be the same as calculated for one single segment, consequently equation (D11) is identical to (D4).

To decide whether the equilibrium positions are stable or not, the signs of the eigenvalues of the Hessian matrix, containing the second derivatives of the total potential energy, are needed. The path is stable where all the eigenvalues are positive. The Hessian matrix of the alternately stiffened mast will take the very simple diagonal form, as the mixed partials will be zero, and each first derivative will be the same:

$$\mathbf{H} = \mathbf{E} \boldsymbol{\Lambda} \quad H_{ii} = \Lambda_i \quad (\text{D11})$$

In equation (D11) \mathbf{E} is the matrix of unity and $\boldsymbol{\Lambda}$ is the vector with the eigenvalues of the Hessian matrix, which is in this case equals the second derivative:

$$\Lambda = \Lambda_i = \frac{\partial^2 \Pi(\mathbf{h}^\varphi)}{\partial h_i^{\varphi 2}} \quad (\text{D12})$$

The half-height of the segments (h_i^φ) will take its critical value where the eigenvalues are zero:

$$\frac{\partial^2 \Pi(\mathbf{h}^\varphi)}{\partial h_i^{\varphi^2}} = -\frac{2EA_i}{r_0} \left\{ 1 - \frac{2}{\sqrt{4 + \frac{(h_0)^2 - (h_i^\varphi)^2}{(r_0)^2}}} - \frac{2(h_i^\varphi)^2}{r_0^2 \left[4 + \frac{(h_0)^2 - (h_i^\varphi)^2}{(r_0)^2} \right]^{3/2}} \right\} \quad (\text{D13})$$

$$\frac{\partial^2 \Pi(\mathbf{h}^\varphi)}{\partial h_i^{\varphi^2}} = 0 \Rightarrow h_i^{\varphi \text{ cr}} = r_0 \sqrt{\left(\frac{h_0}{r_0}\right)^2 - \left[2 \left(\frac{h_0}{r_0}\right)^2 + 8 \right]^{2/3} + 4} \quad (\text{D14})$$

If the self-weight of the structure are not to be ignored then the vertical force acting on the structure is not identical in the segments, but still the mechanical behavior can be calculated from a separate analysis of the segments.

If we consider only concentrated masses in the end nodes of the rigid horizontal bars (see Fig. 3.16) the external potential energy has to be modified to:

$$\Pi_{\text{ext}}(\mathbf{h}^\varphi) = -2N \sum_{i=1}^k (h_0 - h_i^\varphi) - 2mg \sum_{i=k}^1 \sum_{j=1}^i (h_0 - h_j^\varphi) \quad (\text{D15})$$

and the derivative of the total potential energy written in (D9) will have to be modified with the derivative of the second term in (D15):

$$\frac{-\partial [2mg \sum_{i=1}^n \sum_{j=1}^i (h_0 - h_j^\varphi)]}{\partial h_i^\varphi} = i2mg \quad (\text{D16})$$

Methodology

The tracing of the force displacement diagram of the ‘alternately stiffened’ mast can be programmed with a MAPLE code developed specially for these structures. The incremental analysis is carried out with numerically minimizing the total potential energy in (D8). The different bifurcated paths can be obtained by perturbing equilibrated variables with random positive and negative numbers, which will serve as the initial value for the minimum search (See Fig.D1). The random generation uses the time of the processor, as otherwise every calculation would use the same random numbers resulting in identical equilibrium paths. The restriction of ‘post-packed phenomenon’ can be handled by kicking out the segments from the calculation that are heading to be completely closed.

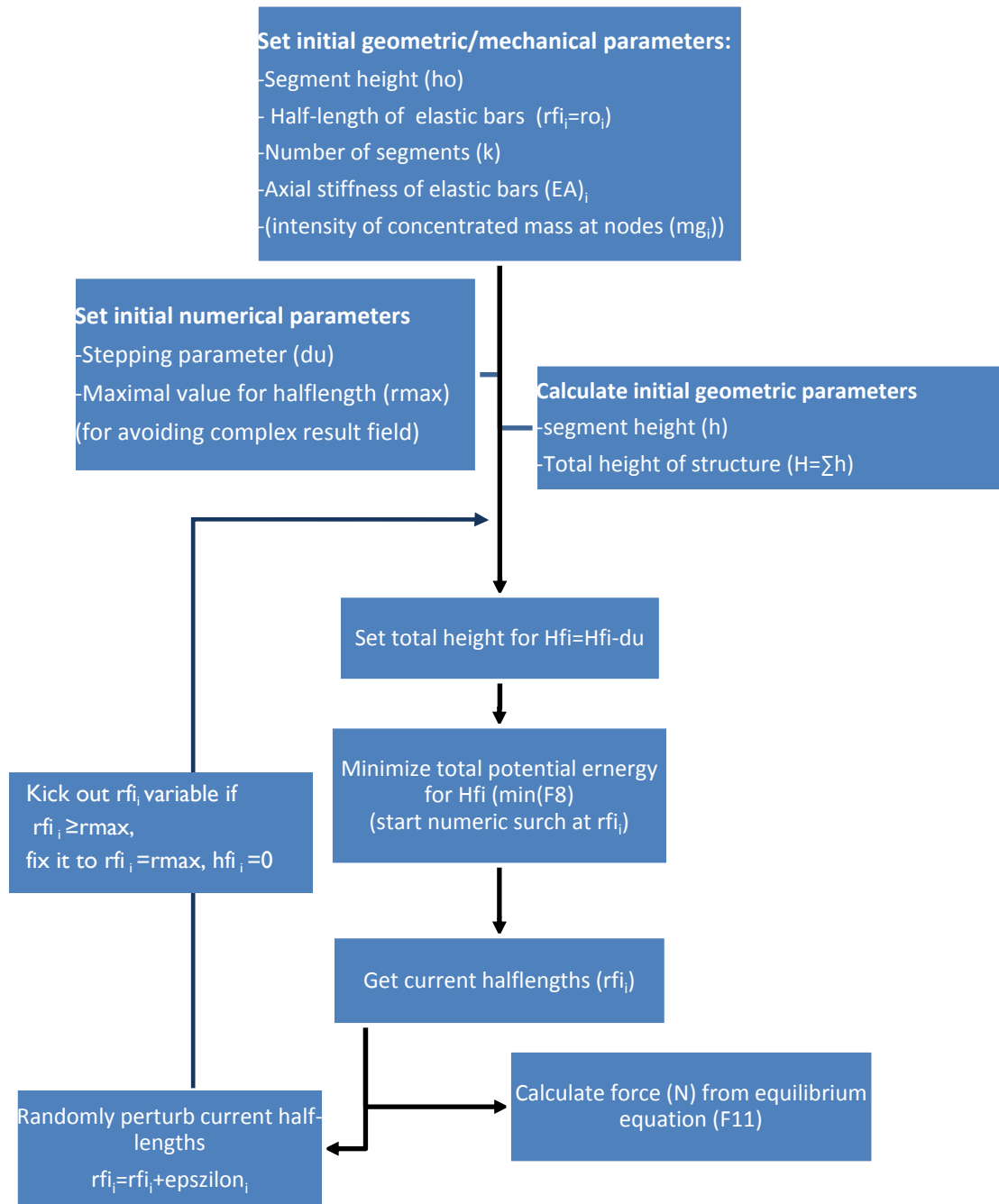


Fig. D1: methodology for tracing force-displacement diagram of multi-storey, ‘alternately stiffened’ masts

D1.3 Analysis of ‘non-stiffened’ multi-storey structures

Equations

For the non-stiffened multi-storey structures, for the sake of simplicity, the total potential energy is herein written in the function of the current half-length of the horizontal elastic bars:

$$\Pi_{\text{ext}}(\mathbf{r}^\varphi) = -N \sum_{i=1}^k [h_0 - h_i^\varphi(r_i^\varphi, r_{i-1}^\varphi)] = -N \sum_{i=1}^k \left[h_0 - \sqrt{l_b^2 - (r_i^\varphi + r_{i-1}^\varphi)^2} \right]$$

$$\begin{aligned}
\Pi_{\text{int}}(\mathbf{r}^\varphi) &= +\frac{1}{2}2r_0 \sum_{i=1}^{k-1} EA_i [\lambda_i(r_i^\varphi) - 1]^2 = r_0 \sum_{i=1}^{k-1} EA_i \left(\frac{r_i^\varphi}{r_0} - 1\right)^2 \\
\Pi(\mathbf{r}^\varphi) &= \Pi_{\text{ext}}(\mathbf{r}^\varphi) + \Pi_{\text{int}}(\mathbf{r}^\varphi) \\
&= -N \sum_{i=1}^k \left[h_0 - \sqrt{l_b^2 - (r_i^\varphi + r_{i-1}^\varphi)^2} \right] + r_0 \sum_{i=1}^{k-1} EA_i \left(\frac{r_i^\varphi}{r_0} - 1\right)^2
\end{aligned} \tag{D17}$$

The first derivatives of the total potential energy:

$$\frac{\partial \Pi(\mathbf{r}^\varphi)}{\partial r_i^\varphi} = -N \left[\frac{r_i^\varphi + r_{i-1}^\varphi}{h_i^\varphi(r_i^\varphi, r_{i-1}^\varphi)} + \frac{r_i^\varphi + r_{i+1}^\varphi}{h_{i+1}^\varphi(r_i^\varphi, r_{i+1}^\varphi)} \right] + 2EA_i \left(\frac{r_i^\varphi}{r_0} - 1\right) \tag{D18}$$

In the equilibrium state the total potential energy has stationary points:

$$\frac{\partial \Pi(\mathbf{r}^\varphi)}{\partial r_i^\varphi} = 0 \Rightarrow N = N_i(r_{i-1}^\varphi, r_i^\varphi, r_{i+1}^\varphi) = \frac{2EA_i}{r_0} \frac{r_i^\varphi - r_0}{\frac{r_i^\varphi + r_{i-1}^\varphi}{h_i^\varphi} + \frac{r_i^\varphi + r_{i+1}^\varphi}{h_{i+1}^\varphi}} \tag{D19}$$

This equilibrium equation corresponds to the equation already given in (3.61).

To decide whether the equilibrium points are stable or not the Hesse matrix has to be calculated. In the case of non-stiffened mast, the Hesse matrix takes a more complex form than a diagonal one. In this case the hessian is a tridiagonal matrix as only the partials

$\frac{\partial^2(\mathbf{r}^\varphi)}{\partial r_i^\varphi \partial r_{i-1}^\varphi}$, $\frac{\partial^2(\mathbf{r}^\varphi)}{\partial r_i^{\varphi 2}}$, $\frac{\partial^2(\mathbf{r}^\varphi)}{\partial r_i^\varphi \partial r_{i+1}^\varphi}$ are nonzero:

$$\frac{\partial^2 \Pi(\mathbf{r}^\varphi)}{\partial r_i^{\varphi 2}} = -N \left[\frac{h_i^\varphi - (r_i^\varphi + r_{i-1}^\varphi)h_i^\varphi}{(h_i^\varphi)^2} + \frac{h_{i+1}^\varphi - (r_i^\varphi + r_{i+1}^\varphi)h_{i+1}^\varphi}{(h_{i+1}^\varphi)^2} \right] + \frac{2EA_i}{r_0} \tag{D20}$$

where

$$\begin{aligned}
h_i^\varphi &= \frac{\partial^2 h_i^\varphi(r_i^\varphi, r_{i-1}^\varphi)}{\partial r_i^{\varphi 2}} = \frac{-1}{2} \frac{1}{h_i^\varphi} 2(r_i^\varphi + r_{i-1}^\varphi) \\
\frac{\partial^2 \Pi(\mathbf{r}^\varphi)}{\partial r_i^{\varphi 2}} &= -N \left[\frac{h_i^\varphi - (r_i^\varphi + r_{i-1}^\varphi)h_i^\varphi}{(h_i^\varphi)^2} + \frac{h_{i+1}^\varphi - (r_i^\varphi + r_{i+1}^\varphi)h_{i+1}^\varphi}{(h_{i+1}^\varphi)^2} \right] + \frac{2EA_i}{r_0} \\
\frac{\partial^2 \Pi(\mathbf{r}^\varphi)}{\partial r_i^{\varphi 2}} &= -N \left[\frac{1}{h_i^\varphi} + \frac{(r_i^\varphi + r_{i-1}^\varphi)^2}{(h_i^\varphi)^3} + \frac{1}{h_{i+1}^\varphi} + \frac{(r_i^\varphi + r_{i+1}^\varphi)^2}{(h_{i+1}^\varphi)^3} \right] + \frac{2EA_i}{r_0}
\end{aligned}$$

Methodology

The same methodology that was used for ‘alternately stiffened masts’ (Dig. F1) can be applied for non-stiffened masts as well. The main difference between the two methods is mainly that it is not possible to kick out closed segments from the calculation. This can not be done due to the possible length-changing of elastic bars after complete closure. For that, these calculations are only carried out until the first segment closure. The critical force can be determined from the program by calculating the determinant of the Hesse matrix in (D25) for every incremental step.

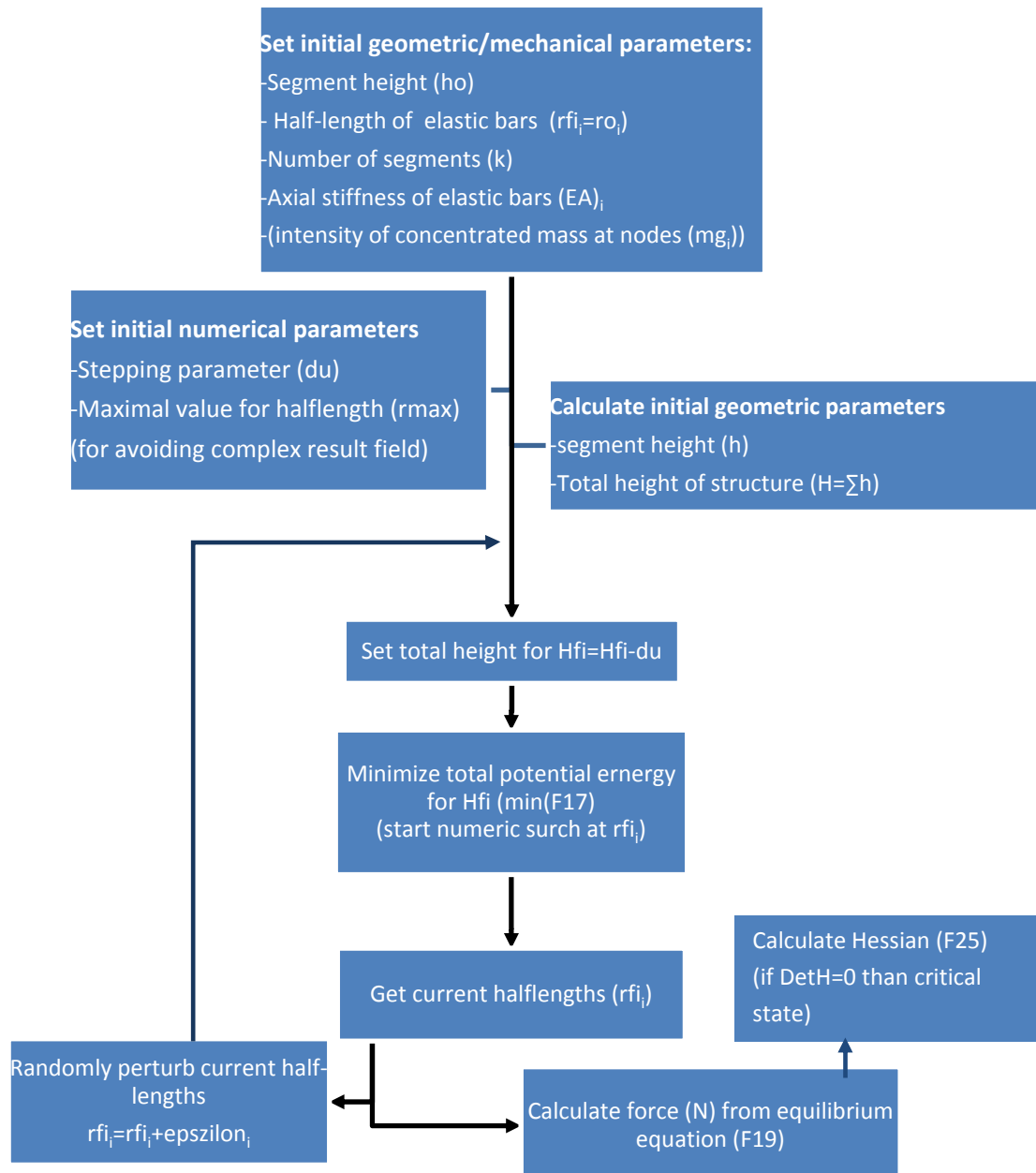


Fig. D2: Methodology for tracing force-displacement diagram of multi-storey, 'non-stiffened' masts until the first segment closure

The simulation developed in MAPLE uses linear constitutive model. The results for the critical forces in case of different segment numbers can be seen in Fig. D3 for two different height per half-length ratios.

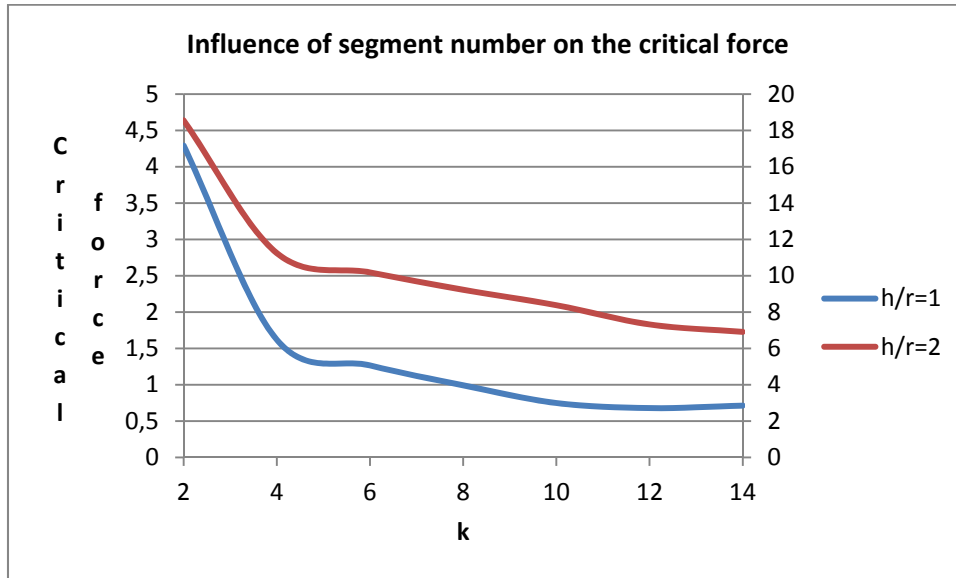


Fig. D3: Influence of segment number on the critical force of 'non-stiffened' masts for two different ratios of segment height and half-length of elastic bars

D2. Calculation of the antiprismatic mast with energetic approach

D2.1 Analysis of basic segment

The total potential energy of the basic segment can be written in the form:

$$\Pi(h^\varphi) = \Pi_{\text{ext}}(h^\varphi) + \Pi_{\text{int}}(h^\varphi) = -2N(h - h^\varphi) + \frac{1}{2}nEAR 2\sin\phi [\lambda(h^\varphi) - 1]^2 \quad (\text{D.26})$$

The equilibrium of the structure will be where the total potential energy takes its minimal value:

$$\begin{aligned} \frac{d\Pi(h^\varphi)}{dh^\varphi} &= 0 \\ \frac{d\Pi(h^\varphi)}{dh^\varphi} &= 2N + 2nEAR \sin\phi [\lambda(h^\varphi) - 1]\lambda'(h^\varphi) \\ &= 2N - 2nEA \sin\phi \frac{h^\varphi}{R} \left[\frac{(\cos\phi - 1)}{\sqrt{\left(\frac{h}{R}\right)^2 - \left(\frac{h^\varphi}{R}\right)^2 + (1 - \cos\phi)^2}} + 1 \right] = 0 \end{aligned} \quad (\text{D.27})$$

$$2N = 2nEA \sin\phi \frac{h^\varphi}{R} \left[\frac{(\cos\phi - 1)}{\sqrt{\left(\frac{h}{R}\right)^2 - \left(\frac{h^\varphi}{R}\right)^2 + (1 - \cos\phi)^2}} + 1 \right] \quad (\text{D.28})$$

where $\lambda'(h^\varphi)$ is the derivative of the equation (4.6):

$$\lambda'(h^\varphi) = \frac{d\lambda(h^\varphi)}{dh^\varphi} = \frac{-h^\varphi}{R^2 \sqrt{\left(\frac{h}{R}\right)^2 - \left(\frac{h^\varphi}{R}\right)^2 + (1 - \cos\phi)^2}} \quad (\text{D.29})$$

The second derivative of the total potential energy:

$$\begin{aligned} \frac{d^2\Pi(h^\varphi)}{d^2h^\varphi} &= \frac{2nEA \sin\phi}{R} \left\{ \left[\frac{(\cos\phi - 1)}{\sqrt{\left(\frac{h}{R}\right)^2 - \left(\frac{h^\varphi}{R}\right)^2 + (1 - \cos\phi)^2}} + 1 \right] \right. \\ &\quad \left. + h^\varphi \frac{1}{2} \frac{2h^\varphi}{R^2} \left[\frac{(\cos\phi - 1)}{\left[\left(\frac{h}{R}\right)^2 - \left(\frac{h^\varphi}{R}\right)^2 + (1 - \cos\phi)^2 \right]^{3/2}} \right] \right\} \end{aligned}$$

$$\frac{d^2\Pi(h^\varphi)}{d^2h^\varphi} = \frac{2nEA \sin \phi}{R} \left\{ (\cos \phi - 1) \frac{R^2 \left[\left(\frac{h}{R}\right)^2 - \left(\frac{h^\varphi}{R}\right)^2 + (1 - \cos \phi)^2 \right] + \frac{(h^\varphi)^2}{R^2}}{R^2 \left[\left(\frac{h}{R}\right)^2 - \left(\frac{h^\varphi}{R}\right)^2 + (1 - \cos \phi)^2 \right]^{3/2}} + 1 \right\}$$

$$\frac{d^2\Pi(h^\varphi)}{d^2h^\varphi} = \frac{2nEA \sin \phi}{R} \left\{ (\cos \phi - 1) \frac{h^2 + R^2(1 - \cos \phi)^2}{R^2 \left[\left(\frac{h}{R}\right)^2 - \left(\frac{h^\varphi}{R}\right)^2 + (1 - \cos \phi)^2 \right]^{3/2}} + 1 \right\}$$
(D30)

The critical state is where:

$$\frac{d^2\Pi(h^\varphi)}{d^2h^\varphi} = 0$$

$$\Rightarrow \left(\frac{h^\varphi_{cr}}{R}\right)^2 = \left(\frac{h}{R}\right)^2 + (1 - \cos \phi)^2 - \left\{ (1 - \cos \phi) \left[\left(\frac{h}{R}\right)^2 + (1 - \cos \phi)^2 \right] \right\}^{2/3}$$
(D31)

D2.2 Analysis of ‘alternately stiffened’ multi-storey structures

The methodology of analyzing the multi-storey structure is the same as explained for the planar case. It is only the equations that will be different. The current height of the mast is:

$$H^\varphi = 2 \sum_{i=1}^k h_i^\varphi$$
(D32)

The total potential energy will take the following form:

$$\Pi_{\text{ext}}(\mathbf{h}^\varphi) = \Pi_{\text{ext}}(h_i^\varphi) = -2N \sum_{i=1}^k (h_0 - h_i^\varphi)$$

$$\Pi_{\text{int}}(\mathbf{h}^\varphi) = +\frac{1}{2} nEAR 2\sin \phi \sum_{i=1}^k [\lambda_i(h_i^\varphi) - 1]^2$$

$$\Pi(\mathbf{h}^\varphi) = \Pi_{\text{ext}}(\mathbf{h}^\varphi) + \Pi_{\text{int}}(\mathbf{h}^\varphi) = -2N \sum_{i=1}^k (h_0 - h_i^\varphi) + \frac{1}{2} nR 2\sin \phi \sum_{i=1}^k EA_i [\lambda_i(h_i^\varphi) - 1]^2$$
(D33)

The equilibrium equation will fall to k separate and identical equations with one only h^φ_i as unknown. The first derivative of the total potential energy:

$$\begin{aligned} \frac{\partial \Pi(\mathbf{h}^\varphi)}{\partial h_i^\varphi} &= 2N + nEA_i R \sin \phi [\lambda_i(h_i^\varphi) - 1] \lambda_i(h_i^\varphi) = \\ &= 2N - 2nEA_i \sin \phi \frac{h_i^\varphi}{R} \left[\frac{(\cos \phi - 1)}{\sqrt{\left(\frac{h}{R}\right)^2 - \left(\frac{h_i^\varphi}{R}\right)^2 + (1 - \cos \phi)^2}} + 1 \right] \end{aligned} \quad (\text{D34})$$

The stationary point is at:

$$\frac{\partial \Pi(\mathbf{h}^\varphi)}{\partial h_i^\varphi} = 0 \Rightarrow N(\mathbf{h}_i^\varphi) = 2nEA_i \sin \phi \frac{h_i^\varphi}{R} \left[\frac{(\cos \phi - 1)}{\sqrt{\left(\frac{h}{R}\right)^2 - \left(\frac{h_i^\varphi}{R}\right)^2 + (1 - \cos \phi)^2}} + 1 \right] \quad (\text{D35})$$

The elements in the diagonal of the Hessian matrix of the alternately stiffened mast are:

$$\mathbf{H} = \mathbf{E}\mathbf{\Lambda} \quad H_{ii} = \Lambda_i \quad (\text{D36})$$

$$\Lambda = \Lambda_i = \frac{\partial^2 \Pi(\mathbf{h}^\varphi)}{\partial h_i^{\varphi 2}} \quad (\text{D37})$$

The half-height of the segments (h^φ_i) will take its critical value where the eigenvalues are zero:

$$\frac{\partial^2 \Pi(\mathbf{h}^\varphi)}{\partial h_i^{\varphi 2}} = \frac{2nEA_i \sin \phi}{R} \left\{ (\cos \phi - 1) \frac{h^2 + R^2(1 - \cos \phi)^2}{R^2 \left[\left(\frac{h}{R}\right)^2 - \left(\frac{h_i^\varphi}{R}\right)^2 + (1 - \cos \phi)^2 \right]^{3/2}} + 1 \right\} \quad (\text{D38})$$

$$\begin{aligned} \frac{\partial^2 \Pi(\mathbf{h}^\varphi)}{\partial h_i^{\varphi 2}} = 0 &\Rightarrow \left(\frac{h_{cri}^\varphi}{R}\right)^2 = \\ &= \left(\frac{h}{R}\right)^2 + (1 - \cos \phi)^2 - \left\{ (1 - \cos \phi) \left[\left(\frac{h}{R}\right)^2 + (1 - \cos \phi)^2 \right] \right\}^{2/3} \end{aligned}$$

(D39)

If the self-weight of the structure are not to be ignored, considering only concentrated masses in the vertices of the rigid polygons the external potential energy has to be modified to:

$$\Pi_{\text{ext}}(\mathbf{h}^\varphi) = -2N \sum_{i=1}^k (h_0 - h_i^\varphi) - 2nmg \sum_{i=k}^1 \sum_{j=1}^i (h_0 - h_j^\varphi) \quad (\text{D40})$$

Taking the self-weight into account, the derivative of the total potential energy written in (D35) will have to be modified with the derivative of the second term in (D40):

$$\frac{-\partial [2mg \sum_{i=1}^n \sum_{j=1}^i (h_0 - h_j^\varphi)]}{\partial h_i^\varphi} = i2mg \quad (\text{D41})$$

D2.3 Analysis of ‘non-stiffened’ multi-storey structures

Investigating a non-stiffened k-storey structure, similarly to the 2D deployable mast without intermediate stiffening, the set of equations will be written in function of the current radii (R^φ), which is now a vector of $k + 1$ elements:

$$\mathbf{R}^\varphi = R_i^\varphi \quad (i = 0..k), \quad R_0^\varphi = R_k^\varphi = R \quad (\text{D42})$$

The current height of the segments in function of the current radius of the horizontal polygons:

$$h_i^\varphi(\mathbf{R}^\varphi) = h_i^\varphi(R_i^\varphi, R_{i-1}^\varphi) = \sqrt{l_b^2 - (R_{i-1}^\varphi \sin \phi)^2 - (R_i^\varphi - R_{i-1}^\varphi \cos \phi)^2} \quad (\text{D43})$$

And the actual stretching of the elastic bars:

$$\lambda_i(\mathbf{R}^\varphi) = \lambda_i(R_i^\varphi) = \frac{R_i^\varphi}{R} \quad (\text{D44})$$

The total potential energy:

$$\begin{aligned} \Pi_{\text{ext}}(\mathbf{R}^\varphi) &= -N \sum_{i=1}^k [h_0 - h_i^\varphi(R_i^\varphi, R_{i-1}^\varphi)] \\ &= -N \sum_{i=1}^k \left[h_0 - \sqrt{l_b^2 - (R_{i-1}^\varphi \sin \phi)^2 - (R_i^\varphi - R_{i-1}^\varphi \cos \phi)^2} \right] \end{aligned}$$

$$\begin{aligned}
\Pi_{\text{int}}(\mathbf{R}^\varphi) &= +\frac{1}{2}nEA2R \sin \phi \sum_{i=1}^{k-1} [\lambda_i(R_i^\varphi) - 1]^2 = nEAR \sin \phi \sum_{i=1}^{k-1} \left(\frac{R_i^\varphi}{R} - 1\right)^2 \\
\Pi(\mathbf{R}^\varphi) &= \Pi_{\text{ext}}(\mathbf{R}^\varphi) + \Pi_{\text{int}}(\mathbf{R}^\varphi) \\
\Pi(\mathbf{R}^\varphi) &= -N \sum_{i=1}^k \left[h_0 - \sqrt{l_b^2 - (R_{i-1}^\varphi \sin \phi)^2 - (R_i^\varphi - R_{i-1}^\varphi \cos \phi)^2} \right] \\
&\quad + nEAR \sin \phi \sum_{i=1}^{k-1} \left(\frac{R_i^\varphi}{R} - 1\right)^2
\end{aligned} \tag{D45}$$

The first derivatives of the total potential energy:

$$\frac{\partial \Pi(\mathbf{R}^\varphi)}{\partial R_i^\varphi} = N \left[\frac{R_{i-1}^\varphi \cos \phi - R_i^\varphi}{h_i^\varphi} + \frac{R_{i+1}^\varphi \cos \phi - R_i^\varphi}{h_{i+1}^\varphi} \right] + 2nEAR \sin \phi \left(\frac{R_i^\varphi}{R} - 1\right) \tag{D46}$$

The equilibrium equation:

$$\frac{\partial \Pi(\mathbf{R}^\varphi)}{\partial R_i^\varphi} = 0 \Rightarrow N = 2nEA \sin \phi \frac{R_i^\varphi - R}{\frac{R_i^\varphi - R_{i-1}^\varphi \cos \phi}{h_i^\varphi} + \frac{R_i^\varphi - R_{i+1}^\varphi \cos \phi}{h_{i+1}^\varphi}} \tag{D47}$$

The Hessian matrix has similar form to the one shown for the 2D structure in (D24), where the non-zero partials are:

$$\begin{aligned}
\frac{\partial^2 \Pi(\mathbf{R}^\varphi)}{\partial R_i^{\varphi^2}} &= N \left[\frac{(R_{i-1}^\varphi \cos \phi - R_i^\varphi)^2}{(h_i^\varphi)^3} - \frac{1}{h_i^\varphi} + \frac{(R_{i+1}^\varphi \cos \phi - R_i^\varphi)^2}{(h_{i+1}^\varphi)^3} - \frac{1}{h_{i+1}^\varphi} \right] + 2nEA \sin \phi \\
\frac{\partial^2 \Pi(\mathbf{R}^\varphi)}{\partial R_{i-1}^\varphi \partial R_i^\varphi} &= \frac{\partial^2 \Pi(\mathbf{R}^\varphi)}{\partial R_i^\varphi \partial R_{i-1}^\varphi} = N \left[\frac{\cos \phi}{h_i^\varphi} + \frac{(R_{i-1}^\varphi \cos \phi - R_i^\varphi)(R_i^\varphi \cos \phi - R_{i-1}^\varphi)}{(h_i^\varphi)^3} \right] \\
\frac{\partial^2 \Pi(\mathbf{R}^\varphi)}{\partial R_{i+1}^\varphi \partial R_i^\varphi} &= \frac{\partial^2 \Pi(\mathbf{R}^\varphi)}{\partial R_i^\varphi \partial R_{i+1}^\varphi} = N \left[\frac{\cos \phi}{h_{i+1}^\varphi} + \frac{(R_{i+1}^\varphi \cos \phi - R_i^\varphi)(R_i^\varphi \cos \phi - R_{i+1}^\varphi)}{(h_{i+1}^\varphi)^3} \right]
\end{aligned} \tag{D48}$$

Fig. D4 shows one of the programs in MAPLE that calculates the equilibrium paths of the multi-storey, non-stiffened antiprismatic mast, with the same methodology explained for planar structures.

```

> with(Optimization):
with (ExcelTools):
> #randomize();
#Initial geometric, mechanic and numeric parameters
> n:=5; #n-gon
> m:=5; #segment number
> EA:=1; #axial stiffness
> mg:=0; #magnitude of mass/segment
> Ro:=1; #initial radius
> Rr:=1;
> So:=1.175571; #length of the bracing
> f:=Pi/n:
> stepn:=100;
> dh:=0.05;
> R[0]:=Ro; R[m]:=Ro; #fix radius at bottom and top
>
#Calculation of segment height and total height
> ht:=0: l:=0:
> for j from 1 to m do
> h[j]:=sqrt(So^2-(R[j-1]*sin(f))^2-(R[j]-R[j-1]*cos(f))^2):
> ht:=ht+h[j]:
> l:=l+ht:
> od:
>
> #Calculation of internal potential energy
> Er:=0:
> for j from 1 to m-1 do
> Er:=EA*sin(f)*n*((R[j]-Rr)/Rr)^2+Er:
> od:
>
> #Total potential energy
> Et:=Er+l*mg:
>
#Initialize parameters
> x[0]:=Ro:
> x[m]:=Ro:
> F[0]:=0:
>
> for trial from 1 to 5 do #for five different bifurcation path
> inistate:=seq(R[i]=1,i=1..m-1)];
> height:=evalf(eval(ht,inistate));
> InPoint:=inistate;
> interface(screenwidth=20+25*(m-1)):
> #excelmatrix:=Array(1..stepn,1..m);
> #strainlimit:=evalf(cos(f)+sqrt((1/Ro)^2+(1-cos(f))^2)):
> #print(strainlimit);
> limits:=seq(R[i]=1..10,i=1..m-1):
>
for j from 1 to stepn do
>
> for i from 1 to m-1 do
> x[i]:=eval(R[i],InPoint):
> y[i]:=x[i]+(-5+rand(11))/1000*Ro:
> excelmatrix(j,i+1):=x[i]:
> od:
>
> for i from 1 to m do
> hhh[i]:=evalf(eval(h[i],InPoint));
> od:
> #Calculate force from equilibrium state
> for i from 1 to m-1 do

```

```

> FF[i]:=evalf(
> (x[i]-Rr)/( ((x[i]-x[i-1]*cos(f))/hhh[i] )+
> ((x[i]-x[i+1]*cos(f))/hhh[i+1]))
> );
> od:
>
> F[j]:=FF[1]:
> dF:=F[j]-F[j-1]:
>
> excelmatrix(j,1):=height:
>
#define initial value for minimization (randomly perturbed last result)
> #print(InPoint);
> InPoint:=seq(R[i]=y[i],i=1..m-1):
> #print(InPoint);
>
> eredmeny:=seq(R[i]=x[i],i=1..m-1):
> print(h=height,eredmeny);
>
> #Start incremental analysis
> height:=height - dh:
> InPoint:=op(2,
> Minimize(Et,
> {ht=height},limits,
> initialpoint=InPoint)): #Minimize strain energy
>
> #print out delta force values
> #print(seq(hhh[i],i=1..m));
> print(j,delta_force=dF,force=F[j]);
> od:
>
> sheet:=cat(trial,".lap");
>
> od; #end of creating several trials
>
> Export(excelmatrix,"proba.xls",sheet);
>
> quit;

```

Fig. D4: Self-developed program in MAPLE for the calculation of equilibrium paths of antiprismatic, non-stiffened structures

ANNEX E: CHOOSING CONSTITUTIVE LAWS IN SMALL AND LARGE DISPLACEMENT DOMAIN

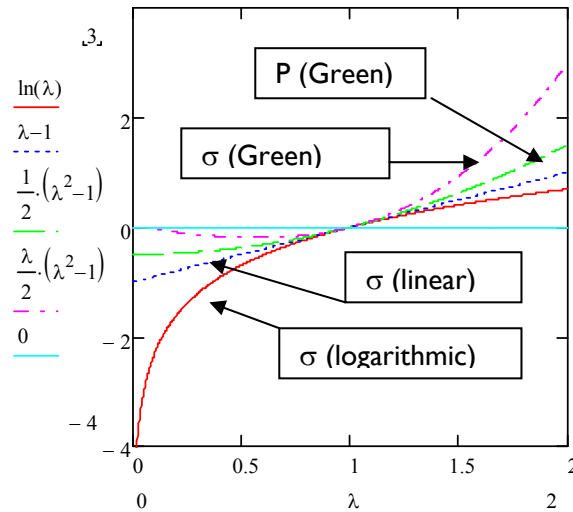


Fig. E1: Different stress definitions for finite displacements

Figs. E1 shows the difference between three different constitutive models; the stresses calculated from linear constitutive model (with blue line), and the stresses derived from two hyper-elastic models are shown: the Saint-Venant-Kirchoff constitutive model in terms of the Green-Lagrange deformation measure and the one in terms of logarithmic measure (with red line). For the former, both the Piola-Kirchoff stress (with green line) and the Cauchy stress (with pink line) are plotted. It is true, that these constitutive models are rather used in the small deformation regime, and for rubber-like materials the models defined also in terms of principal stretches (neo-Hookean, Ogden, Mooney-Rivlin) [van den Bogert and de Borst, 1994] are more common (see a fitting with these models in Fig. E2). However, for the used uni-axial model the logarithmic strain measure might be an applicable choice in the specific strain domain for some polymers. The boundary of the domain depends on the used material. For example an experimental curve is shown in Fig. E2. It can be seen that after the inflexion point of the experimental curve, the logarithmic constitutive model cannot be anymore valid, which is around $\lambda = 1.6$ for that given polymer. For some rubber-like materials this turning-upwards of the diagram occur around $\lambda = 3..4$ (referring to a force-stretch diagrams from tensile tests received from a polymer-factory in Szeged). Concluding, the constitutive model expressed in terms of logarithmic strains seems to be a rationale and acceptable choice.

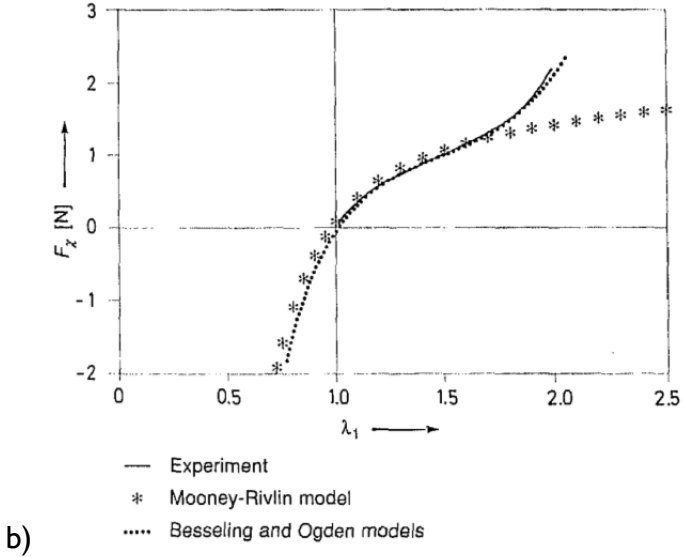


Fig. E2: Force-stretch diagram of rubber-like material from different constitutive models and from experiments [van den Bogert and de Borst, 1994]

LIST OF FIGURES

Chapter 2

- Fig. 2.1: Early movable roof structures: a) Tepee tent from the Sioux Indians [Otto, 1971] (cited by [Walter]); b) Roman Colosseum [Escrig and Brebbia 1996] (cited by [Jensen, 2001] and c) the reconstruction of its convertible roofing system [Gengnagel, 2001] (cited by [Walter])
- Fig. 2.2: a) The US Pavilion for the 1967 World's Fair, Montreal by B. Fuller [Hienstorfer, 2007]; b) Pinero with his movable theatre [Robbin, 1996]
- Fig. 2.3: Scheme of sustainable development: at the confluence of three constituent parts [Friedman et al., 2011/1]
- Fig. 2.4: Classification of rigid retractable constructions: the movement matrix [Otto et al, 1971]
- Fig. 2.5: Pittsburgh Civic Arena (architect: Mitchell and Ritchey) photo [Lorentz, 2008] and original blueprint [Helvenstone, 1959]
- Fig. 2.6: Fukuoka stadium (architect: Takenaka Corp.) a) photo with closed [Yahoo, 2010] and b) with opened roof [Japan Atlas] c) structure [Ishii, 2000]
- Fig. 2.7: Fukuoka stadium a) geometry of a roof panel b) roadbed section c) driving device [Ishii, 2000]
- Fig. 2.8: Oita Stadium (architect: Kisho Kurokawa) a) photo [Ezinemark, 2010]; b) fix structural part [Ishii, 2000] and c) retractable top section [Ishii, 2000]
- Fig. 2.9: a) Retractable roof of the Komjádi swimming pool [Komjádi] b) Qi Zhong stadium (architect: Mitsuru Senda), [Ezinemark]
- Fig. 2.10: Toronto Skydome (architect: Rod Robbie) a) photo of closed and b) opened roof c) The structure of the retractable roof [Ishii, 2000]
- Fig. 2.11: Foldable tube (exhibition object) and dome (paper model) with the Yoshimura pattern [Yoshimura]
- Fig. 2.12: Solid Surface Deployable Antenna and its wrapping fold pattern by the former Deployable Structures Laboratory by Guest and Pellegrino [DSL]
- Fig. 2.13: Cylindrical paper and laminated timber model with the Miura pattern [Buri and Weinand, 2008]
- Fig. 2.14: Adaptive shading system of the Audencia Provincial, Madrid (by Hoberman and Fox+Partners) and the model of a hexagonal retractable panel [Hoberman]
- Fig. 2.15: Details of patented adaptive shading system by Hoberman and Davis [2009]
- Fig. 2.16: Adaptive shading system of the Aldar Central Market in Abu Dhabi, 2010, Madrid (design by Hoberman and Fox+Partners) [Hoberman]
- Fig. 2.17: Some secondary units of scissor like deployable structures: a-b) pyramid type units and c-d) skew types; e-h) foldable shapes [Atake, 1995]
- Fig. 2.18: Photo of Pinero with his movable theatre [Hunter]
- Fig. 2.19: Details of Pinero's reticular 3D structure patent: a) plan view of opened structure; b) fragmentary view; c) connection of three rods of the structure to an intermediate coupling [Piñero, 1965]
- Fig. 2.20: Deployable swimming pool (architect: Prof. Felix Escrig) [Escrig, 1996/2]
- Fig. 2.21: a) Deployable mast controlled by active and passive cables by the former Deployable Structures Laboratory; b) foldable bridge and c) deployable dome by ATAKE Space Design Lab. Co. in the Hanamizuki Park, Japan [Atake]
- Fig. 2.22: a-c) Self-stable deployable structures: secondary units for the planar and d) for spherical structures [Friedman et al., 2008]
- Fig. 2.23: Photo of pop up display and schematic presentation of its installation by Nomadic Display Corp. [Nomadic]

- Fig. 2.24: Zeigler's patent for collapsible self-supporting structure: dome and scissor details [Zeigler, 1977]
- Fig. 2.25: a) Classic SLE, and b) the simple angulated element (illustrated in accordance with [You and Pellegrino, 1997])
- Fig. 2.26.: Iris dome designed by Hoberman, EXPO 2000 [Hoberman]
- Fig. 2.27: a) Schematic model of Hoberman's Iris dome during deployment; b) angulated element on the tangent plane of a conical surface and c) four non-identical hinge axis at the connection of angulated elements [Kovács, 2004/2]
- Fig. 2.28: Deployable sequence of a ring structure developed by Z. You and S. Pellegrino
- Fig. 2.29: 3D model of retractable dome by multi-angulated elements [Kovács, 2004/2] and its physical model at the former Deployable Structures Laboratory
- Fig. 2.30: Retractable dome opening on the spherical surface with telescopic ring, plan view and section of its scissor hinge [Kokawa, 2000]
- Fig. 2.31: Cover of retractable structures with sliding panels by Hoberman: a) schematic model for covering the iris dome (Happold and Hoberman) and b) model of the dome of Abu Dhabi's international airport, United Arab Emirates, 2006 (Kohn Pedersen Fox Architects) [Hoberman]
- Fig. 2.32: Cover solutions for retractable structures by Hoberman: transforming Olympic Arch for the 2002 Winter Olympics (Salt Lake City, USA) designed by Hoberman [Hoberman]
- Fig. 2.33: Schema of the of the pantadome erection [Friedman et al., 2011/4] (in accordance with [Kawaguchi, 2002])
- Fig. 2.34: Erection of Namihaya Dome (Showa Sekkei Corp), Osaka, 1997 [Kawaguchi, 2002]
- Fig. 2.35: Erection of Namihaya Dome [Kawaguchi, 2002]
- Fig. 2.36: Some tensegrity systems: a) the tensegrity tripod b) expanded octahedron [Friedman et al., 2011/4]
- Fig. 2.37: Architectural applications: a) Geodesic tensegrity dome by Fuller, 1953 [Gengnagel, 2002] b) tensegrity roof design of ABDR Arch. Association [ABDR] c) Tensegrity Bridge (Kurilpa Bridge, Brisbane; designer: Cox Rayner Architects and Arup Engineers) [Anupam]
- Fig. 2.38: Single-curved tensegrity grids for responsive architecture by A. Herder [Herder, 2008]
- Fig. 2.39: Deployable masts: a) coilable mast by Mauch (Jet Propulsion Laboratory) [JPL] (b) foldable mast by Hegedús [1993] Fig. 2.40: Deployment of planar truss with length-variation [Mikulas et al., 1992]
- Fig. 2.40: Deployment of planar truss with length-variation [Mikulas et al., 1992]
- Fig. 2.41: Deployable 3D truss units with sliding node: a) unit by Onoda et al. [1996] (cited by [Raskin, 1998]) and b) pyramid in pyramid unit by Krishnapillai [Vu et al., 2006/1-2]
- Fig. 2.42: Two types of cable stiffened pantographic system by Krishnapillai et al. [Vu et al., 2006/2]): stowed state, deployed state and the final, 'locked' configuration
- Fig. 2.43: Deployable arches by cable-strut-pantograph elements for a two-wing butterfly membrane structure: deployment of arches and the model of the structure [Tran et al., 2006]
- Fig. 2.44: Classification of membrane convertible constructions: the movement matrix of structures with stationary supporting structure [Otto, 1971]
- Fig. 2.45: Classification of membrane convertible constructions: the movement matrix of structures with movable supporting structure [Otto, 1971]
- Fig. 2.46: Olympic Stadium in Montreal (architect: Roger Taillibert) [Tolivero] and its original retractable membrane roof [Barnes, 2000]
- Fig. 2.47: The retractable part of the Bullfighting Arena roof in Zaragoza (architect: J. Schlaich) [Sobek, 1999] (cited by [Walter])
- Fig. 2.48: Central spinder for prestressing the cables [Holgate, 1997]
- Fig. 2.49: a) Architectural umbrellas in the courtyard of Mosque in Madinah [Otto, 1995] (cited by [Walter]), Foldable roof in the Rathaus, Vienna [Tillner, 2003] (cited by [Walter])

- Fig. 2.50: a) Inflatable roof for Heathrow airport central bus station (architect: D5) [Lindstrand, 2006]; b) 19.5 m x 40 m Exhibition Hall with air-inflated elements (architect: Festo AG & Co) in Germany [Festo]
- Fig. 2.51: a) Inflation of formwork; b) shotcreting on the inside of the membrane; c) irregular shape structure constructed with pneumatic formwork [Pirs SA.]
- Fig. 2.52: The binishell system: a) expandable reinforcement [Bini, 1972]; b) erection of the dome [Binishell System]; c) vibration of concrete after erection [Bini, 1972]
- Fig. 2.53: Transformation of precast divided planar segments into a hemispherical dome [Dallinger and Kolleger, 2009]
- Fig. 2.54: Segment lift method [Dallinger and Kolleger, 2009]

Chapter 3

- Fig. 3.1: Simplified planar deployable structure
- Fig. 3.2: a) Bottom segment of the simplified structure and its packing b) asymmetric freedom of motion of planar structure
- Fig. 3.3: Equilibrium of one segment of planar structure
- Fig. 3.4: Equilibrium path of basic segment
- Fig. 3.5: Equilibrium path and cumulated internal energy during closure of boundary bars for basic segment with the 'post-packing phenomenon'
- Fig. 3.6: 'Ideal', uniform and successive packing of planar deployable mast of six segments
- Fig. 3.7: Restricted equilibrium paths in function of the actual height of the segments (h^φ) of planar deployable mast consisting two segments
- Fig. 3.8: Different restricted packing sequences following different equilibrium paths (path names in accordance with Fig. 3.7)
- Fig. 3.9: Typical force-displacement diagram - restricted packing of planar deployable mast of six segments (notations: H: total height, u: displacement of the top nodes, N: packing force)
- Fig. 3.10: Nomination of inverse functions
- Fig. 3.11: Shifting and mirroring the force-displacement diagram
- Fig. 3.12: Critical number of segments in function of $x = \frac{h_0}{r_0}$
- Fig. 3.13: Constructing the force-displacement diagram of deployable mast of two segments from the individual diagrams of separated segments without preventing 'post-packed phenomena'
- Fig. 3.14: Packing sequence of deployable mast of two segments without preventing 'post-packed phenomenon'
- Fig. 3.15: Non-restricted equilibrium paths in function of the actual half-segment heights (h^φ) of the planar deployable mast of two segments
- Fig. 3.16: Planar deployable mast with self-weight
- Fig. 3.17: Equilibrium paths in function of the half-heights of the segments (h_1^φ : half-height of top segment, h_2^φ : half-height of bottom segment) of planar deployable mast consisting of two segments taking into account the weight of the structure
- Fig. 3.18: Packing sequences of the planar alternately stiffened mast taking into account the self-weight of the structure (restricted path)
- Fig. 3.19: Constructing the force-displacement diagram - restricted packing of planar deployable mast of six segments with self-weight
- Fig. 3.20: Planar deployable mast without intermediate stiffening
- Fig. 3.21: a) Height of the non-stiffened mast from current bar-lengths and b) equilibrium of forces
- Fig. 3.22: Equilibrium path in function of the half-lengths of the elastic horizontal bars in case of $k = 3$
- Fig. 3.23: Equilibrium path in function of the half-lengths of the elastic horizontal bars in the case of $k=4$

- Fig. 3.24: Packing sequence without intermediate stiffening in case of $k = 3$
- Fig. 3.25: Packing sequence without intermediate stiffening in case of $k = 4$
- Fig. 3.26: The equilibrium path in the parameter field for $k = 4$
- Fig. 3.27: Equilibrium path in function of the half-lengths of the elastic horizontal bars in case of $k = 3$ with the 'post-packed phenomenon'
- Fig. 3.28: Complete packing sequence of three-storey mast without restricting 'post-packing phenomenon'
- Fig. 3.29: Comparing critical forces of 'alternately stiffened' and 'non-stiffened' structures by plotting equilibrium paths in function of the half-lengths of the elastic horizontal bars
- Fig. 3.30: Comparison of logarithmic strain and the one used for small-strain measure for axial force
- Fig. 3.31: Verifying numerical results with analytical solution – packing of basic segment (numerical results with logarithmic strain, analytical results with small strain formulation and with logarithmic strain, $EA = 500, h = 1, r_0 = 1$)
- Fig. 3.32: Numerical models with different packing controls (uniform control, successive control, imperfection control, the non-uniform controls pack the segments successively from the bottom to the top) $-u_i$ is the proportional vertical displacement of the i th boundary in function of the pseudo time (t)
- Fig. 3.33: Uniform and successive packing of 'alternately stiffened' mast – Reaction forces at the end nodes of the rigid horizontal bars (SR1-SR4: reaction forces from successive control respectively from the top to the bottom, UR1, UR4: reaction forces from the uniform control at the top and at the bottom nodes, downward forces are negative)
- Fig. 3.34: Typical packing simulation of a two-storey planar mast without the restriction of 'post-packed phenomenon' controlled by the imperfection of axial stiffness values
- Fig. 3.35: Typical packing simulation of a three-storey planar mast without the restriction of 'post-packed phenomenon' controlled by the imperfection of axial stiffness values
- Fig. 3.36: Packing sequence controlled by the numerical errors of planar pop-up mast consisting of five segments, with simulation without the restriction of 'post-packed phenomena'
- Fig. 3.37: Force-displacement diagram of five-storey planar pop-up mast controlled by numerical errors without the restriction of 'post-packed phenomenon'
- Fig. 3.38: Restricting 'post-packed phenomenon' with contact forces
- Fig. 3.39: Force-displacement diagram of packing a two-storey mast: restricted simulation with contact forces between the end nodes of rigid horizontal bars and packing control by imperfection of axial stiffness values
- Fig. 3.40: Force-displacement diagram and the associated contact forces between the end nodes of rigid horizontal bars of packing two-storey mast with restricted simulation controlled by imperfection of axial stiffness
- Fig. 3.41: Packing sequence controlled by the numerical errors of planar pop-up mast consisting of five segments, with restricted simulation
- Fig. 3.42: Force-displacement diagram of five-storey planar pop-up mast controlled by numerical errors
- Fig. 3.43: Modeling packing of non-stiffened mast by controlling the displacement of the top nodes
- Fig. 3.44: Modeling the uniform and successive packing of non-stiffened mast by controlling the displacement of every node
- Fig. 3.45: Internal forces during packing: packing sequence of non-stiffened mast of three segments with uniform control
- Fig. 3.46: Force-displacement diagram of packing a non-stiffened mast of three segments with uniform control
- Fig. 3.47: Packing sequence of non-stiffened mast of four segments with uniform control
- Fig. 3.48: Force-displacement diagram of packing a non-stiffened mast of four segments with uniform control

- Fig. 3.49: Packing simulation of a non-stiffened mast of five and six segments with uniform control
- Fig. 3.50: Impossible closure of masts with odd number of segments - equilibrium path in function of the half-lengths of the elastic horizontal bars in case of $k = 3$ with the 'post-packed phenomenon'
- Fig. 3.51: Fallacious packing simulation of non-stiffened mast of four segments with successive control - reaction forces
- Fig. 3.52: Modeling successive packing of non-stiffened mast by controlling the displacement of every second node
- Fig. 3.53: Packing sequence from simulation of non-stiffened mast of four segments by successive control of double segments
- Fig. 3.54: Packing simulation of non-stiffened mast of four segments by successive control of double segments -reaction forces and stresses in the horizontal bars
- Fig. 3.55: Non-restricted packing simulation of non-stiffened mast of six segments by controlling only the displacements of the top nodes
- Fig. 3.56: Modeling the restriction of 'post-packed phenomenon' for non-stiffened masts
- Fig. 3.57: Restricted packing of non-stiffened mast -force-displacement diagram and stresses during packing
- Fig. 3.58: Restricted packing of non-stiffened mast -force-displacement diagram and stresses during packing
- Fig. 3.59: Influence of segment number on the critical force of 'non-stiffened' masts for two different ratios of segment height and half-length of elastic bars

Chapter 4

- Fig. 4.1: a) Regular pentagonal antiprism; b) deployable mast offered by Hegedűs [Farkas, Friedman et al., 2011/7]
- Fig. 4.2: Planar and side view of initial -deployed-configuration (on the left) and final - packed - configuration (on the right).Intermediate states with dashed lines
- Fig. 4.3: Asymmetric freedom of motion of antiprismatic structures
- Fig. 4.4: Linear approximation for final stretching of elastic bars
- Fig. 4.5: Highest error of the linear approximation for final stretching of elastic bars for different odd sided n-gons
- Fig. 4.6: Equilibrium of basic deployable unit
- Fig. 4.7: Equilibrium path of basic deployable unit
- Fig. 4.8: Post-packed phenomenon: flipping up the bracings
- Fig. 4.9: Constants for linear approximation of critical height/radius ratio
- Fig. 4.10: Approximation of critical height: critical height/critical radius in function of initial height/initial radius, for pentagonal segment
- Fig. 4.11: Approximation of critical height: critical height/critical radius in function of initial height/initial radius for 9-gonal segment
- Fig. 4.12: Approximation for critical force: critical force in function of initial height/initial radius ratio ($x=h/R$), for pentagonal (on the left) and for 9-gonal segment (on the right) - exact solution with continuous line, linear approximation with dotted line
- Fig. 4.13: Constants for linear approximation of critical force and the error of approximation at the boundaries
- Fig. 4.14: Critical force in function of the number of vertex of the polygon in case of $h/R=1$
- Fig. 4.15: 3D view of 'alternately stiffened' antiprismatic mast from the side (a) and from the top (b)
- Fig. 4.16: Force-displacement diagram in case of successive and uniform packing- restricted packing of antiprismatic deployable mast of six segments
- Fig. 4.17: Uniform restricted packing of antiprismatic deployable mast of two segments

- Fig. 4.18: Typical force-displacement diagram - restricted packing of antiprismatic deployable mast of six segments
- Fig. 4.19: Typical restricted packing of antiprismatic deployable mast of two segments
- Fig. 4.20: Comparison of different constitutive models: stresses/E in function of the stretches analytical and numerical results
- Fig. 4.21: Packing pattern of pentagonal basic unit
- Fig. 4.22: Force-displacement diagram of basic unit in case of different n-gons
- Fig. 4.23: Influence of geometrical configuration — deployment force (maximal reaction force multiplied by the number of vertices) of basic unit in case of different n-gons
- Fig. 4.24: Influence of geometrical configuration - force displacement diagram of basic unit in case of different h/R ratios
- Fig. 4.25: Influence of geometrical configuration on the deployment load in the case of different h/R ratios
- Fig. 4.26: Force displacement diagram of a three-storey 'alternately stiffened' antiprismatic mast
- Fig. 4.27: Packing sequence of perturbation controlled unrestricted simulation
- Fig. 4.28: Force-displacement diagram of three-storey pentagonal mast - perturbation controlled unrestricted simulation
- Fig. 4.29: Perturbation-controlled unrestricted simulation of packing three-storey pentagonal mast - stresses in the elastic bars during packing
- Fig. 4.30: Modeling restriction of 'post-packed phenomenon'
- Fig. 4.31: Force-displacement diagram of three-storey pentagonal mast - perturbation controlled restricted simulation
- Fig. 4.32: Perturbation controlled restricted simulation of packing three-storey pentagonal mast - stresses in the elastic bars during packing
- Fig. 4.33: Packing sequence of three-storey 'alternately stiffened' mast with restricted simulation
- Fig. 4.34: Uniform packing of non-stiffened antiprismatic pentagonal mast with six segments - reaction forces
- Fig. 4.35: Uniform packing of non-stiffened antiprismatic pentagonal mast with six segments - stresses in the elastic bars
- Fig. 4.36: Post-packed phenomenon with controlling only the displacements of every second level
- Fig. 4.37: Checking packability of 'non-stiffened' antiprismatic masts of odd number of segments (continuous line: bottom segment, dashed line: top segment, dotted line: middle segment)
- Fig. 4.38: Checking packability of 'non-stiffened' antiprismatic masts of odd number of segments in case of $n=5,7,9,11,13$ (packability functions 4.36 and 4.37 in function of $x_l = l_b/R$)
- Fig. 4.39: Fallacious packing of non-stiffened mast of three segments
- Fig. 4.40: Fallacious packing of non-stiffened mast of three segments
- Fig. 4.41: Packing of non-stiffened mast of three segments
- Fig. 4.42: Packing of pentagonal, non-stiffened mast of five segments
- Fig. 4.43: Packing of non-stiffened mast of three segments
- Fig. 4.44: Possible packing pattern of masts consisting of five segments or more (only in the case of odd number of segments)
- Fig. 4.45: Packing of pentagonal, non-stiffened mast of five segments
- Fig. 4.46: Theoretically possible packing patterns in the case of odd segment number ($k=3,5,7$)
- Fig. 4.47: Stochastic packing pattern of non-stiffened antiprismatic mast
- Fig. 4.48: Influence of number of the segments on the critical force
- Fig. 4.49: Dynamic deployment of antiprismatic mast: deployment sequence without restriction of post-packed phenomenon
- Fig. 4.50: Dynamic deployment of antiprismatic mast: strain in the elastic bars during deployment

- Fig. 4.51: Dynamic deployment of antiprismatic mast: vertical displacement of polygonal nodes, packing sequence in accordance with Fig. 4.49
- Fig. 4.52: Dynamic deployment of the basic unit of pentagonal antiprismatic mast: deployment sequence with (poorly captured) restriction of segment intersection
- Fig. 4.53: Dynamic deployment of the basic unit of pentagonal antiprismatic mast: deployment sequence with (poorly captured) restriction of segment intersection initial self-stress ($\sigma_{\text{pre_min}} = 5000$) was smaller than $\sigma_{\text{pre_min}} = 5989$
- Fig. 4.54: Failure of damped deploying due to locking strain in the elastic bar (in green), nodal vertical displacements of the top facet (in blue) and of the middle polygon (in red)
- Fig. 4.55: Stretching in function of the current height

Chapter 5

- Fig. 5.1: Physical models
- Fig. 5.2: Difficult control of non-stiffened pentagonal unit
- Fig. 5.3: Asymmetrical freedom of motion
- Fig. 5.4: Non-stiffened pentagonal structure - locking during packing
- Fig. 5.5: Non-stiffened pentagonal structure - novel type of deployable structure
- Fig. 5.6: Deployable bridge (graphical illustration by E. Kiss)
- Fig. 5.7: Deployment control by one single cable (black stream: active cable, white strings: passive cables)
- Fig. 5.8: Artistic exploration of possible utilization (look-out tower, transom window, ventilation of dome by E. Kiss)

Annex A

- Fig. A1: Antiprismatic truss structure
- Fig. A2: Changing stiffness with changing geometry

Annex B

- Fig. B1: shallow truss and its force-displacement diagram
- Fig. B2 Force-displacement diagram with displacement control (in pink), with incremental force control (in yellow) and with additional damping (in blue) (a); Displacements in function of the time with (in brown) and without damping (in pink) with force control
- Fig. B3 Inertial effect of snapping through with damping (in brown) and without damping (in yellow) and the imposed increasing force (in blue), and damping model used for the simulation.
- Fig. B4 Force displacement diagram with only dynamical approach: simulation with three different speeds of force increment and the equilibrium path

Annex C

- Fig. C1: Packing simulation of self-locking pantographic structures: force displacement diagram and the axial forces in the scissors

Annex D

- Fig. D1: methodology for tracing force-displacement diagram of multi-storey, 'alternately stiffened' masts
- Fig. D2: Methodology for tracing force-displacement diagram of multi-storey, 'non-stiffened' masts until the first segment closure

Fig. D3: Influence of segment number on the critical force of 'non-stiffened' masts for two different ratios of segment height and half-length of elastic bars

Fig. D4: Self-developed program in MAPLE for the calculation of equilibrium paths of antiprismatic, non-stiffened structures

Annex E

Fig. E1: Different stress definitions for finite displacements

Fig. E2: Force-stretch diagram of rubber-like material from different constitutive models and from experiments [van den Bogert and de Borst, 1994]

LIST OF TABLES

Table 4.1: Highest error of the linear approximation for final stretching of elastic bars (λ_{\max}) for different odd sided n-gons

Table 4.2: Constants for linear approximation of critical height/radius ratio

Table 4.3: Constants for linear approximation of critical force and the error of approximation at the boundaries

LIST OF REFERENCES

Books, journals, proceedings

- Atake K. (1995): *Diagonal and Variable Frame Structures*, Symmetry Culture and Science Extended Abstracts I, ISIS Symmetry, vol1, pp. 53-56
- Barnes M., Dickson M. (2000): *Widespan Roof Structures*, First ed., Thomas Telford Publishing, London
- Bini D. (1972): *Expandible reinforcement structure for inflatable domes*, US Patent No 3,686,818
- Buhl T., Jensen F.V. (2004): Pellegrino S. *Shape optimization of cover plates for retractable roof structures*, Computers & Structures, Vol. 82, pp. 1227–1236
- Buri H., Weinand Y. (2008): *ORIGAMI-Folded Plate Structures, Architecture*, Proceeding of the 10th World Conference on Timber Engineering, Miyazaki, Japan, 2-5 June 2008.
- Burkhardt R.W. (1994): *A Practical Guide to Tensegrity Design*, Cambridge, Massachusetts: Software Services
- Clarke R.C. (1984): *The kinematics of a novel deployable space structure system*, Proceedings of the 3rd, H. Nooshin: International Conference on Space Structures, University of Surrey, Guildford, UK, London, pp.820-822
- Dallinger S., Kollegger J. (2009): *Pneumatic formwork for concrete and ice shells*, Proceeding of the Int. Conf. on Textile Composites and Inflatable Structures, Structural Membranes, CIMNE, Barcelona
- Emmerich D.G. (1964), *Construction de réseaux autotendants*, French Patent No. 1,377,290
- Escrig F., Valcarcel J.P., Sanchez J.S. (1996/1): *Las Cubiertas Despliegables de Malla Cuadrangular*, Boletín Académico de Universidad de Coruña, Escuela Técnica Superior de Arquitectura, -Nº20 ;
- Escrig F., Brebbia C. (1996/2): *Mobile and Rapidly Assembled Structures*, II, First ed. Computational Mechanics, Southampton, UK
- Friedman, N. Ibrahimbegovic, A. Farkas, Gy.(2008): *Quick Construction by Deployable Structures: A study on Deployable Structures Enabling a Quick Constructional Method*, Proceeding of the NATO-ARW, 2008: *Damage Assessment and Reconstruction After Natural Disasters and Previous Military Activities*, Sarajevo, Bosnia-Herzegovina, 2008.09.05-2008.09.09, Springer, Dordrecht, Hollandia, pp.315-321
- Friedman N., Farkas Gy., Ibrahimbegovic A. (2011/1): *Deployable/retractable structures towards sustainable development*, Pollack Periodica, Vol.6, No.2, pp.85-97
- Friedman, N. Farkas, Gy. Ibrahimbegovic A (2011/2): *Az esernyőtől az adaptív-interaktív épületekig — Nyitható-csukható rúdszerkezetek az építészetben*, Magyar Építőipar, Vol.61. No.2, ed.: Antalffy, K., Budapest, pp. 67-73. 2011.
- Friedman, N. Gidófalvy, K. Hegedűs, I. Farkas, Gy. Ibrahimbegovic, A. (2011/3): *Deployment analysis of an antiprismatic snap-through type cylindrical space truss and proposal for a pop-up bridge construction*, Proceeding of the IASS-IACM 2012: *Computational Mechanics for Spatial Structures* (accepted, not published yet)
- Friedman, N., György Farkas, Adnan Ibrahimbegovic (2011/4): *Overview of highly flexible, deployable lattice structures used in architecture and civil engineering undergoing large displacements*, J. of Multibody Dynamics, (under submitting)
- Friedman, N.; Farkas, Gy.; Ibrahimbegovic, A.: *Parametric study of the elementary segment of an antiprismatic snap-through type deployable lattice column*, J. of Computers and Structures (2011/5), (under submitting)
- Friedman, N.; Weiner, M.; Farkas, Gy.; Hegedűs, I.; Ibrahimbegovic A. (2011/6): *On the snap-back behavior of a self-deploying antiprismatic column during packing*, J. of Computers and Structures (submitted)

- Farkas, Gy.; Friedman, N.; Németh, O.I. (2011/7): Környezetbarát anyagok és technológiák a tartószerkezetek építésénél, Építőmérnöki Kar a Kutatóegyetemért, pp. 49-54, ISBN 978-963-313-042-1
- Fuller B. R. (1962): *Tensile integrity structures*, US Patent No 3063521;
- Fuller B.R., Applewhite, E.J.: Synergetics (1975): *Explorations in the Geometry of Thinking*, Scribner
- Gant C. (1996): Proceedings `Conceptual Design of Structures`, Stuttgart, pp. 222-229
- Gantes C.J. (2001): *Deployable Structures: Analysis and Design*, WIT Press, Southampton, Boston;
- Gengnagel Ch., Barthel, R. (2001): *Bewegliche Dächer*, Detail 5/2001, pp. 841-854
- Gengnagel Ch. (2002): *Arbeitsblätter Tensegrity*, München, Technische Universität, Fakultät für Architektur
- Gioncu V (2005): *Phenomenological Modeling of Instability*, Phenomenological and Mathematical modeling of Structural Instabilities, M. Pignataro, V. Gioncu, SpringerWienNewYork, pp. 85-134
- Arzu GÖNENÇ SORGUÇ, ICHIRO HAGIWARA, Semra ARSLAN SELÇUK (2009): *Origamics in architecture: a medium of inquiry for design in architecture*, METU JFA, Vol. 2 (26:2), pp. 235-247
- Hachem C., Karni, E. Hanaor A. (2004): *Deployable Structures in Nature: Examples, Analysis and Realization*, Extended proceeding of the IASS Symposium (CD-ROM) From Models to Realization, September 20-24, Montpellier, France, Ref. No.: TP 124
- Hanaor A. (1987): "Preliminary Investigation of Double-Layer Tensegrities," in H.V. Topping, ed., Proceedings of International Conference on the Design and Construction of Non-conventional Structures, Vol. 2, Edinburgh, Scotland: Civil-Comp Press
- Hegedűs, I. (1986): *Analysis of Lattice Single Layer Cylindrical Structures*, Space Structures, vol.2, pp.87-91
- Hegedűs I. (1993): *Branching of Equilibrium Paths in a Deployable Column*, International Journal of Space Structures, Special Issue, vol 8, pp.119-125
- van Hennik, P.C., Houtman R. (2008): *Pneumatic Formwork for Irregular Curved Thin Shells*, Textile Composites and Inflatable Structures II, Computational Methods in Applied Sciences, Vol. 8, pp. 99-116, DOI: 10.1007/978-1-4020-6856-0_7
- Hoberman C. (1990): *Reversibly expandable doubly-curved truss structure*, US Patent N° 4,942,700;
- Hoberman C. (1991): *Radial expansion/retraction truss structures*, US Patent No 5,024,031.
- Hoberman C. (2004): *Retractable structures comprised of interlinked panels*, US Patent No 6,739,098;
- Hoberman C, Davis M. (2009): *Panel assemblies for variable shading and ventilation*, Patent No 7,584,777
- Holgate A. (1997): *The Art of Structural Engineering - The work of Jörg Schlaich and his Team*, Axel Menges, Stuttgart/London
- Hugh A. (1976): *An Introduction to Tensegrity*, Berkeley, California: University of California Press
- Ibrahimbegovic A., Taylor R. L. (2003): *Nonlinear Dynamics of Flexible Multibody Systems*, Computers and Structures, 81, pp.1113-1132
- Ibrahimbegovic, A., Schiehlen W. (2001): *Computational Techniques and Applications in Nonlinear Dynamics of Structures and Multibody System*, Proceedings EUROMECH-427, Cachan, September 24-27
- Ibrahimbegovic A., Knopf-Lenoir C., Kucerova A., Villon P. (2004): *Optimal design and optimal control of elastic structures undergoing finite rotations and deformations*, International Journal for Numerical Methods in Engineering, vol. 61, pp.2428-2460
- Ibrahimbegovic A.; Knopf-Lenoir C. (2003): *Shape Optimisation of Elastic Structural Systems Undergoing Large Rotations: Simultaneous Solution Procedure*, Computer Modeling in Engineering Science, vol. 4, pp. 337-344
- Ibrahimbegovic A. (2003): *On the geometrically exact Formulation of Structural Mechanics and Its Applications to Dynamics, Control and Optimization*, Comptes Rendus de l'Academie des Sciences, Part II : Mécanique, vol. 331, pp. 383-394
- Ibrahimbegovic A., Taylor R.L. (2002): *On the role of frame-invariance of structural mechanics models at finite rotations*, Computer Methods in Applied Mechanics and Engineering, 191, pp. 5159-5176;

- Ibrahimbegovic A., Mamouri S., Taylor R.L., Chen A., (2000): *Finite Element Method in Dynamics of Flexible Multibody Systems: Modeling of Holonomic Constraints and Energy-Conserving Integration Schemes*, Multibody System Dynamics
- Ibrahimbegovic A., Mamouri S. (2000): *On Rigid Components and Joint Constraints in Nonlinear Dynamics of Flexible Multibody Systems Employing 3D Geometrically Exact Beam Model*, Computer Methods in Applied Mechanics and Engineering
- Ibrahimbegovic A., Al Mikdad (2000): *Quadratically Convergent Direct Calculation of Critical Points for 3D Structures Undergoing Finite Rotations*, Computer Methods in Applied Mechanics and Engineering
- Ibrahimbegovic, A. (2009): *Nonlinear Solid Mechanics: Theoretical formulations and Finite Element Solution Methods*, Springer, Series Solid Mechanics and its application, vol.160.
- Ishii K. (2000): *Structural Design of Retractable Roof Structures*, WIT Press, Southampton, Boston
- Jáuregui, G. (2010): *Tensegrity Structures and their Application to Architecture*. Santander: Servicio de Publicaciones de la Universidad de Cantabria
- Jensen, F. V. (2001): *Cover Elements for Retractable Roof Structures*, Department of Engineering University of Cambridge, First-year report submitted to the University of Cambridge on the progress of Ph.D.-work
- Jensen F.V., Pellegrino S. (2004): *Expandable "blob" structures*, Extended proceeding of the IASS Symposium (CD-ROM) From Models to Realization, September 20-24, Montpellier, France, Ref. No.: IL 014
- Kassabian P. E.(1997): *Investigation into a type of deployable roof structure*, Final year project, University of Cambridge, Engineering Department
- Kassabian P.E., You Z., Pellegrino S. (1999): *Retractable roof structures*, Proceedings of Institution of Civil Engineers - Structures and Buildings, vol. 134(1), pp.45-56
- Kawaguchi M., Abe M. (2002): *On some characteristics of pantadome system*, IASS 2002: Lightweight Structures in Civil Engineering, proceedings of the international symposium, Warsaw, Poland, 24-28 June, Micro-Publisher Jan B. Obrebski, pp.50-57
- Kibert, Ch. (2007): *Sustainable Construction: Green Building Design and Delivery*, Wiley;
- Kokawa, T. (2000): *Structural idea of retractable loop-dome*, Journal of the International Association for Shell and Spatial Structures (IASS), 1, pp.111-116
- Kollegger J., Nemes R., Preisinger C., Kratochvill A., Torghele H. (2005): *Reinforced concrete shells without formwork – a new approach to the construction of RC – shells* Proceeding of fib Symposium Keep Concrete Attractive, Budapest, Hungary
- Kovács F., Tarnai T., Guest S.D, Fowler P.W., (2004): *Double-link expandohedra: a mechanical model for expansion of a virus*, Proc. Roy. Soc. A, vol. 460, No 2051, pp.3191-3202
- Kovács F. (2004/2): *Symmetry-adapted mobility and stress analysis of spherical and polyhedral generalized bar-and-joint structures*, PhD dissertation submitted to the BME
- Krishnapillai A., Zalewski W. P. (1985): *The design of deployable structures - Kinematic design*, Unpublished Research Report, Department of Architecture, MIT, Cambridge, Massachusetts, USA, October
- Krishnapillai A., Crawley E. (1986): *Deployable structures - Kinematic design*, Unpublished Research Report, Department of Aerospace Engineering, MIT, Cambridge, Massachusetts, USA, October, 1986.
- Krishnapillai A. (1992): *Deployable structures*, US Patent No. 5 167 100
- Krishnapillai A., Liew J.Y.R., Vu K.K. (1994): *Deploy & Stabilize Spatial Structures*, Extended proceeding of the IASS Symposium (CD-ROM) From Models to Realization, September 20-24, Montpellier, France, Ref. No.: PO 020
- Kronenburg R. (2008): *Portable Architecture: Design and Technology*, Birkhäuser Architecture;
- Love A.E.H. (1944): *A treatise on the mathematical theory of elasticity*, Fourth Edition, Dover Publications, New York
- Mikulas M.M.Jr., Wada B.K., Farhat C., Thorwald G., Withnell P. (1992): *Initially Deformed Truss Geometry for Improving the Adaptivity Performance of Truss Structures*, Third International Conference

- on Adaptive Structures, Wada B.K., Natori M, Breitback E, Nov 9-11, San Diego, California, USA, pp. 305-319
- Motro R. (1987): *Tensegrity Systems for Double-Layer Space Structures*, ed. H.V. Topping, Proceedings of International Conference on the Design and Construction of Non-conventional Structures, Vol. 2, Edinburgh, Scotland: Civil-Comp Press
- Motro R., Bouderbala M., Lesaux C., Cévaer F. (2001): *Foldable tensegrities*, Deployable Structures, Springer-Verlag Wien, New York, pp 199-238
- Motro R. (2006): *Tensegrity: Structural Systems for the future*, Butterworth-Heinemann;
- Onoda J., Fu D.-Y., Minesugi K. (1996): *Two-Dimensional Deployable Hexapod Truss*, Journal of Spacecraft and Rockets, Vol. 33, No.3, pp. 416-421
- Otto F et al (1971): *Convertible Roofs*, Institut for Leightweight Structures, Univ. Stuttgart, IL5
- Otto F. (1973): *Tensile structures*, Vol. 1: *Pneumatic structures* and Vol.2: *Cables, nets and membranes*, The MIT Press, Cambridge, Massachusetts
- Otto F., Rasch, B. (1995):, *Finding form*, Deutscher Werkbund Bayern
- Pellegrino S., Kwan A. S. K., You Z. (1993): *Active and passive cable elements in deployable masts*, Int. J. Space Structures, Vol. 8, No. 1-2, , pp. 29–40
- Pellegrino S. (2001): *Deployable Structures*, Springer-Verlag Wien, New York
- Pinero E.P. (1961): *Project for a mobile theatre*, Architectural Design, vol. 12, pp. 154-155
- Pugh, A. (1976): *An Introduction to Tensegrity*, Berkeley, California: University of California Press.
- Raskin I. (1998): *Stiffness and Stability of Deployable Pantographic Columns*, thesis dissertation, University of Waterloo, Ontario, Canada
- Robbin, T. (1996): *Engineering a New Architecture*, Yale University Press, London
- Rosenberg D. (2010): *Designing for Uncertainty: Novel Shapes and Behaviors using Scissor Pair Transformable Structures*, MSC dissertation at the MIT Computation Group
- Roessler, S.R., Bini, D. (1986): *The Binishell system - Thin Shell Concrete Domes*, Concrete International, Vol January
- Sadler, S. (2005), *Archigram: Architecture without Architecture*, Cambridge, MIT Press
- Snelson, K. (2009): *Forces made visible*, Hudson Hills Press LLC
- Sobek, W. (1999): *Art of Engineering*, Bales, Boston
- Tarnai T. (2001): *Infinitesimal and Finite Mechanisms* in S. Pellegrino *Deployable Structures*, Springer Wien New York pp.13-143
- Tibert, G. (2002): *Deployable Tensegrity Structures for Space Applications*, Doctoral Thesis for the Royal Institute of Techn. Dpt. of Mechanics
- Tillner S. (2003): *Mobile Hofüberdachung in Wien*, Deutsche Bauzeitschrift, Wien, 4/2003, S. pp.48-53;
- Tran T.C., Liew R.J.Y. (2006): *Butterfly structure for spatial enclosures*, Journal of the International Association for Shell and Spatial Structures: IASS, Vol47, No. 3
- United Nations (1987): *Report of the World Commission on Environment and Development*, General Assembly Resolution 42/187
- Vincent J.F.V.(2001): *Deployable structures in nature*, S. Pellegrino: *Deployable Structures*, Springer-Verlag Wien, New York, pp 37-51
- Vu K.K, Tran T.C., Liew J.Y.R., Krishnapillai A. (2006/1): *Deployable Tension-Strut Structures : From Concept to Implementation*, Journal of Constructional Steel Research Vol. 62, pp.195-209
- Vu K.K, Tran T.C., Liew J.Y.R., Krishnapillai A. (2006/2): *Deployable Tension-Strut Structures : Design Guidelines*, Adaptable 2006, TU/e, International Conference on Adaptable Building Structures 7-136, Eindhoven, Neatherlands, 03-05 July
- Wada B.K., Fanson J.L., Garba J.A., Chen G.S.(1988): *Adaptive structures to meet future requirements for large precision structures*, Proceeding of the International Conference on Spacecraft Structure and Mechanical Testing, Noordwijk, Netherlands, pp. 121-126
- Webb J.E, Mauch, H.R. (1969): *Deployable Laticce Column*, USA Patent No. 348 627 9

- Whitehead, I. (2000): *Steel mesh and engineering wizardry unfold into a dome*, Architectural Record, 2000.oct. pp. 79-80
- You Z., Pellegrino S. (1997): *Foldable bar structures*, Int J. Solids Struct, vol. 34(15), pp. 1825-1847
- Zeigler T.R. (1976): *Collapsible self-supporting structure*. Us Patent No.3,968,808
- Zeigler T. R. (1977): *Collapsible self-supporting structures*, Us Patent No.4,026,313
- Zuk, W., Clark R. (1970): *Kinetic Architecture*, New York: Van Nostrand Reinhold

Electronical References from the Web

- ABDR: *Design of a tensegrity flat*, source: <http://complexity.com/wp-content/uploads/2010/03/v3-535x800.jpg>
- Anupam: Eco Architecture: Kurilpa Bridge- The world's largest solar-powered footbridge <http://www.ecofriend.com/entry/eco-architecture-kurilpa-bridge-the-world-s-largest-solar-powered-footbridge/>
- Atake K.: Webpage of ATAKE space Design Laboratory Co., Ltd. Japan by Atake, K.: <http://www.atake-i.com/marabwhtm/marabwf2.htm>, <http://www.atakebones.com/atakemannual.pdf>, last visited 07.10.2010.
- DSL: website of the former Deployable Structures Laboratory <http://www2.eng.cam.ac.uk/~sdg/dstruct/ssda.html> last visited: 18.10.2011.
- Binishell System: *Image of the erection of a Binishell Dome*, courtesy of Binishell System, source: http://www.binisystems.com/slide/image/b_3.jpg;
- Festo: Photo of the Airteature Exhibition Hall, courtesy of Festo, source: http://www.tensinet.com/project_files/3753/AIRTEC_ESSLIN_FESTO_EXHIBI_PD01.jpg
- Fox M.A.: Beyond kinetic, Kinetic Design Group, web: <http://robotecture.com/Papers/Pdf/beyond.pdf>, last visited: 02/04/2011
- Fox M.A., Yeh P. (2008): *Intelligent kinetic system*, <http://kdg.mit.edu/Pdf/iksov.pdf> last visited 08/09/2010
- Happold, Hoberman R.: webpage of Adaptive Building Initiative by Buro Happold and Hoberman Associates, <http://www.adaptivebuildings.com/our-interactives-iris.html> last visited: 07.10.2010.
- Herder, A. (2008): *Synchronised Activation of Single-curved Tensegrity Grids for Responsive Architecture*, [http://www.arnoudherder.nl/Figures/Tensegrity/Synchronised 20Activation 20of 20Single-curved 20Tensegrity 20Grids 20for 20Responsive 20Architecture.pdf](http://www.arnoudherder.nl/Figures/Tensegrity/Synchronised%20Activation%20of%20Single-curved%20Tensegrity%20Grids%20for%20Responsive%20Architecture.pdf)
- Hoberman R.: *Portfolio of Hoberman Associates* <http://www.hoberman.com/portfolio.php>, <http://www.hoberman.com/HobermanPortfolio.pdf>
- Hunter S. W.: Webpage of University of Arizona Library by Spencer W. Hunter: <http://www.u.arizona.edu/~shunter/pinero.jpg>, last visited: 10.10.2010.
- JPL: Website of Jet Propulsion Laboratory (California Institute of Technology) http://nmp.nasa.gov/st8/tech/sailmast_tech3.html http://nmp.nasa.gov/st8/images/sailmast_diagram.gif, http://nmp.nasa.gov/st8/images/mast_coiled_labels.jpg last visited 18.03.2010.
- Komjádi: photo of the Komjádi swimming pool source: <http://www.futas.net/hungary/Budapest/photo/budapest-csaszar-komjadi-uszoda.jpg>
- Lindstrand (2006): *Heathrow airport*, courtesy of Lindstrand Technologies, http://www.lindstrandtech.com/pop_heathrow_roofs.html; photo source: http://www.lindstrandtech.com/images/pic_popup_heathrow2.jpg
- Nomadic: Webpage of Nomadic Display Corp.: <http://www.nomadicdisplay.com/displays/custom-portable/> last visited: 07.10.2010.
- Tolivero: *Photo of the Olympic Stadium in Montreal*, source: http://en.wikipedia.org/wiki/File:Le_Stade_Olympeque_3.jpg

- Pirs SA.: Images of inflatable formwork concrete construction and structure, courtesy of PIRS SA.;sources:http://www.domepirs.com/img_gonflage2.jpg;http://www.domepirs.com/img_ferrailbeton.jpg;http://www.domepirs.com/img_poisson3.jpg
- Wadee M.K.: (<http://www.people.ex.ac.uk/mkwadee/yoshimura1.jpg>
http://farm1.static.flickr.com/130/398478818_2d560a1cdd.jpg
- Walter M.: *Convertible Roofs*, Kurs 4: Numerische Optimierung und Formfindung – Realisierung an einem Membrantragwerk, Ferienakademie;
http://www.st.bv.tum.de/content/teaching/ferienakademie/handouts/14_walter_handout.pdf last visited: 09.10.2010, image source:
http://1.1.1.1/bmi/www.instablogsimages.com/images/2009/10/05/kurilpa-bridge_1_og9K7_69.jpg

INDEX

- Abstract, 5
 Absztrakt, 6
 Alternately stiffened antiprismatic structure
 analytical investigation, 117–20
 dynamic analysis, 141–46
 numerical analysis, 125–30
 physical models, 149–53
 Angulated element, 26
 Antiprism, 104
 Approximation
 of critical force, 115–17
 of critical height, 113–15
 of maximal stretching, 107–9
 Arch-length method, 80
 Asymmetric freedom of motion
 of antiprismatic structure, 106
 of planar model, 52
 Bini, 46
 Constitutive laws, 185–86
 Contents, 7–10
 Critical segment number
 for antiprismatic model, 119
 for planar model, 65–66
 Dallinger, 47
 Deployable Antenna, 20
 Deployable structures undergoing instability phenomenon
 Antiprismatic column, 37
 Coilable mast, 37
 Pantographic lattice designs, 24–26
 Shallow truss, 163–67
 Emmerich, 34, 195
 Energetical approach, 178–84
 Escrig, 14, 15, 23, 48, 187, 195
 Fanning, 37
 FEAP, 81
 Folding patterns, 20
 Fuller, 15, 34, 35, 187, 188, 196
 Gantes, 11, 16, 23, 24, 25, 26, 50, 157, 196
 Hegedús, 3, 5, 11, 12, 37, 49, 50, 104, 105, 111, 141, 147, 157, 158, 188, 191, 196
 Herder, 36
 History of transformable structures, 14–16
 Hoberman, 21, 22, 26, 27, 28, 30, 31, 49, 187, 188, 196, 197
 Holloway, 37
 Introduction, 11–13
 Kassabian, 30, 31, 197
 Kawaguchi, 31, 32, 48, 188, 198
 Kolleger, 47
 Krishnapillai, 26, 38, 39, 50, 188, 198, 199
 Liew, 38, 198, 199
 MAPLE, 81
 Membrane structures (foldable), 42–44
 Bullfighting Arena in Zaragoza, 42
 Olympic Stadium in Montreal, 42
 Rathaus, Vienna, 43
 Umbrella structures, 43
 Membrane structures (pneumatic), 45
 Double-layer systems, 45
 Single-layer systems, 45
 Mikulas, 38
 Motro, 15, 34, 35, 36, 198
 Multi-angulated elements, 28
 Non-stiffened antiprismatic structure
 analytical investigation, 120–21
 numerical analysis, 130–40
 physical models, 149–53
 Novel type of deployable structure
 analysis, 132–39
 physical model, 153
 numerical analysis of alternately stiffened structure
 numerical analysis of alternately stiffened structure, 83–91
 Onoda, 38
 Otto, 14, 15, 17, 40, 41, 43, 48, 187, 189, 198, 199
 Packability of ‘non-stiffened’ antiprismatic masts, 132–39
 Pantographic systems, 22–33
 Deployable mast, 24
 Escrig's deployable swimming pool, 23
 Foldable bridge, 24
 Foldable dome, 24
 Pantadome erection, 31–33
 Pinero's foldable theatre, 22–23
 Retractable pantograph structures, 26–31

- Self-locking deployable structures, 24
- Parameter analysis, 122–24
- Pellegrino, 11, 15, 20, 24, 26, 27, 28, 29, 37, 48, 49, 154, 187, 188, 195, 197, 199, 200
- Penalty approach
for antiprismatic model, 128
for planar model, 88–89
- Pinero, 15
- Piola-Kirchoff stress, 185
- Planar (simplified) pop-up model, 50–103
analytical investigation of basic segment, 51–56
analytical investigation of alternately stiffened structure, 56–73
analytical investigation of non-stiffened structure, 73–79
numerical analysis of basic element, 81–83
numerical analysis of non-stiffened structure, 92–101
- Pneumatic systems for erection, 46–48
Binishells, 46
Pneumatic formwork methods, 46
Segmented concrete or ice domes, 47–48
- Post-packed phenomena
for antiprismatic structure, 111–12
for planar model, 54–55
- Pugh, 34
- Resume, 5
- Retractable covering, 17–22
- Retractable roof structures
Abu Dhabi's international airport, 30
Civic Arena, 15
Fukuoka stadium, 17–18
Iris Dome, 27–28
Komjádi swimming pool, 19
Montreal Olympic Stadium, 15
Oita Stadium, 18
Qi Zhong stadium, 19
Roman Colosseum, 14
Toronto Skydome, 19
- Retractable shading systems
Aldar Central Market, 21
Audencia Provincial, 21
Saint-Venant-Kirchoff, 185
Scissor-like element (SLE), 22
Snap-back phenomenon, 5, 12, 61, 62, 65, 66, 80, 86, 90, 100, 147, 159, 160, 166, 189, 196
Snelson, 15, 34, 199
- Soft, membrane structures, 40–45
- Static and kinematic determinacy of antiprismatic structures, 161–62
- Summary
antiprismatic structures, 147–48
architectural background, 48–49
simplified planar model, 102–3
thesis, 157–60
- Sustainable architecture, 16
- Tarnai, 3, 104, 161, 198, 199
- Tensegrity structures, 34–36
Brisbane Bridge, 34
Foldable tensegrities, 35–36
Tensegrity dome, 34
- Transformable lattice structures, 22–40
- Zeigler, 11, 15, 24, 25, 49, 50, 157, 188, 200